# Signal Processing in Microwave SQUID Multiplexer-Based Systems for Readout of Magnetic Microbolometers Detector Arrays

Zur Erlangung des akademischen Grades eines

**DOKTORS DER INGENIEURWISSENSCHAFTEN (Dr.-Ing.)**

von der KIT-Fakultät für Elektrotechnik und Informationstechnik des Karlsruher Instituts für Technologie (KIT)

angenommene

DISSERTATION von

**DIPL.-ING. JUAN MANUEL S. SALUM**

geboren in: Buenos Aires, Argentina

| | |
|---|---|
| Tag der mündlichen Prüfung: | 08.04.2025 |
| Hauptreferent: | Prof. Dr. Marc Weber |
| Korreferent: | Prof. Dr.-Ing. Manuel Platino |

Karlsruher Institut für Technologie

UNSAM

# Signal Processing in Microwave SQUID Multiplexer-Based Systems for Readout of Magnetic Microbolometers Detector Arrays

Para obtener el título académico de

**DOCTOR EN CIENCIAS APLICADAS Y DE LA INGENIERÍA**

de la Escuela de Ciencia y Tecnología de la Universidad Nacional de San Martín (UNSAM)

versión aprobada

DISERTACIÓN de

**ING. JUAN MANUEL S. SALUM**

nacido en: Buenos Aires, Argentina

Fecha de la defensa oral: 08.04.2025
Director por UNSAM: Prof. Dr.-Ing. Manuel Platino
Director por KIT: Prof. Dr. Marc Weber

Karlsruher Institut für Technologie

UNSAM

**Resumen**

El Microbolómetro Magnético (MMB), un novedoso detector de baja temperatura, representa una tecnología prometedora para una amplia gama de experimentos de vanguardia que utilizan arreglos de detectores criogénicos, debido a su alta sensibilidad.

El multiplexor SQUID de microondas ($\mu$MUX) es el sistema seleccionado para la lectura de los MMB debido a su alto factor de multiplexación y gran sensibilidad, gracias al uso de Dispositivos de Interferencia Cuántica Superconductora de radiofrecuencia (rf-SQUID). Al mismo tiempo, el $\mu$MUX requiere de una electrónica de temperatura ambiente (RTE), basada en un esquema de Radio Definida por Software (SDR), que permite la medición simultánea de todo el arreglo de detectores, brindando notable versatilidad y flexibilidad.

Esta tesis contribuye al desarrollo del sistema de RTE para la lectura de arreglos de MMB, presentando el diseño de un sistema de adquisición para 1024 canales de un $\mu$MUX, con un ancho de banda de 4 GHz a 8 GHz. Si bien los requisitos del sistema están basados en el instrumento Q&U Interferómetro Bolométrico para Cosmología (QUBIC), cuya motivacion científica es la detección de la polarización de la Radiación de Fondo de Microondas Cósmica (CMB), la flexibilidad del sistema permite su adaptación a otros experimentos. Esta capacidad lo convierte en una herramienta valiosa para una amplia variedad de instrumentos científicos que utilizan matrices de detectores de bajo ruido.

El objetivo principal de esta investigación es diseñar e implementar la generación de la señal de modulación de los detectores, el diseño de la cadena de señal, que incluye el setup de baja temperatura, y los algoritmos de procesamiento. Además, se realiza la caracterización y verificación de este diseño aplicado a los MMB. Adicionalmente, se implementa un demodulador de múltiples canales para obtener las señales de cada detector, el cual se integra completamente con el sistema de adquisición y procesamiento.

Finalmente, se ensambla un prototipo completo que incluye la RTE y el setup criogénico para la medición de 4 canales de un $\mu$MUX. Como resultado, esta tesis presenta la primera versión de un sistema completamente integrado y funcional para la lectura de un arreglo de MMBs.

**Zusammenfassung**

Das Magnetische Mikrobolometer (MMB), ein neuartiger Tieftemperaturdetektor, stellt dank seiner hohen Empfindlichkeit eine vielversprechende Technologie für eine breite Palette von fortschrittlichen Experimenten dar, die Anordnungen kryogener Detektoren verwenden.

Aufgrund seines hohen Multiplexfaktors und seiner hohen Sensitivität, die durch die Verwendung von Radiofrequenz-Superconducting Quantum Interference Devices (rf-SQUID) erreicht wird, ist der Mikrowellen-SQUID-Multiplexer ($\mu$MUX) das ausgewählte System für die Auslese der MMBs . Gleichzeitig erfordert der $\mu$MUX eine Elektronik bei Umgebungstemperatur (RTE), die auf einem Software-defined Radio (SDR)-Schema beruht, was die gleichzeitige Messung des gesamten Detektorarrays ermöglicht und hohe Vielseitigkeit und Flexibilität bietet.

Diese Dissertation trägt zur Entwicklung des RTE-Systems zur Auslesung von MMB-Arrays bei und stellt das Design eines Erfassungssystems für 1024 Kanäle eines $\mu$MUX mit einer Bandbreite von 4 GHz bis 8 GHz vor. Obwohl die Anforderungen des Systems auf dem Q&U-Bolometer-Interferometer für die Kosmologie (QUBIC) beruhen, dessen wissenschaftliches Ziel die Detektion der Polarisation der Kosmischen Mikrowellen-Hintergrundstrahlung (CMB) ist, ermöglicht die Flexibilität des Systems seine Anpassung an andere Experimente. Diese Anpassungsfähigkeit macht das System zu einem wertvollen Werkzeug für eine Vielzahl wissenschaftlicher Instrumente, die rauscharme Detektorarrays verwenden.

Das Hauptziel dieser Forschung ist es, die Modulationssignal-Generierung der Detektoren zu entwerfen und umzusetzen, das Design der Signalstruktur, einschließlich des Niedrigtemperatur-Setups, sowie die erforderlichen Signalverarbeitungsalgorithmen. Darüber hinaus wird die Charakterisierung und Verifizierung dieses Designs für die Anwendung auf MMBs durchgeführt. Als Teil der Systemintegration wird ein Mehrkanal-Demodulator implementiert, um die Signale jedes Detektors zu extrahieren. Der Demodulator wird vollständig in das Erfassungs- und Verarbeitungssystem integriert.

Schließlich wird ein vollständiger Prototyp assemblierte, der die RTE und das kryogene Setup umfasst, um 4 Kanäle eines $\mu$MUX zu messen. Das Ergebnis dieser Dissertation ist die erste Version eines vollständig integrierten und funktionalen Systems zur Auslesung eines MMB-Arrays.

**Abstract**

The Magnetic Microbolometer (MMB), an innovative low-temperature detector, represents a promising technology for a wide range of cutting-edge experiments utilizing arrays of cryogenic detectors, due to its expected high sensitivity.

The microwave SQUID multiplexer ($\mu$MUX) is the system chosen for readout the MMBs due to its high multiplexing factor and great sensitivity, thanks to the use of radio frequency Superconducting Quantum Interference Devices (rf-SQUIDs). At the same time, the $\mu$MUX requires a room temperature Electronics (RTE), based on a Software-defined Radio (SDR) scheme, which enables the simultaneous measurement of the entire detector array, providing high versatility and flexibility.

This thesis contributes to the development of the RTE system for the measurement of MMB arrays, presenting the design of an acquisition system for 1024 channels of a $\mu$MUX with a bandwidth of 4 GHz to 8 GHz. While the system's requirements are based on the Q&U Bolometric Interferometer for Cosmology (QUBIC), whose scientific motivation is the detection of the polarization of the Cosmic Microwave Background (CMB), the system's flexibility allows its adaptation to other experiments. This adaptability makes the system a valuable tool for a wide range of scientific instruments that require the measurement of high-density, low-noise detector arrays.

The main objective of this research is to design and implement the generation of the modulation signal for the detectors, the design of the signal chain, which includes the low-temperature setup, and the processing algorithms. Additionally, the characterization and verification of this design applied to the MMBs are carried out. As part of the system, a multi-channel demodulator is implemented to extract the signals from each detector. The demodulator is fully integrated into the acquisition and processing system.

Finally, a complete prototype is assembled, which includes the RTE and the cryogenic setup for measuring 4 channels of a $\mu$MUX. As a result, this thesis presents the first version of a fully integrated and functional system for the readout of an MMB array.

# Acknowledgments
# Danksagung
# Agradecimientos

The journey throughout this work has been full of ups and downs, which has required a lot of dedication and effort. Long days and sleepless nights were part of the process. However, this path has not been made alone as many people and institutions have played key roles along the way.

First, I want to thank ITeDA and its former director, Prof. Alberto Etchegoyen, for allowing me to be part of such a wonderful group of people, full of passion and commitment, who inspired and motivated me to grow and improve as a professional. ITeDA is a young institute that celebrated its 15th anniversary on November 24, 2024. In such a short time, it has reached impressive goals and become a recognized name in the scientific community, both nationally and internationally.

I am incredibly grateful to my supervisors, Prof. Manuel Platino and Prof. Marc Weber, for trusting me and giving me the opportunity to be part of the dual PhD program between UNSAM and KIT. Thanks to this privilege, I was able to contribute to a project with big goals focused on developing new and advanced technologies. I would like to particularly acknowledge UNSAM and HIRSAP for their financial contribution throughout these years.

To my colleagues Matias Hampel, Alejandro Almela, Manuel Garcia Redondo, Luciano Ferreyro, Alan Fuster, Jesus Bonilla, Juan Manuel Geria, Nahuel Müller and Juan Bonaparte, thank you for all the time spent in technical discussions and meetings. Without a doubt, those discussions made this work possible. I also want to thank and congratulate you all for your professionalism, passion and dedication. To Adrian Sedosky, for always being an inexhaustible source of software knowledge that I often turned to. To Leonardo Paolucci, whom I had the pleasure of supervising and who helped with key tasks. I also want to extend my thanks to the rest of the engineering team: Lucia Sucunza, Carlos Varela, Diego Silva, Luciana Rosellini, Nestor Del Castillo, Adrian Riello, Gustavo Dominguez, Daniel Gorbeña, Gabriel Innocenti and Pablo Strazzeri, who were always ready to lend a hand or offer their technical perspectives.

I also want to express my gratitude to the IPE and IMS teams at KIT for their support and collaboration. A special thanks goes to Oliver Sander and Nick Karcher for their sharp technical insights and thoughtful advice. To Luis Ardila, Timo Muscheid and

Robert Gartmann for our technical discussions, as well as for providing the Front-end electronic board that enabled the measurements in this work. Most importantly, I am grateful for their friendship, as well as that of Matias Wegner and the time spent together outside of KIT. I also want to thank Prof. Sebastian Kempf for welcoming our group into IMS for the fabrication of the $\mu$MUX utilized in this work.

I can't forget to thank those who weren't directly involved in the project but still contributed in meaningful ways from other places. My family and friends, both those who are with me and those who are no longer here, have been a fundamental part of my life. As social beings, they have shaped me through the countless interactions we've had. I want to especially mention my parents, Musa and Susana and my siblings, Nabil and Barbi, who have done the most for me. And to Melannie, whose love and companionship have changed my life forever.

Finally, I want to express my sincere thanks to Argentina for investing in science and technology to improve the quality of life for its people and for investing in public education, ensuring that everyone has the right to an education, which is what ultimately gives us the freedom to choose our own journey.

# Contents

**Abstract** **i**

**Acknowledgments** **iii**

**1 Introduction** **1**
1.1 High-density Cryogenic Detector Array Experiments . . . 1
1.2 Scientific Motivation . . . 3
1.2.1 Cosmic Microwave Background . . . 3
1.2.2 QUBIC experiment . . . 5

**2 Cryogenic Bolometers** **9**
2.1 Superconductivity . . . 10
2.2 Kinetic Inductance Detector . . . 11
2.3 Transition Edge Sensor . . . 11
2.4 Magnetic Microbolometer . . . 13
2.4.1 Electro-thermal system . . . 13
2.4.2 Noise Estimation . . . 16
2.4.3 Experiment requirements . . . 17

**3 Readout System** **21**
3.1 The Microwave SQUID Multiplexer . . . 21
3.1.1 Superconducting resonator . . . 21
3.1.2 Resonator-SQUID coupling . . . 23
3.1.3 Detector-Channel coupling . . . 27
3.1.4 Flux Ramp Modulation . . . 29
3.1.5 Spectral Occupation . . . 30
3.1.6 Optimal SNR . . . 33
3.2 Software-defined Radio . . . 35
3.2.1 Back-end electronics . . . 36
3.2.2 Signal converters . . . 41
3.2.3 Front-end electronics . . . 45
3.3 Readout Noise . . . 47
3.4 Towards high multiplexing . . . 48

3.5 Proposed readout system . . . 51

**4 Modulation Signal Chain** **55**
4.1 Initial Considerations . . . 55
4.1.1 Digital to Analog Converter Selection . . . 56
4.2 Cryogenic Chain Design . . . 57
4.2.1 Passive Load . . . 58
4.2.2 Active Load . . . 59
4.3 Modulation Signal Synthesizer . . . 61
4.3.1 Digital synthesis . . . 63
4.3.2 I-V Converter . . . 65
4.3.3 Filters . . . 65
4.3.4 Single-ended Voltage Output . . . 68
4.3.5 Differential Current Output . . . 68
4.3.6 Clock . . . 68
4.4 Signal Chain Noise . . . 71

**5 Digital Signal Processing** **77**
5.1 Digital Down Converter . . . 77
5.2 Digital Backend . . . 79
5.3 Flux Ramp Demodulator . . . 82
5.3.1 Error Model . . . 83
5.3.2 Windowing . . . 84
5.4 Flux Ramp Demodulator Implementation . . . 86

**6 Prototype Readout System Characterization** **89**
6.1 MSS Board Characterization . . . 90
6.1.1 Calibration . . . 90
6.1.2 Dynamic Performance . . . 91
6.2 Flux Ramp Demodulator Characterization . . . 98
6.2.1 Microwave SQUID Multiplexer Emulator . . . 98
6.2.2 Signal Recovery . . . 100

**7 Prototype Readout System Measurements** **105**
7.1 Microwave SQUID Multiplexer Characterization . . . 106
7.2 Optimal Readout Measurement Point . . . 108
7.3 Signal Recovery Capability . . . 110
7.4 Noise Comparison . . . 112

**8 Summary and Outlook** **115**

**List of Figures** **117**

**List of Tables** **121**

**List of Acronyms** **125**

**Bibliography** **127**

# Chapter 1

# Introduction

Throughout history, humanity has demonstrated curiosity to understand the Universe that surrounds us. From ancient stargazers to contemporary astrophysicists, our desire to comprehend has driven countless discoveries and innovations. Measurement has emerged as an essential task for quantitative and accurate comprehension of our environment. Early measurements were inherently subjective, relying on the inconsistent sizes of body parts such as hands and feet from one person to another. As societies advanced, the need for standardization became apparent, leading to the development of universal units of measurement and more sophisticated measurement tools.

Progress in science and technology has facilitated the development of complex measurement systems that consist of multiple integrated components working together to perform increasingly sensitive and precise measurements. For instance, the Laser Interferometer Gravitational-Wave Observatory (LIGO) [1] has enabled us to measure gravitational waves, ripples in the fabric of spacetime that were first predicted by Albert Einstein's General Theory of Relativity. LIGO's measurements have opened a new window into the cosmos, allowing us to observe cosmic events billions of light years away, providing valuable insights into the nature of gravity and thereby extending the frontiers of knowledge.

As societies continue to expand the scope and complexity of measurement systems, we draw closer not only to answering the how and why of natural phenomena but also to understanding the reasons for our existence. In doing so, we continue a journey that has been central for the evolution of the human being since the dawn of civilization.

## 1.1 High-density Cryogenic Detector Array Experiments

A fundamental component of measurement systems is the detector, which is designed to translate a physical phenomena of interest into a signal that can be easily manipulated, such as filtering, amplification and conversion, among others. There is a very wide variety of detectors that can be classified according to the physical variable to measure, working principle, application, output signal, etc. Additionally, the characteristics of detectors are

determined by various factors, including resolution, range, responsivity and sensitivity. Resolution is the smallest detectable change in the measured variable. Range is the span of values over which the detector can accurately measure the variable. Responsivity is the conversion factor between the input and output signals, which may involve a change in physical units and the attenuation or amplification of the input signal. Finally, sensitivity is the minimum input signal level that produces a detectable output signal in presence of noise. Each of these characteristics play a crucial role in determining the overall performance and suitability of a detector for a specific application.

Thermal detectors are widely utilized in several science experiments due to their performance. Ideally, thermal equilibrium detectors can achieve arbitrarily large resolution [2] in contrast to ionization detectors which are constrained by the Fano noise [3]. By the law of large numbers, the average of a large amount of measurements in uniformly thermalized structures converges to the expected value, reducing statistical fluctuations.

On the other hand, placing detectors at cryogenic temperatures have been shown to substantially enhance their resolution and sensitivity, offering several key advantages for various scientific and technical applications [4–6]. Over the past few decades, cryostats (specialized devices that maintain the ultra-cold environments) have become increasingly accessible in research centers around the World. This has paved the way for research and practical applications in various fields. Superconductivity, a macroscopic quantum phenomenon that occurs in different metals when their temperature decreases below a characteristic critical temperature ($T_c$) [7], has been a major driving force behind the development of cryostats. The rapid growth of low temperature detector technology has led to the development of readout systems capable of not degrading the performance of the detectors while meeting the demands of groundbreaking experiments [8–13]. These demands include reading out hundreds or even thousands of detectors [14], thereby statistically reducing fluctuations and/or increasing the probability of detecting events. High amounts of detectors can be arranged in what is called a high-density cryogenic detector array, maximizing spatial coverage. However, designing the entire system chain from the detector array to the readout electronics is not an easy task and various electrical, thermal and mechanical requirements must be considered. For instance, part of the system is housed inside a cryostat with limited cooling power and space. Therefore, it is essential to minimize the complexity of the cryogenic system and its connection cables to the outside. This requirement is addressed by implementing multiplexed readout systems.

Various multiplexing techniques can be employed to allow multiple signals to be transmitted over a common medium, including Time-Division Multiplexing (TDM), Frequency-Division Multiplexing (FDM), or Code-Division Multiplexing (CDM) [15]. TDM is a technique for transmitting multiple signals over a shared communication channel by allocating each signal to a specific time slot. The transmission channel is divided into equal-duration intervals, with each interval dedicated to transmitting a particular signal. This arrangement allows a single common electrical connection to serve as the output line, significantly reducing the number of connections needed for multiple channels. One of the main advantage of TDM is its low signal processing requirements compared to other methods. However, this technique is primarily constrained by the sampling time of each channel, which is affected by the number of channels being read,

as they can only be read sequentially.

CDM is an advanced telecommunications technique that enables multiple signals to share the same transmission channel simultaneously by assigning unique codes to each signal. This method, a form of spread spectrum communication, involves spreading each narrow-band signal over a broader bandwidth. By multiplying the signals with individual orthogonal functions, the resulting signal appears as noise to all receivers except the intended one, which can decode it by correlating with these functions. Walsh functions are often employed as the orthogonal basis due to their ease of generation, requiring minimal circuitry and hardware. In this approach, the data for each sample or bit is spread over the duration of the orthogonal basis period. This technique is highly efficient and is widely used in various communication systems, especially in wireless and cellular networks. The capability to accommodate multiple users on the same frequency band with minimal interference makes CDM a core technology in modern telecommunications.

FDM is a technique where multiple signals are transmitted simultaneously over a single communication channel by assigning each signal a unique frequency band within the overall bandwidth. This method effectively utilizes the available spectrum, ensuring that different signals do not interfere with each other, thereby enabling efficient and simultaneous transmission of multiple data streams. The maximum number of channels that can be transmitted over a single line is determined by taking into account the total useful bandwidth of each channel, the distance among them and the total bandwidth of the system.

The Microwave SQUID Multiplexer ($\mu$MUX) is a novel cryogenic microwave multiplexer that employs FDM technique to read out multiple cryogenic detectors at GHz frequencies [16]. In combination with the cryogenic readout, a room temperature Electronics (RTE) performs a readout system based on a Software-defined Radio (SDR) scheme [17]. Currently undergoing continuous improvement by numerous research groups around the world, this readout has already proven capable of measuring different types of detector arrays utilized in multiple experiments ranging from primordial gravitational waves physics [18], neutrino physics [19] to X-ray spectroscopy [20].

This work contributes to the development of the SDR system for multiplexing high-density cryogenic thermal detector arrays. In particular, this development is focused on the readout of the newly introduced Magnetic Microbolometers (MMB) detector [21]. This detector is being designed and optimized for the Cosmic Microwave Background Radiation (CMB) detection for the Q&U Bolometric Interferometer for Cosmology (QUBIC) instrument [22–24].

## 1.2 Scientific Motivation

### 1.2.1 Cosmic Microwave Background

The Big Bang Theory appears as a suitable model for describing the known Universe upon based on the current observations. It is known as the standard cosmology model and proposes a hot and dense primordial Universe 13.800 millions years ago, which cools

down as it expands. In this early Universe, blackbody radiation constantly scattered and interacted with free particles, hence it was an opaque Universe. As the Universe cooled down, free particles began to recombine into the first elements, leading to a transparent Universe around ∼380,000 years after the Big Bang where photons were able to travel almost freely through space. This *remnant light* of the Universe is known as the Cosmic Microwave Background (CMB) and was predicted in 1948 by Ralph Alpher and Robert Herman. In 1964, Arno Penzias and Robert Woodrow Wilson accidentally observed the CMB for the first time while using a radiometer designed for radio astronomy and satellite communications [25]. They measured *microwave noise* that matched the radiation of a black body at 3.5 K. More recently, results from Cosmic Background Explorer (COBE) confirmed that the CMB follows a perfect 2.7 K blackbody spectrum [26].

Even though the Big Bang Theory successfully explains different aspects of the observable Universe, it presents three major problems: planicity, horizon and magnetic monopoles.

1. **Planicity problem:** This phenomenon, also known as the "flatness problem", addresses why the Universe appears to be so close to geometrically flat, given the dynamics of its expansion. In the framework of general relativity, the geometry of the Universe can be described by the Friedmann-Lemaître-Robertson-Walker (FLRW) metric. The FLRW model allows for three possible geometries of the Universe, described by the cosmological density parameter, $\Omega$. For $\Omega > 1$, the geometry is spherical, predicting that the Universe will eventually stop expanding and recollapse. In the case where $\Omega < 1$, the geometry is hyperbolic and the Universe will expand forever. Observations indicate a nearly flat Universe ($\Omega \approx 1$), where the geometry is Euclidean, raising many questions about why this is the case.
2. **Horizon problem:** It concerns the uniformity of the CMB radiation, which is observed to be nearly the same temperature in all directions, despite the fact that regions of the Universe separated by vast distances (a number of light years larger than the age of the universe) should not have been able to exchange information or energy due to the finite speed of light and the age of the Universe. Therefore, these regions were causally disconnected and should not have been able to equilibrate their temperatures or any other properties.
3. **Magnetic Monopoles problem:** this problem arises from the theoretical prediction of magnetic monopoles by grand unified theories and the lack of observational evidence for these objects. Despite extensive searches, magnetic monopoles have not been detected, posing a challenge to our understanding of fundamental physics.

The Inflation Theory was proposed as a solution to these problems by Alan Guth, Andrei Linde, Paul Steinhardt and Andy Albrecht [27–29]. This theory posits that the Universe underwent an exponential expansion in the first fraction of a second after the Big Bang. During inflation, quantum fluctuations in a hypothetical *inflaton* field were amplified to macroscopic scales. The stretching of these quantum fluctuations produced small variations in the density of matter, known as density perturbations, which later evolved into the formation of the Universe's large-scale structures (stars, galaxies and

galaxy clusters). Additionally, inflation predicts the generation of primordial gravitational waves caused by these quantum fluctuations. These gravitational waves are incredibly faint but carry crucial information about the early Universe's dynamics. Their imprint might be detectable in the polarization patterns of the CMB, known as *B-mode polarization* [30, 31], providing a unique window into the inflationary period.

The CMB also contains a separate form of polarization called E-mode polarization, which arises from the density fluctuations in the early Universe. Unlike B modes, which are associated with primordial gravitational waves, E modes are more prominent and are already well observed. However, detecting the faint B-mode polarization requires developing much more sensitive instruments. The tensor-to-scalar ratio $r$ quantifies the relative contribution of primordial gravitational waves to density fluctuations and is currently constrained to be $r < 0.036$ [32]. In Fig. 1.1, the temperature and polarized anisotropies of the CMB measured by the Planck telescope are shown.

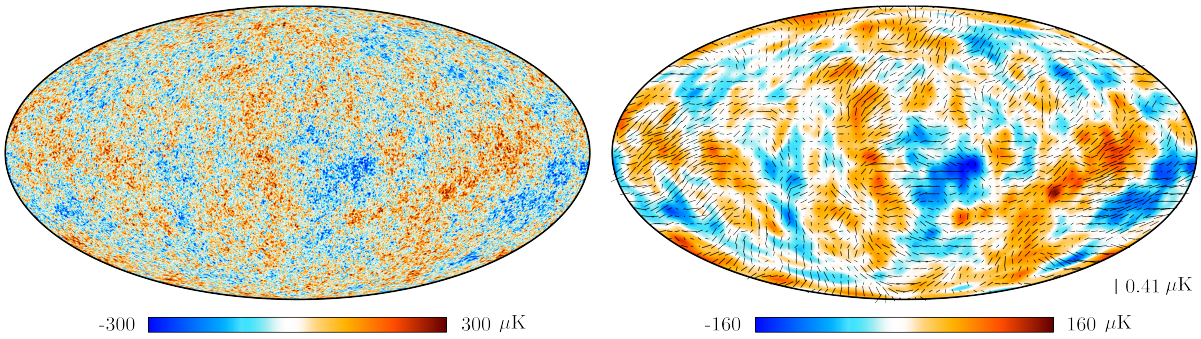


**Figure 1.1:** Planck Telescope 2018 results. CMB temperature anisotropies map (left). Map of the polarized CMB shown as black rods representing the direction and amplitude of the polarization. Background is the CMB anisotropies map smoothed to 5 degrees (right) [33].

Even if such a sensitivity can be achieved using background-limited detectors such as bolometers from low-atmospheric emission suborbital locations or from a satellite, the challenge to face for this detection remains huge because of two main reasons: instrumental systematic effects and foregrounds.

### 1.2.2 QUBIC experiment

The CMB radiation represents the oldest picture of the Universe. This radiation features minute variations in temperature and a polarization that offer insights into the formation and evolution of cosmic structures. Though temperature fluctuations and E-mode polarization in the CMB have been detected and analyzed [34, 35], the next major objective in CMB research is to observe the primordial B-mode polarization. According to inflation theory, this B-mode pattern was created by gravitational waves during a brief period of rapid expansion in the very early Universe.

There is a vast list of experiments aimed at measuring the B-mode polarization of the CMB such as QUBIC [8], LABOCA [36], Bicep2 [37], Boomerang and Maxima [38],

SPT [39], SPT-3G [40], LiteBIRD [41], POLARBEAR-2 and The Simons Observatory [42, 43]. While CMB surveys typically are classical imagers, QUBIC stands out as the first bolometric interferometer [44]. This approach combines the high sensitivity of bolometers with the effective foreground control provided by interferometry.

Polarized astronomical foregrounds refer to the polarized radiation emitted by various sources within our galaxy, which can interfere with the detection of CMB polarization. The main sources of these foregrounds are Galactic Synchrotron Emission and Thermal Dust Emission. Each source overlaps with the CMB spectrum in different regions, as Fig. 1.2 shows. However, by characterizing these foregrounds and identifying the location of the CMB emission peak, it is possible to use techniques for component separation to obtain the CMB signal.

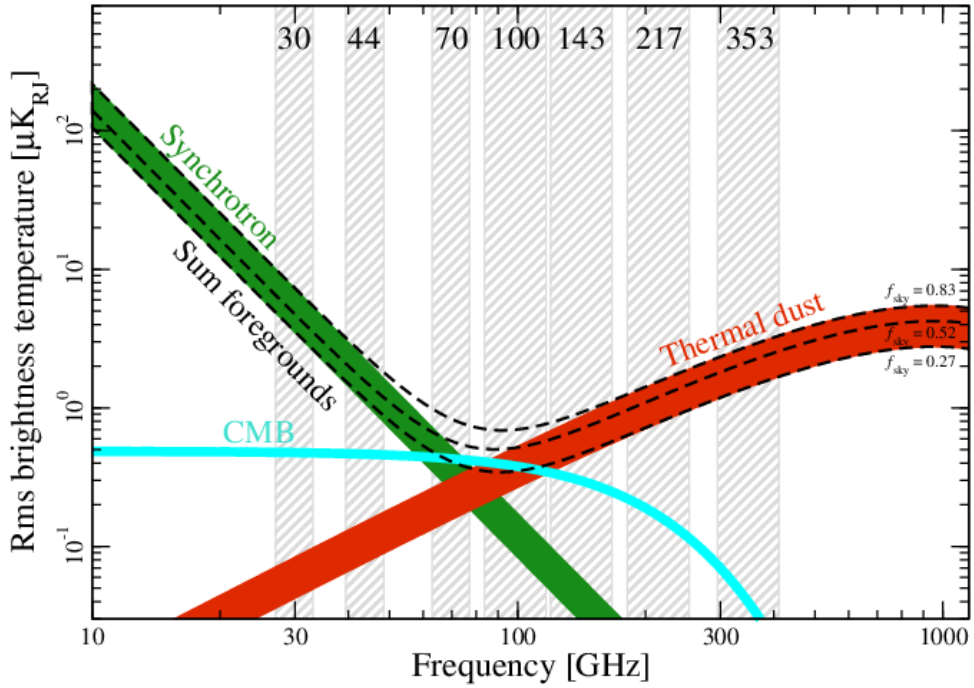


**Figure 1.2:** CMB and main foregrounds polarization spectra obtained by the Planck mission [34].

QUBIC employs a technique named Spectral Imaging [45] which consists of measuring a wide-band frequency interference fringe pattern on the focal plane (where the detectors are placed). The interference signal is the result of convolution between a sky image and the synthesized beam of the instrument. Thereafter, the measured signal is split in multiple frequency sub-bands for foreground mitigation using post-processing.

Fig. 1.3 illustrates a sketch of the QUBIC Telescope. It shows the infrared filters (IR), a rotatory Half-Wave Plate (HWP) [46], a polarizing grid [47], a back-to-back antenna horn array [48], two mirrors and a dichroic that direct the incoming radiation towards the focal plane. Each focal plane contains arrays of Transition Edge Sensor (TES) detectors operating at 150 GHz and 220 GHz and at a temperature of 320 mK [49].

By the use of switches in the back-to-back horns, it is possible to switch on and

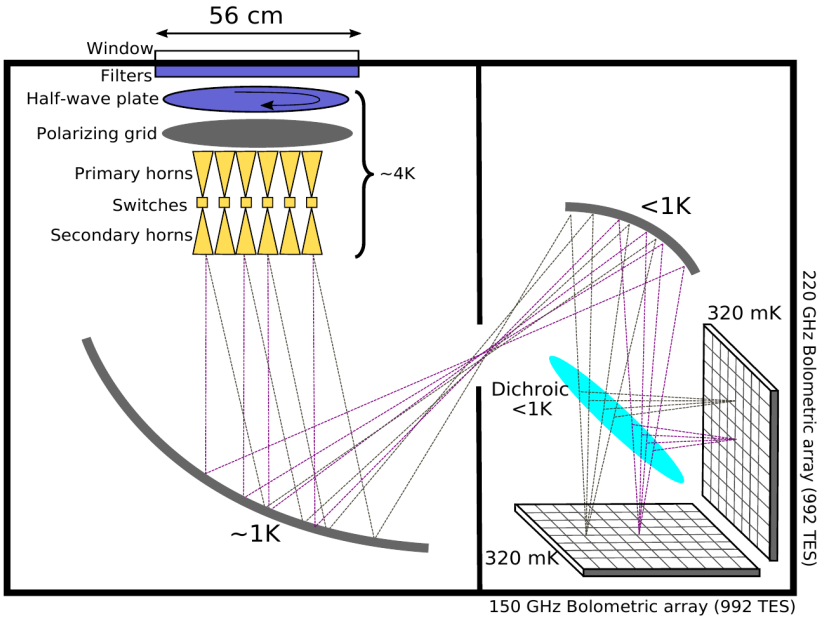


**Figure 1.3:** The QUBIC Telescope internal sketch [8]. Each focal plane consists of 1024 TES bolometers, of which only 992 are exposed to the incoming radiation and the rest are used for temperature monitoring and calibration.

off the transmitted signal of each horn pair. Different horn pairs produce a baseline that can be used for the instrument self-calibration, which is very useful for measuring systematic effects and improving the map-making performance. The synthesized beam is the interference produced when all the switches are open. Fig. 1.4 shows a simulation of a synthesized beam for an ideal combiner detected by a TES at different frequencies.

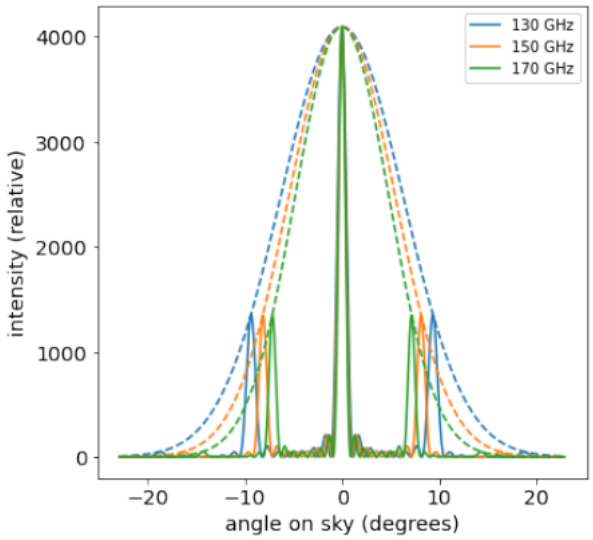


**Figure 1.4:** The synthesized beam contains multiple peaks whose angular separation is linearly dependent on the wavelength.

The Technical Demonstrator (TD) is currently installed in Alto Chorillos, Salta Province, Argentina since November 2022 (see Fig. 1.5) and performing testing measurements. It contains 8x8 back-to-back horns and only one quarter focal plane for the 150 GHz band (256 cryogenic TES detectors of which only 248 are exposed to the incoming radiation and the rest are used for systematic errors studies). The TD is planned to be updated to the Final Instrument (FI) version with 20x20 back-to-back horns and 1024 TES detectors in both focal planes.

**Figure 1.5:** QUBIC telescope TD installed in Argentina since November 2022

# Chapter 2

# Cryogenic Bolometers

As mentioned in Chapter 1, thermal detectors inherently exhibit excellent resolution and sensitivity. Even their performance is further enhanced when operated at low temperatures, achieving unprecedented characteristics [50, 51].

Two major categories within thermal detectors are calorimeters and bolometers. Calorimeters are devices used to measure the energy from absorbed radiation and, therefore, have a fast response time relative to the signal being measured [52]. In contrast, bolometers are designed to sense the time integral of the absorbed flux signal, i.e. the signal power.

Calorimeters and bolometers consist of several components: an absorber, a sensor, a thermal bath and a thermal link (see Fig. 2.1). The absorber's temperature rises when it is impacted by a particle or a flux of particles. The sensor monitors this temperature change in the absorber. The thermal bath acts as a temperature reservoir, cooling the absorber back to its reference temperature $T_\mathrm{b}$ after it has absorbed radiation. Finally, the thermal link is the means by which the absorber and the thermal bath are connected.

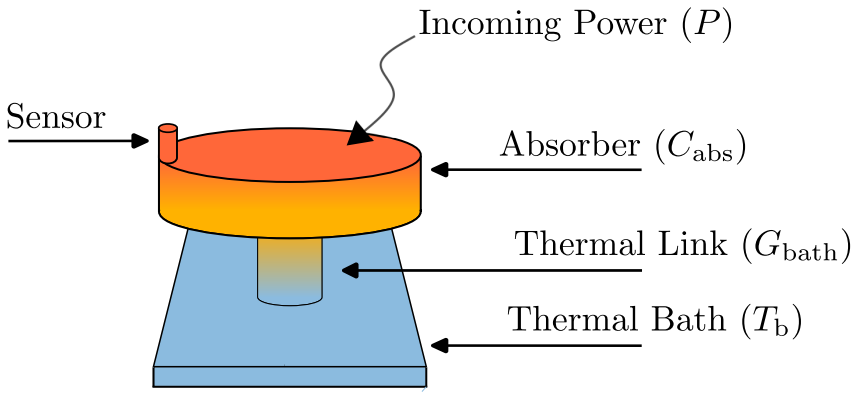


**Figure 2.1:** Thermal detectors measurement principle. A thermal mass with heat capacity $C_\mathrm{abs}$ weakly coupled to a thermal bath with a heat conductance $G_\mathrm{bath}$ absorbs incoming power $P$ and the temperature rise relative to $T_\mathrm{b}$ is measured by a thermometer in tight thermal contact to the structure.

It is worth mentioning that antennas are also employed to absorb incoming radia-

tion [53]. This approach offers an advantage over conventional absorbers, as the antenna can absorb multiple frequency bands and then separate them using filters. Each signal is then directed to a load where its energy is dissipated to heat the sensor.

From now on, this work refer to bolometers whenever the term detector is used. The bolometer conforms a thermal system that depends on several parameters. The interaction between the absorber and the thermal bath determines the detector time constant as

$$\tau = \frac{C_{\text{abs}}}{G_{\text{bath}}} \ , \tag{2.1}$$

where $C_{\text{abs}}$ is the absorber heat capacity and $G_{\text{bath}}$ is the heat conductance of the thermal link. When an incident radiation $P$ heat the absorber, the thermometer measures an increase of temperature $\Delta T$ denoted as

$$\Delta T = \frac{P}{G_{\text{bath}}} \ . \tag{2.2}$$

A trade-off exists between the sensitivity of the detector and its response time, determined by $G_{\text{bath}}$. It also should be noted that the sensor was not considered in Eq. 2.1 and Eq. 2.2. Depending on its nature, the sensor can significantly influence the ultimate characteristics of the detector. In the following subsections, the most relevant cryogenic sensors used in high-density arrays for CMB experiments are explained. Since some of these sensors are made out of superconducting materials, it is essential to first introduce some key concepts related to superconductivity.

## 2.1 Superconductivity

Superconductivity, discovered in 1911 by Kamerlingh Onnes, has seen significant advancements over the past century. Researchers have made substantial progress in understanding its remarkable properties, leading to the development of theories that explain its electrodynamics behavior [54–59].

This phenomenon appears in some metals when they are cooled down below their transition temperature $T_{\text{c}}$ and, as a consequence, their resistance to direct current fades away making them superconductors. This supercurrent is the motion of Cooper pairs, two electrons bounded together due to the electron–phonon interaction as described by the BCS theory [60]. Phonons are quasiparticles produced by quantized vibrational motion in the lattice structure of atoms. The Cooper pairs condense into a single quantum state, the ground state, forming a coherent macroscopic quantum state where the wavefunctions of the Cooper pairs overlaps. This state is described by a phase-locked wavefunction of the form

$$\Psi = \Psi_0 e^{j\phi} \ \text{[7]}. \tag{2.3}$$

The formation of Cooper pairs opens an energy gap $\Delta$ at the Fermi surface. This gap represents the energy required to break a Cooper pair in two quasi-particles (electrons)

and, at zero temperature, it is described by

$$\Delta(0) \approx 1.76 k_{\mathrm{B}} T_{\mathrm{c}} \ , \tag{2.4}$$

where $k_{\mathrm{B}}$ is the Boltzmann constant.

For DC current, a superconductor has zero resistance, meaning the impedance is effectively zero. This allows current to flow indefinitely without energy dissipation, as long as the material remains below its $T_{\mathrm{c}}$.

On the other hand, the impedance for AC current is not zero. Applying an electric field accelerates the Cooper pairs, resulting in kinetic energy from their motion. Unlike conventional inductance, which arises from the magnetic field generated by the current in a wire, kinetic inductance ($L_{\mathrm{k}}$) occurs due to the inertia of the Cooper pairs in a superconductor [61]. Furthermore, due to the anomalous skin effect and even imperfections in the material, a resistance $R_{\mathrm{s}}$ exists. Finally, the surface impedance of a superconductor is defined as $Z_{\mathrm{s}} = R_{\mathrm{s}} + jwL_{\mathrm{k}}$.

## 2.2 Kinetic Inductance Detector

A Kinetic Inductance Detector (KID) exploits the superconductor properties of the inductance that arise from the Cooper pairs kinetic energy [62]. When a photon with energy $hf > 2\Delta$ is absorbed by a superconducting film, it creates quasiparticles following the expression: $N_{\mathrm{qp}} = \eta hf/\Delta$, where $\eta$ is the breaking efficiency. As a consequence, the surface impedance (mainly inductive) of the superconductor varies.

Therefore, the kinetic energy can be obtained by coupling the KID to a capacitor forming a superconductive resonator with a $f_0$ resonance frequency as Fig. 2.2 shows. Depending on the type of resonator design, this detector is called Lumped Element KID (LEKID) or Microwave KID (MKID). Readout of these detectors can be performed by coupling the resonator to a microwave transmission line and monitor it by an input tone located at any frequency within the resonator bandwidth [63].

A KID is an inherent detector and does not require an external radiation coupler. However, by coupling the KID to an absorber [64] or antenna [65], the detector behaves like a bolometer and is referred to as a Thermal KID (TKID). In addition, this modification provides greater flexibility in the design and optimization process of the detector [66].

## 2.3 Transition Edge Sensor

A TES is a superconducting film that operates in the transition from normal to superconductive state. In this range, a minimal change in the temperature of the TES produces large variations in its electrical resistance. In this way it works like a very sensitive thermistor. Fig. 2.3 illustrates this behavior.

One of the outstanding features of the TES is its self-stabilizing electrothermal mechanism. This mechanism operates under voltage-bias conditions and produce a negative electro-thermal feedback (ETF). The Joule power, given by $P_{\mathrm{J}} = V^2/R_{\mathrm{TES}}$ for

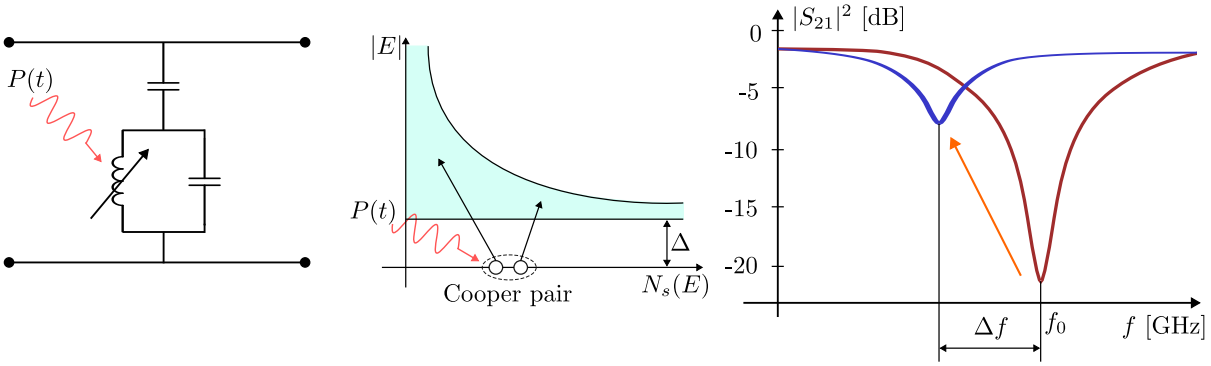


**Figure 2.2:** (**Left**) KID equivalent circuit. The kinetic inductance of the superconducting film changes with the absorption of photons. (**Center**) A photon absorption breaks a Cooper pair into two quasiparticle excitations. $N_s(E)$ is the density of states for quasiparticles and $E$ is the quasiparticle energy. (**Right**) The absorbed photon breaks cooper-pairs, changing the kinetic inductance and hence the frequency response of the device shifting the equilibrium resonance frequency $f_0$ (red curve) towards a smaller frequency (blue curve).

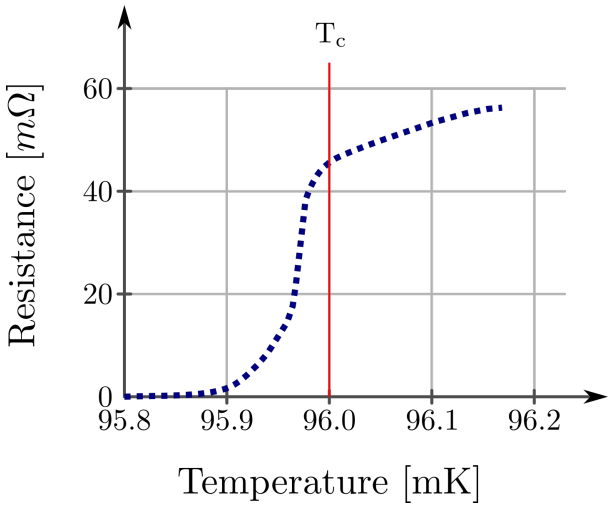


**Figure 2.3:** Transition of a superconducting film (a Mo/Cu proximity bilayer) from the normal to the supercoducting state near 96 mK [67].

$R_{TES} >> R_B$, decreases when the resistance $R_{TES}$ increases due to photon absorption, thereby stabilizing its temperature. $R_{TES}$ and $R_B$ denote the detector and bias resistances, respectively. Fig. 2.4 illustrates a typical voltage-bias and readout circuit used in TES detectors. A TES is commonly readout using a Superconducting Quantum Interference Device (SQUID), which is a highly sensitive magnetometer. The current $i \approx V/R_{TES}$ changes with the detector resistance and couples a magnetic flux $\Phi$ to the SQUID when passing through the inductor $L$.

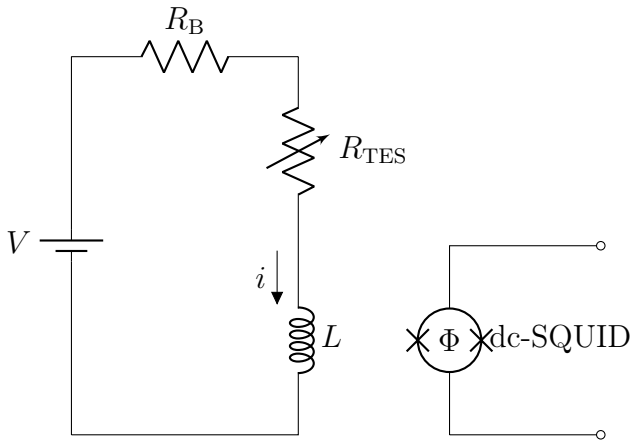


**Figure 2.4:** A typical voltage bias and readout circuit for TES. The current $i$ passing through the inductor $L$ creates a magnetic flux $\Phi$ through the dc-SQUID.

## 2.4 Magnetic Microbolometer

A Magnetic Microbolometer (MMB) is a detector based on the Magnetic Microcalorimeter (MMC) [68]. Both utilize a paramagnetic temperature sensor that consists of a magnetic material with temperature-dependent magnetization properties. When incident electromagnetic radiation strikes the detector, it heats the magnetic material, causing a change in its magnetization. The sensors typically consist of an alloy between a gold (Au) or silver (Ag) host metal doped with hundreds ppm of erbium (Er) paramagnetic material.

MMCs have demonstrated significant performance in single-particle measurement, particularly in high-resolution X-ray spectroscopy, pushing forward the state-of-the-art in resolution [69]. Other notable features of this detector include linear response, a large dynamic range and the absence of Joule dissipation. Given that no previous version of the MMC utilized its benefits in bolometer applications, the MMB was recently proposed to leverage these advantages [21]. Since this Thesis focuses on the design of the readout system for the MMB to be used in the QUBIC instrument, a more detailed explanation of the MMB design is provided.

### 2.4.1 Electro-thermal system

The MMB responsivity $\Re_{\mathrm{MMB}}$ is outlined by the transform relation within the thermal and electrical interaction, including its readout scheme. Fig. 2.5 shows the schematic of the thermal model and a readout scheme of a MMB using a SQUID.

It should be noted that the $\Re_{\mathrm{MMB}}$ is given by the magnetic flux $\Phi_{\mathrm{det}}$ produced in the SQUID after a power absorption. This relation is decomposed in the thermalization function $\partial T/\partial P$ which describes the relation between a temperature increase $T$ after a power absorption $P$, the sensor response function $\partial\Phi/\partial T$ that relates $T$ with the sensor magnetic flux variation $\Phi$ and finally the flux transform between $\Phi$ and $\Phi_{\mathrm{det}}$ defined as $\partial\Phi_{\mathrm{det}}/\partial\Phi$. Thus, $\Re_{\mathrm{MMB}}$ is formally defined as

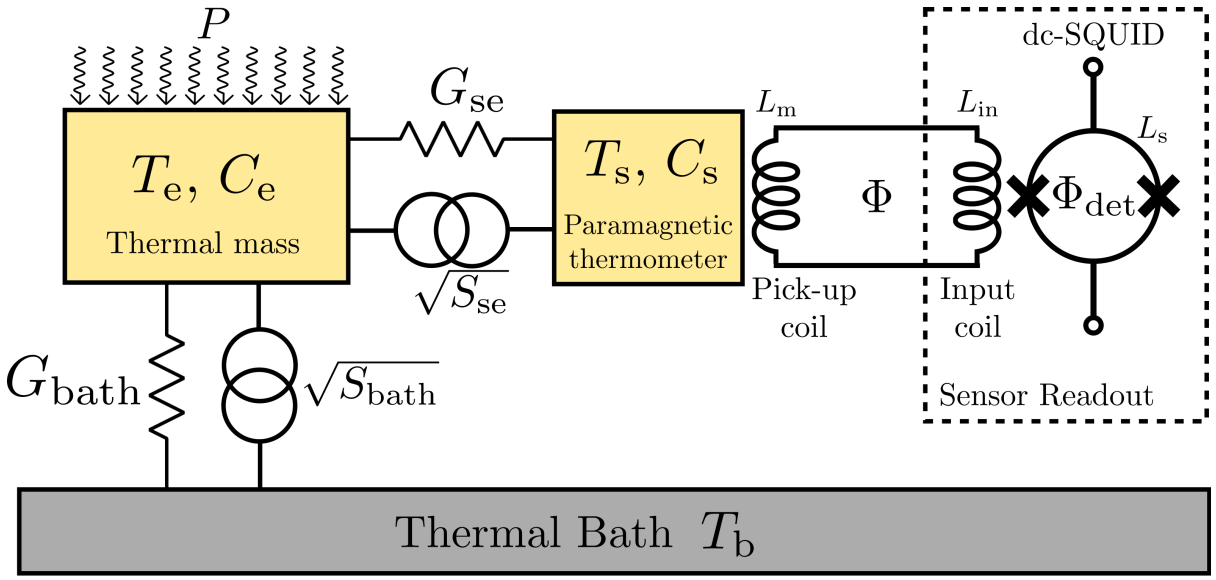


**Figure 2.5:** Schematic of the MMB thermal model and its readout. Incoming power $P$ is absorbed by a thermal mass with heat capacity $C_e$ that is therefore heated to a temperature $T_e$. This thermal mass is linked to a thermal bath with temperature $T_b$ by the weak thermal link $G_{bath}$. A paramagnetic temperature sensor with heat capacity $C_s$ is linked to the thermal mass by a second thermal link $G_{se}$ and is heated to a temperature $T_s$. The paramagnetic thermometer signal is transduced by a superconducting pickup coil magnetically coupled to a low-noise dc-SQUID. Additionally, the model includes the respective thermal noise sources related to the heat conductances.

$$\Re_{MMB} = \frac{\partial \Phi_{det}}{\partial P} = \frac{\partial \Phi_{det}}{\partial \Phi}\frac{\partial \Phi}{\partial T}\frac{\partial T}{\partial P} \ . \tag{2.5}$$

To determine the thermalization function, it is essential to understand the thermodynamic subsystems of metals. The dynamics of electrons and phonons dictate the thermal properties of solids, including heat capacity and thermal conductivity. At low temperatures, significantly below the Debye temperature $\Theta_D$, the heat capacity due to phonons $C_{ph}$ increases to the third power of the temperature because of the simultaneous excitation of higher-energy phonons and the growing number of already excited low-energy phonons. At temperatures much higher than $\Theta_D$, the saturation of $C_{ph}$ is uniquely determined by the latter mechanism. The mathematical expression for both cases follows

$$C_{ph} = \begin{cases} \frac{12\pi^4 n k_B}{5}(\frac{T}{\Theta_D})^3 & \text{for } T << \Theta_D \\ 3nk_B & \text{for } T >> \Theta_D \end{cases} \ , \tag{2.6}$$

where $n$ is the density of ions.

The contribution of electrons to the heat capacity $C_e$ is negligible at high temperatures because they require excitation for energy states above the thermal energy $k_B T$. However, at low temperatures, $C_e$ can become larger than $C_{ph}$ due to its linear dependence on temperature. $C_e$ is proportional to the Sommerfeld constant $\gamma$ as

$$C_e = \gamma T \ . \tag{2.7}$$

In the case of the Au-Er MMB, which is the selected material for the design, $C_e$ dominates the heat capacity at a reference temperature around 100 mK, with the Sommerfeld constant for gold being $\gamma = 6.9 \times 10^{-4}$. Nevertheless, the magnetic moments interactions (spin-spin) must also be considered apart from the electron-phonon influence since the material is doped with erbium. Two mechanisms of spin-spin interaction are important to consider: the dipole-dipole interaction and the RKKY (Ruderman-Kittel-Kasuya-Yosida) interaction, which refers to the energy exchange between the localized $4f$ electrons of the erbium ions and gold's conducting electrons [70]. These mechanisms introduce an additional specific heat $C_s$ of the sensor. Furthermore, the thermal link between the electron and spin subsystems is denoted by $G_{se}$. These two independent thermodynamic subsystems are modeled as an electrical circuit, as shown in fig. 2.6. In this model, the absorbed power $P$ is represented as a current source and the temperatures of the different subsystems are expressed as node voltages. It is important to highlight that this is a near-equilibrium system where temperature fluctuations (spin thermal noise or $\sqrt{S_{se}}$), thermal transitions and relaxation times exist between $T_e$ and $T_s$. The $G_{bath}$ of the thermal link is also illustrated, including its related phonon noise $\sqrt{S_{bath}}$.

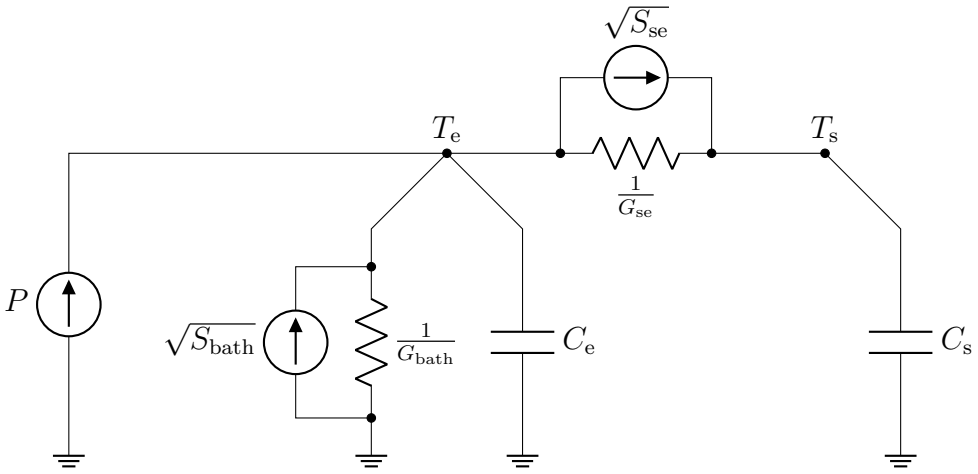


**Figure 2.6:** Equivalent electrical circuit of a MMB.

The thermalization function of the bolometer can be derived from the electrical model circuit as

$$\frac{\partial T}{\partial P} = \frac{1}{G_{bath}} \cdot \left[ 1 - \frac{C_e C_s}{G_{bath} G_{se}} \omega^2 + j\omega \cdot \frac{C_s (G_{bath} + G_{se}) + C_e G_{se}}{G_{bath} G_{se}} \right]^{-1} \ . \tag{2.8}$$

The analytical expression below shows how the temperature variation is transduced into a change of sensor magnetization $M$

$$\frac{\partial M}{\partial T} = \frac{N}{V k_B T^2} \left[ \left\langle E \frac{\partial E}{\partial B} \right\rangle - \langle E \rangle \left\langle \frac{\partial E}{\partial B} \right\rangle \right] \ [70]. \tag{2.9}$$

Where $E$ are the Hamiltonian energy states and $B$ the magnetic field average used to bias the sensor of volume $V$. To determine the $\partial\Phi/\partial T$, a pickup coil geometry has to be defined and solving the integration over $V$,

$$\frac{\partial\Phi}{\partial T} = \int_V \frac{|\vec{B}(\vec{r})|}{I_{\text{field}}} \frac{\partial M}{\partial T}\Big|_{|\vec{B}(\vec{r})|} d^3r \ . \tag{2.10}$$

$I_{\text{field}}$ denotes the persistent supercurrent in the pickup coil that generates $B$. Any change in $M$ and therefore in $\Phi$, produces a change in the current due to flux conservation of closed superconducting circuits.

Changes in current are measured by the SQUID, where the transfer function is governed by the transformation ratio as

$$\frac{\partial\Phi_{\text{det}}}{\partial\Phi} \approx \frac{k\sqrt{L_{\text{in}}L_{\text{s}}}}{L_{\text{m}} + L_{\text{stray}} + L_{\text{in}}} \ . \tag{2.11}$$

where $L_{\text{m}}$ is the inductance of the pickup coil, $L_{\text{in}}$ and $L_{\text{s}}$ are the SQUID input coil inductance and loop inductance, respectively and $k$ is the coupling factor between $L_{\text{in}}$ and $L_{\text{s}}$. $L_{\text{stray}}$ is the parasitic inductance derived from the superconducting lines and wire bonds that connect the detector to the SQUID.

### 2.4.2 Noise Estimation

Noise in bolometric measurements is typically quantified using the Noise Equivalent Power (NEP), which is defined as the minimum Power Spectral Density (PSD) at the input of the detector required to achieve an Signal-to-Noise Ratio (SNR) equal to one in a 1 Hz output bandwidth. The MMB's NEP consists of random fluctuations in photon arrival (Background Noise Equivalent Power ($\text{NEP}_\gamma$)) and the Detector Noise Equivalent Power ($\text{NEP}_{\text{det}}$). The $\text{NEP}_{\text{det}}$ contributions include thermal fluctuation noise (TFN), magnetic Johnson noise (MJN), erbium 1/f excess noise (Er) and readout noise. These contributions are calculated referred at the detector input as follows:

$$\text{NEP}^2_{\text{det}} = \frac{S_{\text{TFN}}}{\left|\frac{\partial T}{\partial P}\right|^2} + \frac{S_{\Phi,\text{MJN}}}{\left|\frac{\partial T}{\partial P}\right|^2\left|\frac{\partial\Phi}{\partial T}\right|^2} + \frac{S_{\Phi,\text{Er}}}{\left|\frac{\partial T}{\partial P}\right|^2\left|\frac{\partial\Phi}{\partial T}\right|^2} + \frac{S_{\Phi,\text{read}}}{\left|\frac{\partial T}{\partial P}\right|^2\left|\frac{\partial\Phi}{\partial T}\right|^2\left|\frac{\partial\Phi_{\text{det}}}{\partial\Phi}\right|^2} \ . \tag{2.12}$$

The terms $S_{\text{TFN}}$, $S_{\Phi,\text{MJN}}$, $S_{\Phi,\text{Er}}$ and $S_{\Phi,\text{read}}$ are the spectral density of each noise source.

TFN exists in both thermal links within the electro-thermal system. Thermal fluctuations in phonon energy are the source of noise in the thermal link to the thermal bath and can be estimated as

$$S_{\text{bath}} = 4\Gamma k_{\text{B}} T^2 G_{\text{bath}} \ , \tag{2.13}$$

where

$$\Gamma = \frac{\beta+1}{2\beta+3} \cdot \frac{1-(T_{\text{b}}/T)^{2\beta+3}}{1-(T_{\text{b}}/T)^{\beta+1}} \tag{2.14}$$

is a numerical factor derived for materials at low temperatures and since there is only phonon transport of heat through the thermal link and no electron contribution, $\beta = 3$ [71].

The energy fluctuations between the conducting electrons and the spin subsystems can be modeled by a similar method, arriving to the following expression

$$S_{\mathrm{se}} = 4k_{\mathrm{B}}T^2G_{\mathrm{se}} \ \text{[68]}.$$

$S_{\Phi,\mathrm{MJN}}$ arises from the thermally induced random motion of conduction electrons within the paramagnetic sensor. This motion creates a fluctuating magnetic field that is readout when it couples to the pickup coil. It is calculated as

$$S_{\Phi,\mathrm{MJN}} = \mathfrak{K} \cdot \sigma \cdot T \ \text{[68]}, \tag{2.15}$$

where $\mathfrak{K}$ is a constant that depends on the geometry of the detector and $\sigma$ is the electrical conductance of the paramagnetic sensor ($\sigma_{\mathrm{Au:Er}} = 4.55 \times 10^7\,\mathrm{S/m}$ for an Erbium concentration of 1000 ppm).

Erbium ions in the MMB exhibits a fluctuating magnetic moment in the form of flicker noise. The origin of this magnetic fluctuation is not fully understood and is experimentally determined as

$$S_{\Phi,\mathrm{Er}} = N_{\mathrm{Er}}\frac{|B(\mathbf{r})|^2}{I_{\mathrm{f}}^2}S_{\mathrm{m}}(f) \ , \tag{2.16}$$

where $N_{\mathrm{Er}}$ is the number of erbium ions and $S_{\mathrm{m}}(f)$ stands for the power Noise Spectral Density (NSD) of the z-component of the magnetic moments of the erbium ions, $S_{\mathrm{m}}(f) = 0.12\mu_{\mathrm{B}}^2 \,/\, f^{\eta}$ where $\eta \approx 0.8 - 1$ [69].

Lastly, the readout noise is determined by the entire system used to measure the detector. In the case of the readout system proposed in this work, the noise is contributed by the $\mu$MUX and RTE, which are described in Section 3. For this analysis, however, a typical SQUID noise given by the scheme depicted in fig. 2.5 is considered. This readout noise can be decomposed into a 1/f dependency at low frequencies, with a typical value in the range of $\sqrt{S_{\Phi,\mathrm{read}}} = 3 - 4\,\mu\Phi_0/\sqrt{\mathrm{Hz}}$ at 1 Hz and a white noise dominant component over a few kHz, where a common value is within $\sqrt{S_{\Phi,\mathrm{read}}} = 0.2 - 0.4\,\mu\Phi_0/\sqrt{\mathrm{Hz}}$ [72]. Here, $\Phi_0$ denotes the magnetic flux quantum.

### 2.4.3 Experiment requirements

The detector requirements are defined by two main constrains: background-limited detection and the telescope scanning strategy. The latter defines the maximum time constant of the detector to avoid signal distortion. In [73, 74], it is demonstrated that fulfilling this condition requires meeting the condition

$$\tau \leq \frac{\Theta_{\mathrm{beam}}}{2\pi\dot{\Theta}} \ , \tag{2.17}$$

where $\Theta_{\text{beam}}$ is the full width at half maximum (FWHM) in degrees of the detector's beam intensity and $\dot{\Theta}$ is the telescope's scan speed.

Considering the 150 GHz band of the QUBIC instrument, covering a 25% of bandwidth, an aperture size of 0.3 m which implies a $\Theta_{\text{beam}} = 0.39$ degrees at the central frequency and an scan velocity of $\dot{\Theta} = 1$ deg/sec. Thus, the maximum time constant of the detector that satisfies the Nyquist-Shannon theorem is $\tau \leq 62$ ms.

Background Limited Photometry (BLIP) is the desirable condition where the $\text{NEP}_\gamma$ dominates and the detector noise do not degrade the incoming radiation signal. The $\text{NEP}_\gamma$ is estimated as

$$\text{NEP}_\gamma^2 = 2hfP_{\text{opt}} + \frac{2P_{\text{opt}}^2}{m\Delta f} \ , \tag{2.18}$$

where $P_{\text{opt}}$ is the mean optical spectral power of the detected radiation, $h$ is Planck's constant, $f$ is the frequency of the radiation, $\Delta f$ is the spectral bandwidth and $m$ the number of polarizations detected [75]. In the case of polarimetric measurements of the CMB, $m = 1$. For the previously indicated QUBIC parameters, the $\text{NEP}_\gamma$= 55.79 aW/$\sqrt{\text{Hz}}$.

A simulation of a non-optimized MMB was conducted for two different types of input radiation coupling schemes (absorber-coupled and antenna-coupled) to verify that they meet the requirements of the experiment. In both cases, the detector time constant remained well below the limit of 62 ms across various design parameters [21]. For a bath temperature of 100 mK, the time constant is 27 ms for the antenna-coupled system and 30 ms for the absorber-coupled system.

In Fig. 2.7 shows the comparison between background noise and the various detector noise contributions for both coupling schemes. All noise components are expressed as normalized flux noise at the SQUID, determined as

$$\sqrt{S_\Phi} = \text{NEP} \cdot \Re_{\text{MMB}} \ . \tag{2.19}$$

In the case of the antenna-coupled detector, the BLIP condition is achieved across a range of more than three decades, from 0.045 Hz to 760 Hz. Meanwhile, the absorber-coupled detector meets the same condition for frequencies between 0.056 Hz and 510 Hz. These estimates demonstrate that the MMB is a suitable detector for CMB surveys.

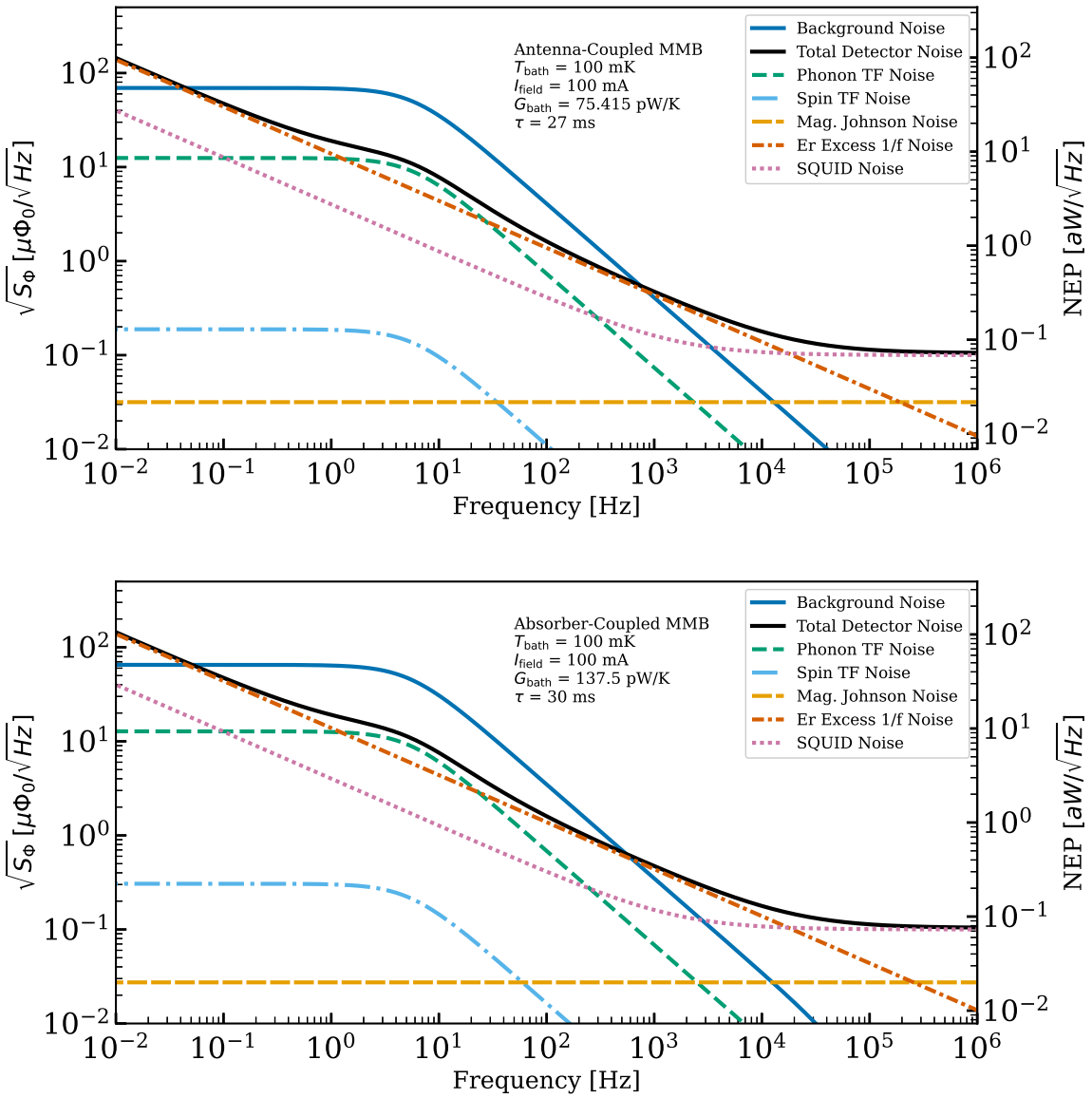


**Figure 2.7:** Magnetic flux noise at the SQUID of a non-optimized MMB is shown for both antenna-coupled (**Top**) and absorber-coupled (**Bottom**) schemes. The solid blue line represents the background magnetic flux noise, while the solid black line represents the total intrinsic MMB magnetic flux noise (considering all contributions plotted in dashed lines). In both schemes, a bandwidth can be established under the BLIP condition.

# Chapter 3

# Readout System

The growing demand for measurement systems consisting of arrays of highly sensitive cryogenic detectors requires a readout system that does not degrade the detector signals and, additionally, is flexible enough to accommodate an increasing number of them. A complex cryogenic device called $\mu$MUX is capable of performing this task employing a FDM technique. The $\mu$MUX consists of a chain of channels connected to the same transmission line, with each channel composed of a unique resonance frequency superconducting resonator magnetically coupled through a radio frequency SQUID (rf-SQUID) to cryogenic detectors [16, 76]. Variations in magnetic flux passing through the rf-SQUID, caused by a detector, modify the corresponding resonator response.

A RTE, composed by a Back-end (BE) and a Front-end (FE), is used to extract the signals from the channels in a SDR scheme continually monitoring all the channels. First, a digital frequency comb is synthesized at baseband (BB) by a Field Programmable Gate Array (FPGA) on the BE. The choice of a FPGA is driven by their high flexibility and ability to process multiple channels in parallel. Then, the digital signal is converted to analog by a high-speed Digital-to-Analog Converter (DAC) and subsequently, conditioned and shifted to the filter resonance frequencies by a radio frequency (rf) FE. The rf-SQUID signals and therefore the detector signals, are imprinted on the amplitude and phase of the monitoring tones as the filter responses vary. Finally, the frequency comb is down-converted by the FE, digitized by an Analog-to-Digital Converter (ADC) and acquired by the BE for processing. The rf-SQUID signals are recovered by filtering each generated tone and obtaining the information from their amplitude or phase. Thereafter, a second demodulation process is performed to obtain the detector signal.

## 3.1 The Microwave SQUID Multiplexer

### 3.1.1 Superconducting resonator

Each channel in the $\mu$MUX contains a superconducting resonator. Resonators can be designed with lumped or distributed elements. The latter is part of the scope of this thesis and correspond to a superconducting Coplanar Waveguide (CPW) quarter-wave resonator terminated by a load inductor ($L_{\mathrm{T}}$), as can be seen in Fig. 3.1. In addition, all

the $\mu$MUX resonators are coupled to a common transmission line by capacitors (illustrated as $C_c$ in the schematic of Fig. 3.1). The transmission line and the resonators exhibit the same characteristic impedance $Z_0$.

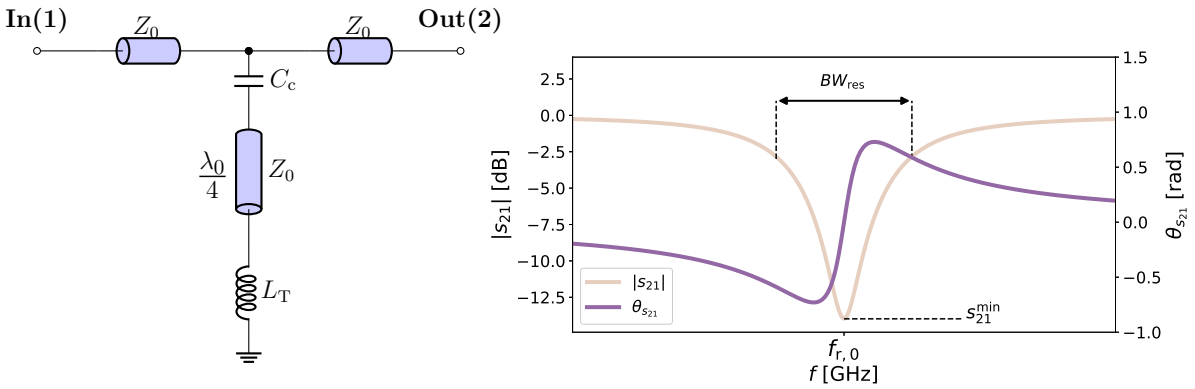


**Figure 3.1:** (**Left**) Schematic of a CPW quarter-wave resonator, coupled to a transmission line via a capacity $C_c$ and terminated with a load inductor $L_T$ and (**Right**) its characteristic frequency response in transmission power (black line) and phase (red line). The resonance frequency $f_{r,0}$ and its corresponding transmission $s_{21}^{min}$ are characteristic parameters of the resonator.

The complex transfer function of the coupled and loaded resonator is given by

$$s_{21} = \frac{s_{21}^{min} + 2j\frac{f-f_{r,0}}{BW_{res}}}{1 + 2j\frac{f-f_{r,0}}{BW_{res}}} \quad [77], \tag{3.1}$$

where $f$ corresponds to the input signal frequency, $BW_{res}$ is the $-3$ dB bandwidth of the resonator and $f_r$ is the channel resonance frequency described as

$$f_{r,0} = f_0 - 4f_0^2\left(C_c Z_0 + \frac{L_T}{Z_0}\right) , \tag{3.2}$$

$f_0$ denotes the resonance frequency of the quarter-wave resonator [78]. $s_{21}^{min}$ indicates the transmission of the filter when $f = f_{r,0}$ and is determined by $s_{21}^{min} = Q_l/Q_i$. $Q_i$ is the intrinsic quality factor, representing the ratio of reactive to active energy in the quarter-wave resonator and its load. $Q_l$ refers to the total quality factor of the coupled and loaded resonator and is calculated as $1/(Q_i^{-1} + Q_c^{-1})$, where $Q_c$ is the quality factor of the coupling capacitor $C_c$. Ideally, the quality factors tend to infinity, indicating no energy dissipation in the circuit, however, there are various sources of loss in reality. Finally, the resonator bandwidth can be computed as $BW_{res} = f_{r,0}/Q_l$.

Eq. 3.1 describes a circle in the complex plane known as the resonance circle shown in Fig. 3.2. From this circle, many of the channel design parameters can be obtained by fitting $f_{r,0}$, $BW_{res}$, $s_{21}^{min}$, $Q_l$ and $Q_c$. The center and radius of the resonance circle correspond to $x_c = (1 + s_{21}^{min})/2$ and $r = 1 - x_c$, respectively. As $f$ tends to 0 or $+\infty$, the circle approaches the real axis at unity.

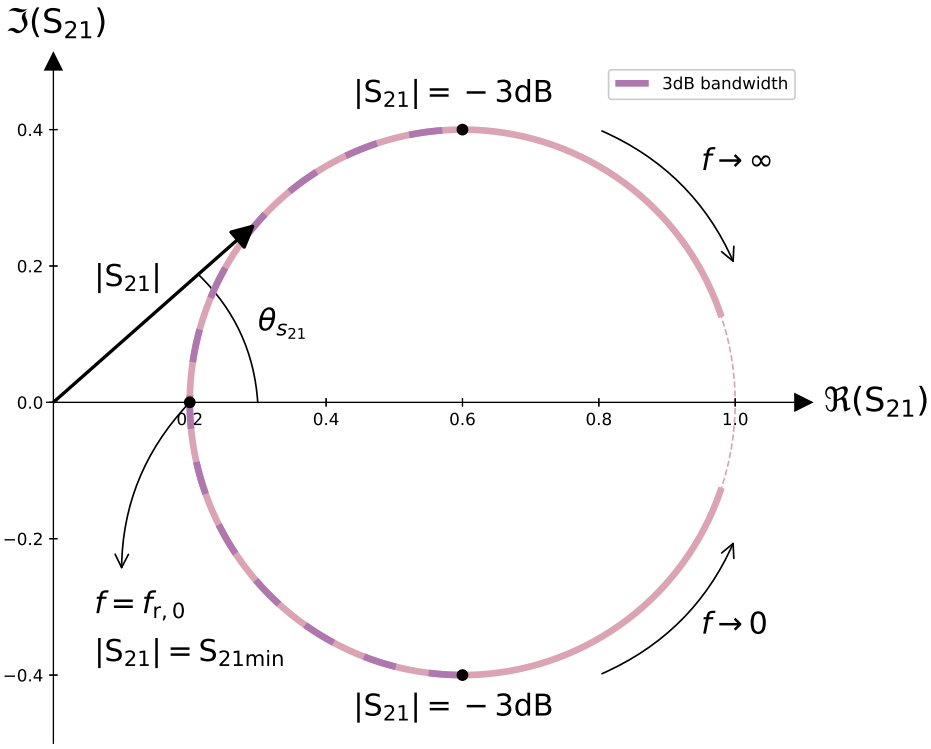


**Figure 3.2:** Resonance circle for a coupled and loaded resonator. The transmission parameter of the resonator traces a circle in the complex plane, where characteristic parameters such as the $f_r$ and $s_{21}^{min}$ can be identified.

### 3.1.2 Resonator-SQUID coupling

In the $\mu$MUX, $L_T$ is coupled to a rf-SQUID, which is a highly sensitive magnetic flux detector that operates based on quantum mechanical principles. It consists of a superconducting loop with one Josephson junction.

The Josephson junction comprises of two superconducting materials separated by a thin insulating or normal metal barrier (see Fig. 3.3). Through this unique structure, the macroscopic wave function of the two superconductors overlap, enabling the tunneling of Cooper pairs and leading to quantum effects. The Josephson Effect is the manifestation of this tunneling in two distinct forms: the DC Josephson Effect and the AC Josephson Effect [79]. The DC Josephson Effect takes place when a direct current flows across the junction without any applied voltage, driven purely by the phase difference between the superconducting wave functions (Eq. 2.3) on either side of the barrier as

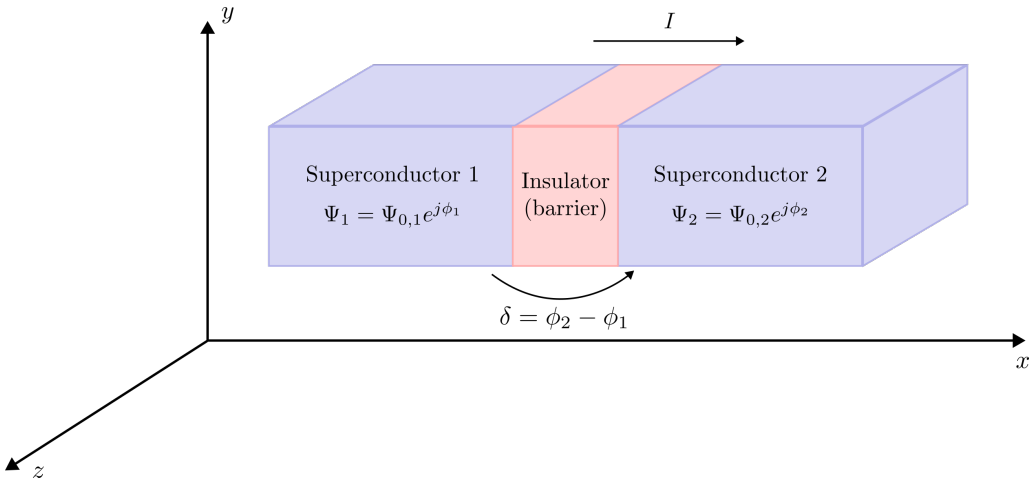


**Figure 3.3:** Josephson junction diagram. $\Psi_1$ and $\Psi_2$ are the coherent wave functions that describe the state of all the Cooper pairs in each superconducting electrode. Quantum mechanical tunneling occur for the Cooper pairs through the barrier. As a result, a supercurrent dependent on the phase difference between both wave functions is generated.

$$I = -I_c \sin(\varphi_1 - \varphi_2) = -I_c \sin(\varphi) \ , \tag{3.3}$$

where $I_c$ is the critical current of the junction, defined as the maximum electric current it can carry before the superconductor switches to the normal state.

In contrast, the AC Josephson Effect arises when a constant voltage is applied across the junction:

$$\frac{\partial \varphi}{\partial t} = \frac{2\pi V}{\Phi_0} \ , \tag{3.4}$$

where $V$ is the voltage across the junction and $\Phi_0$ is the magnetic flux quantum constant defined as the relation between the Planck's constant and the electron charge, $\Phi_0 = h/(2e) \approx 2.067 \times 10^{-15}[Wb]$. The dynamics of equations Eq. 3.3 and Eq. 3.4 can be understood by differentiating the first one and inserting the last one in it. This relationship is captured by the following equation,

$$V = \frac{\Phi_0}{2\pi I_c \cos(\varphi)} \frac{\partial I}{\partial t} \ . \tag{3.5}$$

Eq. 3.5 can be related with the inductance voltage-current equation, $V_L = L\, \partial I_L / \partial t$. Thus, indicating a phase-dependent non-linear inductance

$$L(\varphi) = \frac{\Phi_0}{2\pi I_c \cos(\varphi)} \ . \tag{3.6}$$

When a superconducting loop is interrupted by a Josephson junction a rf-SQUID is formed as Fig. 3.4 shows. In the presence of an external magnetic field ($\Phi_{ext}$), the total normalized flux along the closed contour can be approximated as

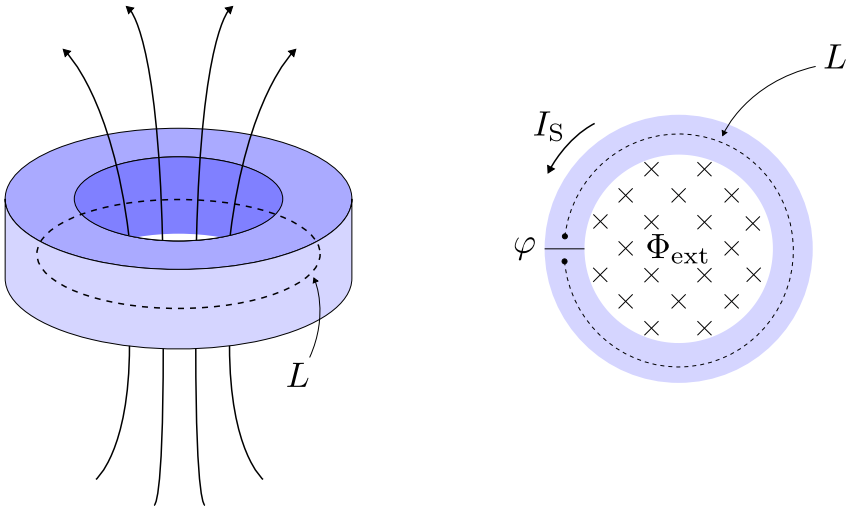


**Figure 3.4:** A superconducting loop interrupted by a Josephson junction forms the rf-SQUID. The integration along the contour of the dashed black line represents the total magnetic flux penetrating the inside of the loop.

$$\varphi \approx \frac{2\pi}{\Phi_0}(\Phi_{ext} + L_s I_S) \text{ [80].} \tag{3.7}$$

$L_s$ is the loop inductance and $I_S$ is the supercurrent that flows in the loop. This supercurrent is defined as

$$I_S = -I_c \sin\left(\varphi_{ext} + \beta_L \frac{I_S}{I_c}\right) , \tag{3.8}$$

where $\varphi_{ext} = 2\pi\Phi_{ext}/\Phi_0$ and $\beta_L$ is the screening factor depicted as

$$\beta_L = \frac{2\pi L_s I_c}{\Phi_0} . \tag{3.9}$$

The $\beta_L$ value is very important as it determines the rf-SQUID regime [81] as Fig. 3.5 shows. If $\beta_L < 1$, the rf-SQUID operates in the non-hysterestic mode and do not dissipate energy, thus, $\varphi = f(\varphi_{ext})$ is a single-valued function. On the contrary, hysterestic rf-SQUID ($\beta_L > 1$) produces flux jumps in the $\varphi = f(\varphi_{ext})$ function, resulting in energy dissipation. Throughout this work, non-dissipative rf-SQUID is considered.

$L_T$ is coupled to the rf-SQUID through a mutual inductance $M_T$. Thus, a readout tone with frequency $f_{exc}$ and power $P_{exc}$, that generates an anti-node current amplitude $I_T = \sqrt{16Q_l^2 P_{exc}/(\pi Q_c Z_0)}$, induces a magnetic flux $\Phi_{exc} = M_T I_T$ in the rf-SQUID. Therefore, the loop supercurrent is equivalent to:

$$I_S = -I_c \sin\left(\varphi_{exc}\sin(\omega_{exc}t) + \beta_L \frac{I_S}{I_c}\right) . \tag{3.10}$$

As a consequence, $I_S$ induces a magnetic flux in $L_T$, generating an opposing current labeled $I'_T$. This results in an effective load inductor $L_{T,eff}$, followed by

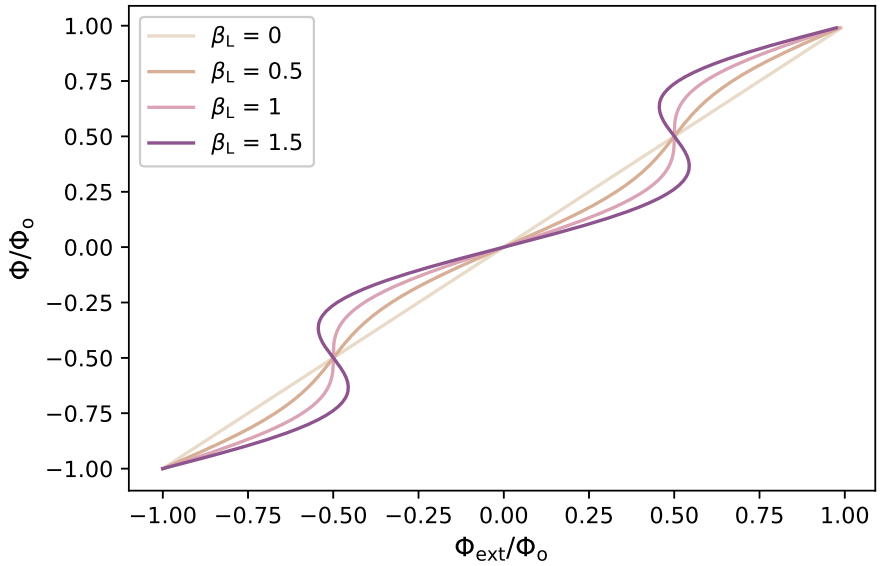


**Figure 3.5:** Magnetic flux inside the rf-SQUID loop ($\Phi$) as the external magnetic flux ($\Phi_{\text{ext}}$) increases for different regimes determined by the $\beta_{\text{L}}$ value. When $\beta_{\text{L}} > 1$ a multi-valued hysterestic function is described. A non-hysterestic regime arises if $\beta_{\text{L}} < 1$.

$$\begin{aligned} L_{\text{T,eff}} &= L_{\text{T}}\left(1 + \frac{I'_{\text{T}}}{I_{\text{T}}}\right) \\ &= L_{\text{T}} - \frac{{M_{\text{T}}}^2}{L_{\text{s}}} \frac{\beta_{\text{L}} \cos(\varphi_{\text{exc}} \sin(\omega_{\text{exc}} t) + \beta_{\text{L}} \frac{I_{\text{S}}}{I_{\text{c}}})}{1 + \beta_{\text{L}} \cos(\varphi_{\text{exc}} \sin(\omega_{\text{exc}} t) + \beta_{\text{L}} \frac{I_{\text{S}}}{I_{\text{c}}})} \quad . \end{aligned} \tag{3.11}$$

In Fig. 3.6 a diagram of a complete channel is presented. This diagram includes the input transformer which couples the magnetic flux given by the detector and a transformer given by the modulation signal that is explained later.

Finally, the analytic equation that describes the channel frequency dependency with the magnetic flux is obtained by replacing $L_{\text{T,eff}}$ in Eq. 3.2:

$$f_{\text{r}}(\varphi) = f_{\text{r,0}} + 4{f_0}^2 \frac{{M_{\text{T}}}^2}{L_{\text{s}}} \frac{\beta_{\text{L}} \cos(\varphi_{\text{exc}} \sin(\omega_{\text{exc}} t) + \beta_{\text{L}} \frac{I_{\text{S}}}{I_{\text{c}}})}{1 + \beta_{\text{L}} \cos(\varphi_{\text{exc}} \sin(\omega_{\text{exc}} t) + \beta_{\text{L}} \frac{I_{\text{S}}}{I_{\text{c}}})} \quad , \tag{3.12}$$

The first two terms on the right-handed side are fixed and depend on the channel design, while the last term is a variable flux-dependent component. Therefore, the channel resonance frequency shift is defined as $f_{\text{r}}(\varphi) = f_{\text{r,0}} + \Delta f_{\text{r}}(\varphi)$, where:

$$\Delta f_{\text{r}}(\varphi) = 4{f_0}^2 \frac{{M_{\text{T}}}^2}{L_{\text{s}}} \frac{\beta_{\text{L}} \cos(\varphi_{\text{exc}} \sin(\omega_{\text{exc}} t) + \beta_{\text{L}} \frac{I_{\text{S}}}{I_{\text{c}}})}{1 + \beta_{\text{L}} \cos(\varphi_{\text{exc}} \sin(\omega_{\text{exc}} t) + \beta_{\text{L}} \frac{I_{\text{S}}}{I_{\text{c}}})} \quad . \tag{3.13}$$

Relating the $\Delta f_{\text{r}}$ peak-to-peak shift ($\Delta f_{\text{r}}^{\text{pp}}$) with $BW_{\text{res}}$ by an $\eta$ factor gives

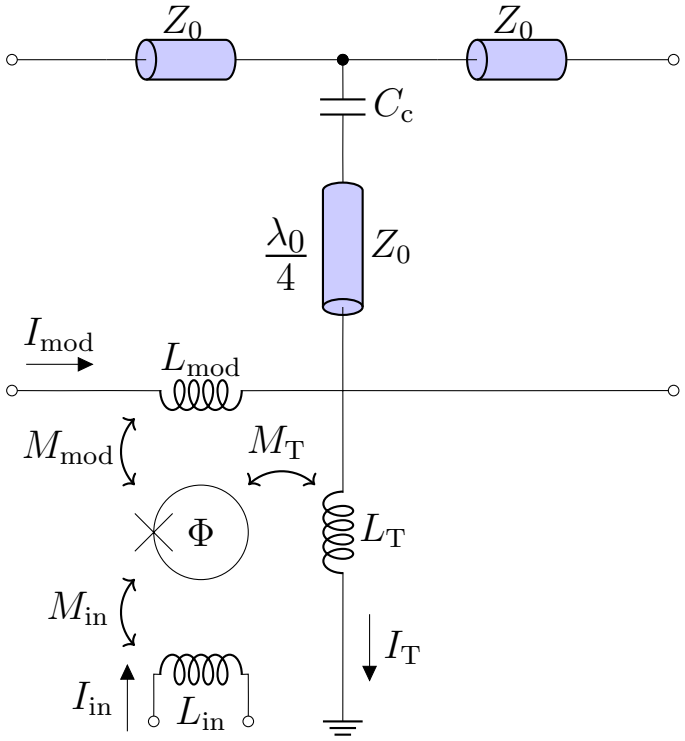


**Figure 3.6:** $\mu$MUX channel. The total magnetic flux in the rf-SQUID, $\Phi$, depends on the external flux produced by the currents $I_T$, $I_{mod}$ and $I_{in}$, which flow through the inductors $L_T$, $L_{mod}$ and $L_{in}$, respectively. Additionally, it is influenced by the screening factor current.

$$\Delta f_r^{pp} = 8 {f_0}^2 \frac{{M_T}^2 \beta_L}{L_s} = \eta BW_{res} \ . \tag{3.14}$$

The parameter $\eta = 1$ is typically sought to ensure optimal readout conditions. This has been confirmed for low $P_{exc}$ levels, where the condition $\eta = 1$ minimizes the white noise of the $\mu$MUX [82]. As $P_{exc}$ increases, the value of $\eta$ that minimizes the white noise of the $\mu$MUX becomes greater than 1.

### 3.1.3 Detector-Channel coupling

A visual and conceptual understanding of the derivations in Section 3.1.2 is represented in Fig. 3.7. In this figure, it can be seen an additional magnetic flux ($\Phi'_{ext}$) passing through the rf-SQUID that yiels a channel resonance frequency described as

$$f_r(\varphi) = f_{r,0} + \Delta f_r^{pp} \frac{\cos(\varphi'_{ext} + \varphi_{exc}\sin(\omega_{exc}t) + \beta_L \frac{I_S}{I_c})}{1 + \beta_L \cos(\varphi'_{ext} + \varphi_{exc}\sin(\omega_{exc}t) + \beta_L \frac{I_S}{I_c})} \ . \tag{3.15}$$

The resonance frequency $f_r$ has a periodic dependency on $\Phi'_{ext}$ with a period of $\Phi_0$. Consequently, the transmission parameter $s_{21}$ also varies with $\Phi'_{ext}$. By setting a fixed readout tone with frequency $f_{exc}$ within the range of $BW_{res} \pm (\Delta f_r^{pp}/2)$, the $\Phi'_{ext}$ signal

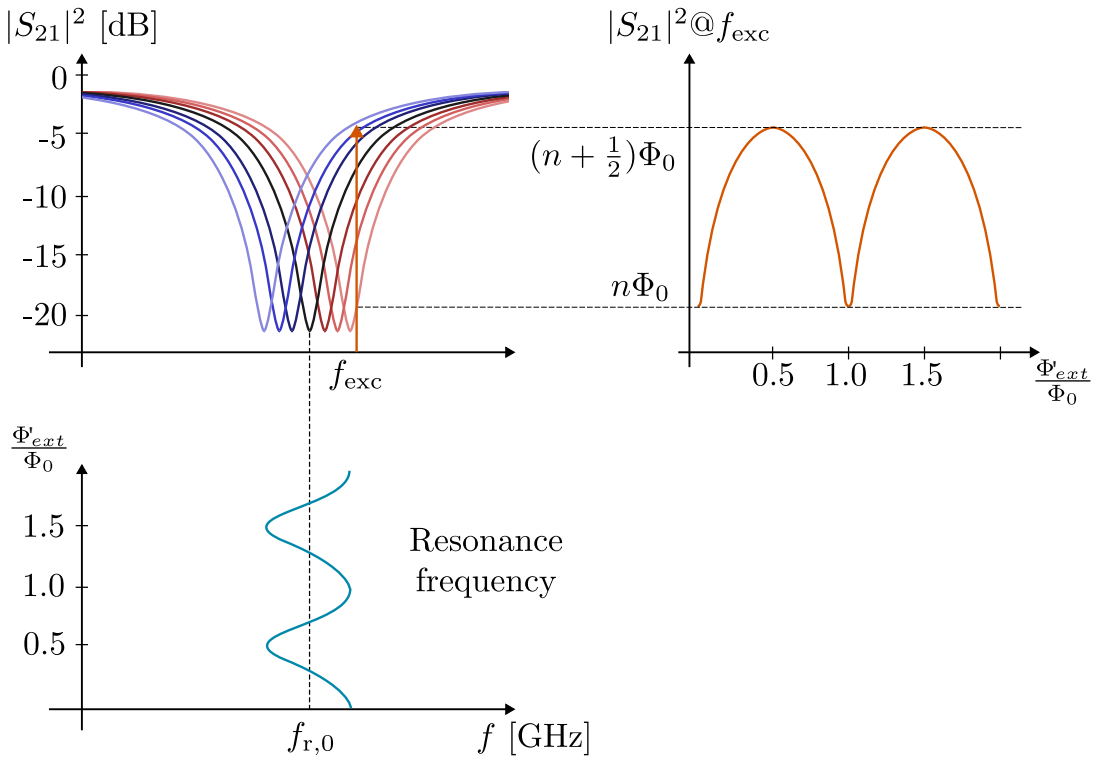


**Figure 3.7:** (**Upper-left**) The $\mu$MUX channel transfer function exhibits periodic behavior as an external magnetic flux ($\Phi'_{\mathrm{ext}}$) concatenated to the rf-SQUID increases. (**Bottom-left**) The channel resonance frequency shows a $1\,\Phi_0$ periodic response. (**Upper-right**) By measuring a monitoring tone located at a frequency within $BW_{\mathrm{res}} \pm (\Delta f_{\mathrm{r}}^{\mathrm{pp}}/2)$, $\Phi'_{\mathrm{ext}}$ can be recovered.

is encoded in the amplitude and phase of the readout tone. This effect is illustrated in Fig. 3.7 for the amplitude case.

$\Phi'_{\mathrm{ext}}$ can be produced by a detector flux $\Phi_{\mathrm{det}} = I_{\mathrm{in}} M_{\mathrm{in}}$ coupled to the rf-SQUID, either directly or through a transformer, as shown in Fig. 2.5 for the MMB. Then, the detector signal is obtained by measuring the phase or, more commonly, the amplitude deviation of the generated tone. This type of detector signal readout is called open-loop and have major disadvantages, such as the nonlinear response of the rf-SQUID, which makes the deviation produced by the detector signal dependent on $f_{\mathrm{exc}}$. More importantly, when the rf-SQUID cools down and transitions to the superconducting phase, the magnetic flux present at that moment is trapped, imposing an arbitrary bias ($\Phi_{\mathrm{bias}}$). This $\Phi_{\mathrm{bias}}$ can result in a useless channel if it is set at the insensitive parts of the $s_{21}(\Phi'_{\mathrm{ext}})$ curve (white regions in Fig. 3.8). This issue becomes statistically more probable as the readout system includes more channels. The optimal bias (dark violet regions in Fig. 3.8) for the selected $f_{\mathrm{exc}}$ and $P_{\mathrm{exc}}$ is given when the open-loop amplitude gain,

$$\gamma(t) = \left.\frac{\partial |s_{21}|}{\partial \Phi'_{\mathrm{ext}}}\right|_{f_{\mathrm{exc}}, P_{\mathrm{exc}}}, \tag{3.16}$$

or phase gain,

$$\theta(t) = \left.\frac{\partial \theta_{s_{21}}}{\partial \Phi'_{\mathrm{ext}}}\right|_{f_{\mathrm{exc}}, P_{\mathrm{exc}}}, \tag{3.17}$$

are maximized.

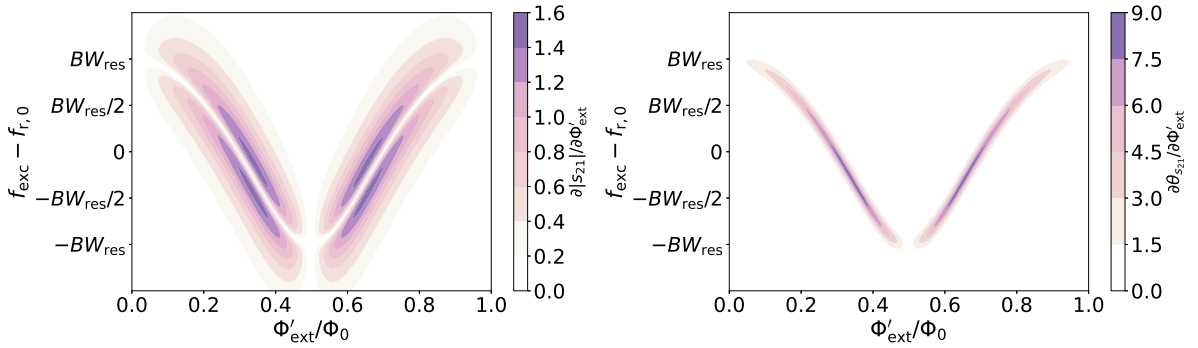


**Figure 3.8:** (**Left**) Amplitude domain open-loop gain. (**Right**) Phase domain open-loop gain.

The Flux Lock Loop (FLL) approach solves these issues by adding a flux feedback circuit to maintain the bias at its optimal point [83]. This scheme restricts $\Phi_{\mathrm{det}}$ values to the vicinity of the optimal bias to preserve linearity and prevent the bias from shifting to the multiple stable operating points of the system [84]. Consequently, the dynamic range of the detector is reduced if the feedback circuit is not fast enough, which can lead to a reduction in the SNR. Moreover, it should be noted that this scheme conflicts with the trend toward high multiplexing arrays, as each channel containing an rf-SQUID requires an independent flux feedback circuit, which increases the wiring inside the cryostat and, consequently, the cooling power required.

### 3.1.4 Flux Ramp Modulation

To drive all of the rf-SQUIDs simultaneously and avoid insensitive bias points when reading out the detectors, a time periodic magnetic flux $\Phi_{\mathrm{mod}}(t)$ is generated. Hence, $\Phi'_{\mathrm{ext}} = \Phi_{\mathrm{mod}}(t) + \Phi_{\mathrm{det}}(t)$, where $\Phi_{\mathrm{det}}(t)$ is a detector magnetic flux coupled to a rf-SQUID. Since the magnetic flux is continuously varying throughout all the rf-SQUIDs, each $\Phi_{\mathrm{bias}}$ related to each rf-SQUID can be considered as part of the $\Phi_{\mathrm{mod}}(t)$ signal. Typically, $\Phi_{\mathrm{mod}}(t)$ results from magnetically coupling a current sawtooth signal with a peak amplitude $I_{\mathrm{ramp}}$ and a frequency $f_{\mathrm{ramp}}$. The sawtooth waveform is used because it is not feasible to create an infinite ramp signal, therefore, it is reset periodically. However, when processing the signal, each sawtooth period ($T_{\mathrm{ramp}}$) is considered separately, avoiding transients. This leads to the following channel frequency equation:

$$f_{\mathrm{r}}(t) = f_{\mathrm{r},0} + \Delta f_{\mathrm{r}}^{\mathrm{pp}} \frac{\cos(2\pi N_{\Phi_0} f_{\mathrm{ramp}} t + \varphi_{\mathrm{det}}(t) + \varphi_{\mathrm{exc}} \sin(\omega_{\mathrm{exc}} t) + \beta_{\mathrm{L}} \frac{I_{\mathrm{S}}}{I_{\mathrm{c}}})}{1 + \beta_{\mathrm{L}} \cos(2\pi N_{\Phi_0} f_{\mathrm{ramp}} t + \varphi_{\mathrm{det}}(t) + \varphi_{\mathrm{exc}} \sin(\omega_{\mathrm{exc}} t) + \beta_{\mathrm{L}} \frac{I_{\mathrm{S}}}{I_{\mathrm{c}}})}$$

$$= f_{\mathrm{r},0} + \Delta f_{\mathrm{r}}^{\mathrm{pp}} z(t) \ , \tag{3.18}$$

where $N_{\Phi_0} = I_{\mathrm{ramp}} M_{\mathrm{mod}} / \Phi_0$ is the number of magnetic flux quantum coupled per period of the sawtooth signal and $M_{\mathrm{mod}}$ is the mutual magnetic coupling with the rf-SQUID loop inductance. Therefore, each rf-SQUID produces a multi-harmonic periodic signal with a fundamental frequency of $f_{\mathrm{mod}} = N_{\Phi_0} f_{\mathrm{ramp}}$. Due to dispersion in parameters during the manufacturing of these devices, there is a slight difference in the signal frequencies of the different rf-SQUIDs.

The magnetic flux sawtooth-shaped signal is named Flux Ramp signal (FR) and the technique is known as Flux Ramp Modulation (FRM) [85] since the rf-SQUID signals are phase modulated by the detector signals, i.e., the modulating signals. As a consequence, the detector signals can be recovered by reading the instantaneous phases of the rf-SQUID responses when the slope of the sawtooth is much higher than the slew rate of the detector signals. As a direct consequence, linearity is preserved regardless of the amplitude of the detector signal.

In Fig. 3.9, an sketch of the $\mu$MUX system is shown. The $\Phi_{\mathrm{det}}(t)$ is typically recovered from the rf-SQUID signal by calculating

$$\Phi_{\mathrm{det}}(t) = \arctan\left( -\frac{\displaystyle\int_{T_{\mathrm{ramp}}} \theta(t)\, \sin(\omega_{mod} t) dt}{\displaystyle\int_{T_{\mathrm{ramp}}} \theta(t)\, \cos(\omega_{mod} t) dt} \right) \frac{\Phi_0}{2\pi} \ , \tag{3.19}$$

where $\omega_{mod} = 2\pi f_{\mathrm{mod}}$. In Eq. 3.19, the signal of the rf-SQUID can also be represented by the amplitude $\gamma(t)$.

Due to the transient response of the resonators [86], there is a maximum frequency $f_{\mathrm{mod}}$ at which they can be driven, given by

$$f_{\mathrm{mod}}^{\mathrm{max}} = \frac{BW_{\mathrm{res}}}{2} \ . \tag{3.20}$$

### 3.1.5 Spectral Occupation

The readout tone is a band-pass signal with amplitude $A_{\mathrm{exc}}$, phase $\varphi_{\mathrm{exc}}$ and angular frequency $\omega_{\mathrm{exc}}$ of the form

$$x_{\mathrm{exc}}(t) = A_{\mathrm{exc}} \Re\{ e^{j(\omega_{\mathrm{exc}} t + \varphi_{\mathrm{exc}})} \} \ . \tag{3.21}$$

At the $\mu$MUX output, the convolution of the readout tone with the channel response is

$$x_{\mathrm{out}}(t) = A_{\mathrm{exc}} |s_{21}(t)| \Re\{ e^{j(\omega_{\mathrm{exc}} t + \varphi_{\mathrm{exc}} + \varphi_{s_{21}}(t))} \} \ , \tag{3.22}$$

where

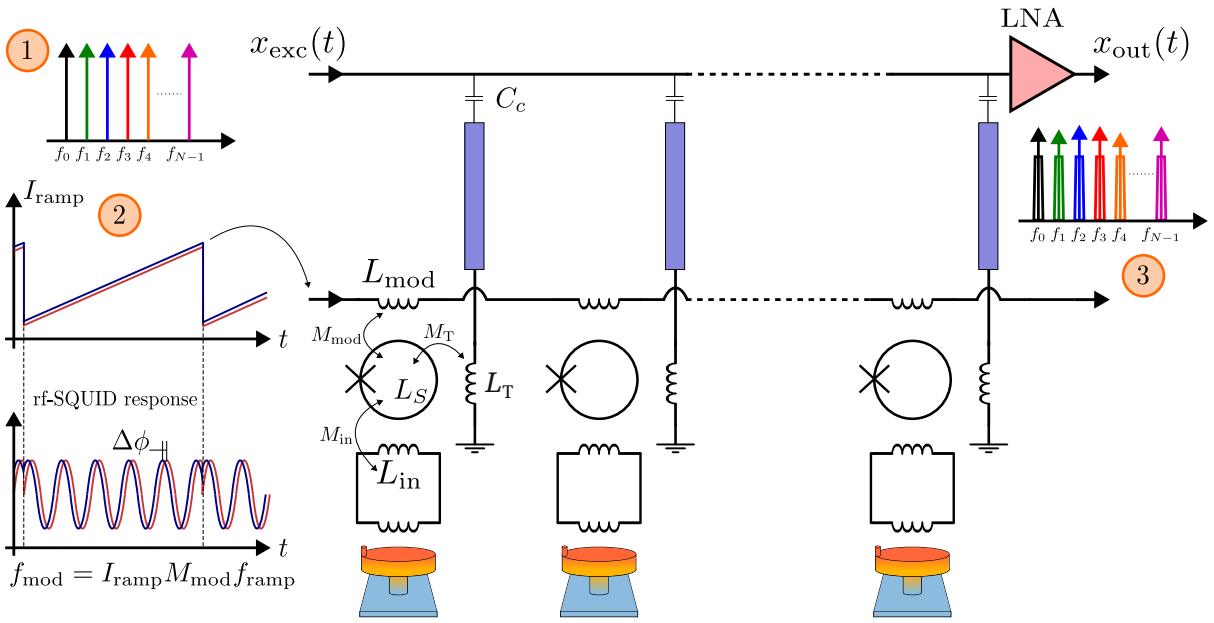


**Figure 3.9:** The $\mu$MUX schematic. (1) A frequency comb excites the $\mu$MUX channels. (2) The FR generates a periodic rf-SQUID signal (shown in red) that modulates each tone in amplitude and phase. An additional magnetic flux generated by the detector couples to the rf-SQUID through $M_{\mathrm{in}}$, causing a phase increment $\Delta\phi$ (shown in blue). (3) At the output of the $\mu$MUX, each tone related to a channel has the information of the corresponding detector signal. A Low-Noise Amplifier (LNA) is placed to amplify the frequency comb signal due to its noise performance.

$$|s_{21}|(t) = \sqrt{\frac{(s_{21}^{\mathrm{min}} BW_{\mathrm{res}})^2 + 4(f_{\mathrm{exc}} - f_{\mathrm{r}}(t))^2}{{BW_{\mathrm{res}}}^2 + 4(f_{\mathrm{exc}} - f_{\mathrm{r}}(t))^2}} \tag{3.23}$$

and

$$\varphi_{s_{21}}(t) = \arctan\left(\frac{2(f_{\mathrm{exc}} - f_{\mathrm{r}}(t))}{s_{21}^{\mathrm{min}} BW_{\mathrm{res}}}\right) - \arctan\left(\frac{2(f_{\mathrm{exc}} - f_{\mathrm{r}}(t))}{BW_{\mathrm{res}}}\right) . \tag{3.24}$$

Therefore, $x_{\mathrm{out}}(t)$ is amplitude and phase modulated by $|s_{21}|(t)$ and $\varphi_{s_{21}}(t)$, respectively. Despite of there is no closed-form solution for the $I_{\mathrm{S}}$ function due to its transcendental nature, it can be numerically approximated. For each element $d$ of the time vector $\varphi_{\mathrm{ext}}(t) = \omega_{\mathrm{mod}} t + \varphi_{\mathrm{exc}} \sin(\omega_{\mathrm{exc}} t)$ the roots of the following equation are obtained for a given $I_{\mathrm{c}}$ and $\beta_{\mathrm{L}}$,

$$I_{\mathrm{S}}(t = t_{\mathrm{d}}) + I_{\mathrm{c}} \sin\left(\varphi_{\mathrm{ext}}(t = t_{\mathrm{d}}) + \beta_{\mathrm{L}} \frac{I_{\mathrm{S}}(t = t_{\mathrm{d}})}{I_{\mathrm{c}}}\right) = 0 \ . \tag{3.25}$$

Thereafter, $s_{21}$ is computed based on a defined set of values for $f_{\mathrm{r},0}$, $f_{\mathrm{exc}}$, $BW_{\mathrm{res}}$, $\eta$ and $s_{21}^{\mathrm{min}}$. $|s_{21}|$ and $\varphi_{s_{21}}$ can be decomposed using a Fourier series,

$$|s_{21}|(t) = c_{\mathrm{m,0}} + \sum_{i=1}^{\infty} \left( c_{\mathrm{m,i}} \cdot \cos\left(\omega_{\mathrm{m,i}} t + \theta_{\mathrm{m,i}}\right) \right) \tag{3.26}$$

and

$$\varphi_{s_{21}}(t) = c_{\mathrm{p,0}} + \sum_{i=1}^{\infty} \left( c_{\mathrm{p,i}} \cdot \cos\left(\omega_{\mathrm{p,i}} t + \theta_{\mathrm{p,i}}\right) \right) \ , \tag{3.27}$$

demonstrating the presence of multiple modulation indices. Employing the same procedure to obtain a general mathematical expansion of a signal modulated in amplitude and frequency by a multi-tonal signal showed in [87], the general expression for $x_{\mathrm{out}}(t)$ is obtained,

$$\begin{aligned} x_{\mathrm{out}}(t) =& A_{\mathrm{exc}} c_{\mathrm{m,0}} \prod_{i=1}^{\infty} \left[ \sum_{n_{\mathrm{i}}=-\infty}^{\infty} J_{n_{\mathrm{i}}}(c_{\mathrm{p,i}}) \right] \cdot \cos\left( \left( \omega_{\mathrm{exc}} + \sum_{i=1}^{\infty} n_{\mathrm{i}} \omega_{\mathrm{p,i}} \right) t + c_{\mathrm{p,0}} + \sum_{i=1}^{\infty} n_{\mathrm{i}} \theta_{\mathrm{p,i}} \right) \\ &+ \frac{A_{\mathrm{exc}}}{2} \sum_{j=1}^{\infty} c_{\mathrm{m,j}} \prod_{i=1}^{\infty} \left[ \sum_{n_{\mathrm{i}}=-\infty}^{\infty} J_{n_{\mathrm{i}}}(c_{\mathrm{p,i}}) \right] \\ &\cdot \Bigg\{ \cos\left( \left( \omega_{\mathrm{exc}} + \omega_{\mathrm{m,j}} + \sum_{i=1}^{\infty} n_{\mathrm{i}} \omega_{\mathrm{p,i}} \right) t + c_{\mathrm{p,0}} + \sum_{i=1}^{\infty} n_{\mathrm{i}} \theta_{\mathrm{p,i}} + \theta_{\mathrm{m,j}} \right) \\ &+ \cos\left( \left( \omega_{\mathrm{exc}} - \omega_{\mathrm{m,j}} + \sum_{i=1}^{\infty} n_{\mathrm{i}} \omega_{\mathrm{p,i}} \right) t + c_{\mathrm{p,0}} + \sum_{i=1}^{\infty} n_{\mathrm{i}} \theta_{\mathrm{p,i}} - \theta_{\mathrm{m,j}} \right) \Bigg\} \ , \end{aligned} \tag{3.28}$$

where $J_{n_{\mathrm{i}}}(c_{\mathrm{p,i}})$ denotes the Bessel functions of the first kind and order $n_{\mathrm{i}}$.

The first term of Eq. 3.28 consists of a tone centered at $\omega_{\mathrm{exc}}$ with infinite sidebands surrounding it at a distance $n_{\mathrm{i}} \cdot \omega_{\mathrm{p,i}}$, where $n_{\mathrm{i}}$ belongs to the integers. The other two components of Eq. 3.28 are also infinite sums of tones, separated by the same distance $n_{\mathrm{i}} \cdot \omega_{\mathrm{p,i}}$ but centered at the frequencies $\omega_{\mathrm{exc}} \pm \omega_{\mathrm{m,j}}$. Since the modulation of $|s_{21}|$ and $\varphi_{s_{21}}$ results from the same signal, the sidebands overlap. It is important to note that the amplitudes of the higher-order components decrease, making the signal's bandwidth practically finite where the energy is primarily distributed among the $f_{\mathrm{exc}}$, $f_{\mathrm{exc}} \pm f_{\mathrm{mod}}$ and $f_{\mathrm{exc}} \pm 2f_{\mathrm{mod}}$ components. Fig. 3.10 shows a typical measurement of the $x_{\mathrm{out}}$ spectrum.

Until now, the detector signal has not been considered to simplify the analysis. However, as previously indicated, the detector signal modulates the rf-SQUID signal in phase, causing the energy to also be distributed among the Bessel components around each sidebands, as Fig. 3.10 shows in dark violet.

Coherent demodulation, whose mathematical expression is detailed in Eq. 3.19, has a narrow bandwidth and is used to demodulate one of the sidebands, effectively filtering out the others. Once the $\mu$MUX is designed, the distribution of energy among the different components is defined by the readout frequency. Additionally, this distribution vary depending on whether the output signal's amplitude or phase is considered. Fig. 3.11

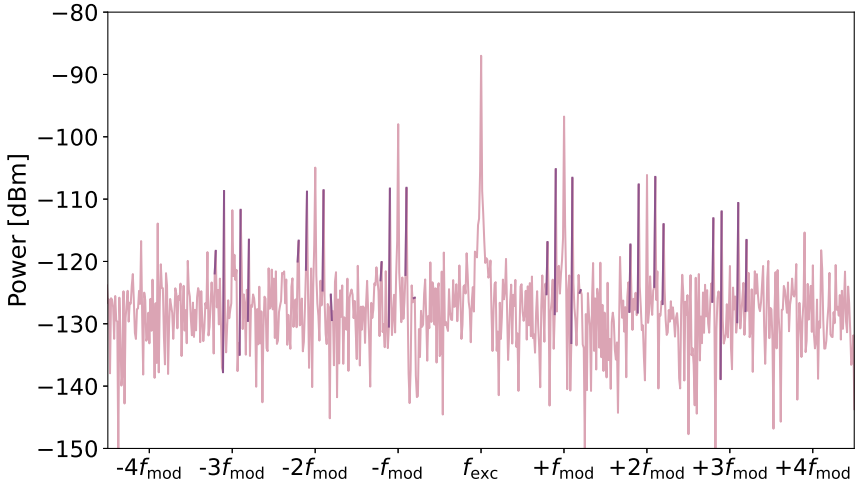


**Figure 3.10:** A simulation of a typical readout tone spectrum at the $\mu$MUX output. The sidebands components indicated are relative to $f_{\mathrm{exc}}$. The simulation parameters are $I_{\mathrm{c}} = 3\,\mu\mathrm{A}$, $\beta_{\mathrm{L}} = 0.3$, $\varphi_{\mathrm{exc}} = 0.3$, $s_{21}^{\mathrm{min}} = 0.2$, $\eta = 1$, $BW_{\mathrm{res}} = 200\,\mathrm{kHz}$, $f_{\mathrm{r},0} = 4\,\mathrm{GHz}$, $f_{\mathrm{exc}} = f_{\mathrm{r}}$ and $f_{\mathrm{mod}} = 10\,\mathrm{kHz}$. The detector signal was simulated as $\varphi_{\mathrm{det}} = 0.6\cos(2\pi 1000t)$ for a better visualization of the spectral occupancy. As a result of the phase modulation caused by the detector signal, the sidebands marked in dark violet emerge.

shows the Fourier coefficients of the components located at $f_{\mathrm{mod}}$ and $2f_{\mathrm{mod}}$ for both $|s_{21}|$ and $\varphi_{s_{21}}$ for various values of $\eta$.

In this example, the maximum energy is obtained in the component located at $f_{\mathrm{mod}}$ for both the amplitude and phase, occurring at $f_{\mathrm{exc}} - f_{\mathrm{r},0} \approx 0.8 \cdot BW_{\mathrm{res}}$ and $\eta \approx 1.13$ and $f_{\mathrm{exc}} \approx f_{\mathrm{r},0}$ and $\eta \approx 0.26$, respectively

The spectrum in Fig. 3.10 shows the influence of a single channel in the $\mu$MUX. In a $\mu$MUX with multiple channels separated by a distance $f_{\mathrm{sep}}$, the $x_{\mathrm{out}}$ spectrum is composed of the sum of the individual spectra of each modulated readout tone. Each individual spectrum is centered at the frequency of the corresponding readout tone. Given the system bandwidth $BW_{\mathrm{sys}}$, the number of channels or the multiplexing factor of the system can be calculated as $N_{\mathrm{ch}} = BW_{\mathrm{sys}}/f_{\mathrm{sep}}$. The level of crosstalk between channels depends on their separation [16, 88]. Greater separation reduces the crosstalk level but also decreases the multiplexing factor. To ensure a crosstalk level of less than $\leq 0.1\%$, the separation between channels must be $f_{\mathrm{sep}} \geq 10BW_{\mathrm{res}}$ [89].

### 3.1.6 Optimal SNR

In the FRM scheme, the gain is determined by integrating all the points through which the $\partial|s_{21}(\Phi_{\mathrm{ext}})|/\partial\Phi_{\mathrm{ext}}$ and $\partial\varphi_{s_{21}}(\Phi_{\mathrm{ext}})/\partial\Phi_{\mathrm{ext}}$ curves periodically vary, expressed for the magnitude as

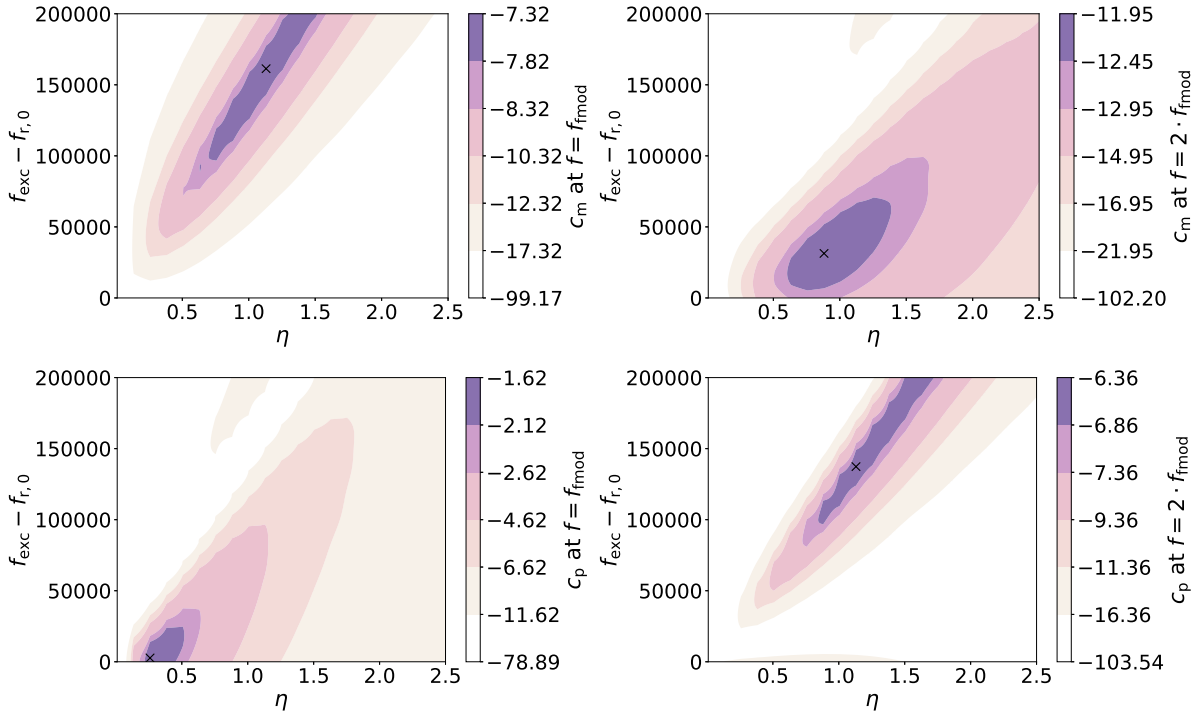


**Figure 3.11:** Simulation of the Fourier coefficient amplitudes for $|s_{21}|$ (top) and $\varphi_{s_{21}}$ (bottom) using parameters $I_c = 3\,\mu A$, $f_{mod} = 100\,kHz$, $s_{21}^{min} = 0.2$, $f_{r,0} = 4\,GHz$, $BW_{res} = 200\,kHz$ $\beta_L = 0.3$ and $\varphi_{exc} = 0.3$. In both cases, the coefficients located at $f_{mod}$ (left) and $2f_{mod}$ (right) are plotted. The maximum levels obtained are marked with a cross.

$$\overline{\gamma^2} = \frac{1}{2\pi}\int_0^{2\pi}\left(\frac{\partial|s_{21}|}{\partial\Phi_{ext}}\right)^2 \partial\Phi_{ext} \quad . \tag{3.29}$$

This includes the points of greatest gain (where the slope of the derivative is maximum) and the extremes of the curves (which are insensitive to the detector). Consequently, this integration clearly demonstrates that the overall gain is less than the optimal open-loop gain in both amplitude and phase cases, resulting in signal degradation. The degradation factor depends on the modulation signal, which explains the use of the sawtooth waveform as it passes through the insensitive parts of the rf-SQUID signal fewer times than other types of modulation. The degradation is determined by

$$b = \sqrt{\frac{\gamma_{max}^2}{\overline{\gamma^2}}} \quad , \tag{3.30}$$

where $\gamma_{max}$ represents the maximum open-loop gain.

It is not sufficient to consider only the optimal $\mu$MUX gain, as this may also be the point of greatest noise power. Therefore, the SNR level of the system must be considered, which is a complex task requiring a multi-parametric characterization of the system. This

involves computing the SNR for different combination values of $f_{\mathrm{exc}}$, $P_{\mathrm{exc}}$ and $f_{\mathrm{mod}}$, among other parameters.

Additionally, part of the signal affected by transients in the sawtooth function must be discarded due to significant noise. Discarding part of the detector signal also reduces the SNR, though to a much lesser extent than if the transients were considered. Leading to an increase in noise degradation by a factor of $b/\sqrt{\alpha}$, where $\alpha$ is the fraction of the FR used for phase demodulation.

It is worth considering the option of generating a FR with very low frequency and performing partial demodulations on specific segments of it. This approach could significantly mitigate noise degradation. To implement this strategy, it is essential to increase the amplitude of the FR, allowing for the generation of multiple periods of the rf-SQUID signal. Besides, when lowering the frequency of the modulation signal, the impact of flicker noise during the generation process must be considered. If this noise is high, the modulation signal may overlap with the $1/f$ noise slope, making filtering more challenging. As a result, both the noise and the modulation signal could couple directly to the rf-SQUID. In this improved scenario, Eq. 3.19 could be reformulated as

$$\Phi_{\mathrm{det}}(t) = \arctan\left(-\frac{\displaystyle\int_{T_{\mathrm{ramp}}/N} \theta(t)\,\sin(\omega_{mod}t)dt}{\displaystyle\int_{T_{\mathrm{ramp}}/N} \theta(t)\,\cos(\omega_{mod}t)dt}\right)\frac{\Phi_0}{2\pi}\ , \tag{3.31}$$

where $N$ represents the number of fractions to demodulate within a single FR period, as illustrated in Fig. 3.12.

Despite these challenges, the FRM scheme offers a significant advantage over open-loop measurement. By shifting the detector signal to higher frequencies defined by the carrier frequency ($f_{\mathrm{mod}}$), the FRM scheme effectively avoids much of the low-frequency noise and prevents the degradation of the detector signal.

## 3.2 Software-defined Radio

The RTE is located outside the cryostat, reducing the complexity of the cryogenic system and preventing thermal overload. The RTE synthesizes a frequency comb that excite the $\mu$MUX and processes the return signal to extract the necessary information as in a SDR scheme (see diagram on Fig. 3.13). Throughout the signal path, various devices condition the signal focusing on spectral efficiency, high SNR, high Spurious Free Dynamic Range (SFDR) and optimal readout power and peak-to-mean ratio. This system is designed with an emphasis on increasing component integration, which reduces the cost of electronics, shortening development time and high flexibility to adapt the system to different requirements. Therefore, high-performance integration platforms that use System-on-Chip (SoC) architectures and combine digital and hardware electronics are employed. These platforms, often customized, are part of the system's BE and are responsible for signal synthesis and acquisition. The BE is complemented by high-speed

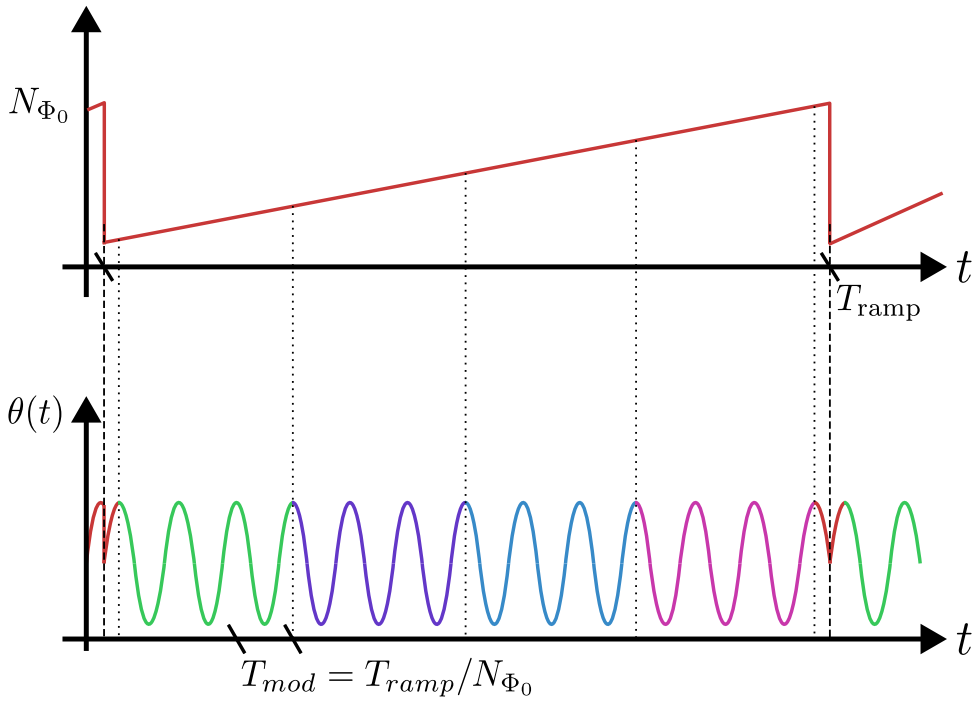


**Figure 3.12:** Diagram of a fractional FR demodulation scheme, aimed at reducing the impact of discarded transients. In this example, the FR period is divided into $N = 4$ sections, each highlighted with a different color on the rf-SQUID signal. The section of $\theta(t)$ highlighted in red represents the portion of the signal to be discarded, equivalent to $T_{\text{ramp}} \cdot (1 - \alpha)$.

DACs and ADCs, which facilitate the use of the large bandwidths required to read all $\mu$MUX channels, typically located in the 4 to 8 GHz band. Usually, the frequency comb is in the MHz range, so additional devices are used to condition the signal to the GHz range optimally. These devices form the so-called FE. However, many research groups are currently investigating and characterizing commercial systems that integrate converters into SoC platforms and use techniques for direct signal generation in the GHz band, eliminating the need for a front-end. This integration aims to further streamline the system and improve performance, flexibility and cost-efficiency.

### 3.2.1 Back-end electronics

The BE is responsible for the digital generation, acquisition and processing of the required signals. Generation corresponds to the frequency comb that readout all the $\mu$MUX channels as the modulation signal. The required high flexibility involves tuning each generated tone to the desired frequency, considering possible dispersion in the design of the $\mu$MUX that can cause undesired frequency shifts in the channels, resulting in non-equally frequency spaced channels. There are several approaches to synthesizing this frequency comb, including Direct Digital Synthesizer (DDS) and the playback of a pre-synthesized waveform stored in memory. The latter involves calculating the sum of those tones uti-

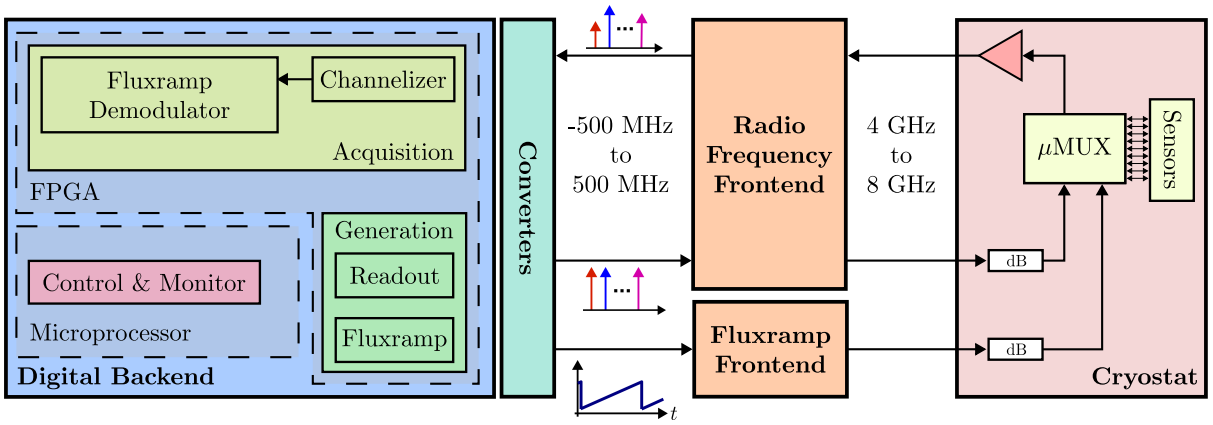


**Figure 3.13:** SDR scheme. The FR and the frequency comb is synthesized in the BE, where each tone monitors a different channel of the $\mu$MUX. Multiple sub-bands with a complex bandwidth of 1 GHz (−500 MHz to 500 MHz) contain the multi-tone signal. Each sub-band is then positioned within the 4 GHz to 8 GHz spectrum by the Radio Frequency FE (see Section 3.5 for more details). On the return path, the FE conditions the signal to be processed by the BE which extracts the detector signals of all the channels by the use of a Channelizer and the Fluxramp Demodulator.

lizing a high-level programming language, such as Python or MATLAB and storing it in memory with a determined width $W_{mem}$ and length $L_{mem}$. The signal is then played by cyclically reproducing $M$ samples from memory at a frequency $f_{clk}^{mem}$. The minimal and maximal output frequencies allowed by this method are determined as

$$f_{out,min}^{mem} = \frac{f_{clk}^{mem}}{L_{mem}} \tag{3.32}$$

and

$$f_{out,max}^{mem} = \frac{f_{clk}^{mem}}{2} \quad , \tag{3.33}$$

respectively. Although this method is quick and easy to implement, it lacks flexibility, as each modification requires re-recording the memory.

A DDS is used to generate a precise and programmable sinusoidal waveform. It can rapidly switch between frequencies with high resolution, making it ideal for applications that require quick frequency changes and operates over a broad spectrum of frequencies. Furthermore, the programmability of DDS allows for easy adjustments and fine-tuning of the output frequency and waveform through digital controls, offering a high level of flexibility that is difficult to achieve by other implementations. The core of a DDS consists of several components as Fig. 3.14 shows. The Phase Accumulator has $2^N$ digital states to represent values from 0 to $2\pi$ of the desired waveform phase. An initial phase, $\theta_0$, is set along with the phase increment, $\Delta\theta$, which occurs at each clock cycle. The setting of $\Delta\theta$ is done in the phase register using a binary tuning word $M$, which defines the waveform frequency. This phase is then fed into the Phase-to-Amplitude Converter,

often implemented as a Look-Up Table (LUT) containing precomputed values of a sine wave that translates the phase into corresponding amplitude values.

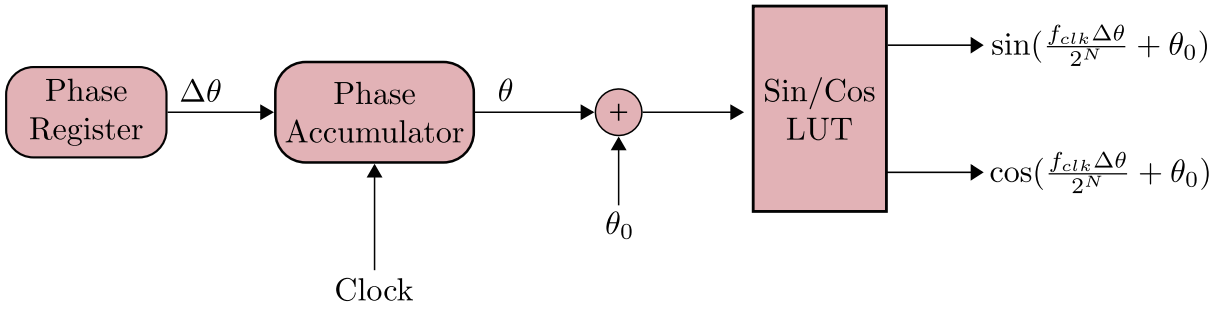


**Figure 3.14:** Direct Digital Synthesizer schematic.

The DDS output frequency depends on the $\Delta\theta$ value and the length of the accumulator as well as the system clock frequency $f_{\text{clk}}^{\text{dds}}$ and is described by

$$f_{\text{out}}^{\text{dds}} = \frac{f_{\text{clk}}^{\text{dds}}\Delta\theta}{2^{\text{N}}} \ . \tag{3.34}$$

Besides, the frequency resolution of the DDS is

$$f_{\text{res}}^{\text{dds}} = \frac{f_{\text{clk}}^{\text{dds}}}{2^{\text{N}}} \ . \tag{3.35}$$

Several DDS blocks can be implemented to create the multi-tone signal. Therefore, any required change in a single tone only needs to change its corresponding tuning word.

The state-of-the-art readout systems based on $\mu$MUX use complex signals, which allow more efficient use of the available bandwidth unlike real signals, whose spectrum stores the same information symmetrically. Figure. 3.15 shows the occupancy bandwidth for a real signal and for a complex signal containing the same non-trivial information. The complex signal uses half the bandwidth compared to the real signal.

Analytically, the relationship between a real signal $x_{\text{real}}(t)$ and Euler's formula can be demonstrated as follows:

$$\begin{aligned} x_{\text{real}}(t) &= A\sin(\omega t + \varphi) \\ &= A\frac{e^{j(\omega t+\varphi)} - e^{-j(\omega t+\varphi)}}{2j} \ . \end{aligned} \tag{3.36}$$

Eq. 3.36 describes two phasors with frequencies $\omega/(2\pi)$ and $-\omega/(2\pi)$. By filtering the negative (or positive) frequencies, as it is depicted in Fig. 3.15, the analytic function is obtained. This function is the associated complex representation of $x_{\text{real}}(t)$,

$$x_{\text{analytic}}(t) = x_{\text{real}}(t) + j\hat{x}_{\text{real}}(t) \ . \tag{3.37}$$

$\hat{x}_{\text{real}}(t)$ is the Hilbert transform of $x_{\text{real}}(t)$. As the Hilbert transform of real-valued signals results in its orthogonal function, $\hat{x}_{\text{real}}(t) = A\sin(\omega t + \varphi + \pi/2) = A\cos(\omega t + \varphi)$. Therefore,

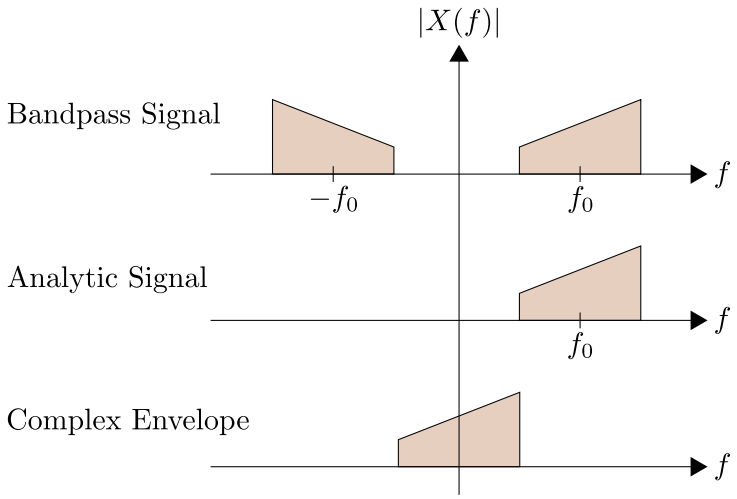


**Figure 3.15:** The spectrum of the analytical function of a bandpass signal. The complex envelope is the base-band representation of the analytical signal, derived by shifting the analytical signal from its center frequency to DC.

$$x_{\text{analytic}}(t) = A\left[\sin(\omega t + \varphi) + j\cos(\omega t + \varphi)\right] \quad . \tag{3.38}$$

The optimization in the bandwidth use is achieved at the expense of greater resources since now two signals must be generated, as specified in Eq. 3.38.

Once the multi-tone signal passes through the $\mu$MUX channels, it is acquired by the BE for digital processing. To extract the information from each modulated tone, a chain of channelizers, filters and downsamplers is first designed. Channelization is the technique used to decompose a wideband signal into several non-overlapping narrowband sub-signals through a bank of bandpass filters [90]. Each filter is finely tuned to pass a specific range of frequencies while attenuating others. The output of each filter represents a distinct portion of the original signal's frequency spectrum, enabling parallel processing of different frequency components. As these narrow-band signals possess lower bandwidths, their sampling rates can be reduced without the risk of distortion due to aliasing. Fig. 3.16 provides a general diagram of a filter bank.

The rf-SQUID signal of each channel of the $\mu$MUX is obtained at the output of the channelizer. Thereafter, a phase demodulator, or FR demodulator in the context of this system, extracts the detector signal from the instantaneous phase of the rf-SQUID signals.

These techniques are within the field of study known as multirate signal processing. Chapter 5 outlines concepts and theories of multirate signal processing, providing a foundation for understanding the chosen FR demodulator. A detailed explanation of the implemented channelizer and downsamplers is provided in [91].

To be able to process the continuous arrival of a large data rate for reading out a highly populated detector array, FPGAs are required. These devices can process thousands of signals in real-time thanks to their inherent parallel processing that allow them to perform multiple operations simultaneously, in contrast to the sequential processing nature of microprocessors. At their core, it consist of a matrix of Configurable Logic Block (CLB)

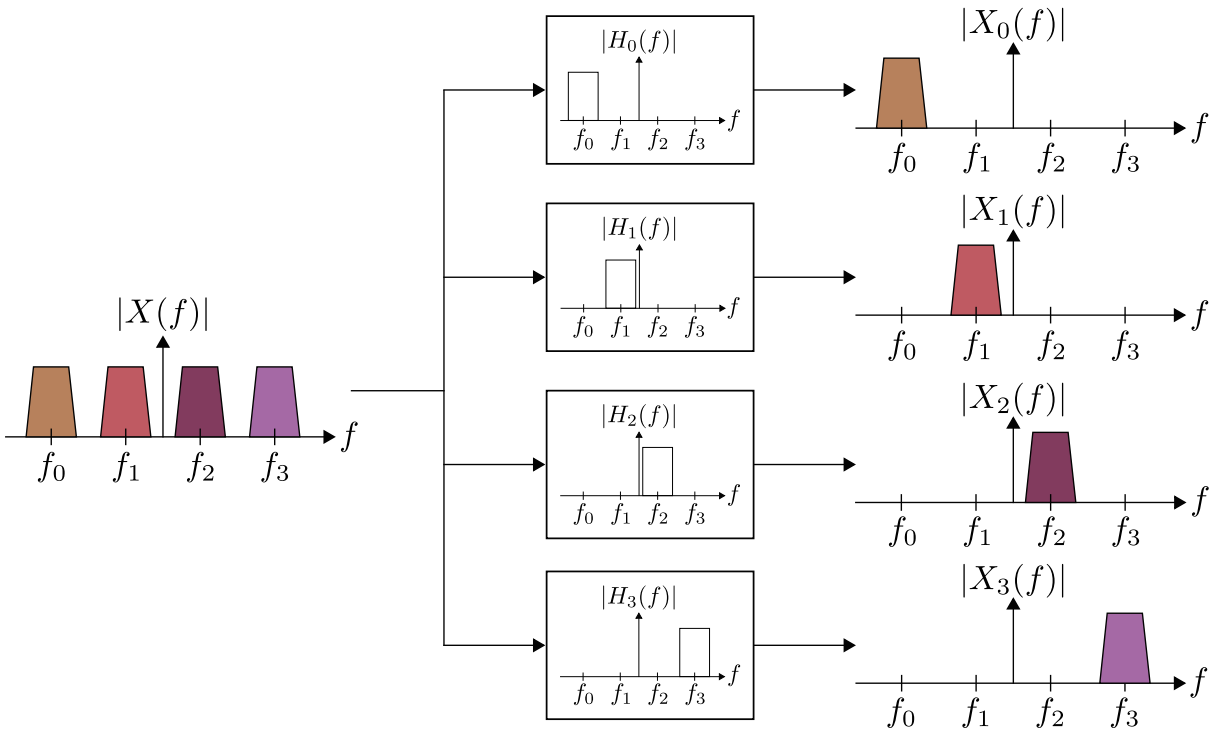


**Figure 3.16:** 4-channel filter bank. The incoming multi-tone signal is filtered through 4 filters set to different frequencies, allowing the selection of the desired tone frequency and filtering out the rest, thus isolating each component of the signal.

surrounded by a network of programmable interconnects. These logic blocks can be programmed to perform complex combinational and sequential logic functions. Additionally, FPGAs incorporate memory elements such as Flip-Flop (FF), LUT and Block Random Access Memory (BRAM), as well as more advanced features like Digital Signal Processing (DSP) slices for efficient addition, multiplication and accumulation operations. This architecture offers a significant flexibility in designing and implementing complex digital circuits, enabling designers to customize their behavior and functionality according to specific application requirements.

Modern electronic platforms, such as those based on the UltraScale+ architecture [92], integrate the flexibility of FPGAs with the performance and functionality of embedded micro-processor ($\mu$P), creating a versatile platform for complex system designs and providing powerful solutions for a wide range of high-performance and real-time applications.

The interface between the analog and digital world is achieved through ADCs and DACs. In the proposed readout system, the DACs are responsible for converting the digital frequency comb and the FR into continuous-time voltage or current signals. Moreover, the ADCs are used to digitize the modulated signal for further processing.

### 3.2.2 Signal converters

ADCs transform a continuous-time analog input into a sequence of binary numbers. This process entails three main tasks: sampling, quantization and coding [93]. Sampling involves taking values from a continuous-time analog signal at regular intervals defined by the sampling frequency ($f_s^{conv}$). Subsequently, the samples are quantized to a finite number of levels, which are then coded into a specific number of bits. The quantizer has a maximum amplitude operating range named the full scale range from which samples are clipped. In addition, it determines the smallest possible difference between two consecutive quantization levels known as the quantization step size **q**. Conversely, DACs perform the inverse function of ADCs by converting digital data into a continuous-time analog signal. Due to the finite number of representation levels, many analog values must be approximated to the nearest level, resulting in an inherent difference known as quantization error ($e_q$). Increasing the number of representation levels by using more bits to code the digital word, i.e., improving the converter resolution, results in a reduction of quantization error. Fig. 3.17 illustrates an example of quantization and 3-bits offset binary codification for both ADCs and DACs.

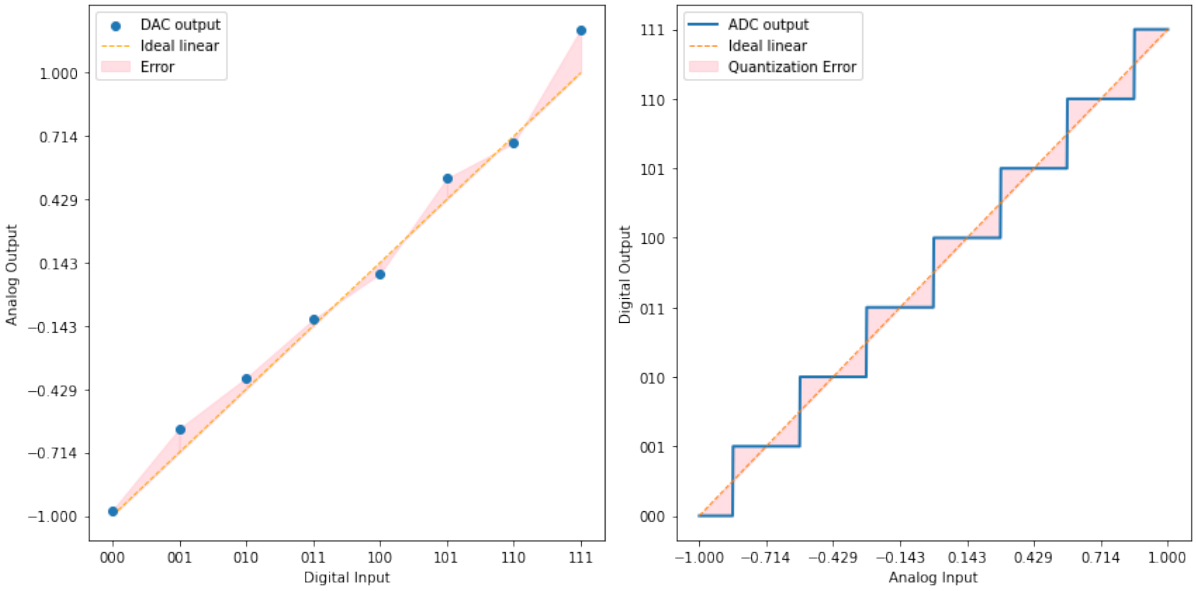


**Figure 3.17:** DAC and ADC quantization. The shaded areas in orange show the quantization error occurring in both converters.

#### Quantization

If the quantization theorem holds [94], the quantization error can be modeled as a uniformly distributed linear function over the interval:

$$\frac{-q}{2} \leq e_q \leq \frac{q}{2} \ . \tag{3.39}$$

By calculating the Root-Mean-Squared (RMS) of the quantization error function, the quantization noise is obtained in the form

$$\sigma_{e_{\mathrm{q}}} = \frac{q}{\sqrt{12}} \ , \tag{3.40}$$

and therefore, the noise power is

$$P_{\mathrm{n}} = \frac{q^2}{12} \ . \tag{3.41}$$

An analog signal of the form $x(t) = A\sin(\omega t + \varphi)$ has an average power defined by

$$P_{\mathrm{s}} = \frac{A^2}{2} \ , \tag{3.42}$$

For an N-bits and $2A$ full-scale range quantizer, $q = 2A/2^{\mathrm{N}}$ and the theoretical converter SNR for the approximated error function is

$$\mathrm{SNR}_{\mathrm{conv}} = \frac{P_{\mathrm{s}}}{P_{\mathrm{n}}} = \frac{A^2}{2} \cdot \frac{2^{2\mathrm{N}}12}{4A^2} = \frac{3}{2} \cdot 2^{2\mathrm{N}} \ . \tag{3.43}$$

The $\mathrm{SNR}_{\mathrm{conv}}$ can be expressed in dB as

$$\mathrm{SNR}_{\mathrm{conv}}\Big|_{\mathrm{dB}} = 10\log_{10}\left(\frac{3}{2} \cdot 2^{2\mathrm{N}}\right) \mathrm{dB} = 1.76\,\mathrm{dB} + 6.02\,\mathrm{dB} \cdot N \ . \tag{3.44}$$

Eq. 3.44 suggests that each additional bit in the quantizer increases the $\mathrm{SNR}_{\mathrm{conv}}$ by 6 dB, which is not entirely true when considering a more realistic model of quantization noise and other noises present in the converter.

In the proposed SDR system, converters are used for an M tones signal with amplitude $A_{\mathrm{i}}$, angular frequency $\omega_{\mathrm{i}}$ and phase $\varphi_{\mathrm{i}}$ of the form

$$x(t) = \sum_{\mathrm{i}=1}^{\mathrm{M}} A_{\mathrm{i}} sin(\omega_{\mathrm{i}} t + \varphi_{\mathrm{i}}) \ , \tag{3.45}$$

which has a determined peak amplitude to RMS ratio, also known as the crest factor. Therefore, it is useful to express Eq. 3.44 as a function of the signal crest factor $k_{\mathrm{s}}$, depicted as

$$\mathrm{SNR}_{\mathrm{conv}}\Big|_{\mathrm{dB}} = 4.77\,\mathrm{dB} + 6.02\,\mathrm{dB} \cdot N - 20\log_{10}(k_{\mathrm{s}}) \ \mathrm{dB} \ \text{[95]}. \tag{3.46}$$

The crest factor of the multi-tone signal depends on the amplitude, frequency and phase of each tone. However, assuming that all the tones have the same amplitude for readout the $\mu$MUX. It can be demonstrated that the RMS value is

$$x_{\mathrm{rms}} = \sqrt{\frac{1}{2}\sum_{\mathrm{i}=1}^{\mathrm{M}} |A_{\mathrm{i}}|^2} = \sqrt{\mathrm{M}}\frac{A_{\mathrm{i}}}{\sqrt{2}} \ . \tag{3.47}$$

The peak amplitude of the multi-tone signal depends on the phase of each tone. By considering the worst-case scenario, where all the individual peaks add coherently reaching the full scale range, it results in

$$A_{\mathrm{s}} = \mathrm{M}A_{\mathrm{i}} \ , \tag{3.48}$$

and the crest factor follows

$$k_{\mathrm{s}} = \frac{A_{\mathrm{s}}}{x_{\mathrm{rms}}} = \sqrt{2\mathrm{M}} \ . \tag{3.49}$$

Finally, replacing Eq. 3.49 in Eq. 3.46 leads to

$$\mathrm{SNR}_{\mathrm{conv}}\Big|_{\mathrm{dB}} = 1.76\,\mathrm{dB} + 6.02\,\mathrm{dB} \cdot N - 10\log_{10}(\mathrm{M}) \ \ \mathrm{dB} \ . \tag{3.50}$$

**Sampling**

The sampling process can be defined as the multiplication of the input signal with a train of dirac pulses repeated at a distance $T_{\mathrm{s}}^{\mathrm{conv}} = 1/f_{\mathrm{s}}^{\mathrm{conv}}$ as it is shown in the following equation

$$x_{\mathrm{p}}(t) = x(t) \sum_{\mathrm{n=-\infty}}^{\infty} \delta(t - nT_{\mathrm{s}}^{\mathrm{conv}}) \ , \tag{3.51}$$

where $n$ is an integer number. The Fourier transform of Eq. 3.51 is described by a convolution in the frequency domain:

$$X_{\mathrm{p}}(f) = X(f) * \frac{1}{T_{\mathrm{s}}^{\mathrm{conv}}} \sum_{\mathrm{n=-\infty}}^{\infty} \delta(f - \frac{n}{T_{\mathrm{s}}^{\mathrm{conv}}}) = \frac{1}{T_{\mathrm{s}}^{\mathrm{conv}}} \sum_{\mathrm{n=-\infty}}^{\infty} X(f - \frac{n}{T_{\mathrm{s}}^{\mathrm{conv}}}) \ . \tag{3.52}$$

Consequently, the spectrum $X(f)$ appears periodically every $f_{\mathrm{s}}^{\mathrm{conv}}$ value, as it is depicted in Fig. 3.18. The spectrum division given by the Nyquist frequency correspond to the so-called Nyquist zones defined by

$$[(K-1)\frac{f_{\mathrm{s}}^{\mathrm{conv}}}{2}, K\frac{f_{\mathrm{s}}^{\mathrm{conv}}}{2}] \ . \tag{3.53}$$

where $K = 1, 2, 3, ...,$ are natural numbers. The repeated $X(f)$ signals over each Nyquist zone are the images of it. As shown in Fig. 3.18, the sampling frequency must be at least twice the signal bandwidth to ensure no loss of information from the original signal. This principle is known as the sampling theorem.

As mentioned, the noise power in Eq. 3.41 considers white noise throughout the bandwidth limited by the Nyquist frequency ($f_{\mathrm{s}}^{\mathrm{conv}}/2$). The total bandwidth of the ADC in the Readout system encompasses the multi-tone signal or a sub-band of it if multiple converters are used. After the signal is digitized by the converter, it is channelized and filtered. Consequently, the SNR of the individual processed channel increases according to the filtering bandwidth $BW_{\mathrm{filt}}$, following the relationship

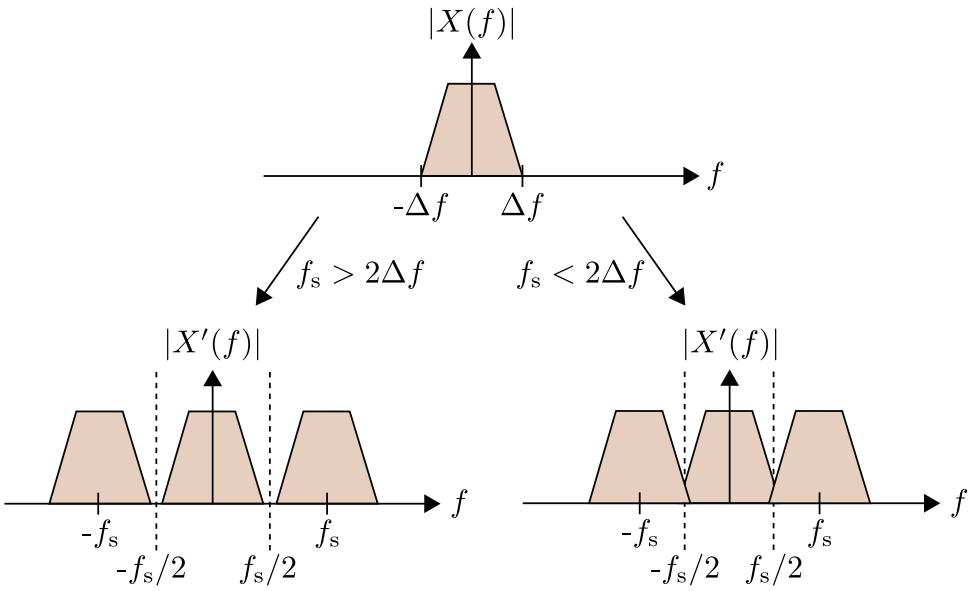


**Figure 3.18:** Spectrum of a sampled signal. It corresponds to a scaled sum of an infinite number of shifted copies of the original signal spectrum. If the sampling theorem is not satisfied, overlap occurs between the different copies, resulting in a loss of information.

$$\mathrm{SNR}^{\mathrm{tone}}_{\mathrm{conv}}\Big|_{\mathrm{dB}} = 1.76\,\mathrm{dB} + 6.02\,\mathrm{dB}\cdot N - 10\log_{10}(\mathrm{M})\ \mathrm{dB} + 10\log_{10}\left(\frac{f_{\mathrm{s}}^{\mathrm{conv}}}{2BW_{\mathrm{filt}}}\right)\ \mathrm{dB}\ . \quad (3.54)$$

This technique is known as signal oversampling and the last factor of Eq. 3.54 is the processing gain.

### Signal Reconstruction

In practice, a DAC requires a certain amount of time to reconstruct a continuos-time signal from the digital samples. Different reconstruction techniques are utilized depending on the required Nyquist zone. The most used is the zero-order hold and consist in retaining the sample value for a time $T_{\mathrm{s}}^{\mathrm{conv}}$ until the next sample arrives. In this way, the sampling resembles narrow pulses of width $T_{\mathrm{s}}^{\mathrm{conv}}$, yielding:

$$x_{\mathrm{zoh}}(t) = \sum_{\mathrm{n}=-\infty}^{\infty} s[n]\mathrm{rect}\left(\frac{t - nT_{\mathrm{s}}^{\mathrm{conv}}}{T_{\mathrm{s}}^{\mathrm{conv}}}\right)\ , \quad (3.55)$$

where rect() is the Rectangular function:

$$\mathrm{rect}\left(\frac{t - nT_{\mathrm{s}}^{\mathrm{conv}}}{T_{\mathrm{s}}^{\mathrm{conv}}}\right) = \begin{cases} 1 & \text{if } |t| \leq (n+\frac{1}{2})T_{\mathrm{s}}^{\mathrm{conv}} \\ 0 & \text{otherwise} \end{cases}\ . \quad (3.56)$$

The Fourier transform of Eq 3.56 is the DAC response function of the form

$$H(f) = \frac{sin(\pi f T_{\mathrm{s}}^{\mathrm{conv}})}{\pi f T_{\mathrm{s}}^{\mathrm{conv}}} e^{-j\pi f T_{\mathrm{s}}^{\mathrm{conv}}} \quad , \tag{3.57}$$

as Fig. 3.19 illustrates.

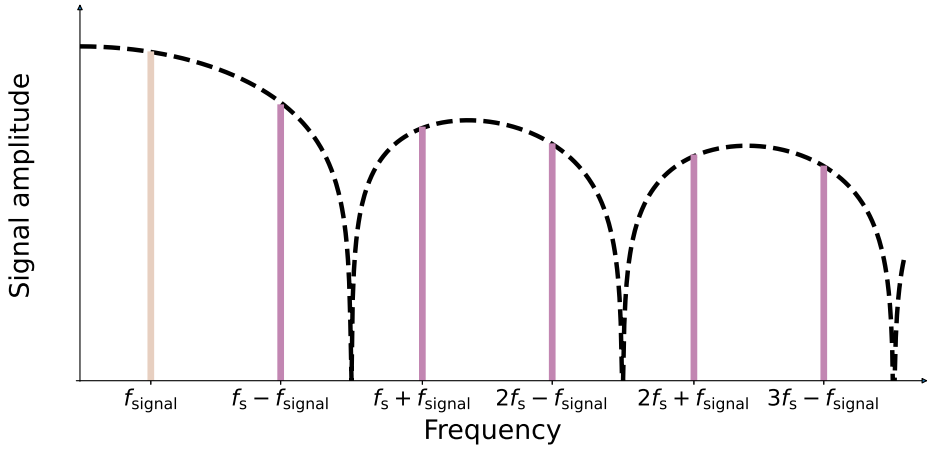


**Figure 3.19:** DAC zero-order hold response. As an illustration, the spectrum of a desired signal is plotted in light color, along with its images, which are shown in dark violet.

The power difference in dBc of the images located at $(f_{\mathrm{s}} - f_{\mathrm{signal}})$ relative to the base-band signal frequency $(f_{\mathrm{signal}})$, i.e. the lowpass signal very near zero frequency, is governed by the following equation,

$$\mathrm{dBc} = 20\log_{10}\left(\frac{f_{\mathrm{signal}}}{f_{\mathrm{s}} - f_{\mathrm{signal}}} \cdot \left|\frac{sin(\frac{\pi(f_{\mathrm{s}} - f_{\mathrm{signal}})}{f_{\mathrm{s}}^{\mathrm{conv}}})}{sin(\frac{\pi f_{\mathrm{signal}}}{f_{\mathrm{s}}^{\mathrm{conv}}})}\right|\right) \text{ [96].} \tag{3.58}$$

### 3.2.3 Front-end electronics

The FE is responsible for conditioning the analog signal between the DAC-$\mu$MUX and $\mu$MUX-ADC interfaces. These tasks may include signal amplification, attenuation, frequency shifting, combining and splitting. Signal amplification and attenuation are primarily required to adapt the signal levels to the optimum range needed to minimize the SNR degradation. Signal combining and splitting are typically employed when multiple DACs and ADCs are used, as a large signal bandwidth needs to be covered. In this process, the different sub-bands generated by each DAC are combined into a single signal, which is then transmitted via a single rf-coaxial cable to the $\mu$MUX inside the cryostat. Subsequently, the $\mu$MUX output signal is split back into sub-bands by the FE to be processed by different ADCs. The frequency shift is used to allocate each sub-band within the corresponding microwave range, covering the entire operational bandwidth of the $\mu$MUX, which, as previously mentioned, typically ranges from 4 to 8 GHz.

By combining two signals, typically one being a Local Oscillator (LO) and the other the input signal, mixers produce new frequencies that are the sum and difference of the original frequencies. This process is known as frequency mixing or heterodyning. A mixer operates based on the principle of non-linear signal processing. When an input signal with a frequency $f_{\text{in}}$ and a LO signal with a frequency $f_{\text{lo}}$ are applied to a non-linear device, the non-linearity generates new frequency components. These new components are at $f_{\text{in}} - f_{\text{lo}}$ and $f_{\text{in}} + f_{\text{lo}}$. Mathematically, if the input signal is represented as $x_{\text{in}}(t) = A_{\text{in}} cos(2\pi f_{\text{in}} t + \varphi_{\text{in}})$ and the LO signal as $x_{\text{lo}}(t) = cos(2\pi f_{\text{lo}} t)$, the mixer output will contain the following terms:

$$\begin{aligned} x_{\text{out}}^{\text{mixer}}(t) &= x_{\text{in}}(t) \cdot x_{\text{lo}}(t) \\ &= \frac{A_{\text{in}}}{2}\left[cos\Big(2\pi(f_{\text{in}} - f_{\text{lo}})t + \varphi_{\text{in}}\Big) + cos\Big(2\pi(f_{\text{in}} + f_{\text{lo}})t + \varphi_{\text{in}}\Big)\right] . \end{aligned} \tag{3.59}$$

One of these terms, either the frequency up-converted ($f_{\text{in}} + f_{\text{lo}}$) or down-converted ($f_{\text{in}} - f_{\text{lo}}$), is the desired signal, while the other is the image signal. The desired signal can then be filtered out by applying the appropriate filtering.

The example above was based on mixing real signals. However, as demonstrated in Section 3.2.1, complex signals (also called quadrature or IQ signals) allow for more efficient use of the spectrum. In this case, the complex mixer internally consists of two mixers, which mix the quadrature components of the input with the signals $cos(2\pi f_{\text{lo}} t)$ and $sin(2\pi f_{\text{lo}} t)$, respectively. Thus, for a quadrature signal described by

$$x_{\text{in}}(t) = A_{\text{in}}\Big[\cos(2\pi f_{\text{in}} t + \varphi_{\text{in}}) + j\sin(2\pi f_{\text{in}} t + \varphi_{\text{in}})\Big] , \tag{3.60}$$

the heterodyning corresponds to:

$$\begin{aligned} x_{\text{out}}^{\text{mixer}}(t) &= \Re\big\{x_{\text{in}}(t)\big\} \cdot \Re\big\{x_{\text{lo}}(t)\big\} + j\Im\big\{x_{\text{in}}(t)\big\} \cdot \Im\big\{x_{\text{lo}}(t)\big\} \\ &= A_{\text{in}}\Big[\cos(2\pi f_{\text{in}} t + \varphi_{\text{in}}) \cdot \cos(2\pi f_{\text{lo}} t)\Big] \\ &\quad + jA_{\text{in}}\Big[\sin(2\pi f_{\text{in}} t + \varphi_{\text{in}}) \cdot \sin(2\pi f_{\text{lo}} t)\Big] \\ &= \frac{A_{\text{in}}}{2}\Big[\cos\Big(2\pi(f_{\text{in}} - f_{\text{lo}})t + \varphi_{\text{in}}\Big) + \cos\Big(2\pi(f_{\text{in}} + f_{\text{lo}})t + \varphi_{\text{in}}\Big)\Big] \\ &\quad + j\frac{A_{\text{in}}}{2}\Big[\cos\Big(2\pi(f_{\text{in}} - f_{\text{lo}})t + \varphi_{\text{in}}\Big) - \cos\Big(2\pi(f_{\text{in}} + f_{\text{lo}})t + \varphi_{\text{in}}\Big)\Big] . \end{aligned} \tag{3.61}$$

Combining the results via a signal combiner allows one to filter the undesired component as

$$x_{\text{out}}^{\text{comb}}(t) = \Re\big\{x_{\text{out}}^{\text{mixer}}(t)\big\} + \Im\big\{x_{\text{out}}^{\text{mixer}}(t)\big\}$$

$$= A_{\text{in}} \cos\left(2\pi(f_{\text{in}} - f_{\text{lo}})t + \varphi_{\text{in}}\right) \ . \tag{3.62}$$

In case this up-converted term is required to be preserved, the local oscillator signal should be $x_{\text{lo}}(t) = cos(2\pi f_{\text{lo}}t) - jsin(2\pi f_{\text{lo}}t)$.

Alternative methods to directly generate signals at microwave frequencies, bypassing the need for the FE, are currently under characterization. These methods aim at reducing costs, production times and the physical space required for electronic PCB boards. The approach involves generating and acquiring the signal employing converters operating at higher-order Nyquist zones beyond the first [97].

## 3.3 Readout Noise

Understanding the sources and implications of noise in the $\mu$MUX is critical for optimizing its performance and sensitivity. This cryogenic readout system has several noise sources that can be broadly categorized into those associated with the rf-SQUID, the resonator and the LNA.

Flicker noise, also known as $1/f$ noise, is a critical noise source in rf-SQUIDs, particularly dominant at low frequencies. This type of noise originates from defects and impurities within the superconducting material and tunnel junctions. Flicker noise presents a challenge because it increases as the frequency decreases, thereby degrading the performance of the rf-SQUID in applications requiring low-frequency sensitivity which is the case for the MMB.

In a $\mu$MUX, resonators are used to encode the signals from multiple rf-SQUIDs onto different frequency channels, allowing for simultaneous readout. However, resonators introduce their own noise sources that can affect the overall system performance. Resonator thermal noise is caused by thermal fluctuations in the resonator circuitry, leading to variations in the amplitude and phase of the resonator signal. This noise is particularly significant at higher operational temperatures. Besides, dielectric loss noise emerges due to losses in the dielectric material of the resonator. These losses can fluctuate over time, introducing noise that increases the noise floor of the resonator. This type of noise reduces the SNR and affects the accuracy of the measurements. The most important noise source in resonators is Two-Level System (TLS) noise, which arises from microscopic defects in the dielectric material. These defects can randomly switch states, causing fluctuations that manifest as noise. Experiments show that TLS is one of the main readout noise contributions in the $\mu$MUX. Especially at low frequencies since its has a $1/f$ behaviour.

Another major noise source belongs to the High-Electron-Mobility Transistor (HEMT) amplifier, which is the preferred LNA located at the $\mu$MUX output. This signal is prior attenuated to excite the different $\mu$MUX channels to their optimal point. The stationary noise in HEMT amplifier is usually the main noise contribution in this readout system and it is proportional to the amplifier's temperature and bandwidth.

All the mentioned noises add to the readout tone in both additive and multiplicative forms. In addition to the readout noise, the spectrum is contaminated with interference signals and spurious signals created in nonlinear processes such as intermodulation prod-

ucts and harmonics. In Fig. 3.20, a sketch of a typical one-sided readout tone spectrum at the $\mu$MUX output is given.

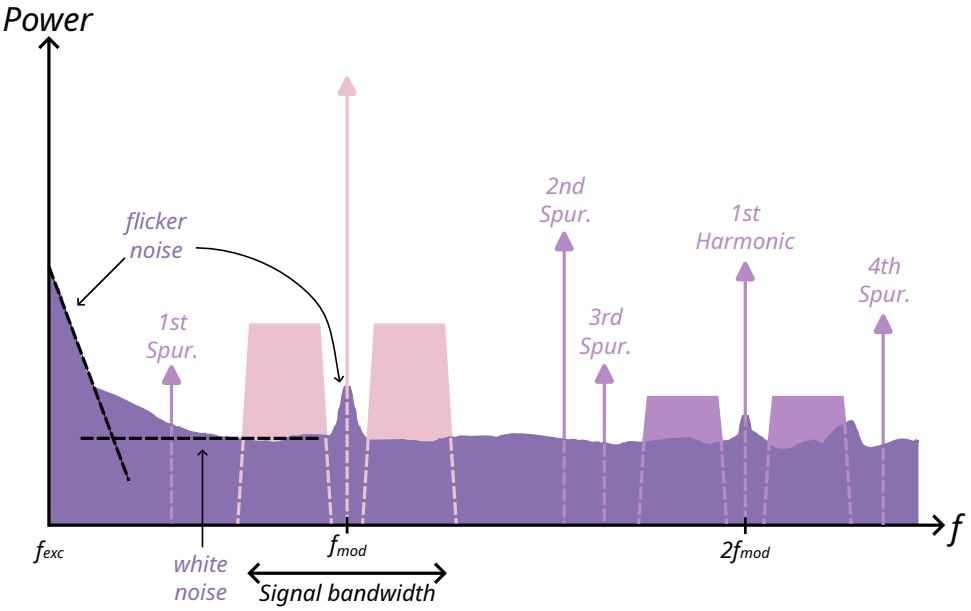


**Figure 3.20:** An illustration of a typical readout tone spectral profile at the $\mu$MUX output. Only the positive frequencies relative to the readout tone are depicted. The dominant component of the rf-SQUID signal, phase-modulated by the detector, is shown in pink. In dark violet, the contributions of white noise and flicker noise are shown. In light violet, spurious signals such as intermodulation products and harmonics are represented in the spectrum.

## 3.4 Towards high multiplexing

To meet the growing demand for highly sensitive detection systems, it is necessary to develop more densely populated detector arrays. This requirement complicates the design of the readout system, as several factors must be optimized. A significant challenge is managing the trade-off between SNR and SFDR [98]. The SFDR measures the amplitude ratio between the desired signal and the strongest spurious signal in the spectrum. As the number of channels increases while maintaining the same readout power per channel, the total frequency comb power also rises. This increase leads to higher intermodulation products and harmonics in active devices, which can reduce the SFDR. An example of this is what happens with the compression point and the intermodulation products of the LNA.

The input 1 dB compression point (P1dB) is the input power level at which the gain of the amplifier is reduced by 1 dB from its small-signal gain due to the onset of compression, as shown in Fig. 3.21. In other words, when the input power to the amplifier increases to a level where the output power no longer increases linearly, this point is reached. This

phenomenon occurs because the amplifier's active devices, such as transistors, start to saturate and cannot amplify the input signal proportionally.

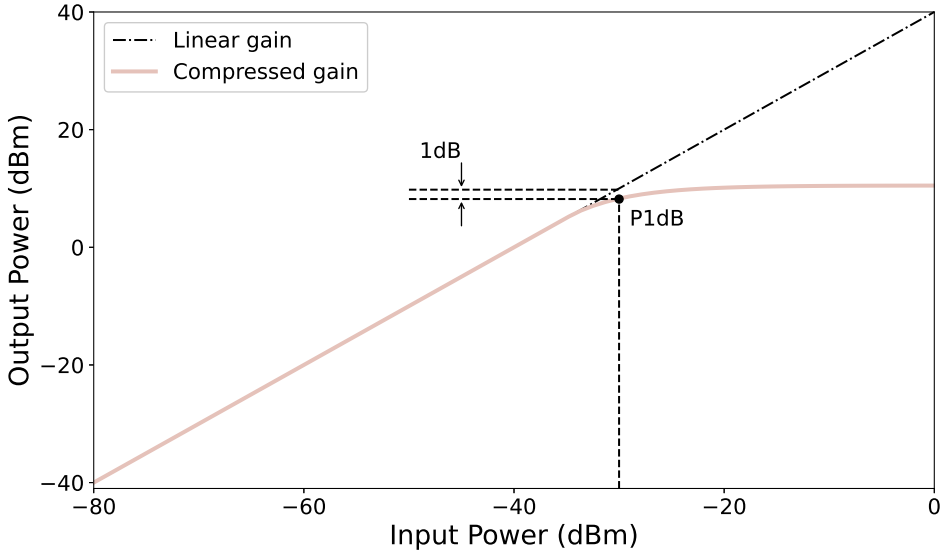


**Figure 3.21:** The output signal power in an LNA increases linearly with the input signal power until the LNA gain compress. The P1dB point indicates the input power at which the output power deviates by 1 dB from the linear output.

Intermodulation products arise when two or more signals are simultaneously present at the input of a non-linear device [99], such as the LNA, which response can be described as

$$y(t) \approx \alpha_1 x(t) + \alpha_2 x(t)^2 + \alpha_3 x(t)^3 \ . \tag{3.63}$$

$y(t)$ is approximated to a third order polynomial which describes the linear, quadratic and cubic gain of the amplifier when an input signal, $x(t)$, is present. The quadratic and cubic term cause the mixing of input signals, resulting in the generation of additional frequencies that are combinations of the original frequencies. For instance, if two signals $A\cos(2\pi f_1 t)$ and $A\cos(2\pi f_2 t)$ are input to an amplifier, Eq. 3.63 follows

$$\begin{aligned}
y(t) &= \alpha_1\big(A\cos(2\pi f_1 t) + A\cos(2\pi f_2 t)\big) + \alpha_2\big(A\cos(2\pi f_1 t) + A\cos(2\pi f_2 t)\big)^2 \\
&\quad + \alpha_3\big(A\cos(2\pi f_1 t) + A\cos(2\pi f_2 t)\big)^3 \\
&= A\alpha_1\cos(2\pi f_1 t) + A\alpha_1\cos(2\pi f_2 t) + A^2\alpha_2\cos(2\pi f_1 t)^2 + A^2\alpha_2\cos(2\pi f_2 t)^2 \\
&\quad + 2A^2\alpha_2\cos(2\pi f_1 t)\cos(2\pi f_2 t) + A^3\alpha_3\cos(2\pi f_1 t)^3 + A^3\alpha_3\cos(2\pi f_2 t)^3 \\
&\quad + 3A^3\alpha_3\cos(2\pi f_1 t)\cos(2\pi f_2 t)\big(\cos(2\pi f_1 t) + \cos(2\pi f_2 t)\big) \\
&= A\alpha_1\cos(2\pi f_1 t) + A\alpha_1\cos(2\pi f_2 t) + A^2\alpha_2 + \frac{A^2\alpha_2}{2}\cos(2\pi(2f_1)t) + \frac{A^2\alpha_2}{2}\cos(2\pi(2f_2)t) \\
&\quad + A^2\alpha_2\cos(2\pi(f_1 - f_2)t) + A^2\alpha_2\cos(2\pi(f_1 + f_2)t) + \frac{3A^3\alpha_3}{4}\cos(2\pi f_1 t)
\end{aligned}$$

$$
\begin{aligned}
&+ \frac{A^3\alpha_3}{4}\cos(2\pi(3f_1)t) + \frac{3A^3\alpha_3}{4}\cos(2\pi f_2 t) + \frac{A^3\alpha_3}{4}\cos(2\pi(3f_2)t) \\
&+ \frac{3A^3\alpha_3}{2}\cos(2\pi f_1 t) + \frac{3A^3\alpha_3}{2}\cos(2\pi f_2 t) + \frac{3A^3\alpha_3}{4}\cos(2\pi(2f_1 - f_2)t) \\
&+ \frac{3A^3\alpha_3}{4}\cos(2\pi(2f_2 - f_1)t) + \frac{3A^3\alpha_3}{4}\cos(2\pi(2f_1 + f_2)t) \\
&+ \frac{3A^3\alpha_3}{4}\cos(2\pi(2f_2 + f_1)t) \\
= {} & A^2\alpha_2 + \left(A\alpha_1 + \frac{9A^3\alpha_3}{4}\right)\cos(2\pi f_1 t) + \left(A\alpha_1 + \frac{9A^3\alpha_3}{4}\right)\cos(2\pi f_2 t) \\
&+ \frac{A^2\alpha_2}{2}\cos(2\pi(2f_1)t) + \frac{A^2\alpha_2}{2}\cos(2\pi(2f_2)t) + \frac{A^3\alpha_3}{4}\cos(2\pi(3f_1)t) \\
&+ \frac{A^3\alpha_3}{4}\cos(2\pi(3f_2)t) + A^2\alpha_2\cos(2\pi(f_1 - f_2)t) + A^2\alpha_2\cos(2\pi(f_1 + f_2)t) \\
&+ \frac{3A^3\alpha_3}{4}\cos(2\pi(2f_1 - f_2)t) + \frac{3A^3\alpha_3}{4}\cos(2\pi(2f_2 - f_1)t) \\
&+ \frac{3A^3\alpha_3}{4}\cos(2\pi(2f_1 + f_2)t) + \frac{3A^3\alpha_3}{4}\cos(2\pi(2f_2 + f_1)t) \ . \qquad (3.64)
\end{aligned}
$$

the non-linearity generates sums and differences of frequencies such as $2f_1$, $2f_2$, $3f_1$, $3f_2$, $f_1 + f_2$, $f_1 - f_2$ and more complex combinations like $2f_1 - f_2$, $2f_2 - f_1$, $2f_1 + f_2$ and $2f_2 + f_1$. The third-order intermodulation products, which occur at frequencies $2f_1 - f_2$ and $2f_2 - f_1$, are particularly important because they fall close to the original signal frequencies and can significantly interfere with the desired signals, degrading its performance.

On the other hand, increasing the number of readout tones while maintaining the total signal power leads to a lower SNR in both the RTE and the $\mu$MUX. As demonstrated in Section 3.2.2, increasing the number of tones in the converters results in a decrease in the SNR. Additionally, when the $\mu$MUX channel readout power drops below the optimal value, noise increases according to a power law [82]. This reduction in SNR can negatively affect the sensitivity of the detection system, undermining the goal of increasing detector array density for advanced detection systems. To overcome this issue, various techniques are being investigated, one of the most promising being tone-tracking. Tone-tracking dynamically adjusts the readout power for each channel, optimizing both the SNR and SFDR [98]. This method helps maintaining system performance even as the number of channels increases.

Another experimental technique to overcome this trade-off is *spectral engineering* [100]. This technique aims to find an optimal rf-SQUID fundamental frequency that sets a lower noise limit for all the demodulated detector signals. Using the FR, the rf-SQUID response can be located in any part of the spectrum of Fig. 3.20 that optimizes SNR and SFDR of the detector signal. However, since the FR is coupled with all the rf-SQUID simultaneously, they can not be individually optimized. But it is possible to find a value for $f_{mod}$ that maximize the SNR and SFDR for the worst-case channel while also setting a lower signal in-band noise limit for the remaining channels.

To do this, first an initial $f_{mod}$ value is set and a multi-tonal signal is generated and processed. Then, the spectrum noise power of all the demodulated detector signals are estimated and the worst case value is stored. After repeating this process for multiple $f_{mod}$ values, the stored values are compared and the best-case is selected. This algorithm is represented in Fig. 3.22. Using this method, an improvement of up to 50 dB between the worst and best stored noise power was achieved [100].

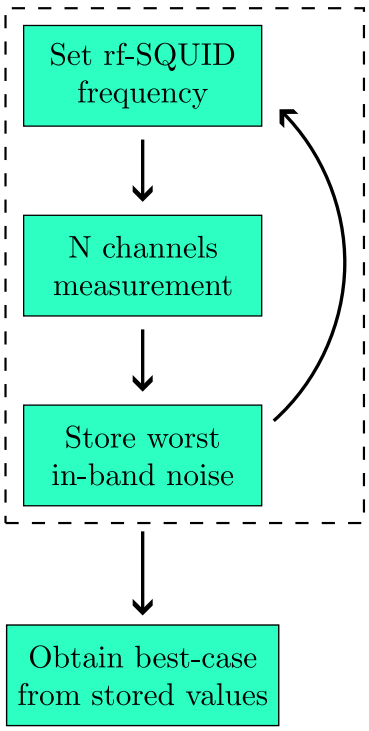


**Figure 3.22:** Spectral Engineering algorithm to simultaneously optimize all demodulated detector signals by setting a lower in-band noise limit for each.

## 3.5 Proposed readout system

The readout system for measuring MMB arrays, shown in Fig. 3.23, is still under development. It must meet the current requirements for the detector array used in the QUBIC instrument, which consists of a focal plane with 1024 bolometers. Therefore, the $\mu$MUX channels must cover the IEEE C band by locating them every 3.9 MHz. Each channel is designed with a bandwidth of $BW_{\text{res}} = 200\,\text{kHz}$ and an $\eta = 1$. Therefore, the fundamental frequency of the rf-SQUID is limited to a maximum of 100 kHz (Eq. 3.20), which sets an upper limit for $f_{\text{ramp}}$. From Eq. 3.19, it can be deduced that ultimately the detector signal is going to be sampled at $f_{\text{ramp}}$. The maximum frequency of the detector that meets the background-limited noise condition is less than 100 Hz, as it is shown in Fig. 2.7 and the possibility of oversampling the detector signal, thereby improving the SNR, establishes a minimum $f_{\text{mod}}$ of at least 10 times the detector bandwidth, namely

1 kHz. The final $f_{\mathrm{mod}}$ value chosen will depend on the characterization of the electronics, primarily the TLS noise of the resonators, considering that higher $f_{\mathrm{mod}}$ make this noise more negligible. The generation of the modulation signal will be conducted through a custom-designed Modulation Signal Synthesizer (MSS) board controlled by the BE (for more details, see Section 4).

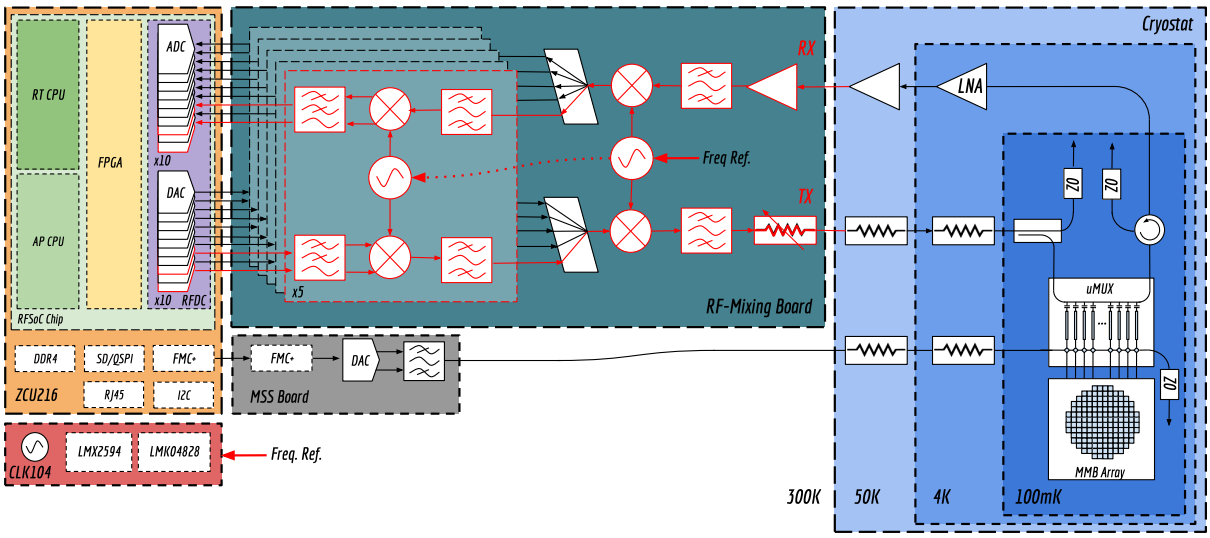


**Figure 3.23:** Readout system under development for measuring an array of MMBs. The system cover the C band through a complex dual-conversion process of five 800 MHz sub-bands. The $\mu$MUX is located inside the cryostat along with electronic devices that condition the signals to the required power levels.

The readout signal generation will be carried out in five complex sub-bands of 800 MHz each. Each sub-band is covered by two DACs sampled at 1 Gsps. Each sub-band is then up-converted using a custom-designed dual-conversion FE that integrates complex mixers. In the first conversion, the sub-bands are allocated in a spectrum between 0.5 GHz and 4.5 GHz. Through a second conversion, the sub-bands covers 4 GHz to 8 GHz. Subsequently, they are combined into a single transmission line that enters the cryostat to readout the $\mu$MUX channels. On the return path, the readout signal is split into five sub-bands again and shifted to low frequencies using the same FE. The down-conversion process follows the inverse path of the transmission, bringing each sub-band to a complex base-band that covers 800 MHz. Finally, each sub-band is acquired by two ADCs.

The Radio Frequency System-on-Chip (RFSoC) ZCU216 [101] is the commercial board selected for the generation and acquisition of the readout signal [102], as well as the FR generation. This board features the ten high-speed ADCs and DACs necessary to cover the five sub-bands. The CLK104 add-on card distributes the clock signal to the ZCU216 and the MSS board. An external 10 MHz reference is fanned out to the CLK104 and the FE board.

Since the readout system is still under development, the measurements for this work were performed on a reduced and already tested system that covers a single sub-band [103, 104]. This setup includes the Multiprocessor System-on-Chip (MPSoC) ZCU102 [105] as

the BE and the AD-FMCDAQ2-EBZ [106] converter board integrating an AD9144 [107] and an AD9680 [108], which have four DACs and two ADCs, respectively. Finally, the FE is a prototype custom-designed for the Electron Capture in $^{163}$Ho Experiment (ECHo) project [109] and capable of covering a single sub-band (see blocks highlighted in red in Fig. 3.23). For this setup, the clock for the MSS board is generated by the commercial evaluation board EVAL-AD9523-1 [110]. The currently available $\mu$MUX has 16 channels and does not have any detectors coupled. Finally, the system responsible for real-time control and for data transmission is described in [111].

# Chapter 4

# Modulation Signal Chain

The electronics involved in generating the modulation signal encompasses digital synthesis and the associated analog devices for signal conversion and conditioning before coupling to the rf-SQUIDs. Noise performance considerations must be taken into account to avoid degrading the detector signal. A critical device in this process is the DAC. A differential current output DAC is selected for this application to be used on signal conversion due to its noise performance. The DAC's output signal range is adjusted to match the current range that produces the desired magnetic flux within the rf-SQUIDs. Since this current is typically in the $\mu$A range, the DAC output must be attenuated before coupling to the rf-SQUIDs. In addition to the noise produced by the converter, the thermal noise conveyed between the various internal stages of the cryostat must also be considered. It is crucial that the thermal noise remains lower than the noise produced by the rf-SQUID. Moreover, sources of power dissipation grouped in the passive and active load must be below the cooling power, which is a parameter that the manufacturer guarantees a steady temperature for the various stages. Each of these considerations is developed in this section to achieve an appropriate setup for the synthesis of the modulation signal.

## 4.1 Initial Considerations

Based on the experiment noise requirements for achieving the BLIP condition (see Fig. 2.7), a total white magnetic flux readout NSD within the rf-SQUID of $\sqrt{S_{\Phi,\text{read}}} = 0.06\,\mu\Phi_0/\sqrt{\text{Hz}}$ is adopted. Hence, the magnetic flux noise translates into a current NSD in the modulation line equal to

$$S_{\text{I,read}} = \sqrt{S_{\Phi,\text{read}}} \cdot \gamma_{\text{mod}} = 26.19 \frac{\text{pA}}{\sqrt{\text{Hz}}} \ , \tag{4.1}$$

where $\gamma_{\text{mod}} = 1/M_{\text{mod}} = 436.5\,\mu\text{A}/\Phi_0$ is the normalized current-flux transfer coefficient between the rf-SQUID and the modulation coil of the available $\mu$MUX in our lab.

Since two circuits were designed for the modulation signal line, one Single-Ended (SE) with a load impedance $Z_{\text{L,se}} = 50\,\Omega$ and the other differential with $Z_{\text{L,diff}} = 100\,\Omega$, the

voltage NSD over the load for both cases achieve

$$S_{\mathrm{V,read}} = S_{\mathrm{I,read}} \cdot Z_{\mathrm{L,se}} = 1.31 \frac{\mathrm{nV}}{\sqrt{\mathrm{Hz}}} \tag{4.2}$$

and

$$S_{\mathrm{V,read}} = S_{\mathrm{I,read}} \cdot Z_{\mathrm{L,diff}} = 2.62 \frac{\mathrm{nV}}{\sqrt{\mathrm{Hz}}} \ . \tag{4.3}$$

Or expressed in dBm units as

$$S_{\mathrm{read}}\Big|_{\mathrm{dBm}} = 10 \log_{10} \left( \frac{\left(S_{\mathrm{V,read}}\right)^2}{1\,\mathrm{mW} \cdot Z_{\mathrm{L,se}}} \right) = -164.65 \frac{\mathrm{dBm}}{\mathrm{Hz}} \tag{4.4}$$

and

$$S_{\mathrm{read}}\Big|_{\mathrm{dBm}} = 10 \log_{10} \left( \frac{\left(S_{\mathrm{V,read}}\right)^2}{1\,\mathrm{mW} \cdot Z_{\mathrm{L,diff}}} \right) = -161.64 \frac{\mathrm{dBm}}{\mathrm{Hz}} \ . \tag{4.5}$$

The calculated noise levels for both circuits represent an upper limit, from which the noise generated by the modulation signal should remain well below in order to avoid degrading the detector's signal.

### 4.1.1 Digital to Analog Converter Selection

A Modulation Signal Synthesizer (MSS) system is designed for the FR, although it is also desirable to be able to generate arbitrary signals in different frequency bands for future research. Therefore, four non-simultaneous frequency bands are designed in the board: DC-221 MHz, DC-710 kHz, 200 Hz-4 MHz and 1 kHz-221 MHz. To generate signals in the first Nyquist zone, a DAC capable of operating at a clock frequency above $f_{\mathrm{s}}^{\mathrm{MAX5891}} > 442\,\mathrm{MHz}$ is selected. Additionally, the converter should have a low NSD and a high level of SFDR. It is also beneficial for the system to work with differential signals, which provide greater immunity to common-mode noise. The MAX5891 meets these objectives, making it the chosen converter for the digital signal generated in the BE. Operating the converter in its full-scale range ensures optimal SNR and SFDR values [112]. Therefore, the full-scale current $I_{\mathrm{FS}}$ range to be supplied is from 2 mA to 20 mA, which produces −19 dBm to 1 dBm full-scale signal levels in a double-terminated 100 Ω load. As the $f_{\mathrm{mod}}$ range is from 1 kHz to 100 kHz, the selected $f_{\mathrm{s}}^{\mathrm{MAX5891}} = 10\,\mathrm{MHz}$ produce image frequencies located in the attenuation band of the second and third mentioned filters. The differential signal NSD reported in the MAX5891 datasheet of −163 dBFS/Hz is below the readout noise in Eq. 4.5 throughout the full-scale output range. Although, the measurement conditions indicated are different ($f_{\mathrm{s}}^{\mathrm{MAX5891}} = 500\,\mathrm{MHz}$, a signal power of 15.5 dBm and a 20 MHz measurement bandwidth), a lower noise is expected under the conditions mentioned for this work.

In addition, the MAX5891 theoretical SNR is

$$\mathrm{SNR_{dB}} = 16\mathrm{bit} \cdot 6.02 + 1.76 = 98\,\mathrm{dB}\ . \tag{4.6}$$

This is equivalent to a NSD of

$$S_{\mathrm{MAX5891}}\Big|_{\mathrm{dBm}} = 1\,\mathrm{dBm} - \mathrm{SNR_{dB}} - 10\log_{10}\left(\frac{f_{\mathrm{s}}^{\mathrm{MAX5891}}}{2}\right) = -164\frac{\mathrm{dBm}}{\mathrm{Hz}} \tag{4.7}$$

which is also lower than the assumed readout noise.

## 4.2 Cryogenic Chain Design

In a cryostat, there are different plates heated to different temperatures. At the first stage, the warmer plate is located and each subsequent stage has a lower temperature. Generally, the stages can be classified as the 50 K plate, the 4 K plate, the Still plate (SP) (around 1 K), the Cold plate (CP) (approximately 100 mK) and the Mixing Chamber plate (MXC) with base temperatures around 10 mK. This last one is found in cryostats with a dilution unit where $^3$He is mixed with $^4$He.

Thermal transmission can occur between these stages through three primary mechanisms: conduction, convection and radiation. Each of these mechanisms can contribute to unwanted heat transfer, which can degrade the performance of the cryogenic system and affect the integrity of the transmitted signals.

Thermal conduction occurs when heat transfers through solid materials in direct contact. Inside a cryostat, conduction can happen through structural supports, wiring and other physical connections between components at different temperatures. To minimize conductive heat transfer, materials with low thermal conductivity, such as stainless steel or fiberglass, are used for structural support.

Thermal convection involves heat transfer through the movement of fluids, which can be either liquid or gas. In a cryostat, convection is typically minimized by creating a vacuum environment, effectively minimizing the presence of particles that can transfer heat. Maintaining a high-quality vacuum ensures that convective heat transfer is negligible.

Thermal radiation is the transfer of heat in the form of electromagnetic waves, primarily in the infrared spectrum. Even in a vacuum, thermal radiation can cause significant heat transfer between warmer and colder surfaces within a cryostat. To mitigate radiative heat transfer, surfaces are often coated with reflective materials like aluminum or gold, which have low emissivity and can reflect infrared radiation away. Additionally, employing multi-layer insulation composed of alternating layers of reflective and insulating materials can further reduce radiative heat transfer.

The thermal mechanisms in the cryostat structure are characterized by the manufacturer, who guarantees a stable temperature in each stage of the cryostat. However, the manufacturer does not know which devices will be connected at each stage, with which cables these devices are going to be interconnected or how much power the devices will dissipate. Therefore, there is a parameter called cooling power, which indicates how much power can be dissipated at each stage without its temperature varying.

The cryogenic chain refers to the sequence of components located inside a cryostat at very low temperatures that condition electrical signals to maintain their integrity and adapt their levels. Signals are generated at room temperature before being transmitted into the cryostat. Once generated, the signals travel through wires designed to operate at cryogenic temperatures through the different cryostat stages. Using wires of superconducting materials like niobium-titanium (NbTi) for electrical connections reduces heat conduction. Proper thermal anchoring of these wires at intermediate stages within the cryostat can also help dissipate heat before it reaches the colder regions. Moreover, devices such as attenuators, filters, insulators or directional couplers are also necessary to thermalize the incoming radiation fields and to reduce the number of thermal photons incident on the cold sample.

Ensuring that the thermal load generated by the cryogenic chain is less than the cooling power capacity is essential for maintaining the cryogenic environment and, therefore, the reliable operation of devices. Thermal management within a cryostat is closely related to the concepts of passive and active load. Passive load refers to the conducted heat that flows through the setup cables. Active load, on the other hand, is power dissipation of applied signals introduced through the operation of components within the cryostat, in addition to the thermal radiation in the cables.

### 4.2.1 Passive Load

One of the primary mechanisms of passive load in cryostats is thermal conduction, described by Fourier's law of heat conduction. Fourier's law states that the heat transferred by conduction between two plates is proportional to the temperature difference between them, the cross-sectional area and the thermal conductivity of the conduction medium and inversely proportional to the length of the conduction path. Mathematically, it is expressed as

$$P_{\mathrm{i}} = \int_{T_{\mathrm{i\text{-}1}}}^{T_{\mathrm{i}}} \frac{\rho_{\mathrm{o}}(T)A_{\mathrm{o}} + \rho_{\mathrm{d}}(T)A_{\mathrm{d}} + \rho_{\mathrm{c}}(T)A_{\mathrm{c}}}{L_{\mathrm{i}}} dT \ , \tag{4.8}$$

where $T_{\mathrm{i\text{-}1}}$ and $T_{\mathrm{i}}$ are the plates temperatures thermally connected by a wire with $\rho_{\mathrm{o}}(T)$, $\rho_{\mathrm{d}}(T)$, $\rho_{\mathrm{c}}(T)$, $A_{\mathrm{o}}$, $A_{\mathrm{d}}$ and $A_{\mathrm{c}}$ outer conductor, dielectric and center conductor thermal conductivities and cross sections, respectively. $L_{\mathrm{i}}$ is the length of the conductor.

The heat load power calculation for the FR cryogenic chain is based on the wiring length of the current electronics setup installed in the QUBIC cryostat [47]. This wiring is summarized in Table 4.1.

The length of the cables connecting each stage are referenced to the room temperature stage ($T_{300\mathrm{K}} = 300\,\mathrm{K}$). Table 4.1 also includes the cooling power for each stage. Since the instrument is equipped with two pulse tube refrigerators, each provides the same cooling power for the 40 K and 4 K stages.

The wires purchased for the modulation signal are 2.19 mm SCuNi-CuNi and 0.86 mm SCuNi-CuNi 50-ohm semi-rigid coaxial cables, both with PTFE as the dielectric. The 2.19 mm SCuNi-CuNi wire connects the cryostat's input to the 4 K stage. It have cross sections of $A_{\mathrm{o}} = 1.58 \times 10^{-6}\,\mathrm{m}^2$, $A_{\mathrm{d}} = 1.99 \times 10^{-6}\,\mathrm{m}^2$ and $A_{\mathrm{c}} = 204.3 \times 10^{-9}\,\mathrm{m}^2$, as

| $T_{\text{stage}}$ [K] | Length [mm] | Cooling power [W] |
|---|---|---|
| 300 | Reference | - |
| 40 | 1000 | 35 (x2) |
| 4 | 2000 | 0.9 (x2) |
| 1 | 2500 | $>1 \times 10^{-3}$ |
| 0.3 | 2735 | $>25 \times 10^{-6}$ |

**Table 4.1:** Wiring length of the electronics currently installed in the QUBIC cryostat and the cooling power of its stages.

specified by the vendor [113]. The 0.86 mm SCuNi-CuNi wire connects the 4 K stage to the 100 mK (since the responsibility of the MMB increases at lower temperatures, the detector is placed at 100 mK). The manufacturer specifies the dimensions $A_{\text{o}} = 239 \times 10^{-9}\,\text{m}^2$, $A_{\text{d}} = 311 \times 10^{-9}\,\text{m}^2$ and $A_{\text{c}} = 31.4 \times 10^{-9}\,\text{m}^2$ for the wire [113]. The different thermal conductivities of the wires are detailed in Table 4.2 for the different temperatures in each stage [114]. Due to the lack of thermal conductivity data at a temperature of 100 mK, the value from the 1 K stage is used as a worst-case estimate.

| | $\rho$ [W · K$^{-1}$ · m$^{-1}$] | |
|---|---|---|
| $T_{\text{stage}}$ [K] | CuNi | PTFE |
| 40 | 15.5 | 0.210 |
| 4 | 0.878 | 0.046 |
| 1 | 0.095 | 0.012 |
| 0.1 | 0.095 | 0.012 |

**Table 4.2:** Thermal conductivities of CuNi and PTFE materials.

Finally, the passive heat for each case is calculated using Eq. 4.8 and the results are shown in Table 4.3.

### 4.2.2 Active Load

Sources of active load are blackbody radiation in wiring and heat generated by powered components within the cryogenic system. The blackbody radiation in cables can be estimated by the Johnson–Nyquist power NSD as

$$S = 2Rhf\eta_{\text{BE}}(f) \ . \tag{4.9}$$

$R$ denotes the cable characteristic impedance, $f$ is the signal frequency and $\eta_{\text{BE}}(f)$ is the photon occupation number described by the Bose-Einstein distribution:

| $T_{\text{stage}}$ [K] | Passive heat [W] |
|---|---|
| 40 | $7.3 \times 10^{-6}$ |
| 4 | $60 \times 10^{-9}$ |
| 1 | $176.5 \times 10^{-12}$ |
| 0.1 | $112.7 \times 10^{-12}$ |

**Table 4.3:** Passive heat in the modulation line.

$$\eta_{\text{BE}}(f) = \frac{1}{e^{\frac{hf}{k_{\text{B}}T}} - 1} \ . \tag{4.10}$$

Attenuators are used to reduce thermal radiation between stages in a cryostat. The ratio between the photon occupation numbers of two stages provides a first approximation of the minimum attenuation needed for the thermal radiation from the warmer stage to match the power level of the colder stage [115]. For example, for a maximum frequency of 710 kHz set by the cutoff frequency of LPF2, the minimum attenuation required to reduce the room temperature thermal photons to the level of the 100 mK stage is 35 dB. This attenuation can be distributed differently across all stages of the cryostat. For instance, the configuration C1=$\{0,0,0,35\}$ dB represents 0 dB attenuation in the warmer stages and 35 dB attenuation at the 100 mK stage. Alternatively, the configuration C2=$\{5,10,10,10\}$ dB indicates 5 dB attenuation at the 50 K stage and 10 dB attenuation at each of the subsequent stages. The selection of the appropriate configuration depends on the desired final value of the $\eta_{\text{BE}}(f)$ at the 100 mK stage and the energy dissipation in each attenuator, which affects the thermal load of each stage.

From Eq. 4.9, the Johnson–Nyquist current NSD can be derived as

$$S_{\text{I}} = \sqrt{\frac{4k_{\text{B}}T}{R}} \ . \tag{4.11}$$

Table 4.4 shows $S_{\text{I}}$ calculated at room temperature and at each cryostat temperature stage for $R = 50\,\Omega$.

| $T_{\text{stage}}$ [K] | $S_{\text{I}}$ [pA/$\sqrt{\text{Hz}}$] |
|---|---|
| 300 | 18.2 |
| 40 | 6.64 |
| 4 | 2.10 |
| 1 | 1.05 |
| 0.1 | 0.332 |

**Table 4.4:** Thermal current noise in the modulation line.

$S_{\mathrm{I}}$ at $T_{300\mathrm{K}}$ degrades the adopted readout current noise $S_{\mathrm{I,read}}$ from Eq.4.1 by 21.77 % generating a total current noise of $S_{\mathrm{I,read2}} = 31.89\mathrm{pA}/\sqrt{\mathrm{Hz}}$. In fact, its equivalent noise temperature is

$$T_{\mathrm{eq,read2}} = \frac{{S_{\mathrm{I,read2}}}^2 R}{4k_{\mathrm{B}}} = 921.33\,\mathrm{K} \ . \tag{4.12}$$

By adding a 10 dB attenuator at the 4 K stage, it is possible to reduce the thermal noise such that the degradation is now 2.4 % and the equivalent noise temperature is

$$T_{\mathrm{eq,read2}} = \frac{{S_{\mathrm{I,read2}}}^2 R}{4k_{\mathrm{B}}} = 651.25\,\mathrm{K} \ . \tag{4.13}$$

## 4.3 Modulation Signal Synthesizer

The MSS system is built around the MAX5891 converter and is divided into a digital BE and a FE board, as shown in Fig. 4.1. The decision to design a custom PCB board for generating the modulation signal is based on the fact that this signal directly affects the overall system noise. A custom design allows for the selection of high-quality components, the optimal design of critical elements such as power supplies and the seamless integration of the entire system. For the latter, the MSS board includes back-to-back FMC+ connectors (see Fig. 4.2) and via-in-pad for the high-density lines routing. One FMC+ connects the MSS board with the BE platform, while the other allows an additional FMC-card to use the available high-speed lines of the BE. In the measurement setup used in this work, the ZCU102 platform and the AD-FMCDAQ2-EBZ evaluation board were connected to the MSS board, as depicted in Fig. 4.3.

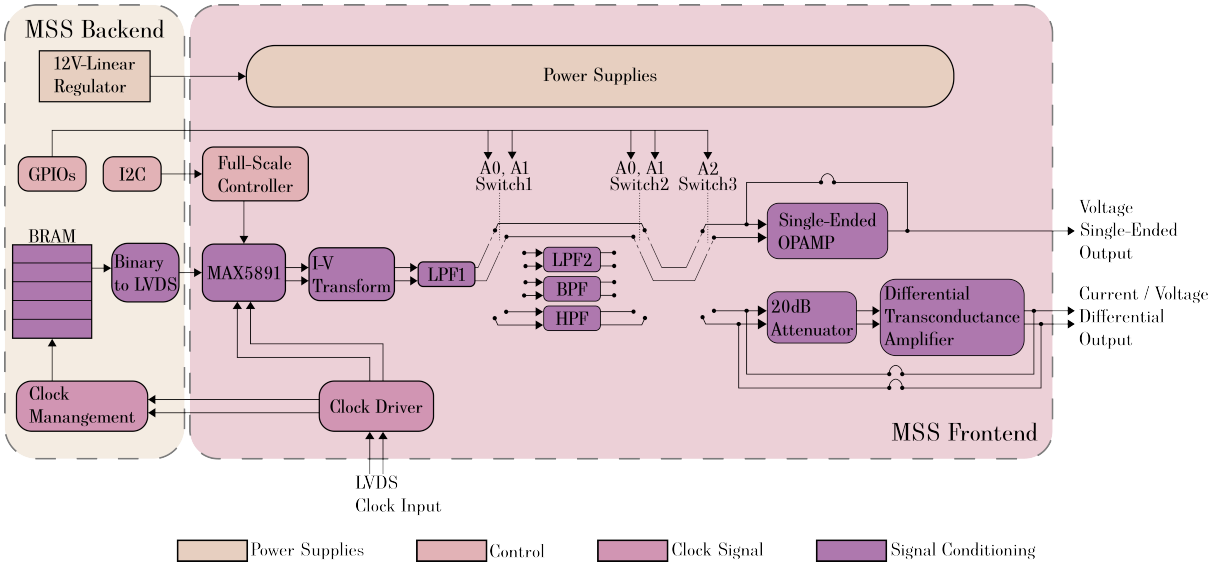


**Figure 4.1:** MSS system build around the MAX5891 DAC. The BE synthesize a digital signal by playing a BRAM in loop which is output in a 16-bit LVDS line to the converter.

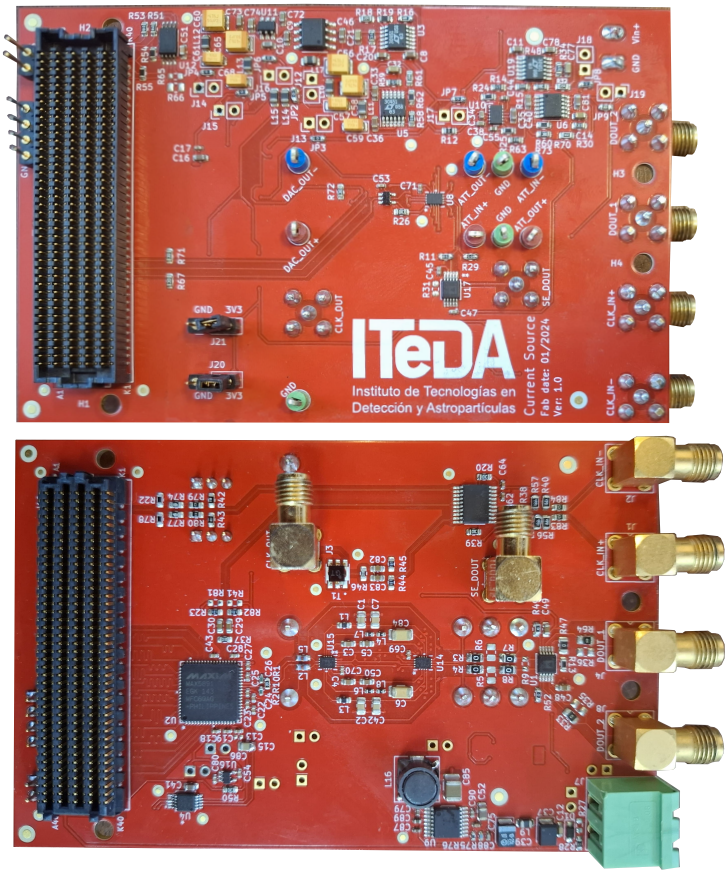


**Figure 4.2:** MSS FE board. (**Top**) Top-side of the board that contains the voltage regulators from 12 V to ±5 V and from 5 V to 3.3 V, 1.8 V and 1.25 V. It also includes an EEPROM to set the $V_{\text{adj}}$ voltage of the BE and a digital potentiometer used to select the $I_{\text{FS}}$ of the MAX5891. (**Bottom**) The bottom part of the board houses the circuits for conditioning the modulation and the clock signals.

A 16-bit binary signal is stored in a BRAM and cyclically reproduced at a frequency $f_{\text{s}}^{\text{MAX5891}}$. This signal is converted to differential and output over high-speed lines under the Low-Voltage Differential Signaling (LVDS) standard to the converter.

The MAX5891 $I_{\text{FS}}$ is converted into a differential voltage by a resistive load. Then, the signal passes through a reconstruction filter, a 221 MHz low-pass filter (LPF1). Thereafter, the signal can take one of four different paths selected by Switch1 and Switch2: a direct path without additional filtering, a second low-pass filter (LPF2) with a cutoff frequency of 710 kHz, a band-pass filter (BPF) with cutoff frequencies of 200 Hz and 4 MHz, or a high-pass filter (HPF) with a cutoff frequency of 1 kHz. Using a third switch (Switch3) different output stages are selected. The signal can be output through a voltage follower in a SE form or a 20 dB attenuator followed by a transconductance amplifier that convert the differential voltage into a differential current output signal. Alternatively, each output can be short-circuited using resistors soldered on the PCB. This latter cases, where the operational amplifiers are disabled, are intended to connect to the modulation

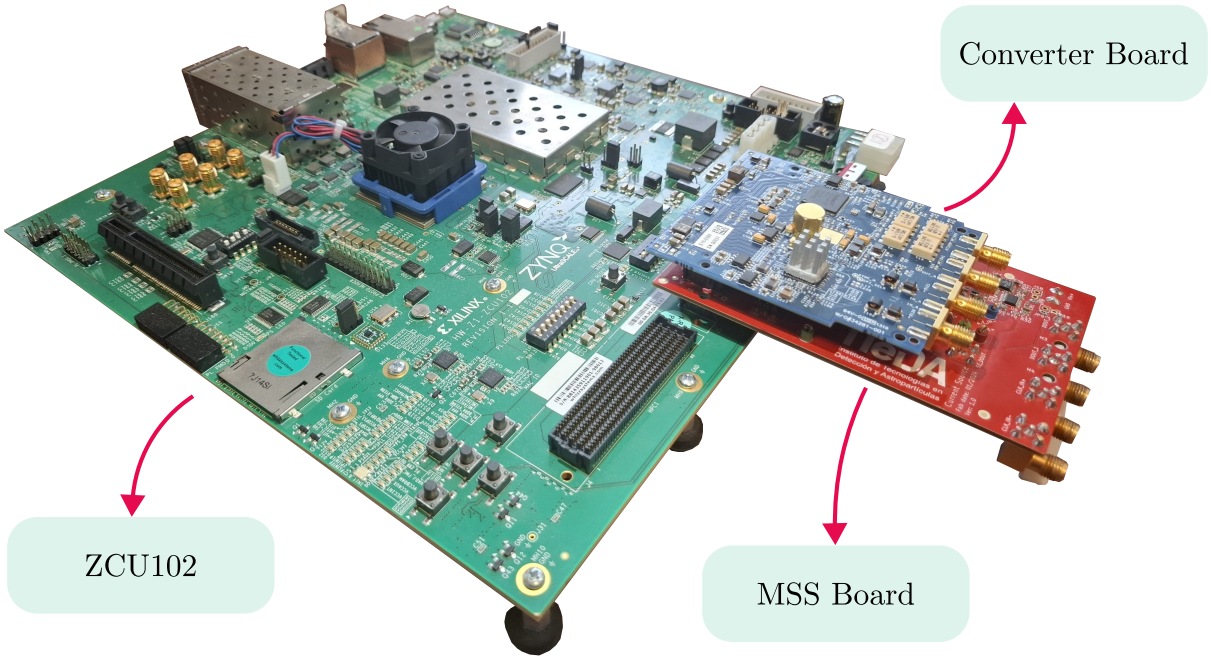


**Figure 4.3:** Stackable board system integration including the ZCU102 platform for end-to-end signal processing, the MSS board for FR conditioning and the AD-FMCDAQ2-EBZ converter board for the multi-tonal signal conversion.

line of the $\mu$MUX.

The opening and closing of the switches are controlled through GPIO lines (A0, A1 and A2). Moreover, a digital potentiometer controlled via I2C allows modification of the full-scale current value of the MAX5891 from 2 mA to 20 mA.

The clock driver generates copies of the input clock and adjusts their levels to meet the requirements of the MAX5891 and the clock manager within the FPGA. The clock manager serves as a frequency synthesizer, jitter cleaner and deskew clock. It also allows for the remote modification of the synthesized frequency phase to meet the setup and hold times of the MAX5891.

### 4.3.1 Digital synthesis

The generation of the digital signal is carried out through the Stimulation and Converter modules which are shown in Fig. 4.4. The Stimulation module consists of a dual-port asynchronous BRAM memory of size $L_{mem} = 65536$. One port is connected to the AXI4-Lite interface, which is used to write in real-time the BRAM with the desired digital signal previously created by the user using a high-level programming language. The digital signal has 16-bit samples but is stored in the BRAM using 32-bit samples, so each position in the BRAM holds two samples of the signal to be reproduced. The other port is used to cyclically output the samples stored in the BRAM and is operated by a $f_s^{MAX5891}$ clock synthesized by the Mixed-Mode Clock Manager (MMCM) [116], which is the clock hardware manager of the BE UltraScale+ architecture. The clock frequency

determines a frequency resolution of $f_{\text{res}} = 152.59\,\text{Hz}$ (see Eq. 3.32).

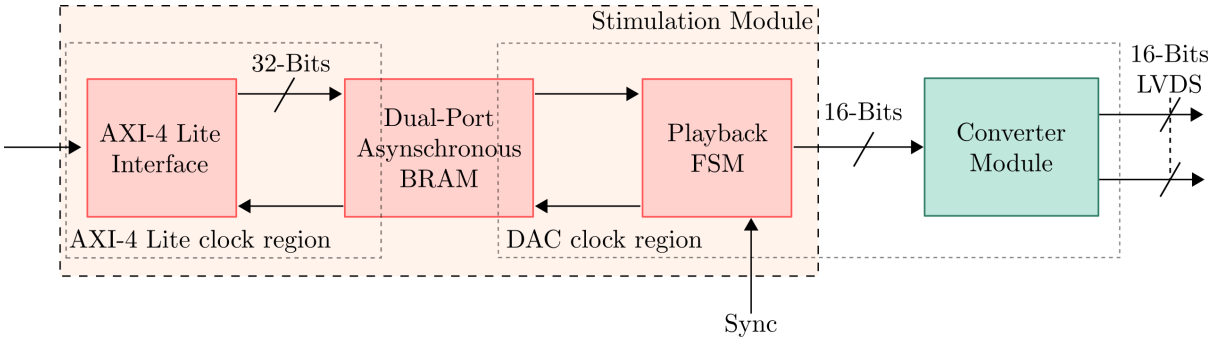


**Figure 4.4:** Digital design for the signal synthesis of the MSS. The design consists of the Stimulation module, which sends 16-bit digital signal samples to the Converter module. The latter outputs the samples in a 16-bit differential format under the LVDS standard. The Stimulation module is synchronized through a Sync signal with the demodulator module.

The output of the Stimulation module is connected to the Converter module, which adapts the 16-bit output to a 16-bit differential format compatible with the MAX5891 input. The output standard used is LVDS, which meets the voltage levels required by the DAC. Fig. 4.5 show the output signal levels of the UltraScale+ architecture [117] and the input signal tolerance level of the MAX5891. Since the converter already has the required $100\,\Omega$ differential resistance internally, it is not necessary to add it.

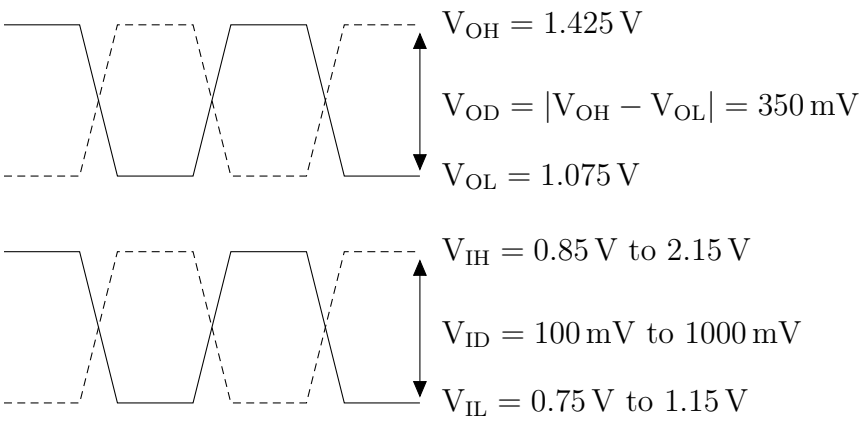


**Figure 4.5:** Voltage level compatibility of the MSS digital signal. (**Top**) The LVDS standard specification of the BE output signal and (**Bottom**) the input signal voltage tolerance of the MAX5891.

It is important to synchronize the start of the FR with the demodulation of the readout signal. Otherwise, a random phase $\varphi_0(t)$ adds to the detector signal and the Eq. 3.19 yields

$$\Phi_{\mathrm{det}}(t) + \Phi_0(t) = \arctan\left( -\frac{\int_{T_{\mathrm{ramp}}} \theta(t+t_0)\ \sin(\omega_{mod} t) dt}{\int_{T_{\mathrm{ramp}}} \theta(t+t_0)\ \cos(\omega_{mod} t) dt} \right) \frac{\Phi_0}{2\pi}\ , \tag{4.14}$$

where

$$t_0 = \frac{\varphi_0(t)}{2\pi f_{\mathrm{ramp}}} \tag{4.15}$$

is the time shift that follows a random distribution. To address this, a synchronization signal is used to reset the output samples of the BRAM which is controlled by the demodulator module (explained in Section 5).

### 4.3.2 I-V Converter

The design of the MSS FE is shown in Fig. 4.6. The MAX5891 output impedance consists of a 1 MΩ differential resistance in parallel with a 5 pF capacitor. The I-V Converter circuit is the first stage, where each output is terminated with a 100 Ω resistor to ground and a 200 Ω resistor between them. The equivalent differential impedance of this stage is 100 Ω for any output frequency. To ensure maximum energy transfer, this stage is loaded with an $R_{\mathrm{L}}^{\mathrm{DAC}} = 100\,\Omega$ resistor, resulting in a double-terminated 100 Ω load. Consequently, the total equivalent resistance loaded to the output of the DAC is $R_{\mathrm{eq}} = 50\,\Omega$. For the specified current range, this setup provides a differential peak-to-peak voltage ($|V_{\mathrm{diff}}| = |V_{\mathrm{A}} - V_{\mathrm{B}}| = I_{\mathrm{FS}} \cdot R_{\mathrm{eq}}$) range from 100 $\mathrm{mV_{pp}}$ to 1 $\mathrm{V_{pp}}$.

### 4.3.3 Filters

Following the I-V converter, four different filters are designed to a $R_{\mathrm{L}}^{\mathrm{DAC}}$ load to accommodate various signal generation conditions, providing versatility for different applications. These filters offer the flexibility to eliminate low-frequency noise, where a power law often dominates, or to limit the signal bandwidth, thereby reducing noise at the output. Moreover, filters with cutoff frequencies in the MHz are integrated into the board, enabling the generation of signals at these frequencies, which is essential for modulating calorimeters [118].

The LPF1 consists of a differential series inductor $L_{\mathrm{LPF1}} = 72\,\mathrm{nH}$ (Fig. 4.7 a)). The cutoff frequency is defined as

$$f_{\mathrm{c,1}} = \frac{R_{\mathrm{L}}^{\mathrm{DAC}}}{2\pi L_{\mathrm{LPF1}}} \approx 221\,\mathrm{MHz}\ . \tag{4.16}$$

The LPF2 is an underdamped second-order low pass filter (Fig. 4.7 b)), implemented with a differential series inductor $L_{\mathrm{LPF2}} = 4.4\,\mu\mathrm{H}$ and a differential shunt capacitor $C_{\mathrm{LPF2}} = 27\,\mathrm{nF}$. This configuration yields the transfer function

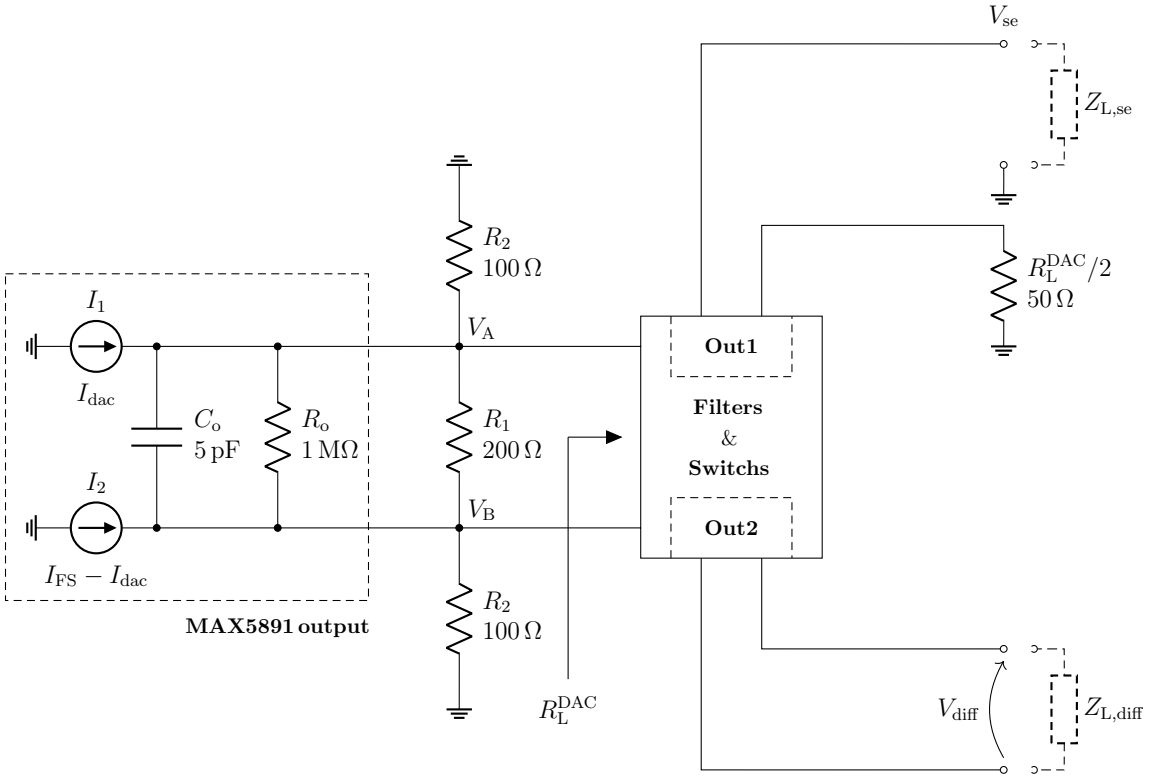


**Figure 4.6:** Signal circuits on the MSS board for FR conditioning are designed to transmit the modulation signal. The SE output ($V_{se}$) and the differential voltage output ($V_{diff}$) are specifically tailored for this purpose. $Z_{L,se}$ and $Z_{L,diff}$ are the dissipation loads inside the cryostat for each circuit in series with the inductors coupled to the rf-SQUIDs.

$$H_{LPF2} = \frac{\frac{1}{(L_{LPF1}+L_{LPF2})C_{LPF2}}}{s^2 + s\frac{1}{R_L^{DAC}C_{LPF2}} + \frac{1}{(L_{LPF1}+L_{LPF2})C_{LPF2}}} \ , \tag{4.17}$$

and a cutoff frequency

$$f_{c,2} = \frac{\omega_2}{2\sqrt{2}\pi Q_2}\sqrt{\left(8Q_2^4 - 4Q_2^2 + 1\right)^{0.5} + 2Q_2^2 - 1} \approx 710\,\text{kHz} \ , \tag{4.18}$$

where

$$\omega_2 = \sqrt{\frac{1}{(L_{LPF1} + L_{LPF2}) \cdot C_{LPF2}}} \quad (4.19)\,\text{and} \quad Q_2 = R_L^{DAC}\sqrt{\frac{C_{LPF2}}{L_{LPF1} + L_{LPF2}}} \ . \tag{4.20}$$

The BPF consists of a first-order low-pass filter formed by a differential series in-

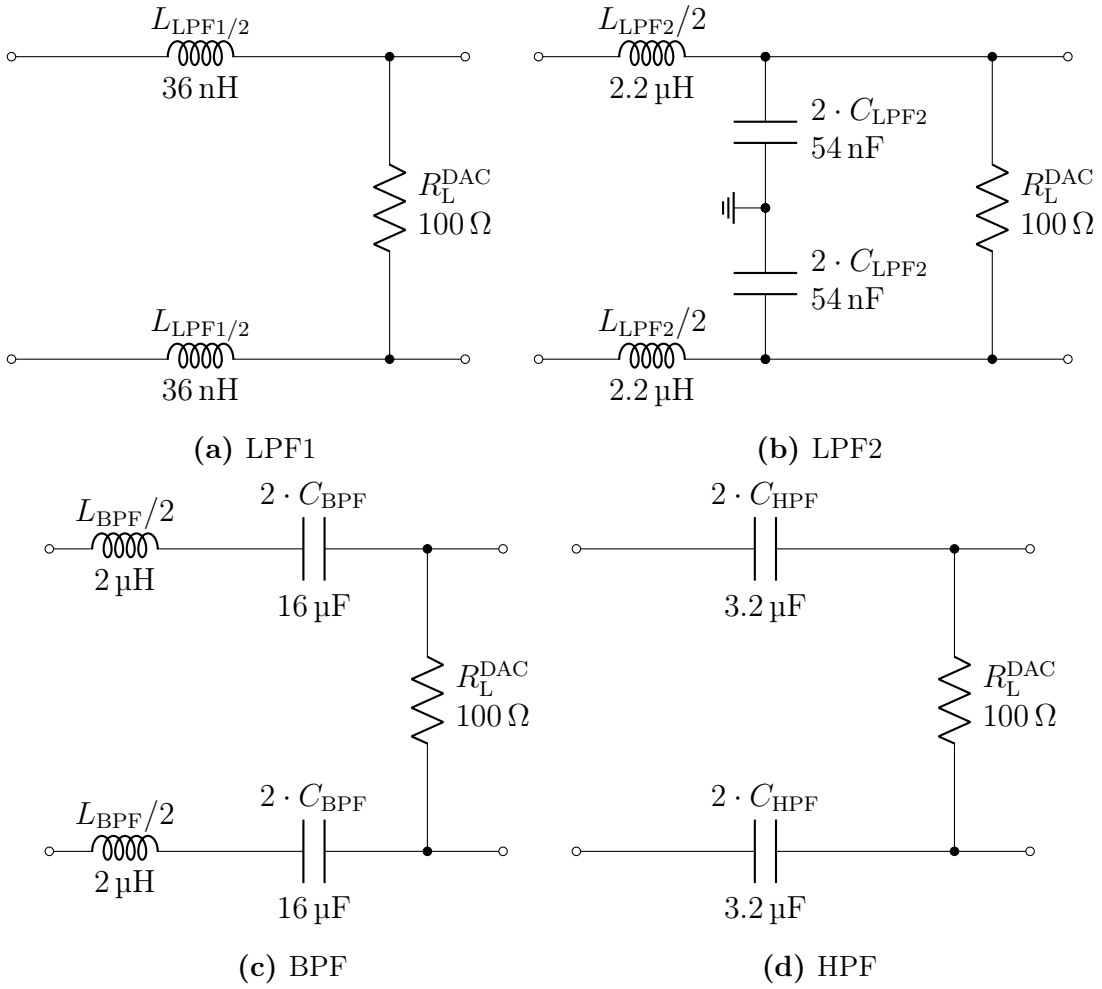


**(a)** LPF1 **(b)** LPF2

**(c)** BPF **(d)** HPF

**Figure 4.7:** The MSS board has four integrated filters. LPF1 sets a maximum output signal frequency of 221 MHz. The other three filters are selected via multiplexers.

ductance $L_{\mathrm{BPF}} = 4\,\mu\mathrm{H}$ and a first-order high-pass filter formed by a differential series capacitance $C_{\mathrm{BPF}} = 8\,\mu\mathrm{F}$ (Fig. 4.7 c)). The lower and upper cutoff frequencies correspond to

$$f_{\mathrm{c,lower}}^{\mathrm{BPF}} = \frac{1}{2\pi R_{\mathrm{L}}^{\mathrm{DAC}} C_{\mathrm{BPF}}} \approx 200\,\mathrm{Hz} \tag{4.21}$$

and

$$f_{\mathrm{c,upper}}^{\mathrm{BPF}} = \frac{R_{\mathrm{L}}^{\mathrm{DAC}}}{2\pi (L_{\mathrm{LPF1}} + L_{\mathrm{BPF)}})} \approx 4\,\mathrm{MHz}\ , \tag{4.22}$$

respectively.

Finally, the HPF is formed by a differential series capacitance $C_{\mathrm{HPF}} = 1.6\,\mu\mathrm{F}$ with a cutoff frequency of

$$f_{\mathrm{c}}^{\mathrm{HPF}} = \frac{1}{2\pi R_{\mathrm{L}}^{\mathrm{DAC}} C_{\mathrm{HPF}}} \approx 1\,\mathrm{kHz} \ , \tag{4.23}$$

as depicted in Fig. 4.7 c).

### 4.3.4 Single-ended Voltage Output

For the SE output stage, the signal $V_{\mathrm{se}}$ is connected to a load $Z_{\mathrm{L,se}} = 50\,\Omega$, as illustrated in Fig. 4.6. This ground-referenced voltage ranges from 83.33 mV to 583 mV for the $I_{\mathrm{FS}} = 20\,\mathrm{mA}$ case. A FR with these levels results in a current range from 1.66 mA to 11.66 mA in the load. This corresponds to a peak-to-peak magnetic flux of $22.9\,\Phi_0$. Using the same analysis, a magnetic flux of $2.29\,\Phi_0$ is obtained for an $I_{\mathrm{FS}} = 2\,\mathrm{mA}$. To generate a magnetic flux lower than the magnetic flux quantum and reduce thermal noise (shown in Eq. 4.13), a 10 dB commercial attenuator is placed in the cryogenic line at the 4 K stage, which generates a flux ranging between $0.72\,\Phi_0$ and $7.24\,\Phi_0$.

The power dissipated in the load is calculated as

$$P_{\mathrm{diss}} = \frac{(\overline{V_{\mathrm{se}}} \cdot A_{\mathrm{TT,10dB}})^2}{Z_{\mathrm{L,se}}} + \frac{(V_{\mathrm{se,RMS}} \cdot A_{\mathrm{TT,10dB}})^2}{Z_{\mathrm{L,se}}} = 263.5\,\mu\mathrm{W} \ . \tag{4.24}$$

$\overline{V_{\mathrm{se}}}$ and $V_{\mathrm{se,RMS}}$ are the dc and RMS values of $V_{\mathrm{se}}$, respectively.

The power dissipation exceeds the cooling power of the cryostat at the 100 mK stage (see Table 4.1), for this reason $Z_{\mathrm{L,se}}$ has to be placed at the 4 K stage.

### 4.3.5 Differential Current Output

The differential voltage $V_{\mathrm{diff}}$ is a $1\,\mathrm{V_{pp}}$ signal with $\overline{V_{\mathrm{diff}}} = 0\,\mathrm{V}$ for the $I_{\mathrm{FS}} = 20\,\mathrm{mA}$ condition. In this case and also including a 10 dB attenuator, the resulting current through the $Z_{\mathrm{L,diff}}$ load is $3.16\,\mathrm{mA_{pp}}$ which also produces a magnetic flux of $7.24\,\Phi_0$. A $0.72\,\Phi_0$ magnetic flux is generated in the $I_{\mathrm{FS}} = 2\,\mathrm{mA}$ case.

The dissipated load is equal to

$$P_{\mathrm{diss}} = \frac{(V_{\mathrm{diff,RMS}} \cdot A_{\mathrm{TT,10dB}})^2}{Z_{\mathrm{L,diff}}} = 83.2\,\mu\mathrm{W} \ . \tag{4.25}$$

Although the dissipated power is lower compared to the SE case since the DC signal contribution is absent, it remains high relative to the cooling power of the mK stage of the cryostat designed for QUBIC. Therefore, the best option is to place the load at the 4 K stage.

### 4.3.6 Clock

The MSS board features a fan-out buffer device selected to distribute two copies of an external input clock. One copy is transmitted to the DAC and the other to the BE through the FMC+ connector. The LMK00725 [119] has the advantage of accepting

multiple standard voltage levels for the input clock signal, including Low-Voltage Positive Emitter-Coupled Logic (LVPECL), LVDS, Stub Series Terminated Logic (SSTL) and SE signals. Its maximum operating frequency is 650 MHz, making it suitable for the entire possible sampling frequency range of the MAX5891. Additionally, the driver can distribute up to five output signals with a maximal skew of 35 ps. The standard used for its outputs is LVPECL at 3.3 V. The corresponding circuit and its output signal is shown in Fig. 4.8.

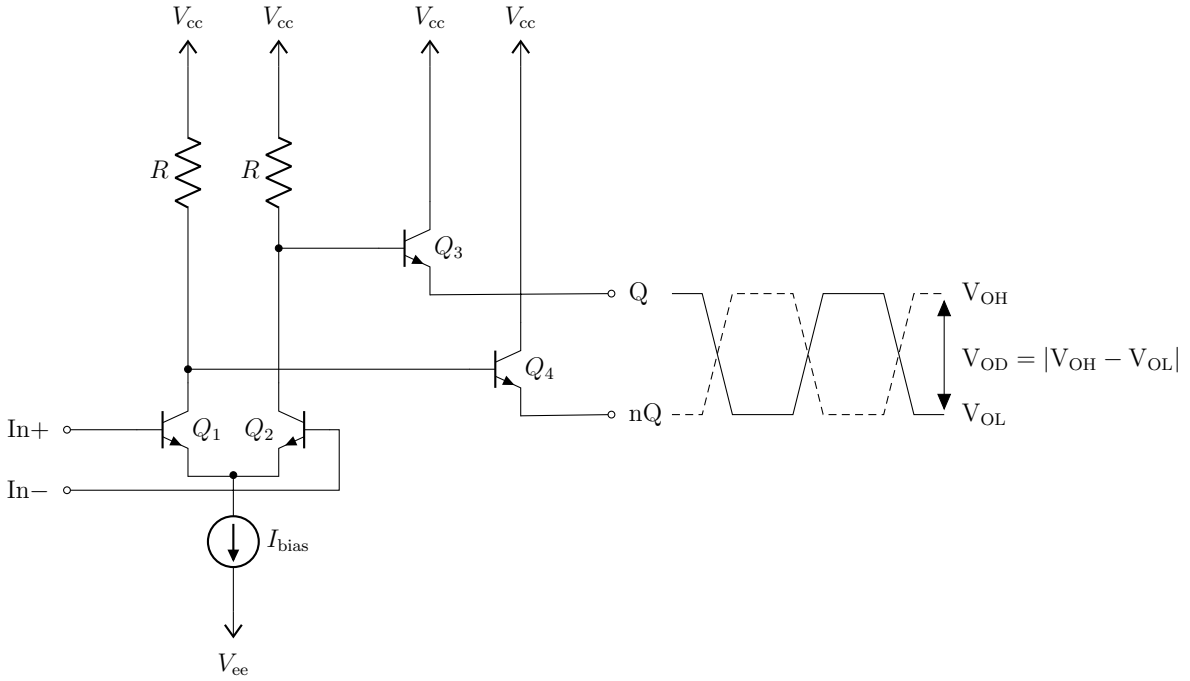


**Figure 4.8:** LVPECL circuit. The differential output must be loaded by an external circuit to obtain a common-mode voltage of Vcc−1.3 V.

From the LVPECL circuit, it can be noted that:

1. The output transistors require emitter resistors to complete the bias path and activate them. These resistors will determine the current consumption and the output common-mode voltage.
2. If the output is not used, it can be left floating to minimize power consumption (this is the case for the 3 unused outputs of the LMK00725).

Level adapters are necessary when interfacing circuits that operate on different voltage standards. These adapters, also known as level shifters, convert signals from one voltage level to another, ensuring compatibility between components. This prevents damage to components and ensures reliable communication between circuits with different voltage standards. The circuits shown in Fig. 4.9 are used to adapt the LVPECL standard to the differential input required by the MAX5891 and the LVDS standard of the MMCM.

The output stage of the LVPECL transmitter is biased to achieve an output current of 14 mA and a common-mode voltage of Vcc−1.3 V. Therefore, a 50 Ω resistor is connected

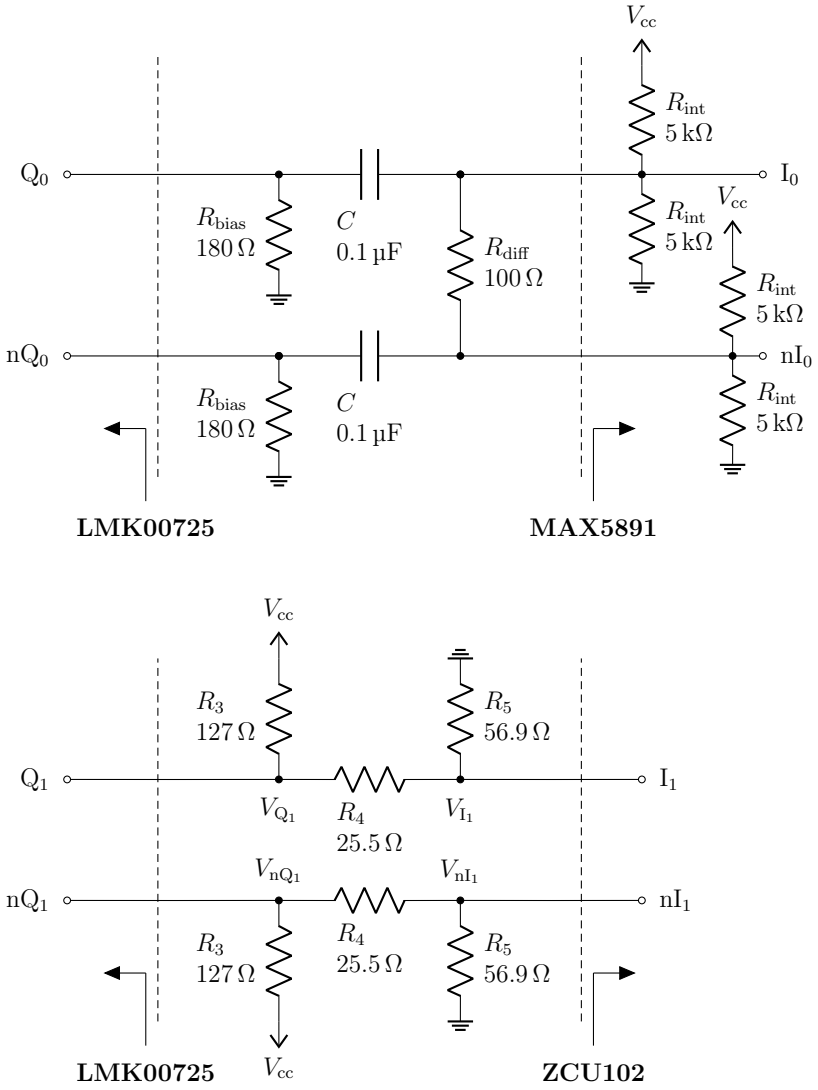


**Figure 4.9:** LVPECL drivers to adapt the LMK00725 output signal to the MAX5891 and FPGA inputs.

to Vcc−2 V at each node Q and nQ. However, to avoid using a separate power supply for Vcc−2 V, the manufacturer indicates that the bias can be achieved by connecting a 180 Ω bias resistor to GND. Additionally, since the MAX5891 has an internal biasing that is incompatible with the driver, the capacitors $C$ are used in series to block the driver's common-mode voltage. The 100 Ω differential resistor provides termination for the signal transmission lines. The differential swing voltage at the output of the LMK00725 ranges between 575 $mV_{pp}$ and 850 $mV_{pp}$, meeting the minimum requirement of 500 $mV_{pp}$ for the MAX5891.

The selected BE input standard is LVDS. The manufacturer specifies a differential input voltage range of 100 $mV_{pp}$ to 600 $mV_{pp}$ and a common-mode voltage range of 0.3 V to 1.425 V [117]. A resistor network is used to generate a bias voltage of 1.3 V at the

output of the LVPECL driver and 0.9 V at the input of the LVDS receiver. This network also reduces the driver's differential voltage range to between $400\,\mathrm{mV_{pp}}$ and $587\,\mathrm{mV_{pp}}$, as required by the receiver. The Thevenin equivalent impedance at each driver node is approximately $50\,\Omega$, which matches the characteristic impedance of the transmission lines.

The voltage $V_{\mathrm{Q_1}} = V_{\mathrm{nQ_1}}$ is calculated as:

$$V_{\mathrm{Q_1}} = \mathrm{Vcc} \cdot \frac{R_4 + R_5}{R_3 + R_4 + R_5} = 1.3\,\mathrm{V} \ , \tag{4.26}$$

while the voltage $V_{\mathrm{I_1}} = V_{\mathrm{nI_1}}$ is given by

$$V_{\mathrm{I_1}} = \mathrm{Vcc} \cdot \frac{R_5}{R_3 + R_4 + R_5} = 0.9\,\mathrm{V} \ . \tag{4.27}$$

The differential load impedance for the transmission line is

$$Z_{\mathrm{diff}} = \frac{2R_3 \cdot (R_4 + R_5)}{R_3 + R_4 + R_5} = 100\,\Omega \ . \tag{4.28}$$

Synchronization of input data with the clock signal in a DAC is essential for accurate conversion. The clock signal ensures that data is sampled at the correct intervals, aligning with the DAC's conversion process. Data must be stable and valid at the precise moment it is sampled by the DAC. This process involves timing constraints such as setup and hold times. Setup and hold times are critical parameters in the operation of DACs and other synchronous digital circuits. They define the timing requirements for data relative to the clock signal to ensure reliable operation. Setup time is the minimum period before the clock edge during which the data must be stable, while hold time is the minimum period after the clock edge during which the data must remain stable. Meeting these timing requirements ensures that data is correctly latched and converted, preventing errors and ensuring accurate analog output.

The MAX5891 has a setup time of $-1.5\,\mathrm{ns}$ and a hold time of 2.6 ns, resulting in a 1.1 ns window during which the data must remain unchanged. The signal path for generating digital data is much longer than the line connecting the output clock of the LMK00725 to the MAX5891. To synchronize the digital word at the DAC input with the clock and meet the timing requirements, the MMCM is implemented in the FPGA for dynamic phase control of the clock that governs the generation of the digital word.

## 4.4 Signal Chain Noise

Several sources contribute to the total noise of the modulation signal. In the case of the SE signal (see Fig. 4.10), the main sources are the MAX5891 ($S_{\mathrm{V,MAX5891}}$), the thermal noise in the I-V Converter ($S_{\mathrm{V,C}}$), the noise of the 10 dB attenuator ($S_{\mathrm{V,A_{TT}}}$) and the load noise ($S_{\mathrm{V,Z_L}}$).

$S_{\mathrm{V,MAX5891}}$ can be derived from Eq. 4.7 as

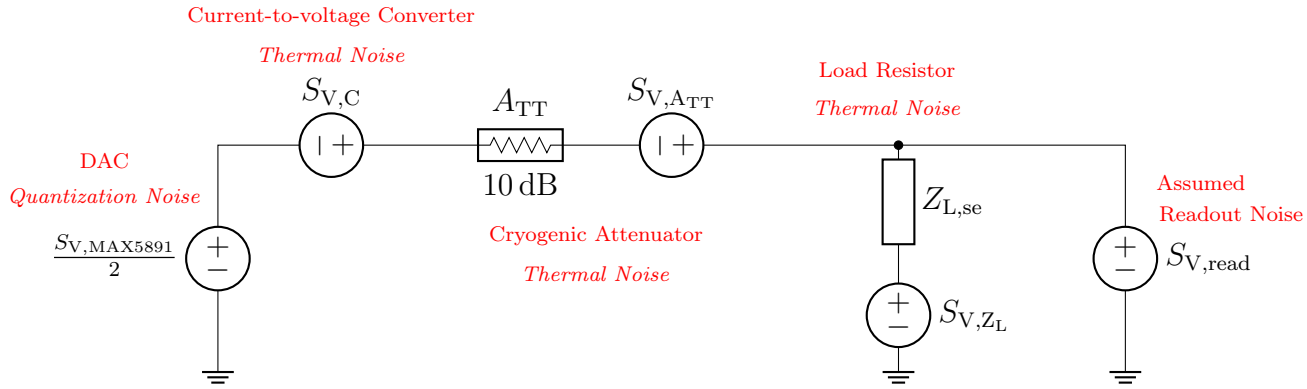


**Figure 4.10:** Noise model in the modulation line for the SE setup. The noise sources originate from the MAX5891 converter, the resistive converter, the cryogenic attenuator and the load connected in series to the $\mu$MUX.

$$S_{\mathrm{V,MAX5891}} = \sqrt{S_{\mathrm{MAX5891}} \cdot R_{\mathrm{eq}}} = 2\frac{\mathrm{nV}}{\sqrt{\mathrm{Hz}}} \ , \tag{4.29}$$

where

$$S_{\mathrm{MAX5891}} = 10^{S_{\mathrm{MAX5891,dBm}}/10} \cdot 1\,\mathrm{mW} \ . \tag{4.30}$$

The I-V Converter noise considers the thermal contributions of the resistances, as illustrated in Fig. 4.11. The thermal noise of a resistor $R$ can be modeled by its Thevenin equivalent circuit with a noiseless resitance $R$ and a voltage source of $S_{\mathrm{V,R}} = \sqrt{4k_{\mathrm{B}}TR}$. Therefore, the noise of the I-V converter is determined by calculating the total noise contribution from each resistor. This involves performing a circuit analysis to evaluate the output contribution of each source while deactivating all other sources. The individual contributions are then combined using a quadratic summation.

The equivalent noise source for each resistor is $S_{\mathrm{V,R_1}} = 1.82\,\mathrm{nV}/\sqrt{\mathrm{Hz}}$, $S_{\mathrm{V,R_2}} = 1.29\,\mathrm{nV}/\sqrt{\mathrm{Hz}}$ and $S_{\mathrm{V,R_L^{DAC}}} = 1.29\,\mathrm{nV}/\sqrt{\mathrm{Hz}}$ and the resultant contribution of each source follows

$$S_{\mathrm{V,C1}} = \frac{S_{\mathrm{V,R_1}} \cdot A}{R_1 + 2A} = 227.5\,\frac{\mathrm{pV}}{\sqrt{\mathrm{Hz}}} \ , \tag{4.31}$$

$$S_{\mathrm{V,C2}} = \frac{S_{\mathrm{V,R_2}}}{R_2 + \left((R_{\mathrm{L}}^{\mathrm{DAC}}/2)//(R_1 + A)\right)} \cdot \frac{(R_{\mathrm{L}}^{\mathrm{DAC}}/2) \cdot A}{(R_{\mathrm{L}}^{\mathrm{DAC}}/2) + R_1 + A} = 53.75\,\frac{\mathrm{pV}}{\sqrt{\mathrm{Hz}}} \ , \tag{4.32}$$

$$S_{\mathrm{V,C3}} = \frac{S_{\mathrm{V,R_2}}}{R_2 + (B//Z_{\mathrm{L,se}})} \cdot \frac{B \cdot Z_{\mathrm{L,se}}}{B + Z_{\mathrm{L,se}}} = 376.25\,\frac{\mathrm{pV}}{\sqrt{\mathrm{Hz}}} \ , \tag{4.33}$$

$$S_{\mathrm{V,C4}} = \frac{S_{\mathrm{V,R_L^{DAC}}}/2}{(R_{\mathrm{L}}^{\mathrm{DAC}}/2) + \Big(R_2//(R_1+A)\Big)} \cdot \frac{R_2 \cdot A}{R_2 + R_1 + A} = 53.75\,\frac{\mathrm{pV}}{\sqrt{\mathrm{Hz}}}\ , \tag{4.34}$$

where $A = R_2//Z_{\mathrm{L,se}}$ and $B = R_1 + (R_{\mathrm{L}}^{\mathrm{DAC}}/2)//R_2$.

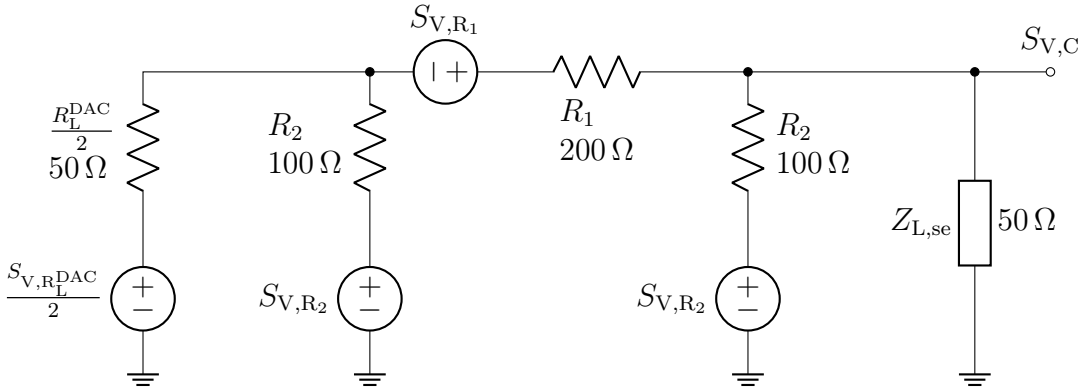


**Figure 4.11:** IV converter noise model for the SE setup. The noise in each resistor is governed by thermal fluctuations and is equivalent to $S_{\mathrm{V,R}} = \sqrt{4k_{\mathrm{B}}TR}$, where $R$ is the resistance value.

Finally, the I-V Converter noise is

$$S_{\mathrm{V,C}} = \sqrt{{S_{\mathrm{V,C1}}}^2 + {S_{\mathrm{V,C2}}}^2 + {S_{\mathrm{V,C3}}}^2 + {S_{\mathrm{V,C4}}}^2} = 446.2\,\frac{\mathrm{pV}}{\sqrt{\mathrm{Hz}}}\ . \tag{4.35}$$

$S_{\mathrm{V,MAX5891}}$ and $S_{\mathrm{V,C}}$ are attenuated by 10 dB reaching ${S_{\mathrm{V,MAX5891}}}' = 630\,\mathrm{pV}/\sqrt{\mathrm{Hz}}$ and ${S_{\mathrm{V,C}}}' = 141\,\mathrm{pV}/\sqrt{\mathrm{Hz}}$.

The attenuator noise is estimated to be $S_{\mathrm{V,A_{TT}}} = 52.37\,\mathrm{pV}/\sqrt{\mathrm{Hz}}$, meanwhile the load located at 4 K has a thermal noise of $S_{\mathrm{V,Z_L}} = \sqrt{4k_{\mathrm{B}}TZ_{\mathrm{L}}} = 105.1\,\mathrm{pV}/\sqrt{\mathrm{Hz}}$.

Finally, the total noise in the modulation line is

$$S_{\mathrm{V,se}} = \sqrt{\left(\frac{{S_{\mathrm{V,MAX5891}}}'}{2}\right)^2 + {S_{\mathrm{V,C}}}'^2 + {S_{\mathrm{V,A_{TT}}}}^2 + {S_{\mathrm{V,Z_L}}}^2} = 365\,\frac{\mathrm{pV}}{\sqrt{\mathrm{Hz}}}\ . \tag{4.36}$$

In conclusion, this noise is negligible compared to the $S_{\mathrm{V,read}}$ calculated in Eq. 4.2, degrading it by 3.8%.

The noise model for the differential setup is shown in Fig. 4.12. The $S_{\mathrm{V,MAX5891}}$ component is the same as for the SE case, while $S_{\mathrm{V,C}}$ is derived from the model shown in Fig. 4.13 and its various contributions are calculated as follows:

$$S_{\mathrm{V,C1}} = \frac{S_{\mathrm{V,R_1}} \cdot \Big((2R_2)//Z_{\mathrm{L,diff}}\Big)}{R_1 + \Big((2R_2)//Z_{\mathrm{L,diff}}\Big)} = 455\,\frac{\mathrm{pV}}{\sqrt{\mathrm{Hz}}}\ , \tag{4.37}$$

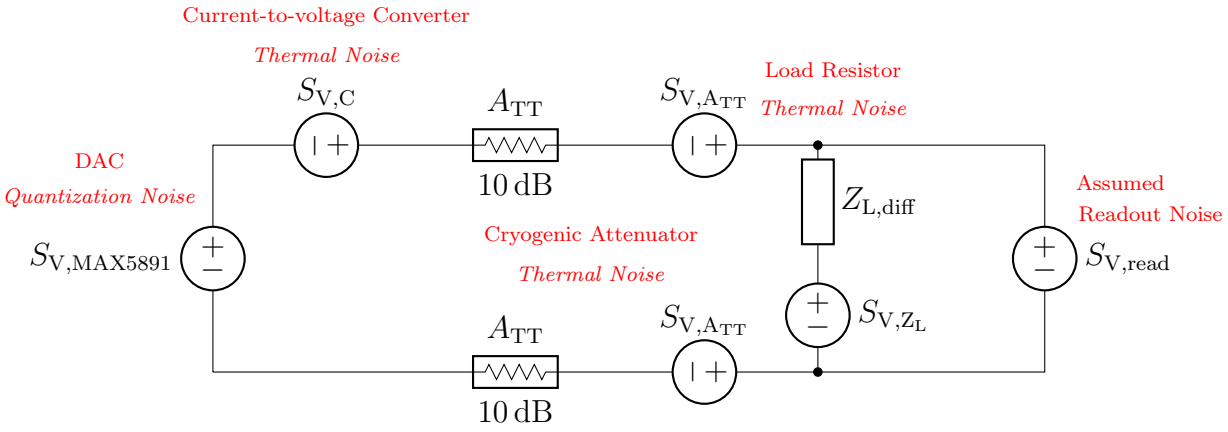


**Figure 4.12:** Noise model in the modulation line for the differential setup. The noise sources originate from the MAX5891 converter, the resistive converter and the load connected in series to the $\mu$MUX. Two commercial 10 dB attenuators are installed in each line.

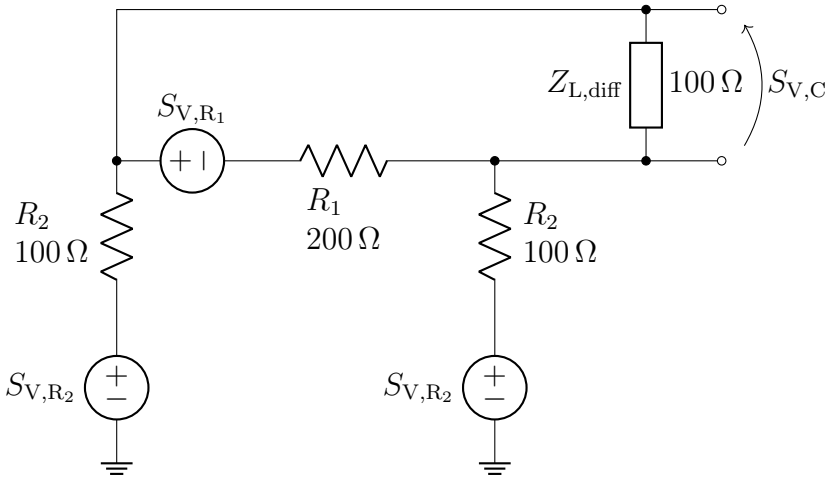


**Figure 4.13:** IV converter noise model for the differential setup.

$$S_{V,C2} = \frac{S_{V,R_2} \cdot (R_1 // Z_{L,diff})}{2R_2 + (R_1 // Z_{L,diff})} = 322.5 \, \frac{pV}{\sqrt{Hz}} \ , \tag{4.38}$$

$$S_{V,C3} = \frac{S_{V,R_2} \cdot (R_1 // Z_{L,diff})}{2R_2 + (R_1 // Z_{L,diff})} = 322.5 \, \frac{pV}{\sqrt{Hz}} \ . \tag{4.39}$$

The total I-V Converter noise is

$$S_{V,C} = \sqrt{{S_{V,C1}}^2 + {S_{V,C2}}^2 + {S_{V,C3}}^2} = 644.23 \, \frac{pV}{\sqrt{Hz}} \ . \tag{4.40}$$

The 10 dB attenuators reduce the noise level to $S_{\mathrm{V,C}}{}' = 203.58\mathrm{pV}/\sqrt{\mathrm{Hz}}$. Therefore, the total noise in the modulation line is

$$S_{\mathrm{V,diff}} = \sqrt{{S_{\mathrm{V,MAX5891}}}'^2 + {S_{\mathrm{V,C}}}'^2 + 2 \cdot {S_{\mathrm{V,A_{TT}}}}^2 + {S_{\mathrm{V,Z_L}}}^2} = 682.58\,\frac{\mathrm{pV}}{\sqrt{\mathrm{Hz}}}\ , \tag{4.41}$$

where $S_{\mathrm{V,Z_L}} = 148.63\,\mathrm{pV}/\sqrt{\mathrm{Hz}}$. In summary, the readout noise from Eq. 4.3 is degraded by less than 3.4%.

# Chapter 5

# Digital Signal Processing

Advanced DSP techniques have revolutionized the field of signal processing enabling the manipulation and analysis of signals utilizing complex and flexible algorithms. A significant development in this aspect is the utilization of FPGAs due to their remarkable parallel processing capabilities that are inherently advantageous for DSP applications, where multiple data streams must be processed simultaneously. Besides, one of its critical application is in the implementation of multirate processing techniques. Multirate processing involves altering the sampling rate of signals within a system to optimize the computational load and enhance processing efficiency. Techniques such as downsampling (reducing the sampling rate) and interpolation (increasing the sampling rate) are employed to match the signal processing requirements of different stages in a system. In the context of a FPGA, these operations can be executed in parallel, leveraging the device's architecture to handle the increased computational demands effectively.

Applying these advanced DSP techniques to the processing of frequency comb generated for the $\mu$MUX readout represents a sophisticated and efficient approach to signal acquisition and analysis. The challenge lies in accurately demodulating and processing these signals to retrieve meaningful data from each detector. Utilizing FPGA for this purpose allows for real-time processing of the frequency comb signal. This device can be programmed to perform the necessary digital down-conversion, filtering and demodulation tasks concurrently, ensuring that the signals from all detectors are processed simultaneously. This parallel processing capability is crucial at maintaining the integrity of the data and ensuring that the timing requirements of the system are met.

## 5.1 Digital Down Converter

A good starting point to comprehend the processing chain in the BE and its respective frequency planning is to understand one of its fundamental modules: the Digital Down Converter (DDC), which is an essential component in multirate signal processing systems. DDCs are primarily used to translate high-frequency signals to lower frequencies, making them easier to process and analyze. This process involves several critical steps, including mixing, filtering and downsampling.

A key aspect of understanding DDCs is their relationship with the Discrete Fourier Transform (DFT), a powerful tool in digital signal processing. The DFT decomposes a discrete-time signal $x[n]$ into its frequency-domain representation $X[k]$ by computing the IQ components of the normalized frequencies $f_k/f_\mathrm{s} = k/N$, accounted as

$$X[k] = \sum_{n=0}^{N-1} x[n] e^{-j2\pi kn/N} \quad , \tag{5.1}$$

where $f_\mathrm{s}$ is the sampling frequency, $N$ the time-domain signal length and $k = 0, 1, 2, ..., N-1$. Each DFT coefficient is obtained by first shifting the input signal by a frequency of $\pm k/N$ and then filtering out the higher frequency components using a low-pass filter, which is implemented by averaging $N$ samples. This averaging has a frequency response equivalent to a Rectangular window function (see Fig. 3.19). When the input signal has a frequency component at $k/N$, the real and imaginary values of it are stored in $X[k]$.

A DDC calculates a single DFT coefficient by mixing a discrete band-pass input signal with a LO signal at a normalized frequency $f_0/f_\mathrm{s}$, where $f_0$ is the center frequency of the input signal. This mixing process generates two frequency-shifted components for both real and imaginary path, one at base-band and the other at $2f_0$. Subsequently, a low-pass filter attenuates the up-converted component. The base-band signal is now over-sampled at $f_\mathrm{s}$, hence, samples can be discarded without violating the sampling theorem. This downsampling process results in resource savings at subsequent processing stages. The downsampling factor is determined by the input signal's bandwidth and the desired output sampling rate.

If the input signal is a complex band-pass signal, complex mixing is performed, as described by Eq. 3.61 for continuous-time signals. The up-converted components are then filtered by the low-pass filter which makes it possible for a subsequent reduction in the sampling rate without any loss of information. The complex DDC diagram together with its frequency translation effect is shown in Fig. 5.1.

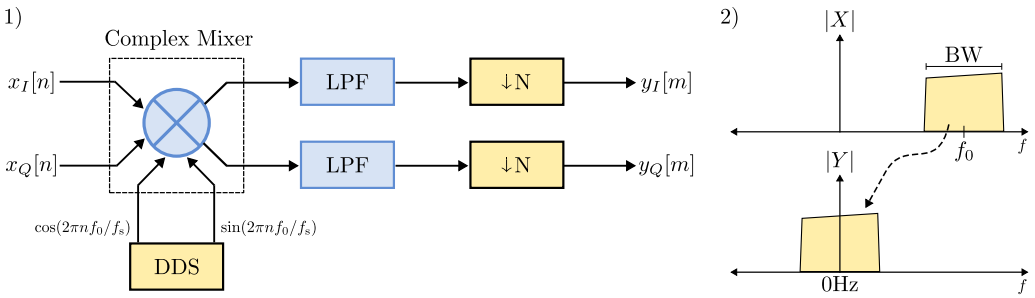


**Figure 5.1:** (**Left**) Complex DDC diagram. The input signal $x_I[n] + jx_Q[n]$ is mixed by a LO $x_\mathrm{lo}[n] = cos(2\pi n f_0/f_\mathrm{s}) + jsin(2\pi n f_0/f_\mathrm{s})$. Typically, two DDSs are used for the synthesis of the complex LO signal. The up-converted components are then filtered, which enables a downsampling by a factor of $N$. (**Right**) The input signal spectrum $|X|$, centered at $f_0$, is translated to base-band at the output of the DDC ($|Y|$).

## 5.2 Digital Backend

The readout signal acquisition and processing begins with the ADCs. As indicated in Section 3.5, the five complex sub-bands of 800 MHz bandwidth each are sampled at a rate of 1 GHz using ten converters. These converters are derived from five dual-converter AD9680 chips. Each chip includes a block of 4 integrated DDCs that allows further sub-division of each sub-band into 4 complex spectra of 250 MHz. The frequency translation of the input comb signal in the DDCs can be controlled individually. This supports setting the translation frequencies to −300 MHz, −100 MHz, 100 MHz and 300 MHz, resulting in overlapping bands that cover a total of 850 MHz, as Fig. 5.2 illustrates. However, the manufacturer specifies an anti-aliasing guard band of 192.5 MHz due to the non-flat frequency response of the DDCs, resulting in an effective bandwidth of 770 MHz. The spectrum division enables downsampling by a factor of 4, achieving a sampling rate of 250 Msps for each band. After this process, each signal is transmitted from the converters to the FPGA, via a JESD204 serial interface.

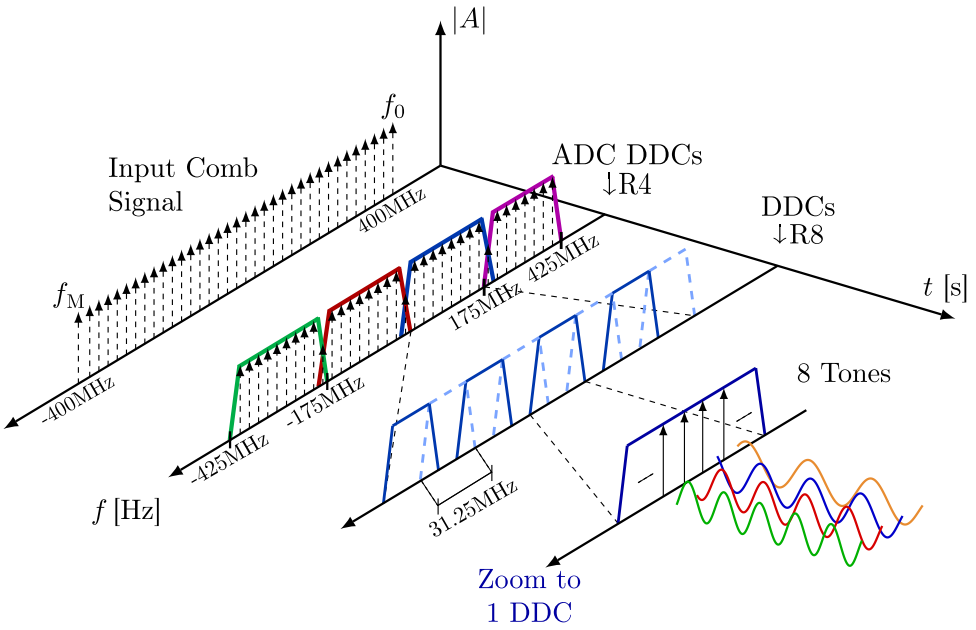


**Figure 5.2:** Downsampling stages for one 800 MHz input signal sub-band. The first stage occurs during the signal acquisition by the ADC, which integrates 4 DDCs tuned to frequencies of −300 MHz, −100 MHz, 100 MHz and 300 MHz. This results in 4 complex bands, each sampled at 250 Msps. A second stage in the FPGA involving 32 DDCs further reduces the sampling rate by a factor of 8, bringing it down to 31.25 Msps.

To further split the tones, a new division chain is implemented using 8 DDCs per DDC effective bandwidth. In this way, each 192.5 MHz spectrum is now divided into 8 overlaping complex spectra with a bandwidth of 31.25 MHz and a sampling rate of 31.25 Msps each. The 31.25 MHz complex signal is comprised of 8 tones separated by 3.9 MHz. Each of these tones must be filtered to obtain the information from the $\mu$MUX channels contained in their amplitude and phase.

Since the sampling frequency has been sufficiently reduced, it is possible to implement a filter bank operating at 250 MHz that processes several tones by implementing TDM. The Goertzel Filter (GF) Bank Channelizer offers the advantage of performing this task while optimizing resources on the FPGA. Additionally, it allows for the extraction of both the magnitude and phase of the signal. This is fundamentally important as it enables the selection of the signal that best meets the optimal SNR levels.

The GF is an efficient technique for calculating a single coefficient of the DFT of a signal. Unlike the Fast Fourier Transform (FFT), which optimizes the computation of all DFT coefficients, the GF focuses on a specific frequency. The set of equations that describes the behavior of the GF in a less computationally demanding form and for non-integer frequency index are divided into Iterative Section (I.S.),

$$\begin{cases} W_0[n] = x[n] + 2W_1[n]\cos(\alpha) - W_2[n] \\ W_1[n] = W_0[n-1] \\ W_2[n] = W_1[n-1] \end{cases} , \tag{5.2}$$

and Non-Iterative Section (N.I.S.),

$$x_k[m] = (W_1[m] - W_2[m] \cdot e^{-j\alpha}) \cdot e^{-j\beta} \ , \tag{5.3}$$

where $\alpha = 2\pi k/N$, $\beta = 2\pi k(N-1)/N$ and $x_k[m]$ is the complex DFT coefficient of the input signal $x[n]$ at frequency $k/N$ (for more details on Eq. 5.2 and Eq. 5.3, refer to [103, 120]). It is important to note that the sampling rate at the output is decimated by a factor of $N$ with respect to the input sampling frequency due to the iterative section. The GF block diagram is represented in Fig. 5.3. An additional filtering stage is introduced, where the filtered samples $x_w[n]$ act as the input to the GF and $N_w = N$ is the filter length.

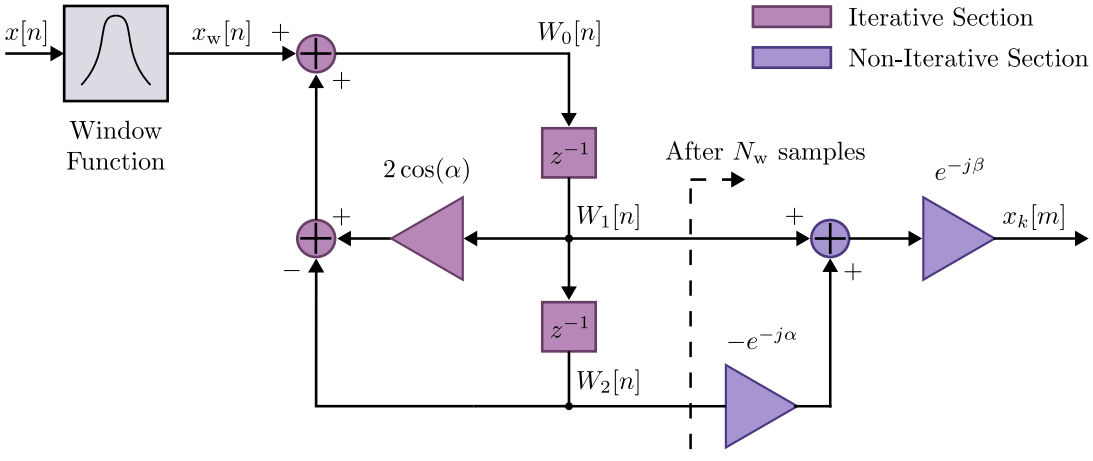


**Figure 5.3:** The GF consists of two distinct processing stages. The first is the I.S., which calculates $W_1$ and $W_2$ using $N$ input samples. Following this, the N.I.S. employs $W_1$ and $W_2$ to compute the complex output value $x_k$. Multiplying the input samples by the coefficients of a window function modifies the frequency response of the GF.

The input signal $x[n]$ is filtered by multiplying the input samples with a window function coefficients. This additional processing module includes a BRAM that allows to write in run-time the filter coefficients and, consequently, modify characteristics of the filter such as pass-band attenuation, stop-band attenuation, crosstalk between channels, etc.

Since the GF I.S. is clocked at $f_{\text{clk}} = 250\,\text{MHz}$, its input can be connected to the output of 4 complex DDCs with an output sampling rate of 31.25 Msps as seen in Fig. 5.4. A Combiner block operating also at 250 MHz is used to arrange the input samples into a TDM sequential stream of 8 samples to be processed by the GF. The GF calculates the DFT coefficient of one specific tone of the 8 tones transmitted by each DDC, filtering out the others. Consequently, 8 iterative blocks are required for every 4 DDCs, leading to a total of 64 blocks to cover the 32 DDCs of the second stage in a 800 MHz sub-band.

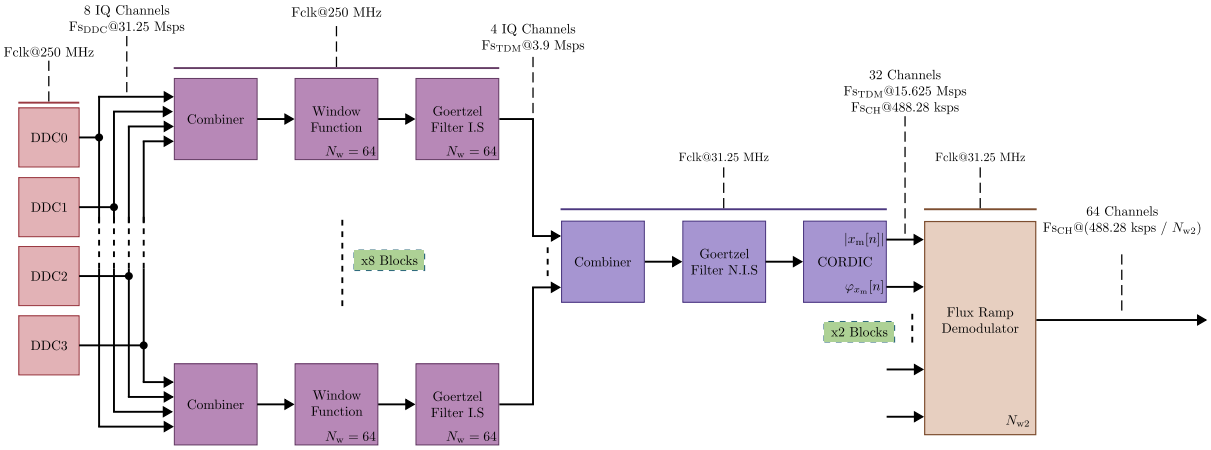


**Figure 5.4:** FPGA backend channelization for 64 $\mu$MUX channels. Only the blocks capable of processing 32 channels corresponding to DDC0, DDC1, DDC2 and DDC3 are shown. By duplicating these blocks for DDC4, DDC5, DDC6 and DDC7, the remaining 32 channels are covered. To process all the channels within the 800 MHz sub-band, 4 blocks of 64 channels are required.

The window function length is set to $N_{\text{w}} = 64$, resulting in an output sampling rate of $fs_{\text{TDM}} = 3.9\,\text{Msps}$, which is then directed to the N.I.S. of the GF. The N.I.S. operates at a frequency of $f_{\text{clk}} = 31.25\,\text{MHz}$, allowing it to receive the output from the 8 iterative blocks through another Combiner, which reorders the samples into a new array.

At the output of the N.I.S., both the IQ samples for each readout tone are obtained. Thereafter, a COordinate Rotation DIgital Computer (CORDIC) [121] module obtains the rf-SQUID responses by computing the magnitude and phase through the rotation of the IQ samples of each channel. The magnitude and phase of the readout tone are then sent with a sampling rate of $fs_{\text{TDM}} = 15.625\,\text{Msps}$ to the final processing block before data transmission, which is the Flux Ramp Demodulator (FRD). The FRD selects either the magnitude or phase signal as input for phase demodulation, as both contain the same information. The FRD is capable of managing the samples from two CORDIC blocks since its clock frequency is 31.25 MHz. Internally, the demodulation block performs

decimation by a factor of $N_{w2}$ (see Section 5.3 for more details.). As a result, each output, corresponding to the detector signal of each channel, is sampled at a rate of $488.28/N_{w2}$ ksps.

## 5.3 Flux Ramp Demodulator

Once each channel is mixed to base-band and isolated, the resulting signal is that of the rf-SQUID, phase-modulated by the detector signal. Therefore, an additional processing stage is required to extract the detector information. The demodulation implemented is a Multi-channel Digital Quadrature Demodulator (DQD) that utilizes a real-input DDC and functions as a coherent demodulator (see Fig. 5.5). The rf-SQUID signal of M-channels $\theta[n]$ are the input of the DDC using TDM. An M-position DDS synthesizes the complex exponential waveforms with a fundamental frequency around $\Omega_{\text{mod}} = 2\pi f_{\text{mod}}/f_s$ that correlates with each input signal. After the DDC filter, the instantaneous phase of the rf-SQUID signals are calculated by the trigonometric function $\varphi_{\text{det}}[m] = arctan(\theta_Q[m]/\theta_I[m])$, where $\theta_I[m]$ and $\theta_Q[m]$ are the DDC output signals.

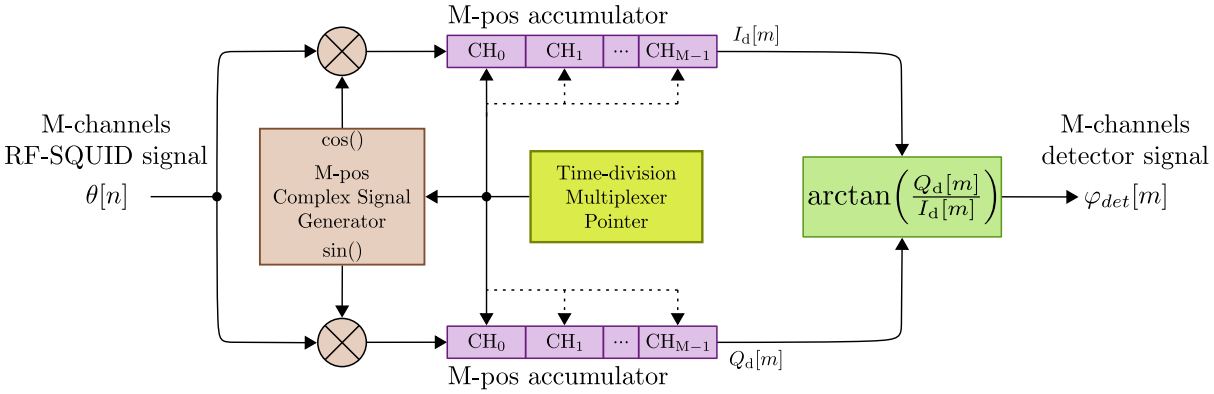


**Figure 5.5:** The Multi-channel Digital Quadrature Demodulator is a coherent demodulator that enables the extraction of the detector signals from the phase of the different rf-SQUID input signals.

The low-pass filter and down-sampler can be implemented as the average of samples indicated by Eq. 5.1 for every $N$ input samples, where $N$ is the number of samples within a single FR period. This filter is a type of Moving Average Filter (MAF), where the averaging window spans $N$ samples. The effective sampling frequency at the output is therefore equal to the $f_{\text{ramp}}$. Finally, the equation describing the DQD for a single channel is:

$$\varphi_{\text{det}}[m] = \arctan\left(-\frac{\sum_{n=Nm}^{N(m+1)-1}\theta[n]\,\sin(\Omega_{\text{mod}}n)}{\sum_{n=Nm}^{N(m+1)-1}\theta[n]\,\cos(\Omega_{\text{mod}}n)}\right) . \tag{5.4}$$

Eq. 5.4 is the discrete-time version of Eq. 3.19. The MAF has the frequency response of a Rectangular window function, as shown in Fig. 5.6.

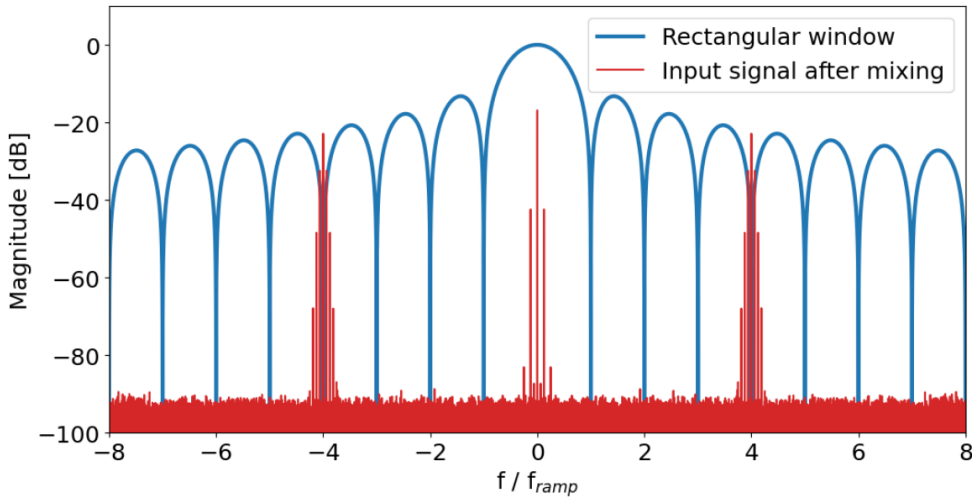


**Figure 5.6:** The MAF magnitude spectrum with normalized gain is shown in blue. A phase modulated rf-SQUID signal after mixing and prior to the convolution with the MAF is shown in red. The modulating signal is a sinusoidal wave for a clear visualization of the sideband components.

A simplified rf-SQUID signal $\theta[n] = \cos(2\pi(N_{\Phi_0} f_{\mathrm{ramp}}/f_{\mathrm{s}})n + \varphi_{\mathrm{det}}[n])$ mixed by the I input of the DDC is also displayed in Fig. 5.6, where $f_{\mathrm{mod}} = 2f_{\mathrm{ramp}}$. It can be noted that the up-converted component at $2f_{\mathrm{mod}}$ falls exactly in a transfer null of the MAF. This is always true if $N_{\Phi_0}$ is an integer. However, the Bessel components around the carrier are much less attenuated. After down-sampling, this remnant signal folds into the first Nyquist zone as aliasing. Consequently, the instantaneous phase of the rf-SQUID signal has an error at the demodulator output produced by the spurious signal, $\varphi'_{\mathrm{det}}[m] = \varphi_{\mathrm{det}}[m] + \epsilon[m]$. In fact, many groups have reported nonlinearities in the readout system [82, 122] which, upon analysis, were attributed to the spectral folding produced in the DQD [123].

### 5.3.1 Error Model

Applying trigonometric identities to Eq. 5.4 and considering $\theta[n] = \cos(2\pi(N_{\Phi_0} f_{\mathrm{ramp}}/f_{\mathrm{s}})n + \varphi_{\mathrm{det}}[n])$, the following equation is derived

$$\varphi'_{\mathrm{det}}[m] = \arctan\left(\frac{\sum_{n=Nm}^{N(m+1)-1}\Big(\sin(\varphi_{\mathrm{det}}[n]) - \sin(2\Omega_{\mathrm{mod}}n + \varphi_{\mathrm{det}}[n])\Big)}{\sum_{n=Nm}^{N(m+1)-1}\Big(\cos(\varphi_{\mathrm{det}}[n]) + \cos(2\Omega_{\mathrm{mod}}n + \varphi_{\mathrm{det}}[n])\Big)}\right). \tag{5.5}$$

The down- and up-converted signals from the numerator and denominator are the carrier components surrounded by Bessel components of Fig. 5.6. These components are

attenuated and phase-shifted by the MAF, thus, Eq. 5.5 can be written as a sum of components given by the phase modulation as

$$\varphi_{\text{det}}^{'}[m] = \arctan\left(\frac{\left(\sum_{k=-\infty}^{\infty} J_k(\beta)\Big(a_k\ \sin(\Omega_{\text{det}}nk+c_k) - b_k\ \sin(2\Omega_{\text{mod}}n+\Omega_{\text{det}}nk+d_k)\Big)\right)\Big|_{N\downarrow}}{\left(\sum_{k=-\infty}^{\infty} J_k(\beta)\Big(a_k\ \cos(\Omega_{\text{det}}nk+c_k) + b_k\ \cos(2\Omega_{\text{mod}}n+\Omega_{\text{det}}nk+d_k)\Big)\right)\Big|_{N\downarrow}}\right) \quad , \tag{5.6}$$

where $a_k$ and $b_k$ are the MAF attenuation coefficients at the down- and up-converted components and $c_k$ and $d_k$ are the phases for the down- and up-converted components, respectively. $\Omega_{\text{det}}$ is the normalized fundamental frequency of the detector, $\beta$ the modulation index and $J_k(\beta)$ is the Bessel function of the first kind of order $k$. The sum of components is affected by the down-sampling as it is showed using the vertical bars. After down-sampling, the spectrum folds into the first Nyquist zone yielding

$$\varphi_{\text{det}}^{'}[m] = \arctan\left(\frac{\sum_{k=-\infty}^{\infty} J_k(\beta)\Big(a_k\ \sin(\Omega_{\text{det}}mk + c_k) - b_k\ \sin(\Omega_{\text{det}}mk + d_k)\Big)}{\sum_{k=-\infty}^{\infty} J_k(\beta)\Big(a_k\ \cos(\Omega_{\text{det}}mk + c_k) + b_k\ \cos(\Omega_{\text{det}}mk + d_k)\Big)}\right) \quad . \tag{5.7}$$

As the $b_k$ values are close to 0, the Multivariate Maclaurin Series is a suitable tool to approximate Eq. 5.7:

$$\begin{aligned}\varphi_{\text{det}}^{'}(b_{-K},...,b_K) = {} & \varphi_{\text{det}} \\ & + \sum_{k=-K}^{K} b_k \frac{\partial \varphi_{\text{det}}^{'}}{\partial b_k}\bigg|_{(b_{-K}=0,...,b_K=0)} \\ & + \sum_{k_1=-K}^{K}\sum_{k_2=-K}^{K} \frac{b_{k_1}b_{k_2}\gamma}{2!}\frac{\partial^2 \varphi_{\text{det}}^{'}}{\partial b_{k_1}\partial b_{k_2}}\bigg|_{(b_{-K}=0,...,b_K=0)} \\ & + ... \ ,\end{aligned} \tag{5.8}$$

where $\gamma$ is equal to 1 if $k_1 = k_2$ and 2 otherwise. For simplicity, only the first 3 orders of the Multivariate Maclaurin Series for $2K+1$ variables are showed in Eq. 5.8. The first component of Eq. 5.8 is the phase shift produced by the detector signal while the spurious signal caused by the demodulator is obtained by adding the remaining terms.

### 5.3.2 Windowing

As $f_{\text{mod}}$ is determined by the slope of the FR, an increment in $I_{\text{ramp}}$, $M_{\text{mod}}$ or $f_{\text{ramp}}$ translates the up-converted components towards greater attenuation in the MAF. This can be the simplest and most straightforward method to improve the attenuation at high-frequencies since it could require minor hardware or software changes. However, some considerations must be taken into account when modifying the FR parameters:

- Increasing $I_{\mathrm{ramp}}$ results in higher power dissipation in the modulation line load located inside the cryostat.
- The increase of the rf-SQUID loop inductance degrades its flux NSD [124].
- A higher $f_{\mathrm{mod}}$ requires a broader resonator bandwidth (see Eq. 3.20), which ultimately reduces the number of $\mu$MUX channels within a given system bandwidth.

It is also important to emphasize that this method does not significantly improve the attenuation of spurious signals as filtering with another window function that offers greater attenuation at higher frequencies would. This can be achieved by a Weighted Moving Average Filter (WMAF). To introduce the WMAF, Eq. 5.4 is rewritten as:

$$\varphi_{\mathrm{det}}[m] = \arctan\left(-\frac{\sum_{n=Nm}^{N(m+1)-1} \theta[n]\,\sin(\Omega_{\mathrm{mod}} n)\,w[n]}{\sum_{n=Nm}^{N(m+1)-1} \theta[n]\,\cos(\Omega_{\mathrm{mod}} n)\,w[n]}\right) . \tag{5.9}$$

where the function $w[n]$ is an array of ones depicting the weighted coefficients of the Rectangular window function. However, there is a vast list of window functions that can be used to enhance the filter attenuation [125]. Each of these window functions has its own weighted coefficients. In [123], it was demonstrated that using Hamming and Bartlett windows significantly improved image attenuation, as shown in Fig. 5.7.

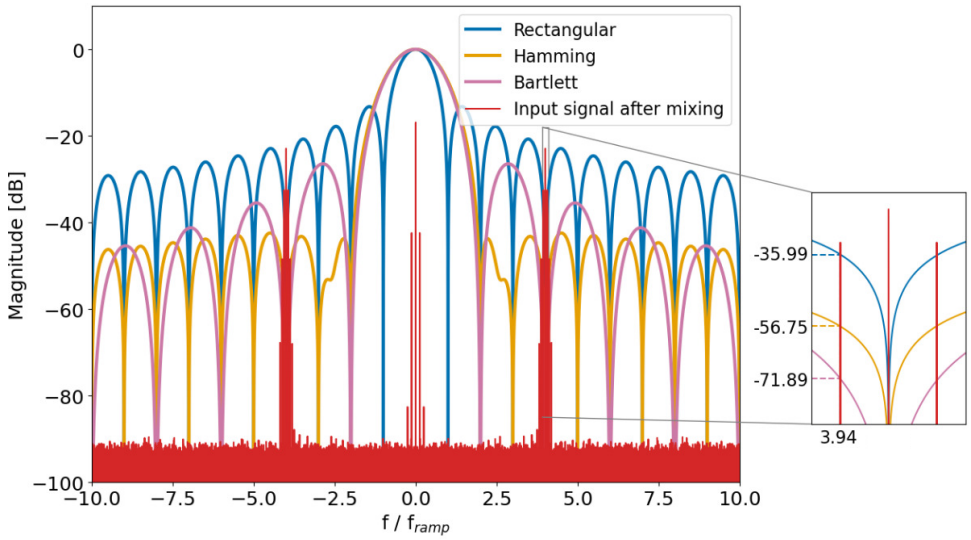


**Figure 5.7:** The WMAF magnitude spectrum with normalized gain for the Rectangular, Hamming and Bartlett windows. This approach was proposed to mitigate the aliasing effect of the MAF, typically implemented as the FRD. For instance, comparing different window functions reveals that the Bartlett window provides 35 dB better residual attenuation than the Rectangular window.

## 5.4 Flux Ramp Demodulator Implementation

The DQD implemented in the FPGA is exhibited in Fig. 5.8. It receives the rf-SQUID samples of $M = 64$ time-multiplexed channels. A Bits Selector is used to choose the lower or upper 32 bits from the 64 bits samples at the input, corresponding to the magnitude and phase demodulation of the readout tone, respectively. Each sample is then multiplied by a cuadrature LO through two multipliers, producing the IQ signals at the output. Each quadrature signal is then summed with the previous samples of the same channel and stored in a $M$ position accumulator, to be added with the next corresponding sample. After $N$ samples, each of the 64 samples in the accumulator is processed by a CORDIC module, which performs the trigonometric operation to obtain the detector signals.

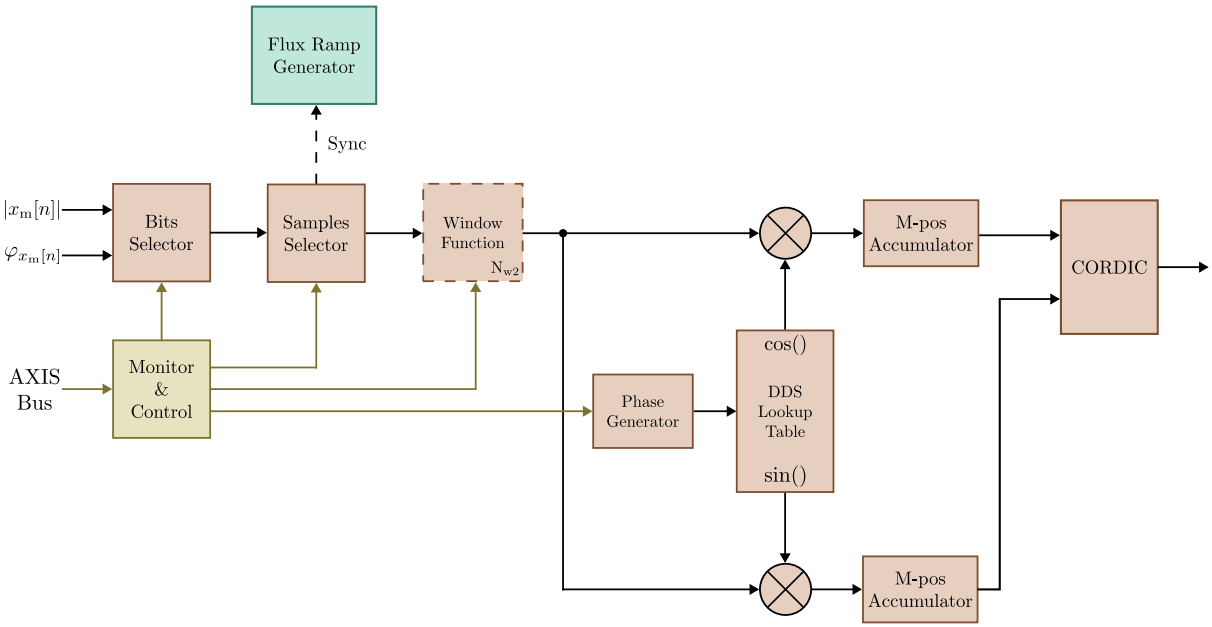


**Figure 5.8:** FRD module implemented in the FPGA. This module is also responsible for triggering the modulation signal via the sync signal. The Monitor & Control block is responsible for adjusting and acquiring the configuration variables of the different stages. Communication with this block is conducted via the AXI bus.

The multiplication is performed by instantiating two Xilinx DSP48E IP Core [126] available in the UltraScale+ architecture (refer to Fig. 5.9). The upper 27 bits of the input samples are fed into the A input of the multipliers, while the 16 bits LO signals connect to the B input of each multiplier. The results are obtained at the P output of the multipliers configured with $P_{\text{bits}} = 43$ bits.

The quadrature signal is generated using a custom phase generator combined with the Xilinx DDS Compiler 6.0 IP Core configured as a SIN/COS lookup table. This approach addresses the limitations in the number of time-multiplexed channels that the IP core can handle, as well as the latency introduced by it after each configuration of the phase generation block. The phase generator can be modified in run-time and has the capability to individually configure the frequencies of each channel. This feature allows

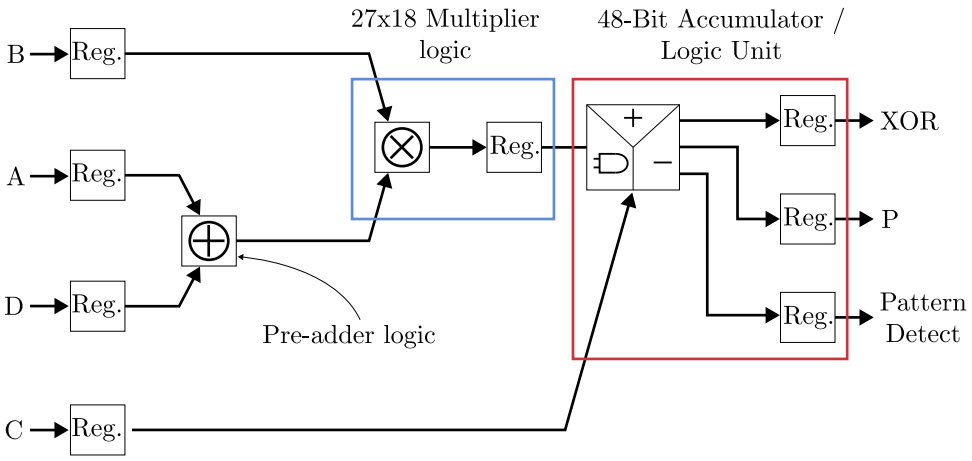


**Figure 5.9:** Xilinx DSP48E IP simplified schematic including the 4 registered input ports, a 27 bits pre-adder, a 27x18 two's complement multiplier and a 48 bits accumulator, among other features.

for minimizing the difference between the actual $f_{\text{mod}}$ value and the one generated by the LO, reducing any additional phase shift introduced to the detector signal. The frequency resolution is given by the multi-channel version of Eq. 3.35 as

$$f_{\text{res}}^{\text{dds}} = \frac{f_{\text{clk}}}{2^{N_{\text{acc}}} \cdot M} \ , \tag{5.10}$$

where $f_{\text{clk}} = 31.25\,\text{MHz}$ and $N_{\text{acc}}$ is the phase accumulator length. Thus, for a 16 bits phase accumulator length the frequency resolution reaches $f_{\text{res}}^{\text{dds}} = 7.45\,\text{Hz}$.

The two accumulators are implemented with two buffers of 64 positions, where each position has a length of $P_{\text{bits}} + \log_2(N) = 60$ bits. Here, $N$ is the number of samples in a FR period, determined by the length of the BRAM instantiated in the Stimulation module as $2 \cdot L_{\text{mem}} = 131072$ (see Section 4.3.1). Finally, once the input samples have been summed in the accumulators, they are transmitted to a Xilinx CORDIC 6.0 IP core, which calculates the arctangent between the two samples.

Optionally, a filter stage can be added during synthesis-time to implement the WMAF, enabling for run-time adjustment of filter characteristics. The filter consists of a BRAM with a length of $N_{\text{w2}} = N$. The multiplication of the input samples with the filter coefficients is performed by a DSP48E.

The Samples Selector block in Fig. 5.8 is responsible for counting the input samples that are processed by the DQD. These samples constitute the integration window, which can include all samples corresponding to the FR period or a smaller subset. The start and end of the integration window can be set at run-time, allowing for the selection of a sample set such that the value of $N_{\Phi_0}$ approaches an integer. This feature also helps to avoid phase jumps that occur due to the FR reset.

Additionally, this block manages synchronization with the modulation signal generation. Once the number of input samples (regardless of whether they are included in the integration window) reaches the trigger value, the sync signal is activated, triggering

the FR generation. This ensures that the signal is always triggered at the same instant, keeping the demodulation of the samples consistent over time. This avoids the addition of random phase shifts (see Eq. 4.14) and prevents the demodulation of samples corresponding to the ramp reset. The $f_{\text{ramp}}$ can be adjusted in real-time by setting the trigger value.

Once the trigger value is reached, the sample counter resets. However, there is a delay between the FR trigger and the first sample corresponding to the reset of the signal entering the FRD module. For this reason, the Samples Selector block supports setting the number of samples to skip after the synchronization signal is asserted, ensuring the correct identification of the initial sample of the modulation signal.

# Chapter 6

# Prototype Readout System Characterization

This chapter addresses the characterization of two fundamental components of the Readout system. The first component is the MSS board that generates the modulation signal. This characterization includes calibrating the modulation signal, which is essential for accurately assessing the analog signal derived from the synthetic signal, as well as analyzing the dynamic performance of the modulation. This is critical for optimal readout operation without compromising system integrity, as the modulation signal, like the detector signal, couples to the rf-SQUID.

The second component to be characterized is the FRD module, evaluated using a prototype system shown in Fig. 6.1. This prototype covers an instantaneous bandwidth of 800 MHz, which can be centered between 4.4 and 7.6 GHz. As mentioned in Section 3.5, the ZCU102 synthesizes the frequency comb, while the AD-FMCDAQ2-EBZ evaluation board handles the analog-to-digital conversion of the $\mu$MUX readout signals. A custom-designed FE frequency up- and down-convert the readout signal. The MSS and AD-FMCDAQ2-EBZ boards are connected to the ZCU102 via the FMC+ connector. The main clock for the FPGA modules is derived from the AD-FMCDAQ2-EBZ and the differential clock that drives the MSS board is obtained from the EVAL-AD9523-1 evaluation board. Synchronization is then achieved through a clock domain crossing block in the modulation signal generation blocks implemented in the FPGA.

The firmware prototype implemented in the FPGA includes, in the generation chain, a Stimulation module for the I&Q multicarrier signal with a frequency resolution of 7629.39 Hz, as well as an additional 152.58 Hz resolution Stimulation module and a single-ended to differential Converter module for the modulation signal.

In the reception side, four tunable DDCs are implemented within the sub-band range of $-250$ MHz to DC of the ADCs. Additionally, four tunable GFs connected to the DDCs feed into a FRD module. Since the iterative and non-iterative parts of the GF are still integrated, both operate at a clock frequency of 250 MHz, as does the FRD module. The GF output provides 64-bit samples, with the lower 32 bits representing the amplitude-demodulated $\mu$MUX signal and the remaining 32 bits representing the phase-demodulated $\mu$MUX signal. The FRD module output in turn consists of 32-bit

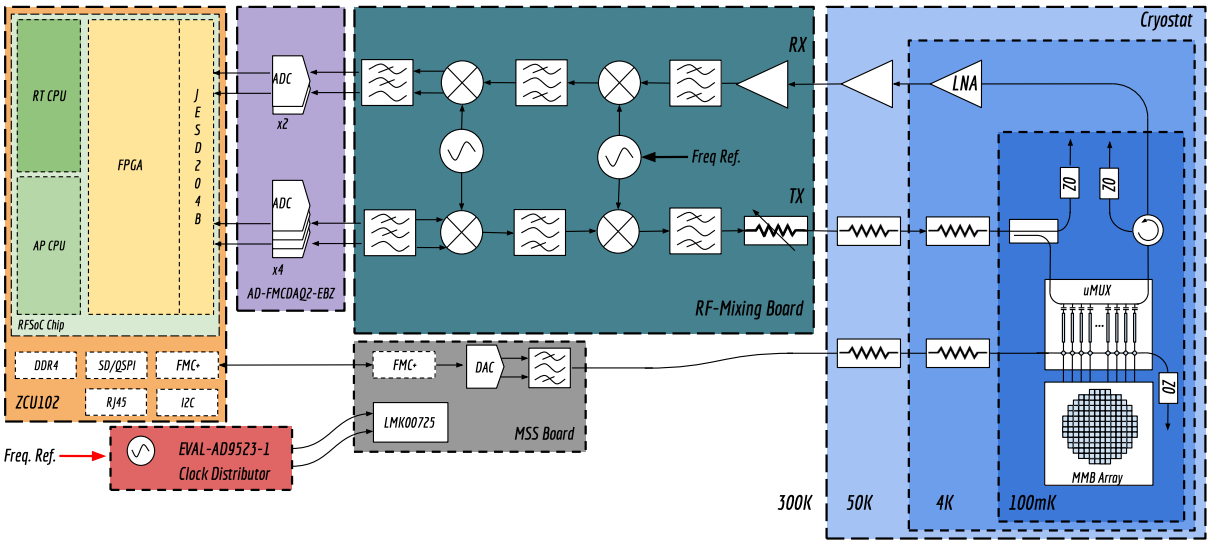


**Figure 6.1:** Prototype Readout system which covers an instantaneous 800 MHz bandwidth.

words corresponding to the detector signal. Samples from the FRD block are transferred to a Direct Memory Access (DMA) and then forwarded to a server via Ethernet. It is also possible to bypass the FRD block and send the GF output samples directly to the DMA. The JESD204B modules are AMD Intellectual Property (IP) cores [127, 128] used for the receiver and transmitter paths between the ZCU102 and the converter board. A block diagram of the implemented firmware is shown in Fig. 6.2. All runtime-configurable firmware modules connect to the main processor system via an AXI4-Lite bus (indicated in red). Additionally, the Platform Information and Management Core (PIMC) is a firmware module providing status information and control options.

## 6.1 MSS Board Characterization

### 6.1.1 Calibration

The primary objective of the calibration is to guarantee that the analog output accurately reflects the intended digital input values. In addition to determining the effective value of the generated signal, which is influenced by the designed circuit, it is also crucial to obtain the full-scale voltage, which is derived from establishing the full-scale current in the DAC using a digital potentiometer. This potentiometer is the AD5272, featuring a 20 kΩ nominal resistance and 1024-position resolution and therefore functioning as a variable attenuator. It achieves a DAC output range from 2 mA to 20 mA in a hyperbolic manner, according to the equation

$$I_{\mathrm{FS}} = 32\frac{V_{\mathrm{ref}}}{R_{\mathrm{set}}}\left(1 - \frac{1}{2^{16}}\right) \quad [112]. \tag{6.1}$$

The MAX5891 is powered by a 1.25 V reference voltage.

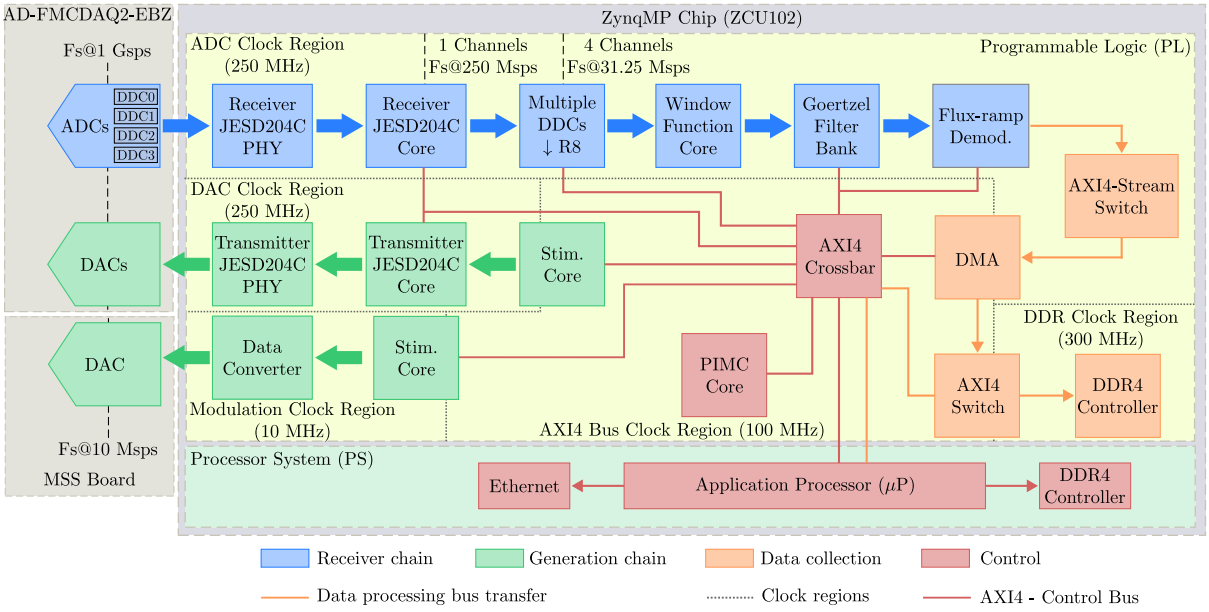


**Figure 6.2:** Prototype firmware implemented in the MPSoC ZCU102.

Calibration is performed through a multi-parametric sweep, setting sinusoidal signals with frequencies between 200 Hz and 100 kHz for various amplitudes of 0 dBFS, −1 dBFS, −3 dBFS, −6 dBFS and −12 dBFS. This procedure is conducted for different configurations of the potentiometer. Both the single-ended and differential outputs are calibrated during this process. The results obtained are illustrated in Fig. 6.3.

### 6.1.2 Dynamic Performance

Characterizing signals with sensitivities better than microvolts as the expected noise level of the MSS board output signal derived in Eq. 4.29 is a highly challenging task. Accurately measuring such signals requires appropriate equipment to ensure that the measurement process does not negatively impact the performance.

Digital oscilloscopes, such as the Tektronix DPO 7104 [129] available in our lab, illustrate these challenges well. Limited by its 8-bit depth ADC, this oscilloscope struggles to accurately capture the full resolution of high-precision signals, such as those generated by the 16-bit DAC under characterization. Quantization noise is an inherent effect of the digitization process, where signal values are approximated to the nearest discrete level. The quantization noise behaves like white noise when the ratio of the sampling frequency to the input frequency is not an integer. This white noise spreads uniformly across the spectrum, causing a slight increase in the overall noise floor. The reason for this is that the signal entering the ADC does not correlate with the quantization noise, meaning that the harmonic components of the input signal are not significantly affected by it.

However, the behavior of quantization noise can become more complex in certain cases where it introduces odd harmonic distortion. On one hand, this occurs when the ratio between the sampling frequency and the input signal frequency is an integer [130]. On the

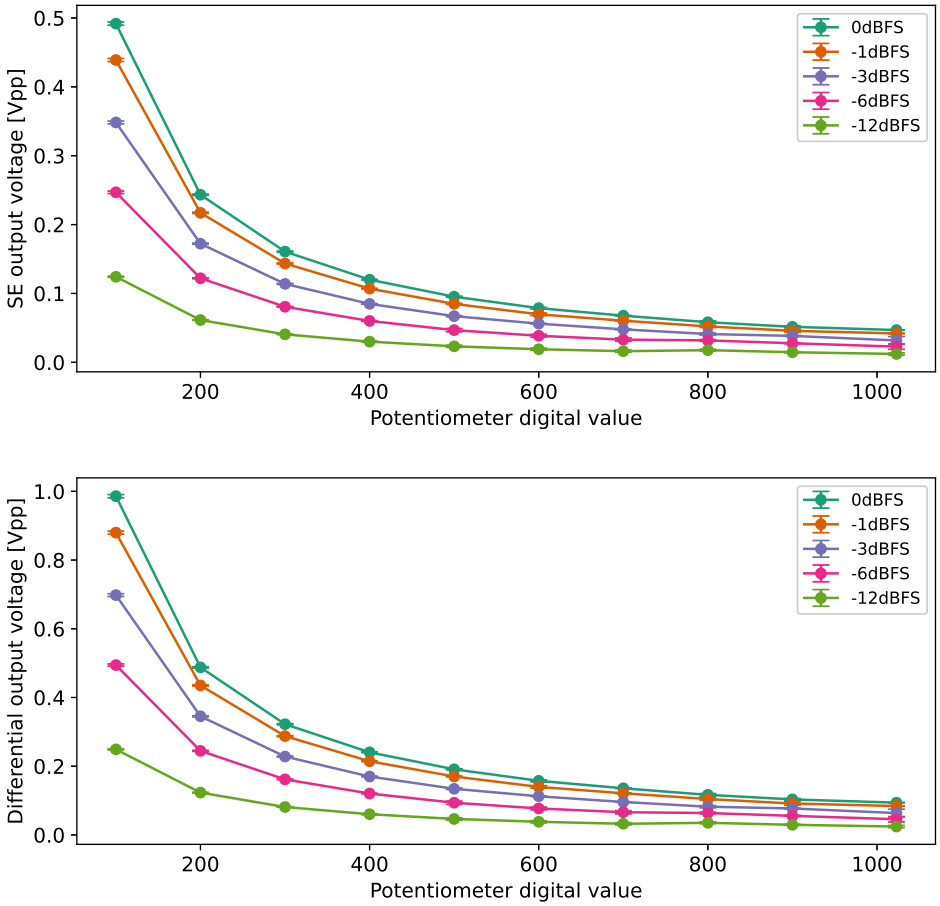


**Figure 6.3:** Calibration performed by measuring the peak-to-peak voltages of sinusoidal signals within the frequency range of 200 Hz and 100 kHz for several settings on the digital potentiometer for the single-ended (**Top**) and the differential (**Bottom**) outputs. The plotted values represent the mean peak-to-peak voltage measured and the error bars indicate the standard deviation of the measurements across all frequencies.

other hand, harmonic distortion can also arise from interactions between the amplitude levels of the input signal and the resolution limitations of the equipment. When the signal's amplitude is low relative to the resolution, nonlinear effects can occur, leading to the generation of additional harmonic components in the quantized signal.

A simple way to understand this is by simulating a sine wave signal with a few LSB of amplitude and its corresponding quantized signal, as shown in [131]. In this case, the quantized signal takes on a rectangular shape, with the fundamental frequency matching that of the sine wave. Consequently, the frequency components of the quantized signal include the fundamental frequency and all associated odd harmonics.

The effect of quantization noise can be mitigated through techniques such as dithering [132]. By adding a small, random noise prior to quantization, dithering decorrelates the signal from the quantization error, smoothing out the step effects caused by quantiza-

tion. This process transforms harmonic distortion into a white noise background, which, while still present, prevents the concentration of noise power at specific frequencies.

Harmonic distortion due to quantization overlaps with the signal's harmonics, preventing accurate characterization. The behavior of quantization noise, which can vary based on the signal's amplitude and the system's resolution, underscores the need for high-bit-resolution equipment to prevent significant artifacts from being introduced into the spectrum during digitization. Fig.6.4 shows the observed increase in odd harmonics due to quantization effects using the DPO 7104.

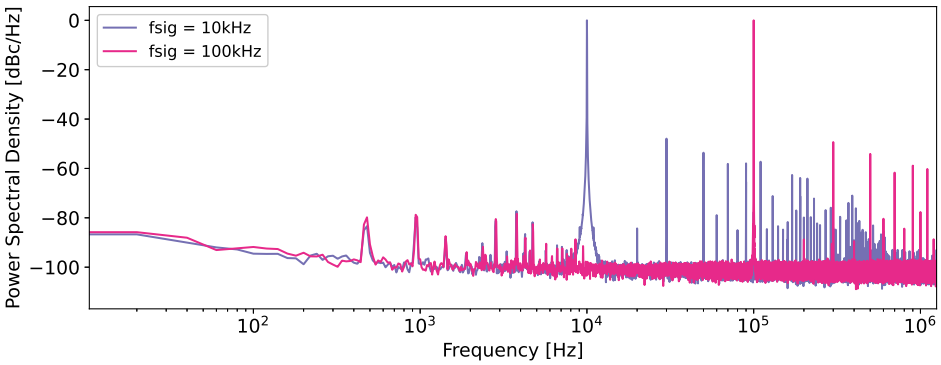


**Figure 6.4:** Effect of harmonic distortion caused by quantization. The cases of generating sinusoidal waves at 10 kHz and 100 kHz are presented, where a harmonic distortion of more than −50 dBc/Hz is observed in the worst-case scenario for both signals.

Furthermore, spectrum analyzers also present challenges in characterizing base-band low-noise signals, especially given the presence of phase noise around DC as a consequence of the internal mixing that degrades the measurement quality, making it difficult to distinguish the true characteristics of the original signal. For example, the Agilent N9000A analyzer [133] has a relatively high phase noise from 0 Hz up to several MHz compared to higher frequency bands, which impacts its ability to characterize the MSS board at the required sensitivity. Fig.6.5 illustrates the analyzer's baseline, demonstrating its limitations in low-frequency applications. In addition, the analyzer is specified for the range of 9 kHz to 9 GHz, making it unsuitable for the intended frequencies below 9 kHz to be characterized.

Besides, the harmonic distortion of the spectrum analyzer plays a critical role when evaluating the spurious performance of the DAC. It is possible that the noise or various spurious components measured are actually due to the spectrum analyzer itself. It is possible to mitigate these effects through the internal attenuator, however, this impacts the characterization of the signal noise. Depending on the DAC's performance, different methods may be required for accurate measurement.

This comprehensive approach to signal characterization highlights the critical importance of selecting equipment with the appropriate resolution and noise floor specifications to accurately evaluate low-noise signals. To best fit these requirements, the commercial Red Pitaya (RP) 125-14 platform [134] was chosen for characterization. Although its 14-bit ADC resolution does not fully capture the theoretical 16-bit performance of the

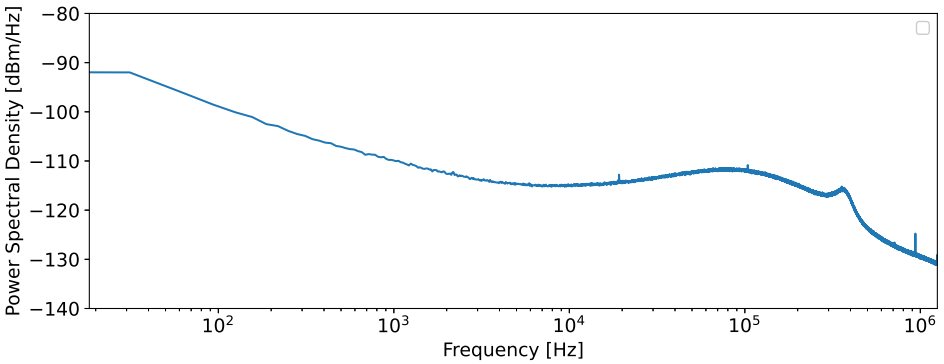


**Figure 6.5:** N9000A spectrum analyzer baseline noise.

MAX5891, it provides DC-coupled inputs and is more suitable than the Tektronix DPO 7104 and the Agilent N9000A. This measurement allows a reliable upper-limit assessment of the noise present in the signal generated by the MSS board.

The firmware image used in the RP was obtained from an open-source project [135] that allows for continuous signal acquisition, which is not possible with the image downloaded from the RP website. Through the prescaler set value P, the measurement bandwidth of the signal can be selected, which is initially sampled at 125 Msps. In this way, the signal is downsampled to $f_s^{\mathrm{RP}} = 125/\mathrm{P}\,\mathrm{Msps}$.

Fig.6.6 top depicts the RP baseline from the difference between the two inputs loaded with 50 Ω while acquiring $1.250 \times 10^9$ samples per input and setting P = 50. The 50 Hz residential line signal and its harmonics adversely interfere with the board's baseline. To address this issue, the board was shielded to ground with aluminum tape, as shown in Fig.6.6 bottom, resulting in significant improvements.

The theoretical noise of both the DAC and ADC are also displayed in Fig.6.6 for reference. The DAC noise is calculated from Eq. 4.7 as

$$\begin{aligned} S_{\mathrm{MAX5891}}\Big|_{\mathrm{dBm}} &= 1\,\mathrm{dBm} - \mathrm{SNR}_{\mathrm{dB}} - 10\log_{10}\left(\frac{f_s^{\mathrm{MAX5891}}}{2}\right) - 10\log_{10}\left(\frac{f_s^{\mathrm{MAX5891}}}{2f_{c,2}}\right) \\ &= -172.6\frac{\mathrm{dBm}}{\mathrm{Hz}}\ , \end{aligned} \tag{6.2}$$

with the last factor on the right-hand side of Eq.6.2 representing the effect of the LPF2 filter applied at the output of the MSS board, which is similar to the processing gain in digital signals as outlined in Eq. 3.54. For the ADC, the noise is derived from Eq. 3.41 as

$$S_{\mathrm{RP}}\Big|_{\mathrm{dBm}} = 10\log_{10}\left(\frac{q^2}{12}\cdot\frac{1}{Z_{\mathrm{in}}\cdot 1\,\mathrm{mW}}\right) - 10\log_{10}\left(\frac{f_s^{\mathrm{RP}}}{2}\right) - 10\log_{10}\left(\frac{f_s^{\mathrm{RP}}}{2f_{c,\mathrm{RP}}}\right)\ , \tag{6.3}$$

where $Z_{\mathrm{in}}$ denotes the converter input load. The image implemented on the RP includes a digital filter with a cutoff frequency around $f_{c,\mathrm{RP}} = 1\,\mathrm{MHz}$, which provides a

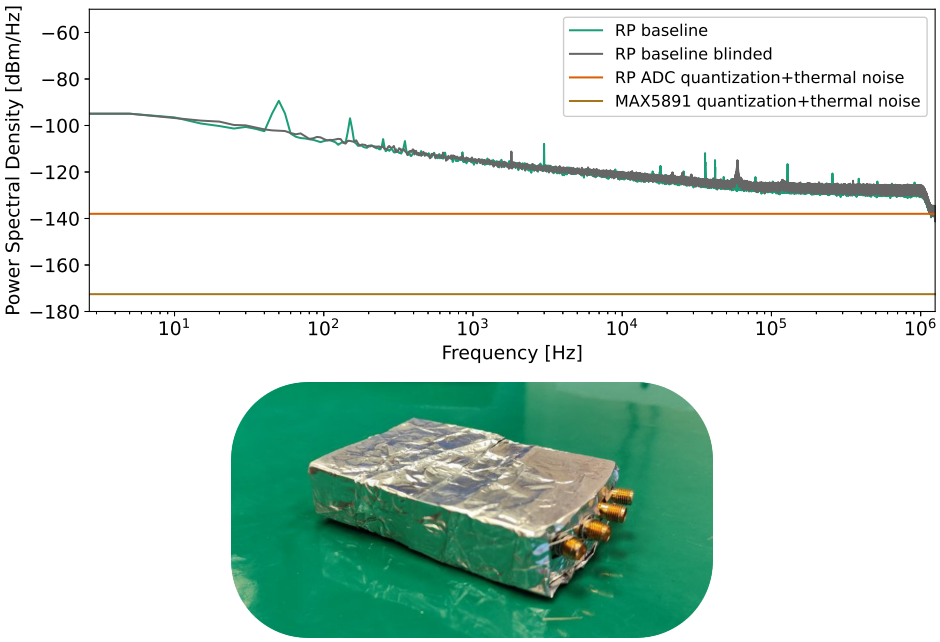


**Figure 6.6:** (**Top**) Red Pitaya differential signal baseline. 50 traces of $25 \times 10^6$ samples were averaged for each input, prior to performing the subtraction. The difference between the baseline with the shielded and unshielded RP can be observed, where in the first case, 50 Hz line interference and other sources are effectively mitigated. Additionally, the theoretical quantization noise level combined with thermal noise is plotted for the 14-bit ADC used in the RP and for the MAX5891 DAC on the MSS board. (**Bottom**) Photo of the RP shielded to ground utilizing aluminum tape.

processing gain of 1 dB. The quantized step size of the converter $q = V_{\mathrm{FS}}/2^{\mathrm{N}}$ is determined by the dynamic range at the RP's input, with $N = 14$ representing the converter's bit depth. The dynamic range can be configured between ±20 V and ±1 V using jumpers, with the latter being the configuration used. In SE measurements, $q = 122.07\,\mu\mathrm{V}$ and $Z_{\mathrm{in}} = 50\,\Omega$, resulting in a quantized noise of −141dBm/Hz. In contrast, $q = 244.14\,\mu\mathrm{V}$ and $Z_{\mathrm{in}} = 100\,\Omega$ for differential measurements, leading to a noise of −138dBm/Hz. The quantization noise is then added quadratically to the thermal noise at room temperature.

The measurement setup is illustrated in Fig.6.7. Given the RP's high input impedance, an SMA tee connector is employed to load the MSS output with 50 Ω. Measurements were conducted generating a differential signal and single-ended signals at 0 dBFS, −1 dBFS, −3 dBFS, −6 dBFS and −12 dBFS for two full-scale current values of 20 mA and 2 mA. The characterization is performed by selecting the LPF2 filter, explained in Sect. 4.3.3. For all measurements, the spectral noise level, the SFDR and the Total Harmonic Distortion (THD) were calculated. Fig.6.8 shows the signal spectra of sinusoidal signals within the frequency range of 200 Hz to 100 kHz for the 0 dBFS case.

Fig. 6.9 presents the results of the dynamic performance analysis for the differential output of the MSS board. It presents a high spectral purity level of 80 dBc/Hz. The calculated THD, accounting for all visible harmonics in the spectrum, indicates high

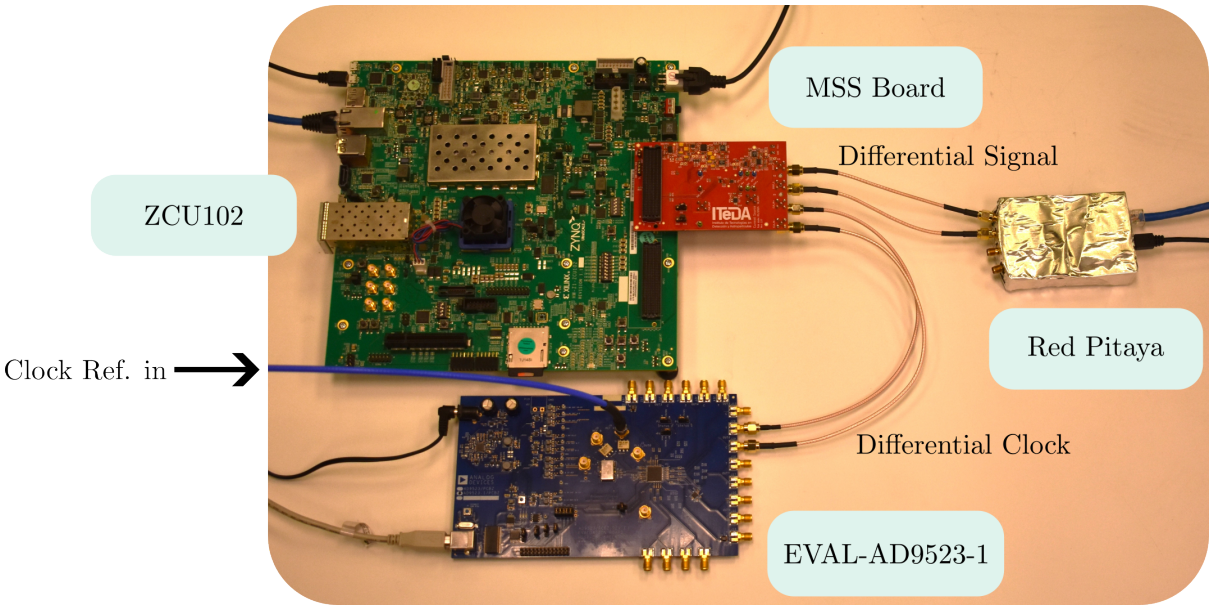


**Figure 6.7:** The measurement setup used for characterizing the MSS board. The MSS board is connected to the J5 port of the ZCU102. The EVAL-AD9523-1 board provides the differential clock for signal generation, which is then acquired by the RP. A signal generator is used as the reference for the clock synthesizer board.

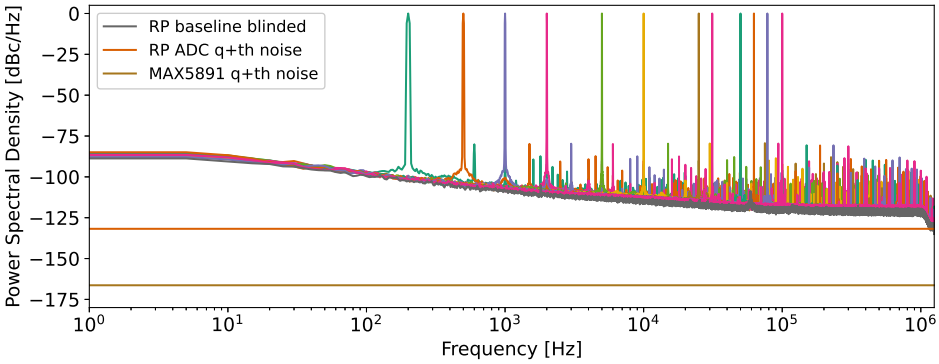


**Figure 6.8:** Spectra of multiple differential signals generated between 200 Hz and 100 kHz at 0 dBFS for an $I_{FS}$ = 20mA. The baseline noise of the Red Pitaya is also plotted in gray. It can be observed that the noise floor in all cases aligns with that of the Red Pitaya, indicating that the generation noise is well below this level. The theoretical noise of the DAC and ADC are plotted for reference.

performance, staying below 0.15% in all cases.

The strong performance is also related to the intrinsic rejection of even-order harmonics when working with differential signals. For example, in the case of a second-order signal:

$$y(t) = \alpha_1 x(t) + \alpha_2 x(t)^2 \ . \tag{6.4}$$

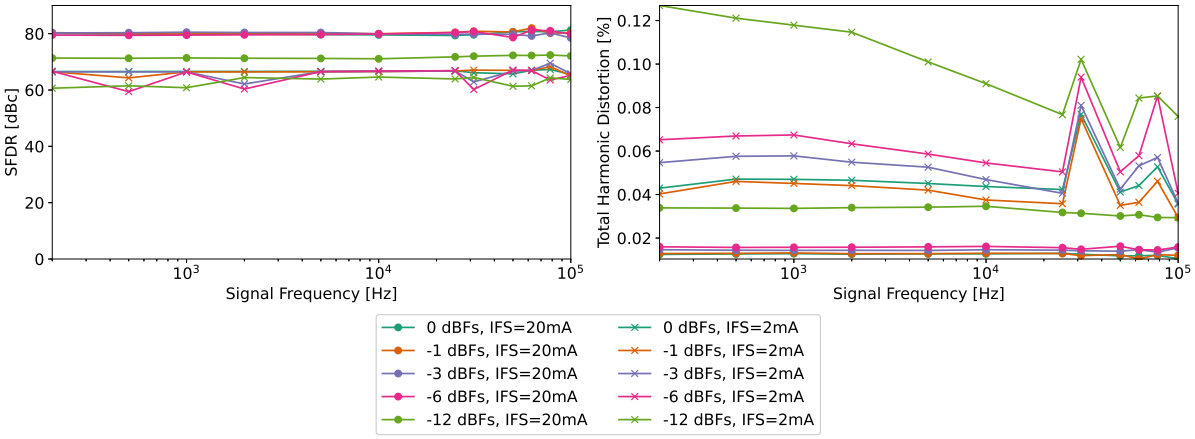


**Figure 6.9:** MSS board dynamic performance of the differential output. (**Left**) The SFDR measured across the entire bandwidth as a function of the generated signal frequency. In all cases, the spectral purity exceeds 60 dBc/Hz, reaching over 80 dBc/Hz for signals at or higher than −6 dBFS at $I_{\mathrm{FS}} = 20\,\mathrm{mA}$. (**Right**) The THD as a function of the generated signal frequency remains below 0.15% in all cases. For signals at or above −3 dBFS at $I_{\mathrm{FS}} = 20\,\mathrm{mA}$, the THD does not exceed 0.015%.

By using differential signals $x(t)$ and $-x(t)$ the resulting outputs yields

$$\begin{aligned} y_1(t) - y_2(t) &= \alpha_1 x(t) + \alpha_2 x(t)^2 - (-\alpha_1 x(t) + \alpha_2 x(t)^2) \\ &= 2\alpha_1 x(t) \ . \end{aligned} \tag{6.5}$$

Due to the output stage circuit designed in the single-ended output of the MSS board, this characteristic is lost, which is reflected in the results shown in Fig. 6.10.

The total Noise Power is dominated by the RP setting an upper-limit. Even after modifying the setup by adding a Gali-84+ amplifier with a gain of approximately 26 dB [136] to the SE output or both differential outputs, the noise continued to be dominated by the RP, as shown in Fig. 6.11 for the SE case. It is important to note that the amplifier used, being AC-coupled, has a cutoff frequency around 40 kHz. To measure the amplified signal, the RP dynamic range was adjusted to ±20 V. In this case, the RP was not shielded, which allowed 50 Hz interference and its harmonics to be noticeable.

The signal in the modulation line must be carefully designed to ensure that noise does not impair the performance of the $\mu$MUX. To obtain the modulation signal flux noise, it is essential to account for the design of the cryogenic setup (refer to Sect. 4), considering the attenuation of each line. Additionally, an extra 26 dB attenuation was considered given that the noise floor of the MSS board is at least that much lower than that of the Red Pitaya. Consequently, the theoretical flux noise establishes the upper limit of the expected noise in the $\mu$MUX. Fig. 6.12 shows the magnetic flux noise for the single-ended and differential signals. It can be observed that the noise is below the simulated total magnetic flux noise of the MMB in the antenna-coupled condition (see Fig. 2.7). This

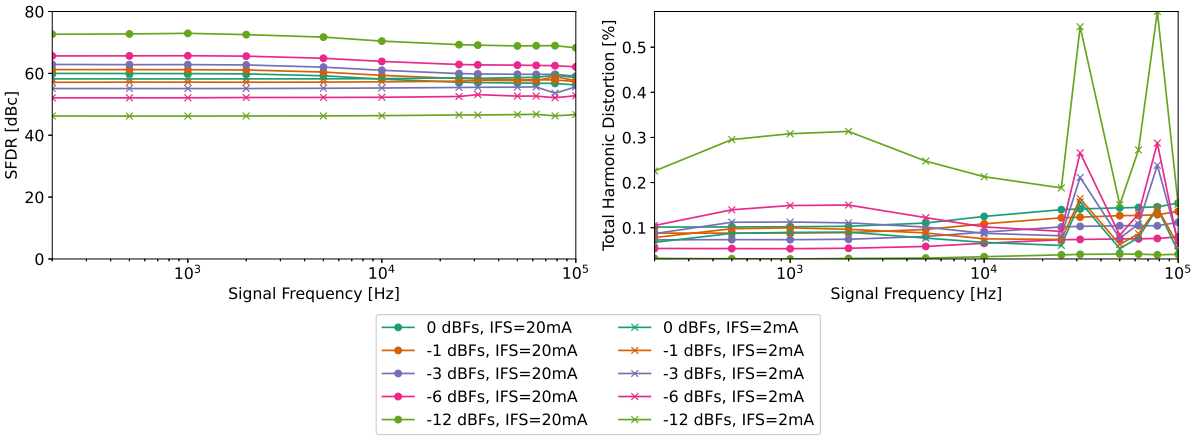


**Figure 6.10:** MSS board dynamic performance of the SE output. (**Left**) The SFDR measured across the entire bandwidth as a function of the signal frequency. Unlike the differential signal, the second harmonic does not cancel out and degrades performance. (**Right**) The THD as a function of the signal frequency.

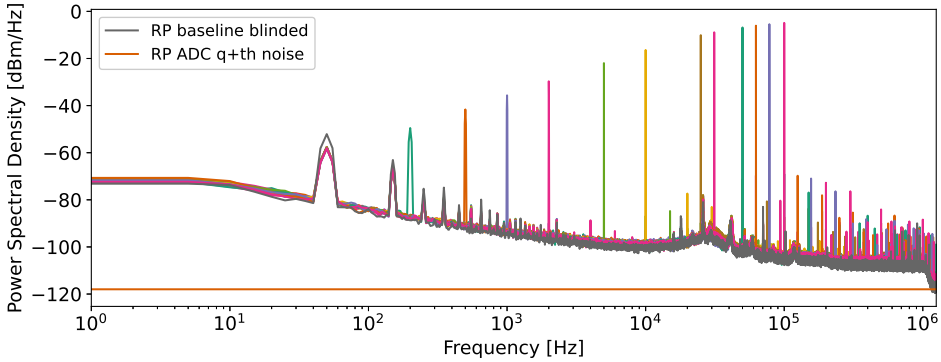


**Figure 6.11:** MSS board SE signal with a $I_{\mathrm{FS}} = 20\,\mathrm{mA}$, amplified by 26 dB using the Gali-84+. The signal was captured using an unshielded RP which baseline noise shown in gray.

suggests, a priori, that the MSS board does not affect the system's noise if it is dominated by the detector noise.

## 6.2 Flux Ramp Demodulator Characterization

### 6.2.1 Microwave SQUID Multiplexer Emulator

To evaluate the proper operation of the FRD, a Notch resonator was designed to emulate the behavior of a $\mu$MUX channel. The characterization is performed in an emulator due to the ease of conducting measurements in a more controlled environment, which is less susceptible to external interferences. The resonator feature structural similarities to a

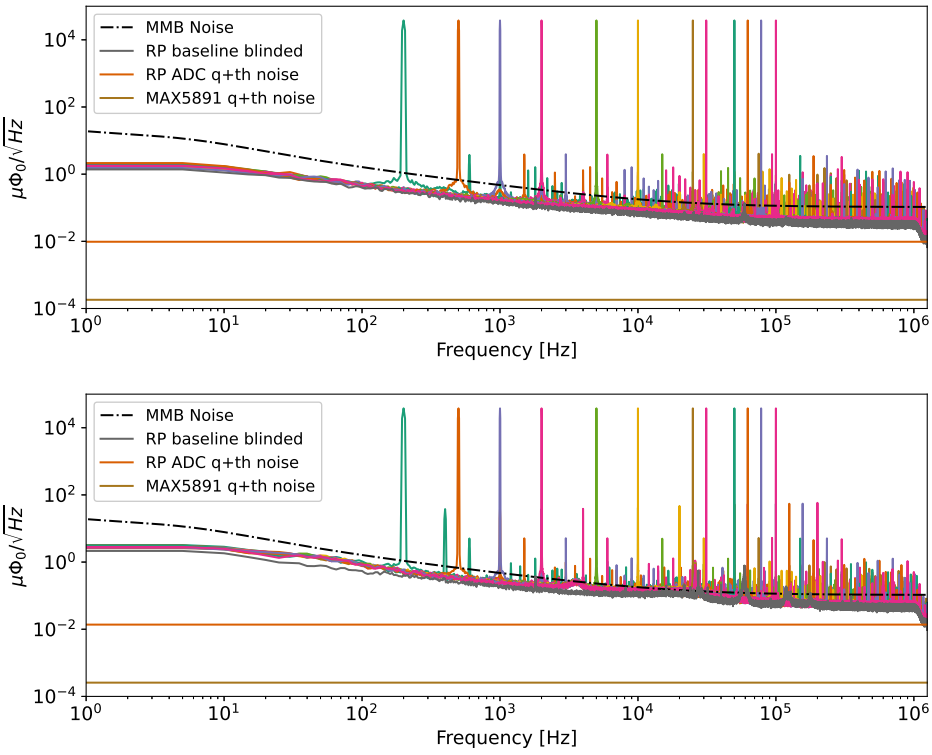


**Figure 6.12:** MSS board signal in magnetic flux density for the differential (**Top**) and SE (**Bottom**) outputs. The signals were generated at 0 dBFS.

$\mu$MUX superconducting channel. Specifically, it consists of two ports connected by a microstrip transmission line with a characteristic impedance of $Z_0 = 50\,\Omega$, serving as the input and output paths for the readout signal. The transmission line is also coupled to a half-wavelength resonant line terminated with a Pi filter, composed of two capacitors and an inductor, as depicted in Fig. 6.13 left.

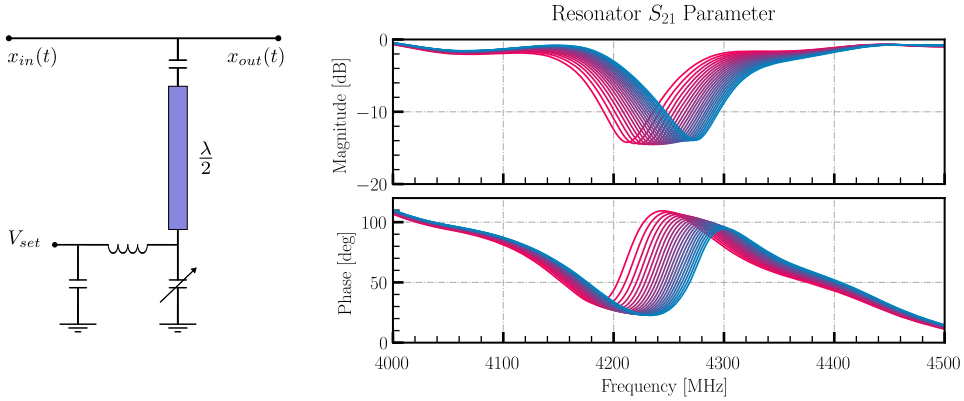


**Figure 6.13:** (**Left**) Room temperature Notch resonator using a varicap to emulate a $\mu$MUX channel. (**Right**) Notch resonator frequency response with the set voltage $V_{\text{set}}$ varying from 0 VDC to 10 VDC in steps of 0.5 VDC.

In particular, one of the capacitors is a varicap, which allows its capacitance to be adjusted by applying a DC voltage $V_{\text{set}}$ through a third port on the resonator. In Fig. 6.13 right illustrates its frequency response, showcasing a bandwidth of 120 MHz and a resonance frequency of 4.2 GHz at $V_{\text{set}} = 0$.

The complete measurement setup, as detailed in Fig. 6.14, includes a Picotest G5100A [137], which is an arbitrary waveform generator (AWG). Using this generator, a phase-modulated signal is synthesized to emulate the rf-SQUID signal, enabling its subsequent demodulation by the FRD.

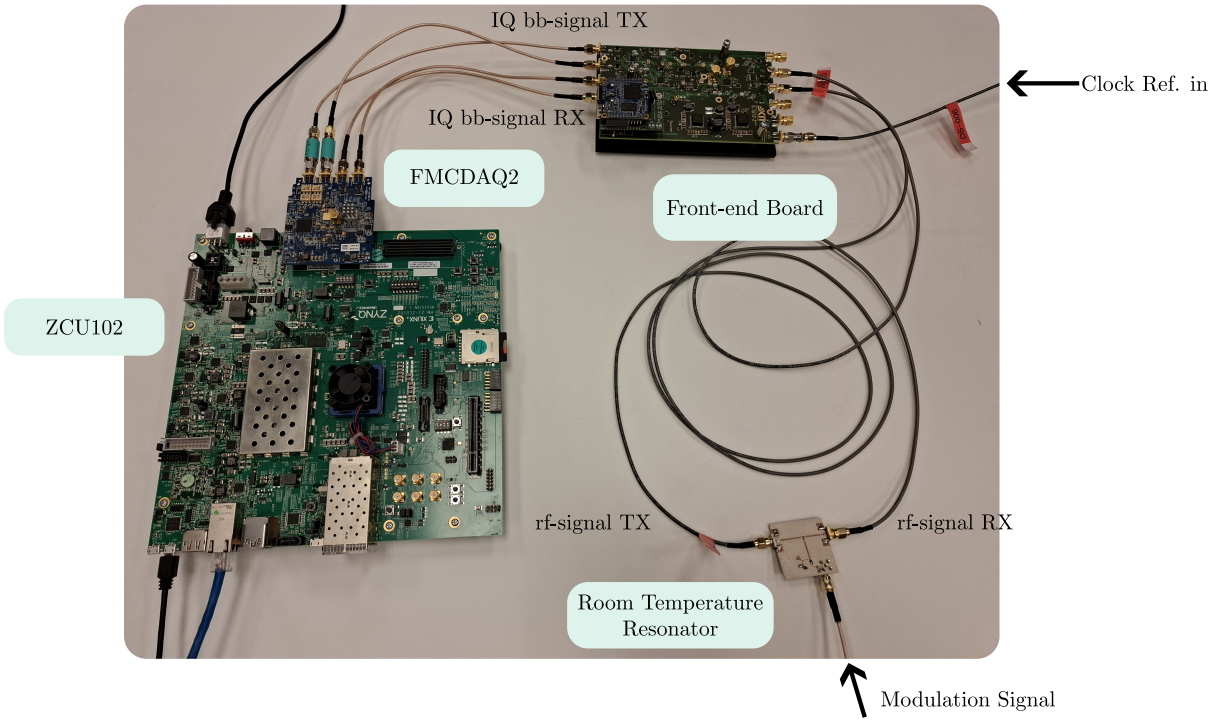


**Figure 6.14:** Setup for the room temperature resonator Readout. The modulation line is connected to the Picotest AWG. A 10 MHz clock reference is connected to the FE board.

### 6.2.2 Signal Recovery

The measurement was undertaken by generating four readout tones at frequencies of 4.16 GHz, 4.20 GHz, 4.24 GHz and 4.28 GHz. The FE local oscillator was set to 4.4 GHz, resulting in base-band readout tones at −240 MHz, −200 MHz, −160 MHz and −120 MHz after down-conversion. For signal acquisition, the DDCs were configured to center frequencies of 109.25 MHz, 78.125 MHz, 46.875 MHz and −15.625 MHz. Additionally, the GFs were set to 5.625 MHz, −3.125 MHz, −11.875 MHz and 10.625 MHz, respectively.

To modulate the resonator, three separate measurements were conducted. For each measurement, a sinusoidal signal was synthesized using the Picotest with a peak-to-peak amplitude of 4 $V_{\text{pp}}$ and centered at 4 $V_{\text{DC}}$ to drive the $V_{\text{set}}$ input of the resonator. The

sinusoidal signal was set to frequencies of 15 258.78 Hz, 30 517.57 Hz and 61 035.15 Hz, respectively, for each of the three cases. Additionally, in each measurement, this sinusoidal signal was phase-modulated with another waveform that varied in frequency, amplitude and shape, introducing additional modulation complexity.

The resulting spectra at the output of the resonator is presented in Fig. 6.15, which shows the signal spectrum measured using a spectrum analyzer.

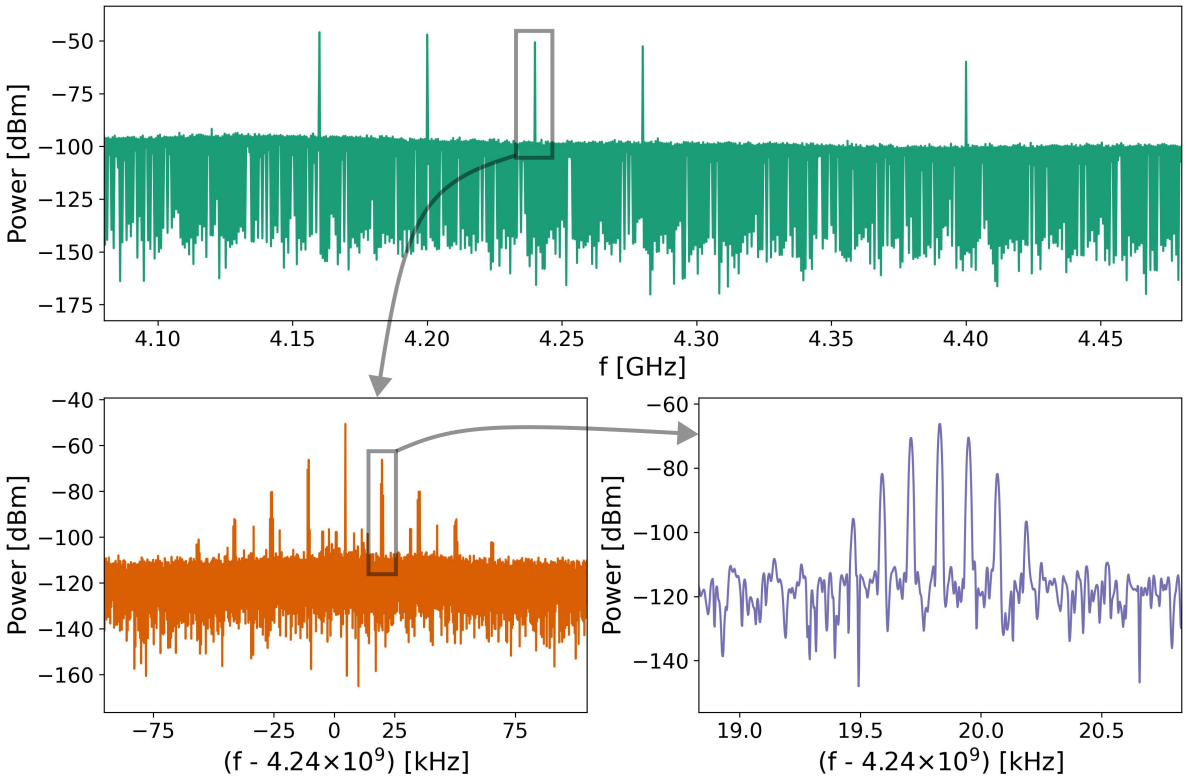


**Figure 6.15:** (**Top**) Readout signal spectrum at the resonator output. Four readout tones are generated at 4.16 GHz, 4.20 GHz, 4.24 GHz and 4.28 GHz, along with the local oscillator at 4.4 GHz. All tones are modulated by a phase-modulated signal with a carrier frequency of 15 258.8 Hz and a modulation frequency of 119.2 Hz and a 60° phase-deviation.(**Bottom-left**) A zoomed-in view around the 4.24 GHz tone and its phase-modulation Bessel components separated every 15 258.8 Hz. (**Bottom-right**) A close-up of one of the Bessel components, with additional Bessel components appearing as a result of the 119.2 Hz modulating signal.

The demodulation results are shown in Fig. 6.16. Several scenarios were tested, including monotonal signals at different frequencies, as well as signals with higher harmonic content or abrupt changes, such as triangular and rectangular waveforms. In all cases, the demodulated signal was adjusted and the residuals were computed. The results consistently demonstrated that the system is highly reliable, successfully recovering the emulated signal from the detector with a high degree of fidelity.

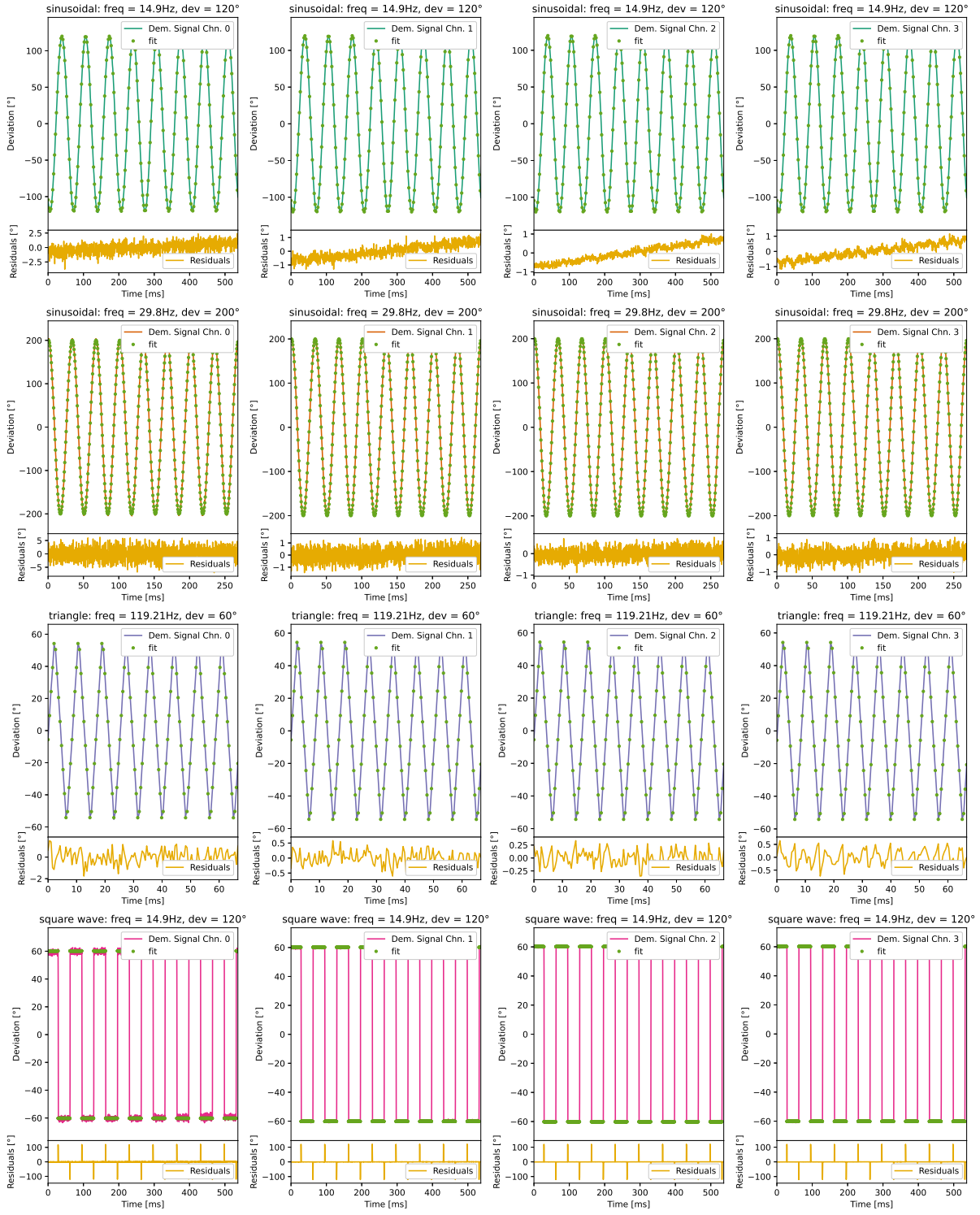


**Figure 6.16:** Demonstration of the prototype system's capability to obtain signals across 4 channels. Different signals emulating the detector signal were generated in various configurations using sinusoidal, triangular and square waveforms.

Although the results obtained visually appear to be satisfactory, it is important to spectrally characterize the signals to assess the noise introduced by the FRD. To achieve this, the system is first configured with the FRD disabled, allowing the signal to be obtained directly from the output of the GF. In this configuration, offline demodulation is performed using floating-point arithmetic, providing a high-precision reference for comparison. The results of this demodulation process are then compared with the signals demodulated using channel 0 (see in Fig. 6.16). The corresponding outcomes are presented in Fig. 6.17, clearly illustrating the differences in signal quality between the two methods.

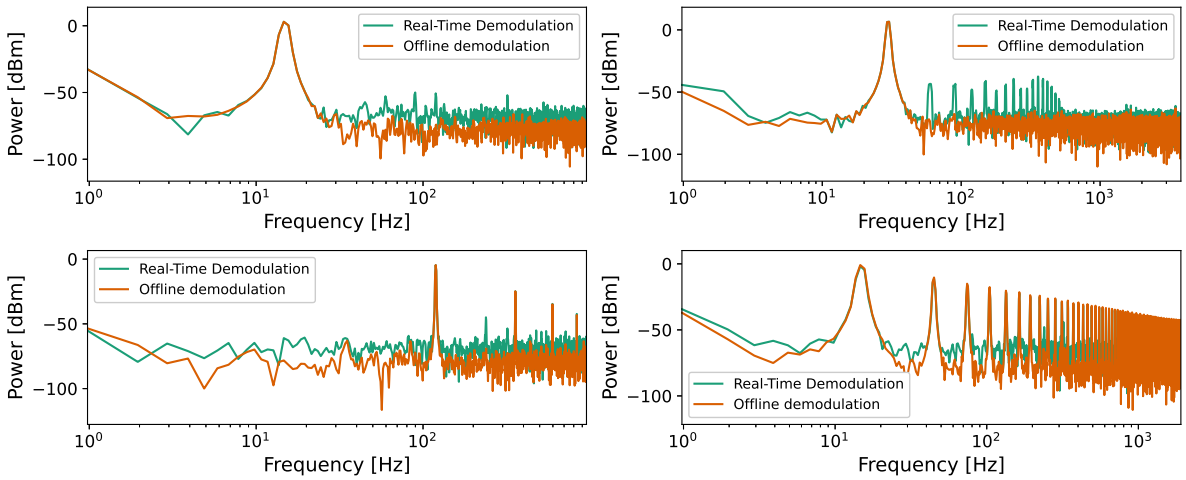


**Figure 6.17:** Comparison of the FRD implemented using a 16-bit fixed-point DDS with an post-processing offline demodulation using floating-point. Spurious signals and noise degradation are observed in the former, which is attributed to the quantization of the DDS stage in the FRD module.

Upon analysis, significant degradation in the noise floor is observed, indicating that the FRD introduces additional noise to the system. Furthermore, spurious signals are observed in the demodulated output. This increase in noise and the appearance of spurious signals was primarily attributed to the quantization of the DDS, which was implemented using 16-bit fixed-point arithmetic. Increasing the DDS by 2 bits helps mitigate the issue, as shown in Fig. 6.18. It is evident that the FRD no longer affects the noise at the output of the GF or boost unwanted signals power.

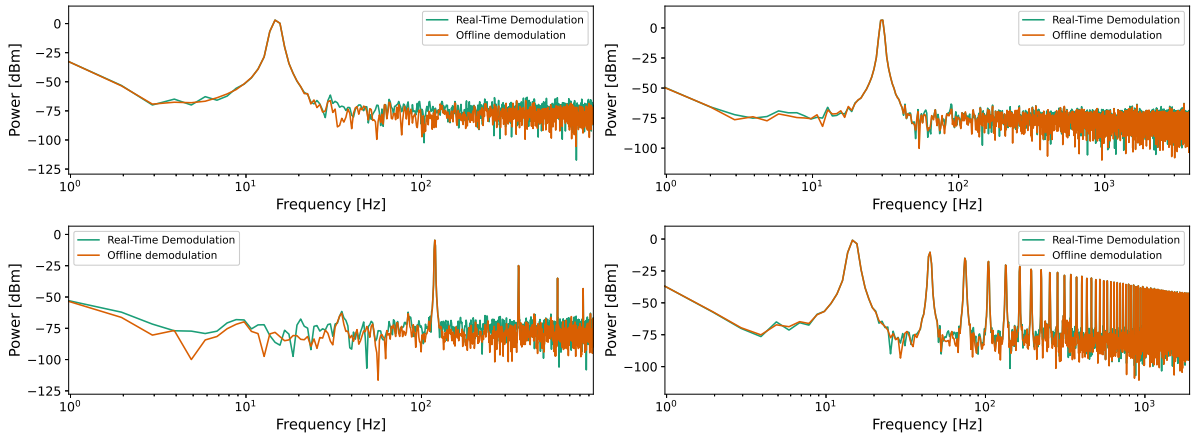


**Figure 6.18:** Comparison of the FRD implemented using a 18-bit fixed-point DDS with an post-processing offline demodulation using floating-point. Unlike the 16-bit implementation, the FRD module neither degrades the output signal noise nor increases the power of spurious signals.

# Chapter 7

# Prototype Readout System Measurements

The measurements conducted in this section aim to verify the correct operation of the prototype system (see Section 6) for $\mu$MUX readout. Initially, the $\mu$MUX channels are identified within the spectrum by measuring their transmission parameter, $s_{21}$. This process involves performing a frequency sweep to detect the resonance frequencies of the channels, which are characterized by distinct peaks in the magnitude of $s_{21}$.

Then, the $\mu$MUX channels are characterized in order to set the appropriate parameters for optimal measurement. By analyzing the frequency response to the magnetic flux of the channels, it is possible to extract their characteristic parameters, such as resonance frequencies, bandwidth and quality factors.

Next, a simplified analysis is carried out using the prototype system to determine the optimal point for channel readout. Although the optimal point may vary depending on system or application-specific requirements, in this work, the measurement parameters are optimized by evaluating the SNR of the detector's output. By computing the SNR under various conditions, the system parameters can be adjusted to enhance the detector signal.

Once the optimal measurement point is established, demodulated data from the characterized channels are collected to demonstrate the proper functionality of the system. The extracted signal is an emulation of the detector's output, which is combined with the FR. This combined signal is generated using the MSS board. Lastly, a comparative analysis of the demodulated noise is performed across different stages of the system. This comparison allows for assessing the noise performance at each stage.

The cryogenic setup used for these measurements is depicted in Fig. 7.1. The cryostat is a Bluefors LD250 model [138], equipped with five thermal stages: 50K, 4K, Still Plate, Cold Plate and Mixing Chamber. Each signal line is fitted with attenuators attached to each stage, which not only aid in thermalization but also condition the signal to the appropriate levels.

The readout line features 40 dB attenuation during transmission and 40 dB gain during reception that are achieved using a LNA LNF-LNC4_8F [139] mounted at the 4K stage. A circulator installed in the system prevents signal reflections back to the $\mu$MUX.

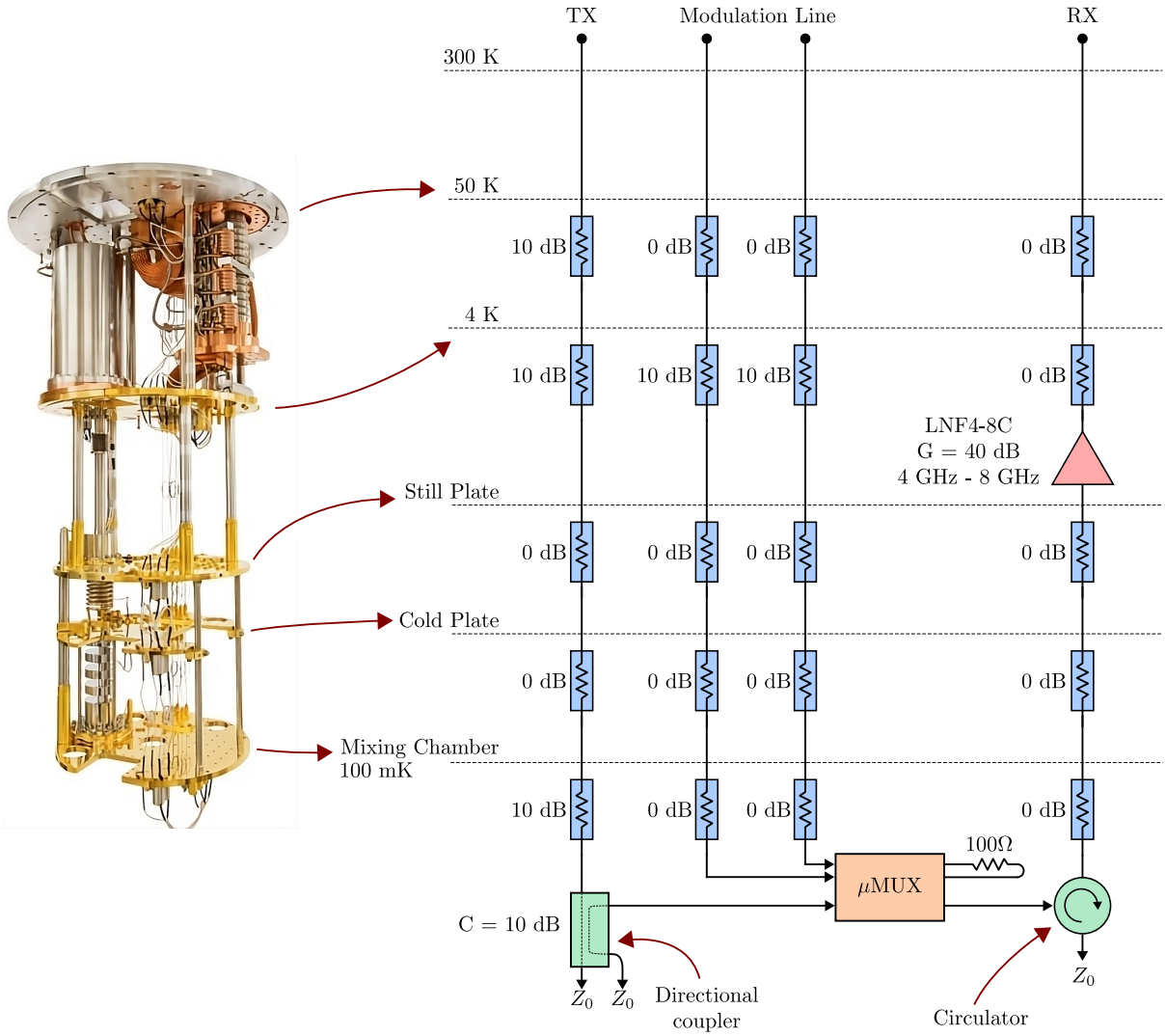


**Figure 7.1:** Cryogenic Setup for $\mu$MUX measurements.

Additionally, the cables introduce an extra 20 dB of attenuation throughout the circuit, resulting in a signal that exits the cryostat with a total net attenuation of 20 dB when it is outside a $\mu$MUX channel bandwidth. For this work, the modulation line was configured differentially, with a total attenuation of 10 dB and a termination load of 100 Ω.

Since the measurements were conducted with 4 readout tones with $P_{\text{exc}} = -25\,\text{dBm}$ each, the maximum total power at the LNA input is −70 dBm, which is several decades below the input compression point P1dB and the input third-order intercept point IIP3.

## 7.1 Microwave SQUID Multiplexer Characterization

The designed $\mu$MUX system comprises of 16 channels, each operating in the frequency range of 5.8 GHz to 6.4 GHz, with an approximate spacing of 33 MHz between adjacent channels. This configuration is compatible with the 800 MHz bandwidth of the RTE.

Each individual channel was designed with a bandwidth of 200 kHz. This results in a ratio of $f_{\text{sep}}/BW_{\text{res}} = 165$ and consequently, a crosstalk level much lower than 0.1% [89] is expected. Furthermore, the $\mu$MUX channels are designed with a normalized current-flux transfer coefficient of $\gamma_{\text{mod}} = 1/M_{\text{mod}} = 436.5\,\mu\text{A}/\Phi_0$. A photograph of the $\mu$MUX mounted on a sample holder, along with its corresponding transmission parameter $|s_{21}|$ measurement, is shown in Fig. 7.2. The measurements were conducted using the Keysight N5242B PNA-X [140] network analyzer.

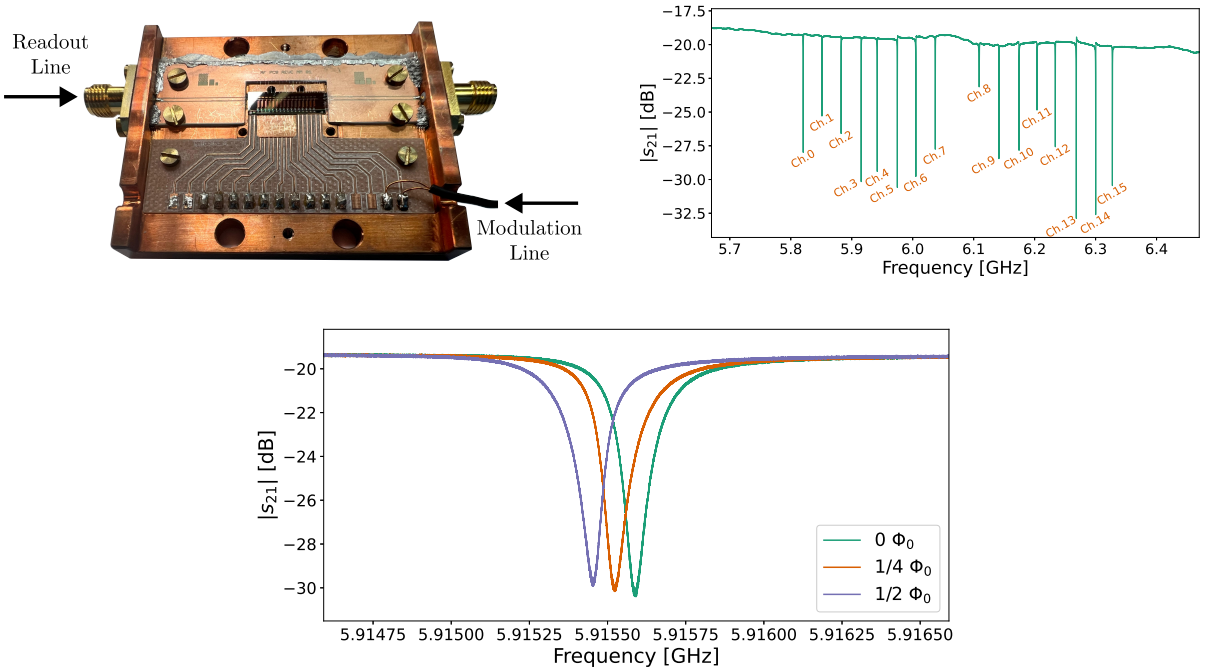


**Figure 7.2:** (**Top-left**) 16 channels $\mu$MUX located in the 5.8 GHz to 6.4 GHz band. The sample holder was designed to have its resonance frequencies outside of the $\mu$MUX band. (**Top-right**) Transmission coefficient of the $\mu$MUX. (**Bottom**) The frequency response of $\mu$MUX channel 5 in relation to the coupled magnetic flux quantum in the rf-SQUID

The dependence of the $\mu$MUX channels on the magnetic flux is also illustrated in Fig. 7.2 bottom. This dependence is periodic, as mathematically demonstrated in Section 3.1.3 and provides insight into the actual current-flux transfer coefficient and the value of $\eta$, which measures the relationship between the resonator bandwidth $BW_{\text{res}}$ and the peak-to-peak shift frequency $\Delta f_{\text{r}}^{\text{pp}}$. In Fig. 7.3, this dependence is depicted for channels 3, 4, 5 and 6. The measurements were performed using a DC current applied to the modulation line, which generated two magnetic flux quanta in the rf-SQUIDs. For each DC current value, the frequency response of the channels was obtained.

From the measurement results, the fixed resonance frequency $f_{\text{r},0}$, the bandwidth of the resonators $BW_{\text{res}}$, the minimum $f_{\text{r,min}}$ and maximum $f_{\text{r,max}}$ resonance frequencies, as well as the peak-to-peak shift of the resonance frequency $\Delta f_{\text{r}}^{\text{pp}}$, the $\eta$ factor, the resonance depth $|s_{21}^{\text{min}}|$ and the total quality factor $Q_{\text{l}}$, are derived. The results are shown in Table 7.1.

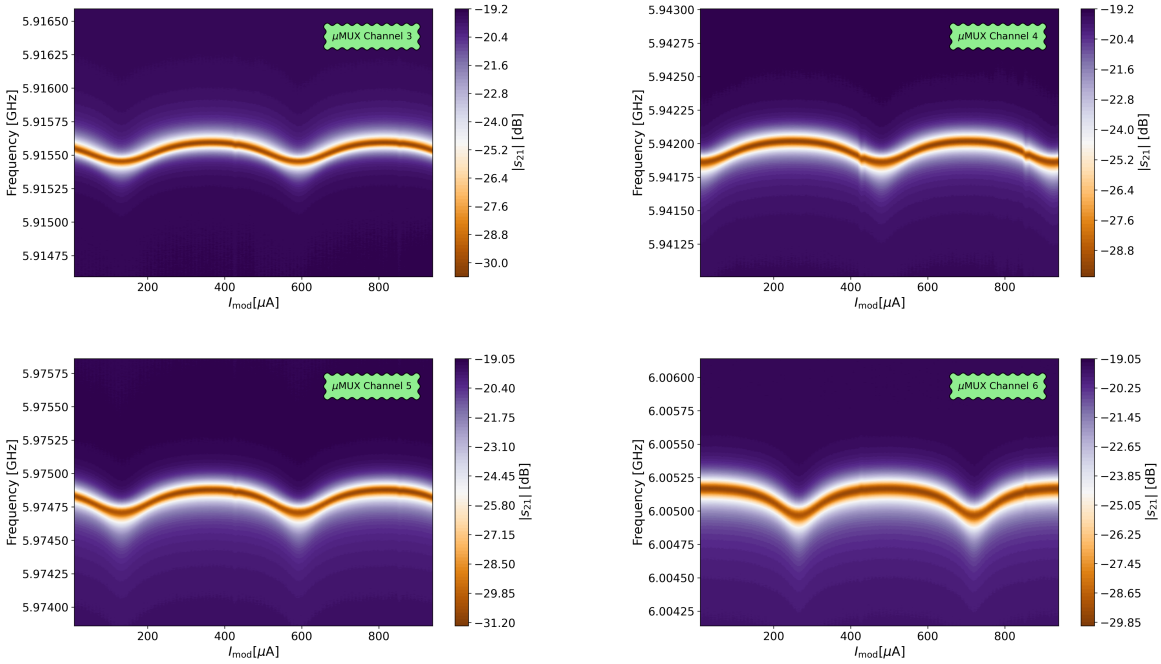


**Figure 7.3:** Periodic response of $\mu$MUX channels 3, 4, 5 and 6 as a function of modulation current. A readout tone power $P_{exc} = -25\,\text{dBm}$ was used for the measurements. For each DC current in the modulation line, the transmission of the channels was measured over a 2 MHz bandwidth around the maximum resonance frequencies.

| | Ch. 3 | Ch. 4 | Ch. 5 | Ch. 6 |
|---|---|---|---|---|
| $\lvert s_{21}^{\min}\rvert$ [dB] | -30.55 | -29.84 | -31.2 | -29.9 |
| $f_{r,0}$ [GHz] | 5.915534 | 5.941953 | 5.974811 | 6.005102 |
| $f_{r,\min}$ [GHz] | 5.915452 | 5.941858 | 5.974705 | 6.004965 |
| $f_{r,\max}$ [GHz] | 5.915596 | 5.942019 | 5.97488 | 6.005169 |
| $\Delta f_r^{pp}$ [kHz] | 143.72 | 160.26 | 174.42 | 204.2 |
| $BW_{res}$ [kHz] | 175 | 216.46 | 220.8 | 267.36 |
| $\eta$ | 0.82 | 0.74 | 0.79 | 0.764 |
| $Q_l$ | 33795 | 27450 | 27059 | 22460 |

**Table 7.1:** Parameters of the $\mu$MUX channels.

## 7.2 Optimal Readout Measurement Point

In order to optimize the system's performance, a multi-parametric sweep is performed to identify the optimal measurement point for each $\mu$MUX channel. This process involves

varying multiple parameters simultaneously, such as the readout tone frequency $f_{\mathrm{exc}}$ and modulation signal frequency $f_{\mathrm{mod}}$, to find the settings that maximize the detector signal's power while minimizing its noise.

Based on the parameters obtained for each channel, multiple data acquisitions are performed connecting the RTE to the cryogenic setup, as shown in Fig. 7.4. A 4-tone signal is generated to readout the 4 channels starting at the resonance frequency $f_{\mathrm{r},0}$ of each channel and gradually increasing in subsequent measurements up to $f_{\mathrm{r},0} + BW_{\mathrm{res}}/2$. A ramp modulation signal is generated on the MSS board, to which an emulated detector signal is added. Three different ramp modulation frequencies $f_{\mathrm{ramp}}$ are used: 15.258 kHz, 7.629 kHz and 3.814 kHz. For all cases, $N_{\Phi_0} = 4$ was set, resulting in modulation frequencies $f_{\mathrm{mod}}$ of 61 035.15 kHz, 30 517.6 kHz and 15 258.8 kHz, respectively. Finally, a modulated spectrum similar to the one shown in Fig. 6.15 is obtained.

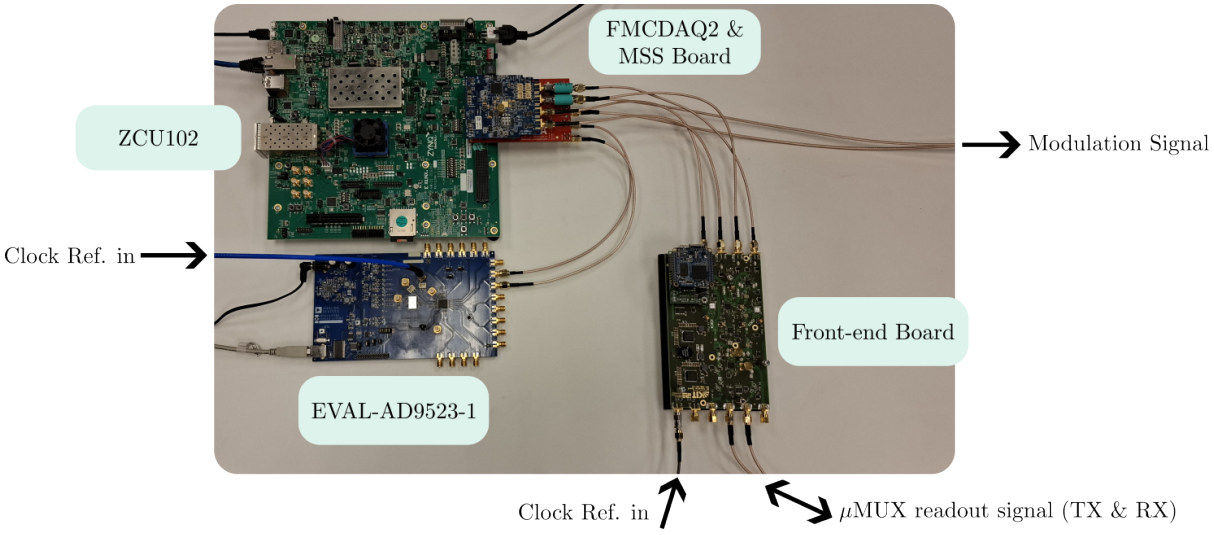


**Figure 7.4:** Room temperature setup for the $\mu$MUX readout. The 10 MHz clock reference is distributed to the EVAL-AD9523-1 board, which generates a cleaner clock signal for the MSS board. The same clock reference is shared with the FE board.

For each acquisition, the outputs of the 4 corresponding GFs are obtained and the SNR of the main sideband component generated by the detector around the fundamental frequency of the rf-SQUID signal are computed. As a result, the $f_{\mathrm{exc}}$ and $f_{\mathrm{mod}}$ which maximize the SNR of the detector's signal were obtained, as shown in Fig. 7.5.

Since 4 channels were measured, it is possible that each one has a different SNR value. However, the final result takes into account the worst SNR obtained from the 4 channels, thus setting a minimum SNR floor for each case.

The optimal point of SNR=49.43 dB is achieved for $f_{\mathrm{exc}} = f_{\mathrm{r},0} + 106\,811.52$ Hz and for $f_{\mathrm{mod}} = 61\,035.15$ Hz. This same analysis can be performed for the second harmonic of the rf-SQUID signal, with the results shown in Fig. 7.6.

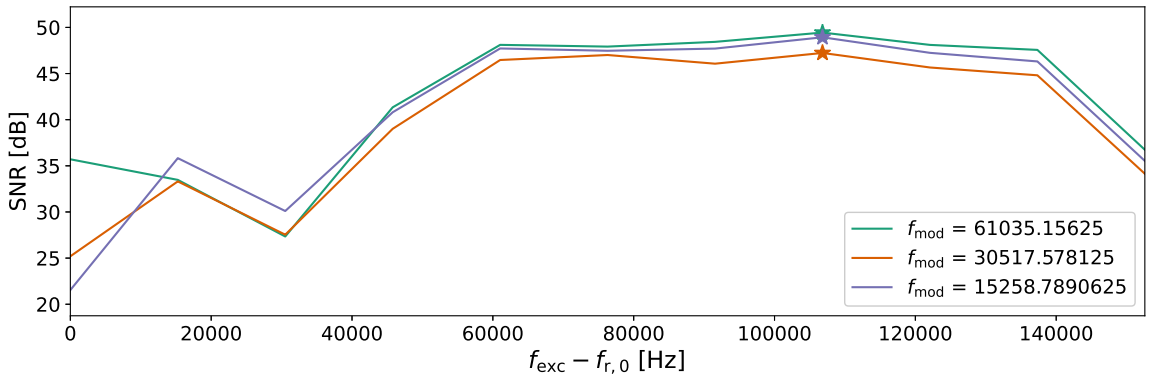


**Figure 7.5:** Optimal measurement point of the $\mu$MUX that maximizes the SNR of the detector's signal for different values of $f_{exc}$ and $f_{mod}$. Four $\mu$MUX channels were measured for each condition and the worst-case scenario was plotted.

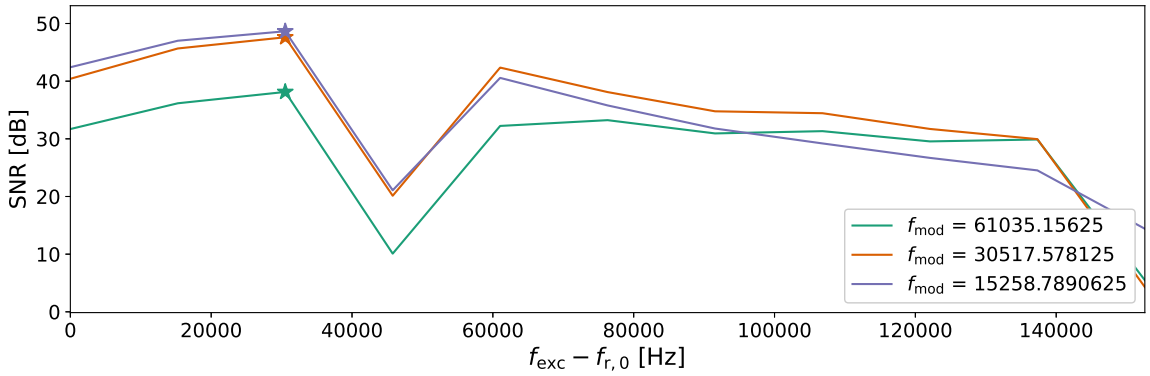


**Figure 7.6:** Optimal measurement point of the $\mu$MUX based on the SNR of the detector signal around the second harmonic of the rf-SQUID signal. Four $\mu$MUX channels were measured for each condition and the worst-case scenario was plotted.

## 7.3 Signal Recovery Capability

The performance of the system in demodulating 4 $\mu$MUX channels is shown in this section. To ensure optimal operation, the system was configured at the previously determined optimal measurement point, where the SNR is maximized for the channels under test. Therefore, the readout tones were synthesized at 5.915 641 GHz, 5.942 06 GHz, 5.974 917 GHz and 6.005 208 GHz.

For the purpose of this demonstration, the detector signal was emulated using two different signal types: a 238 Hz sinusoidal wave and a 476 Hz square wave. These signals were selected to test the system's ability to handle both smooth, continuous waveforms and more abrupt, multi-tonal signals.

The results of the demodulation for the 4 channels are presented in Fig. 7.7 for the 238 Hz sinusoidal signal and in Fig. 7.8 for the 476 Hz square wave.

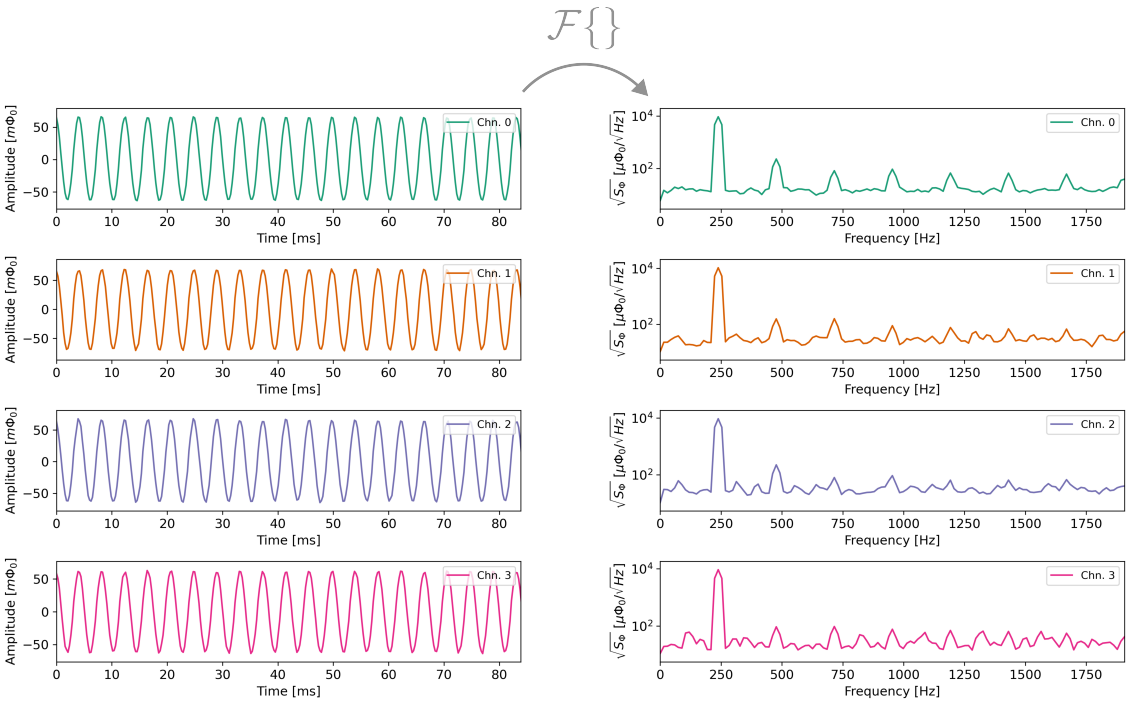


**Figure 7.7:** Readout system demonstration for recovering 4 single-tone 238 Hz sinusoidal signals.

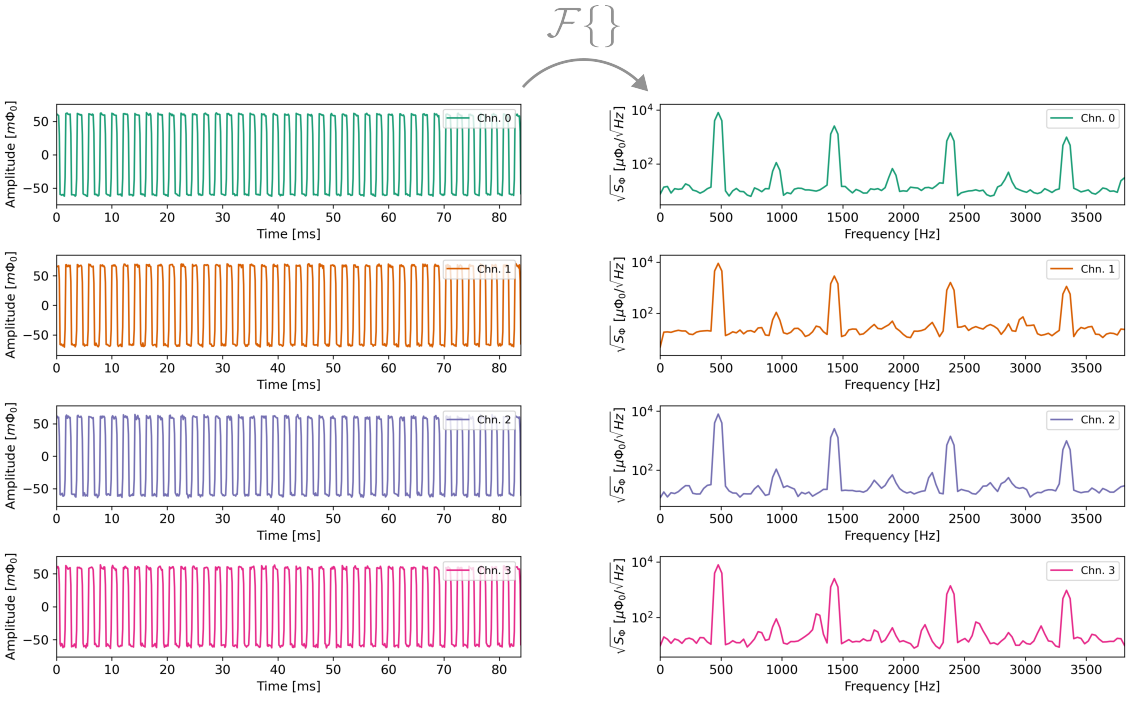


**Figure 7.8:** Readout system demonstration for recovering 4 multi-tonal 476 Hz square signals.

## 7.4 Noise Comparison

A comparison was performed to evaluate the flux noise generated by the RTE alone and the flux noise with the cryogenic setup connected. For this last case, measurements were taken both with and without the MSS board, as depicted in Fig. 7.9.

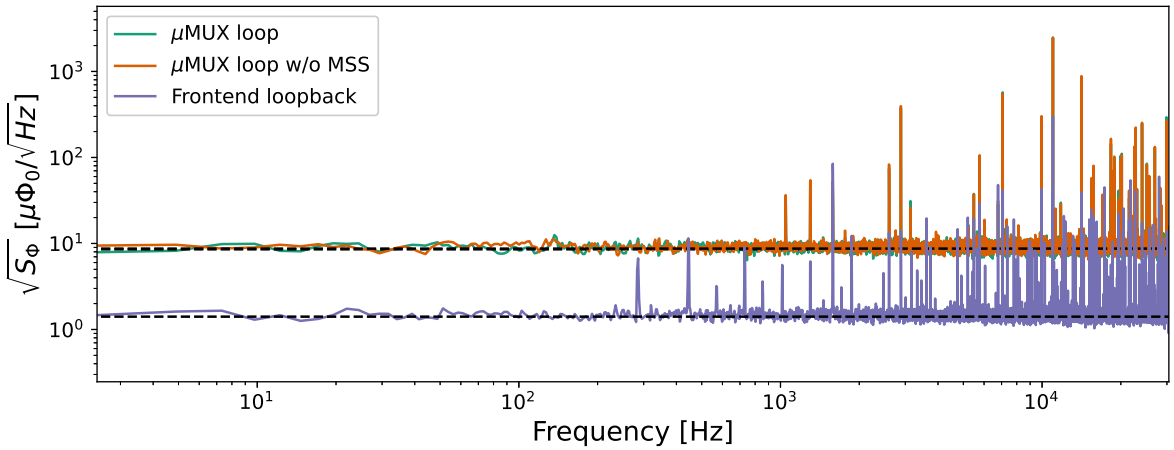


**Figure 7.9:** Comparison of demodulated magnetic flux noise for three scenarios: 1) Performing a loopback at the FE output, i.e. without the cryogenic circuit. 2) Including the cryogenic circuit with the MSS board connected. 3) Same as scenario 2) but with the modulation line input connected to two 50 Ω loads. In the first scenario, phase noise was demodulated and converted to magnetic flux for comparison with the flux obtained using the μMUX.

In the first case, a loopback was established at the FE output and the phase noise was acquired at one channel of the FRD module output. The measured phase noise was then converted to normalized equivalent magnetic flux noise by dividing by $2\pi$.

Subsequently, the cryogenic setup was connected and the demodulated phase noise was measured again. This measurement was performed with the readout tone set to the previously calculated optimal point, but this time the measurement was carried out in open-loop mode, i.e. without FR. In this configuration, the modulation signal corresponded to a DC signal that couples an integer number of magnetic flux quantum units to the rf-SQUID.

To assess whether the MSS board affects the noise of the μMUX, the same measurement was repeated without the MSS board connected. Instead, the lines were terminated with two 50 Ω loads.

As a result, the noise generated by the RTE is measured at $\sqrt{S_\Phi} = 1.41\,\mu\Phi_0/\sqrt{Hz}$. However, in the cryogenic setup this noise increases significantly to $\sqrt{S_\Phi} = 8.55\,\mu\Phi_0/\sqrt{Hz}$. This substantial increase suggests that, under these specific measurement conditions, the noise contribution from the cryogenic system is dominant over that of the RTE. The observed rise in noise highlights future work challenges to decrease this noise to ensure the detector noise is the dominant in the system.

Moreover, the demodulated phase noise remains primarily influenced by the cryogenic system when the MSS board is connected. This observation leads to the conclusion that, under the given measurement conditions, the performance of the designed MSS board does not significantly impact the overall noise characteristics of the system. This result is important as it suggests that the MSS board operates as expected without introducing additional noise or disturbances into the cryogenic setup, thereby ensuring the integrity of the measurements.

It is important to remark the presence of interferences and/or spurious signals that adversely affect the system's performance. These unwanted signals contribute to additional noise and signal degradation, which compromises the accuracy and reliability of the measurements. Identifying the sources and points of coupling for these signals is essential for improving system performance. In future work, efforts will be focused on locating the sources of these interferences to enable the implementation of appropriate shielding techniques or filtering mechanisms. By mitigating these external influences, the system's sensitivity and overall measurement quality can be significantly enhanced.

# Chapter 8

# Summary and Outlook

This work presents the development and implementation of a signal processing system for the readout of Microwave SQUID Multiplexer ($\mu$MUX) devices, enabling the measurement of low-temperature Magnetic Microbolometer (MMB) arrays. The system is specifically tailored to meet the requirements of the Q&U Bolometric Interferometer for Cosmology (QUBIC) experiment, whose scientific motivation is to detect the Cosmic Microwave Background (CMB) polarization.

The proposed system addresses the challenges of reading out such detectors through a comprehensive design framework based on a Software-defined Radio (SDR) architecture, leveraging the advantages of a Frequency-Division Multiplexing (FDM) scheme. This framework includes the development of room temperature Electronics (RTE), featuring Field Programmable Gate Array (FPGA)-based hardware for efficient multirate signal processing, custom digital and analog PCB designs for base-band and radio frequency (rf) operations, software for monitoring and controlling system parameters as well as data acquisition and storage and a cryogenic setup to ensure signal thermalization and conditioning, meeting the $\mu$MUX readout requirements.

The significant contributions of this thesis include the design and implementation of the modulation signal chain, which integrates specific modules on the FPGA and the development and characterization of a mixed-signal PCB, named Modulation Signal Synthesizer (MSS) board and cryogenic setup optimized for the requirements of the $\mu$MUX measurement device.

The modulation signal chain was designed to include a FPGA module for generating arbitrary waveforms, synchronized with the demodulation process of the detector signal. This module offers flexibility in signal generation, as it is based on cyclic playback from a Block Random Access Memory (BRAM). Additionally, it provides excellent frequency resolution, which can be easily adapted to meet the system's specific requirements.

Additionally, a digital signal conditioning module was developed to adapt the output format to the specific requirements of the selected Digital-to-Analog Converter (DAC). Linux drivers were also created to control and monitor these FPGA modules, leveraging the gRPC framework for seamless communication. The AXI-Stream bus was used to establish efficient data transfer between the microprocessor and FPGA on the Multiprocessor System-on-Chip (MPSoC) ZCU102 platform.

The MSS board was designed to generate single-ended and differential analog signals for $\mu$MUX modulation, integrating all the necessary components for system-level compatibility. This approach prioritizes signal integrity and minimizes noise, ensuring good performance when interfaced with the cryogenic setup. The cryogenic setup itself was carefully engineered to adapt the generated signals to the $\mu$MUX device, taking into account the required signal levels and noise analysis to prevent degradation of the cryogenic system's noise performance.

Moreover, the MSS board was characterized, achieving the desired dynamic performance levels. The results demonstrated a Spurious Free Dynamic Range (SFDR) of 80 dBc and a maximum noise floor less than the expected MMB noise, validating its suitability for $\mu$MUX-based readout.

The work also focused on implementing a Digital Quadrature Demodulator (DQD) intended to handle multiple time-multiplexed signals. This demodulator was integrated into the full signal acquisition and processing firmware. It includes a multi-channel Direct Digital Synthesizer (DDS) with runtime configurability, allowing for dynamic adjustments to frequency and phase parameters. This flexibility enables the demodulation of multiple $\mu$MUX channels, accommodating the different dispersions present in its fabrication.

Additionally, a study of the aliasing effects caused by high-frequency components created during the demodulation process was carried out. These unwanted components affect the integrity of the detector's signal, prompting the exploration of various methods to reduce them. One effective proposal involved applying windowing techniques to the signal, which significantly improved attenuation in the sidebands.

To validate the proposed system, a demonstration was conducted with a 4-channel readout and demodulation setup. Although no physical detectors were used, the system emulated detector outputs, successfully showcasing the feasibility of the readout architecture.

Finally, this work establishes a strong foundation for MMBs readout. Future developments can aim to optimize resource usage by efficiently adapting and integrating all FPGA modules. In addition to this goal, expanding the system's capability to generate, acquire and process 1024 tones, while preventing noise degradation, will be crucial. Techniques such as tone-tracking will be essential for this purpose. Furthermore, improving the demodulated flux noise of the $\mu$MUX is a key objective to enable the readout of the first generation of MMBs array.

# List of Figures


1.1 Planck results 2018 . . . 5
1.2 CMB and the main foregrounds polarization spectra . . . 6
1.3 The QUBIC telescope . . . 7
1.4 Synthesized beam . . . 7
1.5 QUBIC telescope in Argentina . . . 8

2.1 Thermal detectors measurement principle . . . 9
2.2 Kinetic Inductance Detector . . . 12
2.3 Transition of a superconducting film . . . 12
2.4 TES voltage bias circuit . . . 13
2.5 MMB thermal model . . . 14
2.6 MMB electrical model . . . 15
2.7 MMB flux noise . . . 19

3.1 CPW quarter-wave resonator . . . 22
3.2 $\mu$Mux channel resonance circle . . . 23
3.3 Josephson junction diagram . . . 24
3.4 rf-SQUID diagram . . . 25
3.5 rf-SQUID regimes . . . 26
3.6 $\mu$MUX channel . . . 27
3.7 $\mu$MUX channel - flux dependency . . . 28
3.8 $\mu$MUX channel open-loop gain . . . 29
3.9 The $\mu$MUX schematic . . . 31
3.10 $\mu$MUX readout tone spectrum . . . 33
3.11 $\mu$MUX channel Fourier coefficients . . . 34
3.12 Fractional Flux Ramp demodulation . . . 36
3.13 Software-defined Radio scheme . . . 37
3.14 DDS schematic . . . 38
3.15 Analytic signal spectrum . . . 39
3.16 Filter Bank . . . 40
3.17 Converters quantization . . . 41
3.18 Spectrum of a sampled signal . . . 44
3.19 DAC zero-order hold response . . . 45
3.20 Readout tone noise . . . 48

3.21 LNA compression point . . . 49
3.22 Spectral Engineering algorithm . . . 51
3.23 Proposed Readout system . . . 52

4.1 MSS system . . . 61
4.2 MSS FE board . . . 62
4.3 Stackable board system integration . . . 63
4.4 MSS digital modules . . . 64
4.5 MSS digital signal level . . . 64
4.6 MSS board design . . . 66
4.7 MSS board filters . . . 67
4.8 LVPECL circuit . . . 69
4.9 LVPECL driver . . . 70
4.10 Single-ended setup noise model . . . 72
4.11 IV converter noise model for the single-ended setup . . . 73
4.12 Differential setup noise model . . . 74
4.13 IV converter noise model for the differential setup . . . 74

5.1 Complex DDC . . . 78
5.2 Readout signal downsampling stages . . . 79
5.3 Goertzel Filter . . . 80
5.4 FPGA Backend channelization . . . 81
5.5 Multi-channel Digital Quadrature Demodulator . . . 82
5.6 Moving Average Filter response . . . 83
5.7 Weighted Moving Average Filter response . . . 85
5.8 Flux Ramp Demodulator module . . . 86
5.9 Xilinx DSP48E IP . . . 87

6.1 Prototype Readout system . . . 90
6.2 Prototype firmware . . . 91
6.3 MSS board calibration . . . 92
6.4 Quantization distortion effect . . . 93
6.5 Spectrum Analyzer baseline . . . 94
6.6 Red Pitaya 125-14 baseline . . . 95
6.7 MSS board characterization setup . . . 96
6.8 MSS board generation spectra . . . 96
6.9 MSS board dynamic performance . . . 97
6.10 MSS board dynamic performance . . . 98
6.11 MSS board characterization using Gali-84+ . . . 98
6.12 MSS board signal in magnetic flux density . . . 99
6.13 Room temperature Notch resonator . . . 99
6.14 Setup for the room temperature resonator Readout . . . 100
6.15 Readout signal at the room temperature resonator output . . . 101
6.16 Signal recovery capability of the Prototype system . . . 102

6.17 Flux Ramp Demodulator comparison: 16-bit real-time demodulation vs. floating-point offline post-processing . . . . . 103
6.18 Flux Ramp Demodulator comparison: 18-bit real-time demodulation vs. floating-point offline post-processing . . . . . 104

7.1 Cryogenic setup for $\mu$MUX measurements . . . . . 106
7.2 The Microwave SQUID Multiplexer . . . . . 107
7.3 $\mu$MUX channels as a function of modulation current . . . . . 108
7.4 Room temperature setup for the $\mu$MUX readout . . . . . 109
7.5 $\mu$MUX optimal point demodulating 1st harmonic . . . . . 110
7.6 $\mu$MUX optimal point demodulating 2nd harmonic . . . . . 110
7.7 Readout system demonstration for Recovering 4 Single-Tone Signals . . . 111
7.8 Readout system demonstration for Recovering 4 Multi-Tonal Signals . . . 111
7.9 Demodulated magnetic flux noise comparison . . . . . 112

# List of Tables


4.1 QUBIC wiring length and cooling power . . . . . 59
4.2 Thermal conductivities of CuNi and PTFE materials . . . . . 59
4.3 Passive heat in the modulation line. . . . . 60
4.4 Thermal current noise in the modulation line . . . . . 60

7.1 Parameters of the $\mu$MUX channels . . . . . 108

# List of Acronyms

| | |
|---|---|
| $NEP_{\gamma}$ | Background Noise Equivalent Power |
| $NEP_{det}$ | Detector Noise Equivalent Power |
| $\mu$MUX | Microwave SQUID Multiplexer |
| $\mu$P | micro-processor |
| **ADC** | Analog-to-Digital Converter |
| **AWG** | arbitrary waveform generator |
| **BB** | baseband |
| **BE** | Back-end |
| **BLIP** | Background Limited Photometry |
| **BRAM** | Block Random Access Memory |
| **CDM** | Code-Division Multiplexing |
| **CLB** | Configurable Logic Block |
| **CMB** | Cosmic Microwave Background Radiation |
| **COBE** | Cosmic Background Explorer |
| **CORDIC** | COordinate Rotation DIgital Computer |
| **CP** | Cold plate |
| **DAC** | Digital-to-Analog Converter |
| **DDC** | Digital Down Converter |
| **DDS** | Direct Digital Synthesizer |
| **DFT** | Discrete Fourier Transform |
| **DMA** | Direct Memory Access |
| **DQD** | Digital Quadrature Demodulator |
| **DSP** | Digital Signal Processing |
| **ECHo** | Electron Capture in $^{163}$Ho Experiment |
| **Er** | erbium 1/f excess noise |
| **ETF** | electro-thermal feedback |
| **FDM** | Frequency-Division Multiplexing |
| **FE** | Front-end |
| **FF** | Flip-Flop |

**FFT** . . . . . Fast Fourier Transform
**FLL** . . . . . Flux Lock Loop
**FPGA** . . . . . Field Programmable Gate Array
**FR** . . . . . Flux Ramp signal
**FRD** . . . . . Flux Ramp Demodulator
**FRM** . . . . . Flux Ramp Modulation
**GF** . . . . . Goertzel Filter
**HEMT** . . . . . High-Electron-Mobility Transistor
**I.S.** . . . . . Iterative Section
**IP** . . . . . Intellectual Property
**KID** . . . . . Kinetic Inductance Detector
**LIGO** . . . . . Laser Interferometer Gravitational-Wave Observatory
**LNA** . . . . . Low-Noise Amplifier
**LO** . . . . . Local Oscillator
**LUT** . . . . . Look-Up Table
**LVDS** . . . . . Low-Voltage Differential Signaling
**LVPECL** . . . . . Low-Voltage Positive Emitter-Coupled Logic
**MAF** . . . . . Moving Average Filter
**MJN** . . . . . magnetic Johnson noise
**MMB** . . . . . Magnetic Microbolometers
**MMC** . . . . . Magnetic Microcalorimeter
**MMCM** . . . . . Mixed-Mode Clock Manager
**MPSoC** . . . . . Multiprocessor System-on-Chip
**MSS** . . . . . Modulation Signal Synthesizer
**MXC** . . . . . Mixing Chamber plate
**N.I.S.** . . . . . Non-Iterative Section
**NEP** . . . . . Noise Equivalent Power
**NSD** . . . . . Noise Spectral Density
**PIMC** . . . . . Platform Information and Management Core
**PSD** . . . . . Power Spectral Density
**QUBIC** . . . . . Q&U Bolometric Interferometer for Cosmology
**rf** . . . . . radio frequency
**rf-SQUID** . . . . . radio frequency SQUID
**RFSoC** . . . . . Radio Frequency System-on-Chip
**RMS** . . . . . Root-Mean-Squared
**RP** . . . . . Red Pitaya
**RTE** . . . . . room temperature Electronics

**SDR** . . . . . Software-defined Radio
**SE** . . . . . Single-Ended
**SFDR** . . . . . Spurious Free Dynamic Range
**SNR** . . . . . Signal-to-Noise Ratio
**SoC** . . . . . System-on-Chip
**SP** . . . . . Still plate
**SQUID** . . . . . Superconducting Quantum Interference Device
**SSTL** . . . . . Stub Series Terminated Logic
**TD** . . . . . Technical Demonstrator
**TDM** . . . . . Time-Division Multiplexing
**TES** . . . . . Transition Edge Sensor
**TFN** . . . . . thermal fluctuation noise
**THD** . . . . . Total Harmonic Distortion
**TLS** . . . . . Two-Level System
**WMAF** . . . . . Weighted Moving Average Filter

# Bibliography


[1] B. P. Abbott, R. Abbott, R. Adhikari, P. Ajith, B. Allen, G. Allen et al. "LIGO: the Laser Interferometer Gravitational-Wave Observatory." *Reports on Progress in Physics*, vol. 72(7), p. 076901, Jun. 2009. URL http://dx.doi.org/10.1088/0034-4885/72/7/076901.

[2] D. McCammon. Thermal Equilibrium Calorimeters – An Introduction, p. 1–34. Springer Berlin Heidelberg, Jul. 2005. URL http://dx.doi.org/10.1007/10933596_1.

[3] U. Fano. "Ionization Yield of Radiations. II. The Fluctuations of the Number of Ions." *Physical Review*, vol. 72(1), p. 26–29, Jul. 1947. URL http://dx.doi.org/10.1103/PhysRev.72.26.

[4] J. Meier, P. Egelhof, C. Fischer, A. Himmler, G. Kirchner, A. v. Kienlin et al. "Energy sensitive detection of heavy ions with transition edge calorimeters." *Journal of Low Temperature Physics*, vol. 93(3–4), p. 231–238, Nov. 1993. URL http://dx.doi.org/10.1007/BF00693425.

[5] H. K. Hans Kraus. "Superconducting Radiation Detectors and Their Future Perspectives." *Japanese Journal of Applied Physics*, vol. 37(12R), p. 6273, Dec. 1998. URL http://dx.doi.org/10.1143/JJAP.37.6273.

[6] H. Muramatsu, K. Nagayoshi, T. Hayashi, K. Sakai, R. Yamamoto, K. Mitsuda et al. "Design and Performance of a TES X-ray Microcalorimeter Array for Energy Dispersive Spectroscopy on Scanning Transmission Electron Microscope." *Journal of Low Temperature Physics*, vol. 184(1–2), p. 91–96, Feb. 2016. URL http://dx.doi.org/10.1007/s10909-016-1547-3.

[7] R. Gross, A. Marx, and F. Deppe. Applied superconductivity. De Gruyter Textbook. Walter de Gruyter, Jun. 2017.

[8] J.-C. Hamilton, L. Mousset, E. Battistelli, P. de Bernardis, M.-A. Bigot-Sazy, P. Chanial et al. "QUBIC I: Overview and science program." *Journal of Cosmology and Astroparticle Physics*, vol. 2022, p. 034. doi:10.1088/1475-7516/2022/04/034, 4 2022.

[9] O. Sander, N. Karcher, O. Krömer, S. Kempf, M. Wegner, C. Enss et al. "Software-Defined Radio Readout System for the ECHo Experiment." *IEEE Transactions on Nuclear Science*, vol. 66(7), pp. 1204–1209. doi:https://doi.org/10.1109/TNS.2019.2914665, 2019.

[10] H. McCarrick, E. Healy, Z. Ahmed, K. Arnold, Z. Atkins, J. E. Austermann et al. "The Simons Observatory Microwave SQUID Multiplexing Detector Module Design." *The Astrophysical Journal*, vol. 922(1), p. 38, Nov. 2021. URL https://doi.org/10.3847/1538-4357/ac2232.

[11] S. M. Stanchfield, P. A. R. Ade, J. Aguirre, J. A. Brevik, H. M. Cho, R. Datta et al. "Development of a Microwave SQUID-Multiplexed TES Array for MUSTANG-2." *Journal of Low Temperature Physics*, vol. 184(1-2), pp. 460–465, Mar. 2016. URL https://doi.org/10.1007/s10909-016-1570-4.

[12] D. A. Bennett, J. A. B. Mates, S. R. Bandler, D. T. Becker, J. W. Fowler, J. D. Gard et al. "Microwave SQUID multiplexing for the Lynx x-ray microcalorimeter." *Journal of Astronomical Telescopes, Instruments, and Systems*, vol. 5(02), p. 1, Mar. 2019. URL https://doi.org/10.1117/1.jatis.5.2.021007.

[13] D. Akerib, P. Barnes Jr., P. Brink, B. Cabrera, R. Clarke, R. Gaitskell et al. "Design and performance of a modular low-radioactivity readout system for cryogenic detectors in the CDMS experiment." *Nuclear Instruments and Methods in Physics Research Section A: Accelerators, Spectrometers, Detectors and Associated Equipment*, vol. 591(3), p. 476–489, Jul. 2008. URL http://dx.doi.org/10.1016/j.nima.2008.03.103.

[14] K. Abazajian, G. Addison, P. Adshead, Z. Ahmed, S. W. Allen, D. Alonso et al. "CMB-S4 Science Case, Reference Design, and Project Plan.", 2019. URL https://arxiv.org/abs/1907.04473.

[15] J. G. Proakis and M. Salehi. Communication systems engineering. Pearson, Upper Saddle River, NJ, 2 edn., Aug. 2001.

[16] J. A. B. Mates. The Microwave SQUID Multiplexer. Ph.D. thesis, 2011. URL https://scholar.colorado.edu/concern/graduate_thesis_or_dissertations/gt54kn14d.

[17] R. Akeela and B. Dezfouli. "Software-defined Radios: Architecture, state-of-the-art, and challenges." *Computer Communications*, vol. 128, p. 106–125, Sep. 2018. URL http://dx.doi.org/10.1016/j.comcom.2018.07.012.

[18] S. W. Henderson, Z. Ahmed, D. Brown, S. Chaudhuri, H.-M. S. Cho, J. M. D'Ewart et al. "Highly-multiplexed microwave SQUID readout using the SLAC Microresonator Radio Frequency (SMuRF) electronics for future CMB and sub-millimeter surveys." In J. Zmuidzinas and J.-R. Gao, eds., "Millimeter, Submillimeter, and Far-Infrared Detectors and Instrumentation for Astronomy IX," SPIE, Jul. 2018. URL http://dx.doi.org/10.1117/12.2314435.

[19] F. K. Ahrens. "Cryogenic read-out system and resonator optimisation for the microwave SQUID multiplexer within the ECHo experiment." 2022. URL https://archiv.ub.uni-heidelberg.de/volltextserver/id/eprint/32038.

[20] W. Yoon, J. S. Adams, S. R. Bandler, D. Becker, D. A. Bennett, J. A. Chervenak et al. "Toward Large Field-of-View High-Resolution X-ray Imaging Spectrometers: Microwave Multiplexed Readout of 28 TES Microcalorimeters." *Journal of Low Temperature Physics*, vol. 193(3–4), p. 258–266, Apr. 2018. URL http://dx.doi.org/10.1007/s10909-018-1917-0.

[21] J. M. Geria, M. R. Hampel, S. Kempf, J. J. F. Bonaparte, L. P. Ferreyro, M. E. G. Redondo et al. "Suitability of magnetic microbolometers based on paramagnetic temperature sensors for CMB polarization measurements." *Journal of Astronomical Telescopes, Instruments, and Systems*, vol. 9(01). doi:10.1117/1.jatis.9.1.016002, Feb. 2023.

[22] L. Mele, P. Ade, J. G. Alberro, A. Almela, G. Amico, L. H. Arnaldi et al. "The QUBIC instrument for CMB polarization measurements." *Journal of Physics: Conference Series*, vol. 1548(1), p. 012016, May 2020. URL http://dx.doi.org/10.1088/1742-6596/1548/1/012016.

[23] M. Hampel, A. Almela, J. Bonaparte, J. B. Neira, L. Ferreyro, A. Fuster et al. "The Magnetic Microbolometer: A Proposal for QUBIC Next Gen." *Journal of Low Temperature Physics*, vol. 217(3–4), p. 401–408. doi:10.1007/s10909-024-03203-0, Aug. 2024. URL http://dx.doi.org/10.1007/s10909-024-03203-0.

[24] M. Platino, M. E. García Redondo, L. P. Ferreyro, J. M. Salum, N. A. Müller, J. D. Bonilla-Neira et al. "The Magnetic Microbolometer Detection Chain: A Proposed Detection System to Observe the B Modes of the Cosmic Microwave Background." *Journal of Low Temperature Physics*, vol. 217(5–6), p. 762–771. doi:10.1007/s10909-024-03230-x, Oct. 2024. URL http://dx.doi.org/10.1007/s10909-024-03230-x.

[25] A. A. Penzias and R. W. Wilson. "A Measurement of Excess Antenna Temperature at 4080 Mc/s." *The Astrophysical Journal*, vol. 142, p. 419. doi:10.1086/148307, 7 1965.

[26] J. C. Mather, E. S. Cheng, J. Eplee, R. E., R. B. Isaacman, S. S. Meyer, R. A. Shafer et al. "A preliminary measurement of the cosmic microwave background spectrum by the Cosmic Background Explorer (COBE) satellite." *The Astrophysical Journal*, vol. 354, p. L37, May 1990. URL http://dx.doi.org/10.1086/185717.

[27] A. H. Guth. "Inflationary universe: A possible solution to the horizon and flatness problems." *Phys. Rev. D*, vol. 23, pp. 347–356. doi:10.1103/PhysRevD.23.347, Jan 1981.

[28] A. Linde. "A new inflationary universe scenario: A possible solution of the horizon, flatness, homogeneity, isotropy and primordial monopole problems." *Physics Letters B*, vol. 108(6), pp. 389–393. doi:10.1016/0370-2693(82)91219-9, Feb. 1982.

[29] A. Albrecht and P. J. Steinhardt. "Cosmology for Grand Unified Theories with Radiatively Induced Symmetry Breaking." *Phys. Rev. Lett.*, vol. 48, pp. 1220–1223. doi:10.1103/PhysRevLett.48.1220, Apr 1982.

[30] D. N. Spergel and M. Zaldarriaga. "Cosmic Microwave Background Polarization as a Direct Test of Inflation." *Physical Review Letters*, vol. 79, pp. 2180–2183. doi:10.1103/PhysRevLett.79.2180, 9 1997.

[31] U. Seljak and M. Zaldarriaga. "Signature of Gravity Waves in the Polarization of the Microwave Background." *Physical Review Letters*, vol. 78, pp. 2054–2057. doi:10.1103/PhysRevLett.78.2054, 3 1997.

[32] P. Ade, Z. Ahmed, M. Amiri, D. Barkats, R. B. Thakur, C. Bischoff et al. "Improved Constraints on Primordial Gravitational Waves using Planck, WMAP, and BICEP/Keck Observations through the 2018 Observing Season." *Physical Review Letters*, vol. 127(15), Oct. 2021. URL http://dx.doi.org/10.1103/PhysRevLett.127.151301.

[33] E. S. A. ESA. "Planck Image Gallery." URL https://www.cosmos.esa.int/web/planck/picture-gallery.

[34] N. Aghanim, Y. Akrami, F. Arroja, M. Ashdown, J. Aumont, C. Baccigalupi et al. "Planck2018 results: I. Overview and the cosmological legacy ofPlanck." *Astronomy & Astrophysics*, vol. 641, p. A1, Sep. 2020. URL http://dx.doi.org/10.1051/0004-6361/201833880.

[35] J. M. Kovac, E. M. Leitch, C. Pryke, J. E. Carlstrom, N. W. Halverson, and W. L. Holzapfel. "Detection of polarization in the cosmic microwave background using DASI." *Nature*, vol. 420(6917), p. 772–787, Dec. 2002. URL http://dx.doi.org/10.1038/nature01269.

[36] G. Siringo, E. Kreysa, A. Kovács, F. Schuller, A. Weiß, W. Esch et al. "The large APEX BOlometer CAmera LABOCA." *Astronomy and Astrophysics*, vol. 497, pp. 945–962. doi:10.1051/0004-6361/200811454, 4 2009.

[37] P. A. Ade, R. W. Aikin, D. Barkats, S. J. Benton, C. A. Bischoff, J. J. Bock et al. "Detection of B-mode polarization at degree angular scales by BICEP2." *Physical Review Letters*, vol. 112. doi:10.1103/PhysRevLett.112.241101, 6 2014.

[38] J. R. Bond, P. Ade, A. Balbi, J. Bock, J. Borrill, A. Boscaleri et al. "CMB Analysis of Boomerang & Maxima & the Cosmic Parameters $\Omega_{tot}, \Omega_b h^2, \Omega_{cdm} h^2, \Omega_\Lambda, n_s$." 11 2000.

[39] J. E. Carlstrom, P. A. R. Ade, K. A. Aird, B. A. Benson, L. E. Bleem, S. Busetti et al. "The 10 Meter South Pole Telescope." *Publications of the Astronomical Society of the Pacific*, vol. 123, pp. 568–581. doi:10.1086/659879, 5 2011.

[40] B. A. Benson, P. A. R. Ade, Z. Ahmed, S. W. Allen, K. Arnold, J. E. Austermann et al. "SPT-3G: a next-generation cosmic microwave background polarization experiment on the South Pole telescope." In W. S. Holland and J. Zmuidzinas, eds., "SPIE Proceedings," SPIE, Jul. 2014. doi:10.1117/12.2057305.

[41] A. Suzuki, P. A. R. Ade, Y. Akiba, D. Alonso, K. Arnold, J. Aumont et al. "The LiteBIRD Satellite Mission: Sub-Kelvin Instrument." *Journal of Low Temperature Physics*, vol. 193(5-6), pp. 1048–1056. doi:10.1007/s10909-018-1947-7, May 2018.

[42] Y. Inoue, P. Ade, Y. Akiba, C. Aleman, K. Arnold, C. Baccigalupi et al. "POLARBEAR-2: an instrument for CMB polarization measurements." In W. S. Holland and J. Zmuidzinas, eds., "SPIE Proceedings," SPIE, Aug. 2016. doi:10.1117/12.2231961.

[43] A. Suzuki, P. Ade, Y. Akiba, C. Aleman, K. Arnold, C. Baccigalupi et al. "The Polarbear-2 and the Simons Array Experiments." *Journal of Low Temperature Physics*, vol. 184(3-4), pp. 805–810. doi:10.1007/s10909-015-1425-4, Jan. 2016.

[44] C. O'Sullivan, D. Burke, M. De Petris, M. Gradziel, J.-C. Hamilton, S. Torchinsky et al. "QUBIC – The Q & U Bolometric Interferometer for Cosmology." In "2023 17th European Conference on Antennas and Propagation (EuCAP)," IEEE, Mar. 2023. URL http://dx.doi.org/10.23919/EuCAP57121.2023.10133731.

[45] L. Mousset, M. G. Lerena, E. Battistelli, P. de Bernardis, P. Chanial, G. D'Alessandro et al. "QUBIC II: Spectral polarimetry with bolometric interferometry." *Journal of Cosmology and Astroparticle Physics*, vol. 2022(04), p. 035. doi:10.1088/1475-7516/2022/04/035, Apr. 2022.

[46] G. D'Alessandro, L. Mele, F. Columbro, G. Amico, E. Battistelli, P. de Bernardis et al. "QUBIC VI: Cryogenic half wave plate rotator, design and performance." *Journal of Cosmology and Astroparticle Physics*, vol. 2022(04), p. 039. doi:10.1088/1475-7516/2022/04/039, Apr. 2022.

[47] S. Masi, E. Battistelli, P. de Bernardis, C. Chapron, F. Columbro, A. Coppolecchia et al. "QUBIC V: Cryogenic system design and performance." *Journal of Cosmology and Astroparticle Physics*, vol. 2022(04), p. 038. doi:10.1088/1475-7516/2022/04/038, Apr. 2022.

[48] F. Cavaliere, A. Mennella, M. Zannoni, P. Battaglia, E. Battistelli, P. de Bernardis et al. "QUBIC VII: The feedhorn-switch system of the technological demonstrator." *Journal of Cosmology and Astroparticle Physics*, vol. 2022(04), p. 040. doi:10.1088/1475-7516/2022/04/040, Apr. 2022.

[49] M. Piat, G. Stankowiak, E. Battistelli, P. de Bernardis, G. D'Alessandro, M. D. Petris et al. "QUBIC IV: Performance of TES bolometers and readout electronics." *Journal of Cosmology and Astroparticle Physics*, vol. 2022, p. 037. doi:10.1088/1475-7516/2022/04/037, 4 2022.

[50] N. E. Booth, B. Cabrera, and E. Fiorini. "LOW-TEMPERATURE PARTICLE DETECTORS." *Annual Review of Nuclear and Particle Science*, vol. 46(1), p. 471–532, Dec. 1996. URL http://dx.doi.org/10.1146/annurev.nucl.46.1.471.

[51] D. E. Newbury, D. A. Wollman, G. C. Hilton, K. D. Irwin, N. F. Bergren, D. A. Rudman et al. "The Approaching Revolution in X-Ray Microanalysis: The Microcalorimeter Energy Dispersive Spectrometer." *Journal of Radioanalytical and Nuclear Chemistry*, vol. 244(3), p. 627–635, 2000. URL http://dx.doi.org/10.1023/A:1006777606703.

[52] H. Kraus. "Superconductive bolometers and calorimeters." *Superconductor Science and Technology*, vol. 9(10), p. 827–842, Oct. 1996. URL http://dx.doi.org/10.1088/0953-2048/9/10/001.

[53] J. Geria, A. Almela, J. Bonaparte, J. Bonilla-Neira, L. Ferreyro, A. Fuster et al. "Antenna-Coupled Magnetic Microbolometers for CMB Polarization Surveys." *Journal of Low Temperature Physics*, vol. 217(3–4), p. 472–480. doi:10.1007/s10909-024-03217-8, Sep. 2024. URL http://dx.doi.org/10.1007/s10909-024-03217-8.

[54] W. Meissner and R. Ochsenfeld. "Ein neuer Effekt bei Eintritt der Supraleitfähigkeit." *Die Naturwissenschaften*, vol. 21(44), pp. 787–788. doi:10.1007/bf01504252, Nov. 1933.

[55] V. L. Ginzburg and L. D. Landau. "On the Theory of superconductivity." *Zh. Eksp. Teor. Fiz.*, vol. 20, pp. 1064–1082. doi:10.1016/B978-0-08-010586-4.50035-3, 1950.

[56] L. N. Cooper. "Bound Electron Pairs in a Degenerate Fermi Gas." *Phys. Rev.*, vol. 104, pp. 1189–1190. doi:10.1103/PhysRev.104.1189, Nov 1956.

[57] J. Bardeen, L. N. Cooper, and J. R. Schrieffer. "Theory of Superconductivity." *Phys. Rev.*, vol. 108, pp. 1175–1204. doi:10.1103/PhysRev.108.1175, Dec 1957.

[58] A. A. Abrikosov. "On the Magnetic properties of superconductors of the second group." *Sov. Phys. JETP*, vol. 5, pp. 1174–1182, 1957.

[59] L. P. Gor'kov. "Microscopic derivation of the Ginzburg–Landau equations in the theory of superconductivity." *Sov. Phys. - JETP (Engl. Transl.); (United States)*, 1 1959. URL https://www.osti.gov/biblio/7264935.

[60] C. Enss and S. Hunklinger. Low-Temperature Physics. Springer-Verlag, 2005. URL http://dx.doi.org/10.1007/b137878.

[61] A. J. Annunziata, D. F. Santavicca, L. Frunzio, G. Catelani, M. J. Rooks, A. Frydman et al. "Tunable superconducting nanoinductors." *Nanotechnology*, vol. 21(44), p. 445202, Oct. 2010. URL http://dx.doi.org/10.1088/0957-4484/21/44/445202.

[62] P. K. Day, H. G. LeDuc, B. A. Mazin, A. Vayonakis, and J. Zmuidzinas. "A broadband superconducting detector suitable for use in large arrays." *Nature*, vol. 425(6960), p. 817–821, Oct. 2003. URL http://dx.doi.org/10.1038/nature02037.

[63] B. A. Mazin, P. K. Day, H. G. LeDuc, A. Vayonakis, and J. Zmuidzinas. "Superconducting kinetic inductance photon detectors." In H. A. MacEwen, ed., "Highly Innovative Space Telescope Concepts," SPIE, Dec. 2002. URL http://dx.doi.org/10.1117/12.460456.

[64] A. Wandui, J. J. Bock, C. Frez, M. Hollister, L. Minutolo, H. Nguyen et al. "Thermal kinetic inductance detectors for millimeter-wave detection." *Journal of Applied Physics*, vol. 128(4), Jul. 2020. URL http://dx.doi.org/10.1063/5.0002413.

[65] P. Day, H. Leduc, A. Goldin, T. Vayonakis, B. Mazin, S. Kumar et al. "Antenna-coupled microwave kinetic inductance detectors." *Nuclear Instruments and Methods in Physics Research Section A: Accelerators, Spectrometers, Detectors and Associated Equipment*, vol. 559(2), p. 561–563, Apr. 2006. URL http://dx.doi.org/10.1016/j.nima.2005.12.057.

[66] T. W. Cecil, L. Gades, T. Madden, D. Yan, and A. Miceli. "Optimization of thermal kinetic inductance detectors for x-ray spectroscopy." *IEEE Transactions on Applied Superconductivity*, vol. 25(3), p. 2400805 (5 pp.), Jun. 2015. URL http://dx.doi.org/10.1109/TASC.2014.2384995.

[67] K. Irwin and G. Hilton. Transition-Edge Sensors, p. 63–150. Springer Berlin Heidelberg, Jul. 2005. URL http://dx.doi.org/10.1007/10933596_3.

[68] A. Fleischmann, C. Enss, and G. Seidel. Metallic Magnetic Calorimeters, pp. 151–216. 7 2005. doi:10.1007/10933596_4.

[69] S. Kempf, A. Fleischmann, L. Gastaldo, and C. Enss. "Physics and Applications of Metallic Magnetic Calorimeters." *Journal of Low Temperature Physics*, vol. 193(3–4), p. 365–379, Mar. 2018. URL http://dx.doi.org/10.1007/s10909-018-1891-6.

[70] A. Fleischmann. "Magnetische Mikrokalorimeter : Hochauflösende Röntgenspektroskopie mit energiedispersiven Detektoren." 2012. URL http://archiv.ub.uni-heidelberg.de/volltextserver/id/eprint/12877.

[71] J. C. Mather. "Bolometer noise: nonequilibrium theory." *Applied Optics*, vol. 21(6), p. 1125, Mar. 1982. URL http://dx.doi.org/10.1364/AO.21.001125.

[72] D. Drung, J. Beyer, J.-H. Storm, M. Peters, and T. Schurig. "Investigation of Low-Frequency Excess Flux Noise in DC SQUIDs at mK Temperatures." *IEEE Transactions on Applied Superconductivity*, vol. 21(3), p. 340–344, Jun. 2011. URL http://dx.doi.org/10.1109/TASC.2010.2084054.

[73] C. Perbost. Matrices de bolomètres supraconducteurs pour la mesure de la polarisation du fond diffus cosmologique : application à l'expérience QUBIC. Theses, Université Sorbonne Paris Cité, Dec. 2016. URL https://theses.hal.science/tel-01909133.

[74] S. Hanany, A. H. Jaffe, and E. Scannapieco. "The effect of the detector response time on bolometric cosmic microwave background anisotropy experiments." *Monthly Notices of the Royal Astronomical Society*, vol. 299(3), p. 653–660, Sep. 1998. URL http://dx.doi.org/10.1046/j.1365-8711.1998.01705.x.

[75] J. M. Lamarre. "Photon noise in photometric instruments at far-infrared and submillimeter wavelengths." *Applied Optics*, vol. 25(6), p. 870, Mar. 1986. URL http://dx.doi.org/10.1364/ao.25.000870.

[76] S. Kempf, M. Wegner, A. Fleischmann, L. Gastaldo, F. Herrmann, M. Papst et al. "Demonstration of a scalable frequency-domain readout of metallic magnetic calorimeters by means of a microwave SQUID multiplexer." *AIP Advances*, vol. 7(1), p. 015007. doi:https://doi.org/10.1063/1.4973872, Jan. 2017.

[77] R. Barends. Photon-detecting superconducting resonators. 2009.

[78] J. Gao. The Physics of Superconducting Microwave Resonators. Ph.D. thesis, 2008. URL https://resolver.caltech.edu/CaltechETD:etd-06092008-235549.

[79] B. W. Petley. "The Josephson effects." *Contemporary Physics*, vol. 10(2), p. 139–158, Mar. 1969. URL http://dx.doi.org/10.1080/00107516908220105.

[80] R. Kleiner and W. Buckel. Superconductivity. Wiley-VCH Verlag, Weinheim, Germany, 3 edn., Dec. 2015.

[81] T. Ryhänen, H. Seppä, R. Ilmoniemi, and J. Knuutila. "SQUID magnetometers for low-frequency applications." *Journal of Low Temperature Physics*, vol. 76(5–6), p. 287–386, Sep. 1989. URL http://dx.doi.org/10.1007/BF00681735.

[82] C. Schuster, M. Wegner, and S. Kempf. "Simulation framework for microwave SQUID multiplexer optimization." *Journal of Applied Physics*, vol. 133(4), Jan. 2023. URL http://dx.doi.org/10.1063/5.0135124.

[83] J. Clarke and A. I. Braginski. The SQUID handbook: Fundamentals and technology of SQUIDs and SQUID systems. The SQUID Handbook. Set. Wiley-VCH Verlag, Weinheim, Germany, Jun. 2004. URL http://dx.doi.org/10.1002/3527603646.

[84] D. Prele, M. Piat, L. Sipile, and F. Voisin. "Operating Point and Flux Jumps of a SQUID in Flux-Locked Loop." *IEEE Transactions on Applied Superconductivity*, vol. 26(2), p. 1–5, Mar. 2016. URL http://dx.doi.org/10.1109/TASC.2015.2510606.

[85] J. A. B. Mates, K. D. Irwin, L. R. Vale, G. C. Hilton, J. Gao, and K. W. Lehnert. "Flux-Ramp Modulation for SQUID Multiplexing." *Journal of Low Temperature Physics*, vol. 167(5–6), p. 707–712, Feb. 2012. URL http://dx.doi.org/10.1007/s10909-012-0518-6.

[86] S. Schmid, L. G. Villanueva, and M. L. Roukes. Fundamentals of Nanomechanical Resonators. Springer International Publishing, 2023. URL http://dx.doi.org/10.1007/978-3-031-29628-4.

[87] L. Giacoletto. "Generalized Theory of Multitone Amplitude and Frequency Modulation." *Proceedings of the IRE*, vol. 35(7), p. 680–693, Jul. 1947. URL http://dx.doi.org/10.1109/JRPROC.1947.233906.

[88] J. C. Groh, Z. Ahmed, S. W. Henderson, J. Hubmayr, J. A. B. Mates, M. Silva-Feaver et al. "Crosstalk Effects in Microwave SQUID Multiplexed TES Bolometer Readout." *Journal of Low Temperature Physics*, vol. 216(1–2), p. 225–236, May 2024. URL http://dx.doi.org/10.1007/s10909-024-03126-w.

[89] J. A. B. Mates, D. T. Becker, D. A. Bennett, B. J. Dober, J. D. Gard, G. C. Hilton et al. "Crosstalk in microwave SQUID multiplexers." *Applied Physics Letters*, vol. 115(20), Nov. 2019. URL http://dx.doi.org/10.1063/1.5116573.

[90] F. Harris, E. Venosa, and X. Chen. Multirate Signal Processing for Software Radio Architectures, p. 339–422. Elsevier, 2014. URL http://dx.doi.org/10.1016/B978-0-12-396502-8.00007-3.

[91] L. Ferreyro, M. García Redondo, M. Hampel, A. Almela, A. Fuster, J. Salum et al. "An implementation of a channelizer based on a Goertzel Filter Bank for the readout of cryogenic sensors." *Journal of Instrumentation*, vol. 18(06), p. P06009, Jun. 2023. URL http://dx.doi.org/10.1088/1748-0221/18/06/P06009.

[92] AMD Xilinx. UltraScale Architecture and Product Data Sheet: Overview. URL https://docs.amd.com/v/u/en-US/ds890-ultrascale-overview.

[93] J. G. Proakis and D. K. Manolakis. Digital Signal Processing: Pearson New International Edition. Pearson custom library. Pearson Education, London, England, 4 edn., Jul. 2013.

[94] F. Puente León and U. Kiencke. Messtechnik. Springer, Berlin, Germany, 9 edn., Sep. 2012.

[95] S. Boyd. "Multitone signals with low crest factor." *IEEE Trans. Circuits Syst.*, vol. 33(10), pp. 1018–1022, Oct. 1986.

[96] D. Brandon and K. Gentile. "DDS-Based Clock Jitter Performance vs. DAC Reconstruction Filter Performance." Applications Note AN-837. Analog Devices, Inc. URL https://www.analog.com/media/en/technical-documentation/application-notes/351016224an_837.pdf.

[97] AMD Xilinx. Zynq UltraScale+ RFSoC RF Data Converter v2.6 Gen 1/2/3/DFE LogiCORE IP Product Guide (PG269), 2024. URL https://docs.amd.com/r/en-US/pg269-rf-data-converter/RF-DAC-Nyquist-Zone-Operation.

[98] C. Yu, Z. Ahmed, J. C. Frisch, S. W. Henderson, M. Silva-Feaver, K. Arnold et al. "SLAC Microresonator RF (SMuRF) Electronics: A tone-tracking readout system for superconducting microwave resonator arrays." *Review of Scientific Instruments*, vol. 94, p. 014712. doi:10.1063/5.0125084, 8 2022.

[99] B. Razavi. RF microelectronics. Prentice Hall, Philadelphia, PA, 2 edn., Sep. 2011.

[100] J. M. Salum, M. E. García Redondo, L. P. Ferreyro, J. Bonilla-Neira, N. Müller, J. M. Geria et al. "Spectral Engineering for Optimal Signal Performance in the Microwave SQUID Multiplexer." *Journal of Low Temperature Physics*, vol. 214(3–4), p. 272–279, Feb. 2024. URL http://dx.doi.org/10.1007/s10909-024-03049-6.

[101] AMD Xilinx. Zynq UltraScale+ RFSoC ZCU216 Evaluation Kit. URL https://www.xilinx.com/products/boards-and-kits/zcu216.html.

[102] M. E. G. Redondo, T. Muscheid, R. Gartmann, J. M. Salum, L. P. Ferreyro, N. A. Müller et al. "RFSoC Gen3-Based Software-Defined Radio Characterization for the Readout System of Low-Temperature Bolometers." *Journal of Low Temperature Physics*, Apr. 2024. URL http://dx.doi.org/10.1007/s10909-024-03079-0.

[103] L. Ferreyro. "Back-end Design of the Readout System for Cryogenic Particle Detectors.", 2024. URL https://publikationen.bibliothek.kit.edu/1000169242.

[104] N. Karcher. "Ausleseelektronik für magnetische Mikrokalorimeter im Frequenzmultiplexverfahren." 2022. URL https://publikationen.bibliothek.kit.edu/1000148040.

[105] AMD Xilinx. Zynq UltraScale+ MPSoC ZCU102 Evaluation Kit. URL https://www.xilinx.com/products/boards-and-kits/ek-u1-zcu102-g.html.

[106] Analog Devices. AD9680 14-Bit, 1.25 GSPS/1 GSPS/820 MSPS/500 MSPS JESD204B, Dual Analog-to-Digital Converter, 2019. URL https://www.analog.com/en/resources/evaluation-hardware-and-software/evaluation-boards-kits/eval-ad-fmcdaq2-ebz.html.

[107] Analog Devices. Quad, 16-Bit, 2.8 GSPS, TxDAC+® Digital-to-Analog Converter. URL https://www.analog.com/en/products/ad9144.html.

[108] Analog Devices. 14-Bit, 1.25 GSPS/1 GSPS/820 MSPS/500 MSPS JESD204B, Dual Analog-to-Digital Converter, 2019. URL https://www.analog.com/en/products/ad9680.html.

[109] R. Gartmann, N. Karcher, R. Gebauer, O. Krömer, and O. Sander. "Progress of the ECHo SDR Readout Hardware for Multiplexed MMCs." *Journal of Low Temperature Physics*, vol. 209(3–4), p. 726–733, Sep. 2022. URL http://dx.doi.org/10.1007/s10909-022-02854-1.

[110] Analog Devices. AD9523/AD9523-1 Evaluation Board. URL https://www.analog.com/en/resources/evaluation-hardware-and-software/evaluation-boards-kits/eval-ad9523-1.html#eb-overview.

[111] N. Karcher, R. Gebauer, R. Bauknecht, R. Illichmann, and O. Sander. "Versatile Configuration and Control Framework for Real-Time Data Acquisition Systems." *IEEE Transactions on Nuclear Science*, vol. 68(8), p. 1899–1906, Aug. 2021. URL http://dx.doi.org/10.1109/TNS.2021.3084355.

[112] A. Devices. Datasheet. URL https://www.analog.com/media/en/technical-documentation/data-sheets/MAX5891.pdf.

[113] Bluefors. Webpage. URL https://bluefors.com/.

[114] P. Duthil. "Material Properties at Low Temperature.", 2014. URL http://cds.cern.ch/record/1973682.

[115] S. Krinner, S. Storz, P. Kurpiers, P. Magnard, J. Heinsoo, R. Keller et al. "Engineering cryogenic setups for 100-qubit scale superconducting circuit systems." *EPJ Quantum Technology*, vol. 6(1), May 2019. URL http://dx.doi.org/10.1140/epjqt/s40507-019-0072-0.

[116] AMD Xilinx. UltraScale Architecture Clocking Resources User Guide (UG572). URL https://docs.amd.com/r/en-US/ug572-ultrascale-clocking/MMCMs.

[117] AMD Xilinx. Zynq UltraScale+ MPSoC Data Sheet: DC and AC Switching Characteristics (DS925), 2023. URL https://docs.amd.com/r/en-US/ds925-zynq-ultrascale-plus/LVDS-DC-Specifications-LVDS.

[118] M. Malnou, J. A. B. Mates, M. R. Vissers, L. R. Vale, D. R. Schmidt, D. A. Bennett et al. "Improved microwave SQUID multiplexer readout using a kinetic-inductance traveling-wave parametric amplifier." *Appl. Phys. Lett.*, vol. 122(21), May 2023.

[119] T. Instrument. Datasheet. URL https://www.ti.com/lit/ds/symlink/lmk00725.pdf?ts=1722384040797&ref_url=https%253A%252F%252Fwww.google.com%252F.

[120] L. P. Ferreyro, M. E. García Redondo, J. M. Salum, T. Muscheid, M. Hampel, A. Almela et al. "Advances in the Goertzel Filter Bank Channelizer for Cryogenic Sensors Readout." *Journal of Low Temperature Physics*, vol. 217(3–4), p. 409–417. doi:10.1007/s10909-024-03204-z, Sep. 2024. URL http://dx.doi.org/10.1007/s10909-024-03204-z.

[121] J. E. Volder. "The CORDIC Trigonometric Computing Technique." *IRE Transactions on Electronic Computers*, vol. EC-8(3), p. 330–334, Sep. 1959. URL http://dx.doi.org/10.1109/TEC.1959.5222693.

[122] Richter, Daniel Philipp. Multikanal-Auslesung von metallischen magnetischen Kalorimetern mittels eines vollständigen Mikrowellen-SQUID-Multiplexer-Systems. Ph.D. thesis, Kirchhoff Institute for Physics, July 2021. doi:https://doi.org/10.11588/heidok.00030266.

[123] J. M. Salum, T. Muscheid, A. Fuster, M. E. Garcia Redondo, M. R. Hampel, L. P. Ferreyro et al. "Aliasing Effect on Flux Ramp Demodulation: Nonlinearity in the Microwave Squid Multiplexer." *Journal of Low Temperature Physics*, vol. 213(3–4), p. 223–236, Aug. 2023. URL http://dx.doi.org/10.1007/s10909-023-02993-z.

[124] M. Schmelz, V. Zakosarenko, T. Schönau, S. Anders, S. Linzen, R. Stolz et al. "Nearly quantum limited nanoSQUIDs based on cross-type Nb/AlOx/Nb junctions." *Superconductor Science and Technology*, vol. 30(1), p. 014001. doi:https://doi.org/10.1088/0953-2048/30/1/014001, Nov. 2016.

[125] F. Harris. "On the use of windows for harmonic analysis with the discrete Fourier transform." *Proceedings of the IEEE*, vol. 66(1). doi:https://doi.org/10.1109/PROC.1978.10837, 1978.

[126] AMD Xilinx. UG579 - UltraScale Architecture DSP Slice User Guide, 2021. URL https://docs.xilinx.com/v/u/en-US/ug579-ultrascale-dsp.

[127] AMD Xilinx. JESD204. URL https://www.xilinx.com/products/intellectual-property/ef-di-jesd204.html#overview.

[128] AMD Xilinx. JESD204 PHY. URL https://www.xilinx.com/products/intellectual-property/ef-di-jesd204-phy.html.

[129] Tektronix. DPO7000 Series Digital Phosphor Oscilloscopes. URL https://www.tek.com/en/datasheet/dpo7000-series.

[130] P. Perez-Alcazar and A. Santos. "Relationship between sampling rate and quantization noise." In "2002 14th International Conference on Digital Signal Processing Proceedings. DSP 2002 (Cat. No.02TH8628)," vol. 2 of *ICDSP-02*, p. 807–810. IEEE. URL http://dx.doi.org/10.1109/ICDSP.2002.1028213.

[131] S. Arar. URL https://www.allaboutcircuits.com/technical-articles/what-is-dithering-using-noise-dithering-for-eliminating-the-quantization-distortion/.

[132] S. Dawson. URL https://www.hifi-writer.com/he/dvdaudio/dither.htm.

[133] Keysight. N9000A CXA Signal Analyzer, 9 kHz to 26.5 GHz. URL https://www.keysight.com/us/en/product/N9000A/cxa-signal-analyzer-9khz-26-5ghz.html.

[134] R. Pitaya. URL https://redpitaya.com/stemlab-125-14/?srsltid=AfmBOoqj8J9xiuDsBZyJ0f7l3ghy3GBkEQz4WEN0hxYMmUydG2Uotn3v.

[135] N. Hackelberg. URL https://github.com/tknopp/RedPitayaDAQServer.

[136] Mini-Circuits. URL https://www.minicircuits.com/pdfs/Gali-84+.pdf?srsltid=AfmBOorsSQ5jFSCY9HOmeh2lgtw6nXSh0k8YOvIW3RMT-u8gTVcX58dh.

[137] Picotest. G5100A Waveform Generator. URL https://www.picotest.com/products_G5100A.html.

[138] Bluefors. Dilution Refrigerator Measurement Systems - LD250. URL https://bluefors.com/products/dilution-refrigerator-measurement-systems/ld-dilution-refrigerator-measurement-system/.

[139] Low Noise Factory. LNF - LNC 4-8 GHz Ultra Low Noise Amplifier. URL https://lownoisefactory.com/product/lnf-lnc4_8f/.

[140] Keysight. URL https://www.keysight.com/us/en/product/N5242B/pna-x-microwave-network-analyzer-900-hz-10-mhz-26-5-ghz.html.